Revista de Ciencia y Tecnología

ARGENTINE JOURNAL OF SCIENCE AND TECHNOLOGY

Engineering, Technology and Informatics, Health, Biology and Genetics, Science and Technology Education, and Technical Note

YEAR 27 / Nº 43 / 2025

INDEX

Argentine Journal of Science and Technology on line: www.fceqyn.unam.edu.ar/recyt. Made the deposit of Law 11723. Printed in Argentina. ISSN of the printed journal: 0329-8922. ISSN of the electronic journal: 1851-7587.

All correspondence related to the Journal should be addressed to Argentine Journal of Science and Technology. Félix de Azara 1552, 3300, Posadas, Misiones, Argentina. E-mail: recyt@fceqyn.unam.edu.ar.
Biannual journal.

Argentine Journal of Science and Technology on line: www.fceqyn.unam.edu.ar/recyt. Made the deposit of Law 11723. Printed in Argentina. ISSN of the printed journal: 0329-8922. ISSN of the electronic journal: 1851-7587.

All correspondence related to the Journal should be addressed to Argentine Journal of Science and Technology. Félix de Azara 1552, 3300, Posadas, Misiones, Argentina. E-mail: recyt@fceqyn.unam.edu.ar.
Biannual journal.

Argentine Journal of Science and Technology on line: www.fceqyn.unam.edu.ar/recyt. Made the deposit of Law 11723. Printed in Argentina. ISSN of the printed journal: 0329-8922. ISSN of the electronic journal: 1851-7587.

All correspondence related to the Journal should be addressed to Argentine Journal of Science and Technology. Félix de Azara 1552, 3300, Posadas, Misiones, Argentina. E-mail: recyt@fceqyn.unam.edu.ar.

Biannual journal.

Argentine Journal of Science and Technology on line: www.fceqyn.unam.edu.ar/recyt. Made the deposit of Law 11723. Printed in Argentina. ISSN of the printed journal: 0329-8922. ISSN of the electronic journal: 1851-7587.

All correspondence related to the Journal should be addressed to Argentine Journal of Science and Technology. Félix de Azara 1552, 3300, Posadas, Misiones, Argentina. E-mail: recyt@fceqyn.unam.edu.ar.
Biannual journal.

RECyT Revista de Ciencia y Tecnología
Argentine Journal of Science and Technology

Presentation Note Nº 43

The Editorial Board presents in this opportunity the first issue of the year 2025 of the Argentine Journal of Science and Technology (Facultad de Ciencias Exactas, Químicas y Naturales, Universidad Nacional de Misiones).

It is available on the web page http://www.fceqyn.unam.edu.ar/recyt/.

This issue corresponds to number 43 and the following thematic areas are involved: Engineering, Technology and Informatics, Health, Biology and Genetics, Science and Technology Education, and Technical Note.

The institutions where the papers published in this issue were developed are the following:

- Centro de Investigaciones Apícolas Tropicales. Facultad de Ciencias de la Tierra y el Mar. Universidad Nacional de Costa Rica. Costa Rica.
- Centro Nacional de Biotecnología. Costa Rica.
- Escuela de Medicina Veterinaria, Facultad de Salud. Universidad Nacional de Costa Rica. Costa Rica.
- Laboratorio de Productos Naturales y Ensayos Biológicos. Escuela de Química. Facultad de Ciencias Exactas y Naturales. Universidad Nacional de Costa Rica. Costa Rica.
- Departamento de Gestión Ambiental. Centro de Ingeniería Ambiental de Camagüey. Cuba.
- Escuela de Biología, Facultad de Ciencias Exactas y Naturales. Universidad Nacional de Costa Rica.
- Facultad de Ciencias Aplicadas. Universidad de Camagüey "Ignacio Agramonte Loynaz". Cuba.
- University of Physical Culture and Sport Sciences "Manuel Fajardo". Cuba.
- Brazilian Agricultural Research Corporation. Brazil.
- Federal Institute of Education, Science and Technology of Rio Grande do Norte. Brasil.
- Federal Institute of Education, Science and Technology of Southeast Minas Gerais. Brasil.
- Federal University of Viçosa. Brazil.
- Instituto de Tecnologia. Universidade Federal do Pará. Belém, Pará, Brasil.
- Instituto Federal de Santa Catarina. Brasil.
- Universidade Estadual do Oeste do Paraná. Brasil.
- Universidade Federal da Grande Dourados. Brasil.
- Universidade Tecnológica Federal do Paraná. Brasil.
- Centro de Investigaciones en Fitopatología. Facultad de Ciencias Agrarias y Forestales. Universidad Nacional de La Plata. Argentina.

- Departamento de Evaluación Sensorial de Alimentos. Instituto Superior Experimental de Tecnología Alimentaria. Argentina.
- Instituto de Materiales de Misiones (IMAM-CONICET). Facultad de Ciencias Exactas, Químicas y Naturales. Universidad Nacional de Misiones. Argentina.
- Instituto Multidisciplinario de Investigación y Transferencia Agroalimentaria y Biotecnología (IMITAB-CONICET). Instituto de Ciencias Básicas y Aplicadas. Universidad Nacional de Villa María. Argentina.
- Laboratorio de Biotecnología Molecular. Instituto de Biotecnología Misiones "Dra. María Ebe Reca". Facultad de Ciencias Exactas, Químicas y Naturales. Universidad Nacional de Misiones. Argentina.

Special thanks are given to the guest editors of this issue: PhD. Nancy Lovera (Guest), Mgter. Williams Pedrozo (Guest), Dra. Andrea Micaela Dallagnol (Guest), Mgter. Sergio Surkan (Guest), Dra. Alejandra Roman (Guest).

Likewise, we want to thank the Science and Technique General Secretariat of the Universidad Nacional de Misiones, the Administrative Secretariat and the Research, Development and Innovation Secretariat of the Facultad de Ciencias Exactas, Químicas y Naturales for their financial support, as well as, the Editorial Team for their constant work (Agustina Gaona Duarte, Marcos Oliva, Lara Granada Lanús, Ana Paula Maier, José Roa, Fernanda Villamil, Lara Granada Lanús, PhD. Nancy Ganz, and ASC. Víctor Narváez).

PhD. Alicia E. ARES
Editor-in-Chief
Revista de Ciencia y Tecnología (RECyT)
Argentine Journal of Science and Technology
Facultad de Ciencias Exactas, Químicas y Naturales
Universidad Nacional de Misiones
recyt@fceqyn.unam.edu.ar
www.fceqyn.unam.edu.ar/recyt

RECyT
Year 27 / Nº 43 / 2025 /
DOI: https://doi.org/10.36995/j.recyt.2025.43.001

Improving the efficiency of photovoltaic generation by adapting to meteorological elements

Mejora de la eficiencia de la generación fotovoltaica adaptándose a los elementos meteorológicos

Melhoria da eficiência da geração fotovoltaica por meio da adaptação aos elementos meteorológicos

Elisardo do Prado, Porto[1, *]; Cássio Aurélio, Suski[1]

1- Santa Catarina Federal Institute. Brazil.
* E-mail: elisardo.porto@ifsc.edu.br

Received: 01/12/2023; Accepted: 12/11/2024

Abstract
The production of clean electricity, which does not harm environmental systems, has been one of the main global priorities in recent times. The range of ultraviolet radiation, sent through sunlight, which can be captured by photovoltaic cells and transformed into electrical energy, makes the sun the most promising source to supply the electrical needs of human beings. The climate is of considerable importance in capturing solar energy, as the efficiency of a cell system is directly related to local climate conditions. This paper aims to analyse the influence of meteorological elements on the efficiency of photovoltaic energy generation and its climatic effect. The methodology is based on measuring the generation of electricity through photovoltaic cells, compiling meteorological elements and panel temperature, studying the relationship between electricity generation using photovoltaic cells and other parameters, and surveying parameters to improve the efficiency of clean energy generation. The results show a relationship between the generation of electricity through photovoltaic cells and the other parameters, providing an average generation 11% higher in wind directions between 330 and 360° at the study site, as well as enabling an alternative to reduce of up to 5.3% of the emission of greenhouse gases through the expansion of photovoltaic energy generation and reduction of energy generation by hydroelectric and thermoelectric plants, which are currently positioned as the largest sources in Brazil.

Keywords: Photovoltaic, Solar energy, Climate and environment, Meteorological elements, Greenhouse gases.

Resumen
La producción de electricidad limpia que no dañe los sistemas medioambientales ha sido una de las principales carreras mundiales de los últimos tiempos. Los niveles de radiación ultravioleta, enviada a través de la luz solar, que pueden ser captadas por células fotovoltaicas y transformar la luz en energía eléctrica, hacen del sol la fuente más prometedora para satisfacer las necesidades eléctricas de los seres humanos. El clima tiene una importancia considerable a la hora de captar energía solar, ya que la eficiencia de un sistema celular está directamente relacionada con las condiciones climáticas locales. Este trabajo tiene como objetivo analizar la influencia de los elementos meteorológicos en la eficiencia de la generación de energía fotovoltaica y su efecto climático. La metodología se basa en la medición de la generación de electricidad mediante celdas fotovoltaicas, en la recopilación de elementos meteorológicos y temperatura del panel; en el estudio de la relación entre la generación de electricidad mediante células fotovoltaicas y el resto de parámetros y en el estudio de los parámetros para la mejora de la eficiencia de la generación de energía limpia. Los resultados muestran una relación entre la generación de electricidad a través de células fotovoltaicas y el resto de parámetros, proporcionando una generación promedio un 11% mayor en direcciones del viento entre 330 y 360° en el sitio de estudio, además de permitir una alternativa de reducción de hasta 5,3 % de la emisión de gases de efecto invernadero a través de la expansión de la generación de energía fotovoltaica y la reducción de la generación de energía por centrales hidroeléctricas y termoeléctricas, que actualmente se posicionan como las mayores fuentes de Brasil.

Palabras clave: Fotovoltaica, Energía solar, Clima y medio ambiente, Elementos meteorológicos, Gases de efecto invernadero.

Resumo
A produção de eletricidade limpa, que não agride os sistemas ambientais, tem sido uma das principais corridas globais dos últimos tempos. As faixas de radiação ultravioleta, enviadas através da luz solar, que podem ser captadas pelas células fotovoltaicas e transformar a luz em energia elétrica, fazem do sol a fonte mais promissora para suprir as necessidades elétricas do ser humano. O clima tem considerável importância na captação de energia

solar, pois a eficiência de um sistema celular está diretamente relacionada às condições climáticas locais. Este artigo tem como objetivo analisar a influência dos elementos meteorológicos na eficiência da geração de energia fotovoltaica e seu efeito climático. A metodologia baseia-se na medição da geração de energia elétrica por meio de células fotovoltaicas, na compilação de elementos meteorológicos e temperatura do painel; no estudo da relação entre a geração de energia elétrica por meio de células fotovoltaicas e os demais parâmetros e no levantamento dos parâmetros para melhoria da eficiência da geração de energia limpa. Os resultados mostram uma relação entre a geração de energia elétrica através de células fotovoltaicas e os demais parâmetros, proporcionando uma geração média 11% maior nas direções do vento entre 330 e 360° no local de estudo, além de possibilitar uma alternativa de redução de até 5,3 % da emissão de gases de efeito estufa através da expansão da geração de energia fotovoltaica e redução da geração de energia pelas usinas hidrelétricas e termelétricas, que atualmente se posicionam como as maiores fontes do Brasil.

Palavras-chave: Fotovoltaica, Energia solar, Clima e meio ambiente, Elementos meteorológicos, Gases de efeito estufa.

Introduction

Global warming and clean energy production are important concerns related to climate and the environment. The lack of investment, combined with the lack of information and practical projects on the part of public authorities, justifies the slow progress in the conquest of clean energies.

The increase in global temperature is exacerbated by anthropogenic actions that disrupt the planet's natural greenhouse effect, primarily due to rising greenhouse gas emissions. This is caused by the burning of fossil fuels in thermoelectric plants, the decomposition of organic matter left over from the cutting of trees and the carbon present in the soil flooded by hydroelectric plants, among other emission sources.

The energy generated by the sun, an inexhaustible source on the timescale of planet Earth's existence, in its two main functions of heat and light, is undoubtedly one of the most promising energy alternatives for providing the energy necessary for human development. When talking about energy, it should be remembered that the sun is responsible for the origin of virtually all other energy sources on Earth (Hayat *et al.*, 2018).

Atmospheric factors generally observed in the production of solar energy are cloudiness, air humidity and ambient temperature, but the availability of solar radiation, which is the incident energy on the earth's surface, is also influenced by the inclination of the planet in relation to the sun that varies during the day, month and year (ANEEL, 2008).

The duration of sunlight varies according to the region of the planet and time of year, specifically mentioning the issue of the solstices that occur at the North Pole, when on December 21st there may even be no sun exposure, or on June 21st, when it can reach up to 24 hours of sun exposure (Raza *et al.*, 2019).

The first studies on the photovoltaic effect were observed in 1839 and improved with the use of other materials. The first significant advances in these studies occurred between the 1930s and 1950s of the last century, with the development of photovoltaic cells composed of silicon crystals, which form the basis of current cells (Wolfe, 2018).

The photoelectric effect is a physical process of the element that converts sunlight into electrical energy, and the light energy absorbed by the photovoltaic cell is transferred to its atoms and electrons. These electrons are released from the component atoms of the semiconductor material, allowing for the electric current to flow through in an ordered manner (Hanifi *et al.*, 2018).

Photovoltaic modules are a set of encapsulated photovoltaic cells, whose purpose is to protect the cells from the weather, mainly from air humidity (Kholod *et al.*, 2018).

Pure photovoltaic generation is one that does not involve any other form of electricity generation. Since the system generates electricity only during sunny hours, autonomous or off-grid systems are equipped with accumulators that store energy for periods without sunlight, which take place every night, and during rainy or cloudy periods. Accumulators are batteries sized according to the autonomy of the system. Conventional off-grid power systems for charging battery banks require a charge controller with Maximum Power Point Tracking (MPPT) technology (Jain *et al.*, 2021).

According to the National Electric Energy Agency (ANEEL, 2018), Brazil has an installed solar generating plant capacity of

1,797,580 kW, which represents 1% of the total power of projects in Brazil. However, the number of solar photovoltaic generating centres is 2,273 units, representing approximately 32% of the total number of installed projects, second only to thermoelectric plants.

Regarding the effective participation in the generation of electricity in the Brazilian electrical system, solar energy has evolved in recent years, with 5.7% in 2016, 7.2% in 2017, and 8.3% in 2018. That is, investments in new generating units have been increasing (ANEEL, 2018).

However, according to Matin *et al.* (2020), only 33.33% of the light energy incident on photovoltaic cells is absorbed for the generation of electricity; that is, the generation efficiency of photovoltaic cells is still quite low and influenced by temperature, solar irradiance and, consequently, by meteorological elements. Despite this, few studies evaluate the meteorological variables that are related to the efficiency of electric power generation.

Climatic conditions play a crucial role in solar energy generation, as the excess or lack of specific phenomena can impact energy capture. A climate with high humidity and no wind can generate excessively hot conditions near the cells, which impairs energy production, and, in addition, humidity can create precipitation and clouds that cover up and make it difficult to absorb solar radiation. Wind is one of the key elements, as it moves air masses, pushing moisture and clouds and cooling the photovoltaic system (Navntoft *et al.*, 2019).

This study is justified by the excellent opportunity for research work to assess the influence of meteorological elements on the efficiency of electricity generation by photovoltaic cells, aiming to enable the increased participation of solar power plants in electricity generation. With this objective in mind, among other subjects, the primary sources of electricity generation, the respective greenhouse gas emissions and how meteorological elements can affect the generation of energy by photovoltaic cells will be analysed.

Methodology

For the development of research and analysis of the influence of meteorological elements on the efficiency of electricity generation using photovoltaic cells, the study was divided into the following stages: measurement of electricity generation using photovoltaic cells; compilation of meteorological elements and panel temperature; relationship between the generation of electricity through photovoltaic cells and the other parameters, and parameters for improving the efficiency of clean energy generation.

Study area

The study was carried out in the city of Itajaí (Figure 1), located on the north coast of the state of Santa Catarina (Latitude 26° 55' 51" S and Longitude 048° 41' 05" W), on the right bank of the mouth of the Itajaí-Açu river, in the southern region of Brazil.

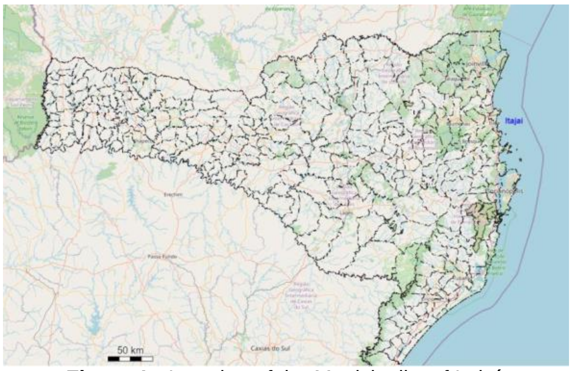

Figure 1 - Location of the Municipality of Itajaí.
Source: Map generated from Interactive Map information - GeoSEUC / Unofficial basemap, © OpenStreetMap contributors.

Measurement of electricity generation using photovoltaic cells

The measurement of local electricity generation was conducted from December 2022 to April 2023. For this measurement, a solar energy generator kit with photovoltaic cells, model CS6U-325P, manufactured by Canadian Solar, was used. It was installed in the Northwest direction (282° NW).

The kit was attached to the Sanches prototype meteorological station (2020), with wind direction (HMC-5883 sensor), wind speed (Hall sensor - US-1881), relative humidity (HDC-1080 sensor), atmospheric pressure and temperature sensors (BMP-180), as well as UV sensors ML8511, Type K Thermocouple Temperature Sensor of the solar cell and data transmission via RS485 communication cable to USB with reading software installed.

The set, comprising mechanical and electrical-electronic structures, was installed in a free area on a roof, approximately 12 meters above the ground.

The electro-electronic structure is composed of an XTRA4210N-XDS2 battery charge and discharge controller and 40A flow current with MPPT (Maximum Power Point Tracking) technology, together with a bank of 03 Model 12MN105 batteries, the Model IP2000-22 inverter module and the protection system with circuit breakers, earthing and lightning protection devices.

Figure 2 demonstrates the layout scheme formed by the photovoltaic cell system, weather station and protection devices.

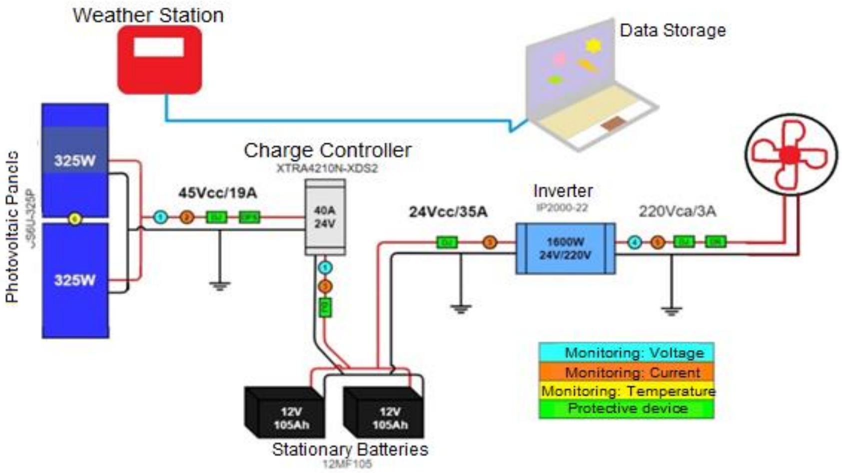

Figure 2 - Sensor installation scheme.
Source: Author.

The power generation set was installed and later calibrated by checking the voltage and current at the input and output of the controller using a multimeter (ET-1002 Minipa). This verification ensured that the voltage (37.0 V) and current (8.0 V, 78 A) were adequate, and consequently, power was generated (325 W).

The system operates off-grid (i.e., it is not connected to the official energy distributor's network) and is connected to consumer equipment with approximately 500W of power during the entire period of energy generation.

The reading of the generated voltage (V), current produced (A), and calculated power (W) was performed every 10 minutes using the XTRA4210N-XDS2 charge controller, which is available in real time on a display and in LandStar B software (LS-B).

Subsequently, the voltage, current, and power reading data were correlated with the meteorological elements and panel temperature.

Compilation of meteorological elements and panel temperature

The meteorological station performed readings of meteorological elements, including wind speed and direction, relative humidity, atmospheric pressure, air temperature, UV radiation, and panel temperature, synchronised with the reading of the charge controller (electricity) every 10 minutes.

The meteorological station utilised an electronic prototyping platform featuring free hardware and a single-board microcontroller (Arduino) that employs the C++ programming language. This platform generated a database of the parameters above.

Relationship between the generation of electricity through photovoltaic cells and the other parameters

After measuring and compiling the data obtained in C++ and LS-B (Embedded) programming languages, Table 1 was formatted, along with correlation graphs for discussion and analysis of the influence of

meteorological elements on energy generation.
In this step, the power generated by the panel was correlated with meteorological elements (wind speed and direction, relative humidity, atmospheric pressure, temperature, and ultraviolet radiation) and panel temperature to assess the efficiency of the photovoltaic cells in generating electric energy. Such correlations, as well as basic statistics, were obtained using Minitab, with support from Spearman's Rho method.

Table 1 - Relationship between the generation of electricity through photovoltaic cells and the other parameters.

DT	H	GER	PT	T	RH	UV	WS	WD	AP
d/m/y	h:m:s	W	°C	°C	%	Index	m/s	°	mmHg

Where: DT = Date, H = Time, GER = Generation, PT = Panel Temperature, T = Ambient Temperature, RH = Relative Humidity of Air, UV = Ultraviolet, WS = Wind Speed, WD = Wind Direction, AP = Atmospheric Pressure,
Source: Author.

The analysis first considered the average generation of the four quadrants of the wind direction (WD), between 0 and 360°, of the third quartile (above 175 W of photovoltaic energy generation) and, subsequently, it was possible to identify more specifically the wind directions (330-360°) that had the highest mean power generation for the third quartile.
From these data, correlations were made between the variables wind speed, relative humidity, atmospheric pressure, temperature, radiation (UV) and panel temperature.

Parameters for improving the efficiency of clean energy generation

Through the interpolation of the relationship of the parameters, the hypothesis of use was generated in relation to the installation position and the meteorological elements to obtain the best efficiency of the photovoltaic cells, providing the reduction of the use of electric energy generated by hydroelectric and thermoelectric plants and, consequently, predicting their influence on the environmental impact and the generation of greenhouse gases (GHG).
The effect of improving the efficiency of clean energy generation on the environment was measured through a survey of the possible reduction of hydroelectric plants and by the decrease in fuel consumption (oil, biomass and coal) in thermoelectric plants and, consequently, the emission of GHG.
For the evaluation of the reduction of GHG emissions in this study, three scenarios were proposed (Table 2), in addition to the current scenario. The scenario categorised as current is based on the percentage of electricity generation in Brazil in 2018. The other scenarios were determined with gradual reductions in the percentage of use of hydroelectric (hydraulic) and thermoelectric (biomass, oil and coal) plants. Based on the proposed scenarios, GHG emission reductions were calculated using the emission factors for each emission source.
To estimate CO_2 emissions in hydraulic, wind, natural gas, oil, coal and nuclear energy generation, the emission factors estimated by Miranda[1] (2012) were considered.
The biomass and solar emission factors were obtained from the Low Carbon Study for Brazil[2] - Land Use, Land Use Change and Forests by Soares Filho *et al.* (2010) and the Covenant of Mayors for Climate and Energy[3] by Neves *et al.* (2016), respectively (Table 3). For the case of energy in hydroelectric plants, Life Cycle Assessment studies were considered that encompass stages of construction, generation, and emissions from reservoirs, as these have significant emissions and characterise the operation phase of the plant. Additionally, the total installed capacity of electricity-generating sources in Brazil is 164,187 MW.

Table 2 - Proposed scenarios for analysis of greenhouse gas emissions (%).

Percentage of energy generation by type of source									
Scenario	**Hydraulics**	**Biomass**	**Wind**	**Natural gas**	**Oil**	**Coal**	**Nuclear**	**Solar**	**Total**
Current (2018)	63.7	9.0	8.8	8.0	6.1	2.2	1.2	1.0	100
1	63.2	8.8	8.8	8.0	6.0	2.0	1.2	2.0	

2	62.6	8.7	8.8	8.0	5.9	1.8	1.2	3.0
3	62.0	8.6	8.8	8.0	5.8	1.6	1.2	4.0

Source: ANEEL, 2018

Table 3 - GHG emission factors from generation sources.

	Hydraulics[1]	Biomass[2]	Wind[1]	Natural Gas[1]	Oil[1]	Coal[1]	Nuclear[1]	Solar[3]
Factor (gCO $_{2eq}$ /kWh)	86	1580	16	518	829	1144	14	50

Source: Author.

The methodology for calculating carbon emissions for energy generation sources (E_{GHG}) is based on the installed energy production capacity (C_{PLANT}) and the GHG emission factor (F_{GHG}), and the calculation can be represented by Equation 1:

$$E_{GHG} = (CP_{PLANT} \; x \; F_{GHG}) \quad (1)$$

Where:
E_{GHG} - Estimate of GHG generation (ton CO_{2eq})
CP_{PLANT} - Installed Energy Production Capacity (kWh)
F_{GHG}- GHG emission factor (gCO_{2eq} /kWh)

To calculate the reduction in the area of the hydroelectric reservoir due to the decrease in generation through this source, Equations 2 and 3 are used.

$$E_{GHG\ at} = (E_{GHG} \; x \; A_{RES\ CUR}) \quad (2)$$

Where:
$E_{GHG\ at}$ - GHG generation in hydroelectric plants for the total flooded area (ton CO_{2eq});
E_{GHG} - GHG emissions ton CO_{2eq} per km^2;
$A_{RES\ CUR}$ - Total reservoir area in the current scenario (km^2).

$$R_{ARES} = (A_{RES\ CUR} - A_{RES\ SCEN3}) \quad (3)$$

Where:
R_{ARES} - Reduction of hydroelectric reservoir area (km^2);
$A_{RES\ CUR}$ - Area of the hydroelectric reservoir in the current scenario (km^2);
$A_{RES\ SCEN3}$ - Hydroelectric reservoir area in scenario 3 (km^2).

Results and discussions

Measurement and relationship of electricity generation with other parameters

Figure 3 shows scatter plots between power generation and wind direction in four different situations. One can observe the increasing trend of generations as the wind direction approaches the fourth quadrant (Figure 3a). By filtering the data for the third quartile of generation, that is, where the highest generation of energy occurs, it is also possible to perceive the increasing trend of the data (Figures 3b and 3c), which makes it possible to observe a higher average generation of energy in the wind direction of 330 - 360° (Figure 3d).
Table 4 shows the average energy generation (general data) of 100.18 W, and Table 5 shows the energy generation correlations with the other parameters, with the most significant values of UV and panel temperature, 0.483 and 0.442, respectively.

a. General generation data for all WD

b. Generation data greater than 175 W (third quartile) for all WD

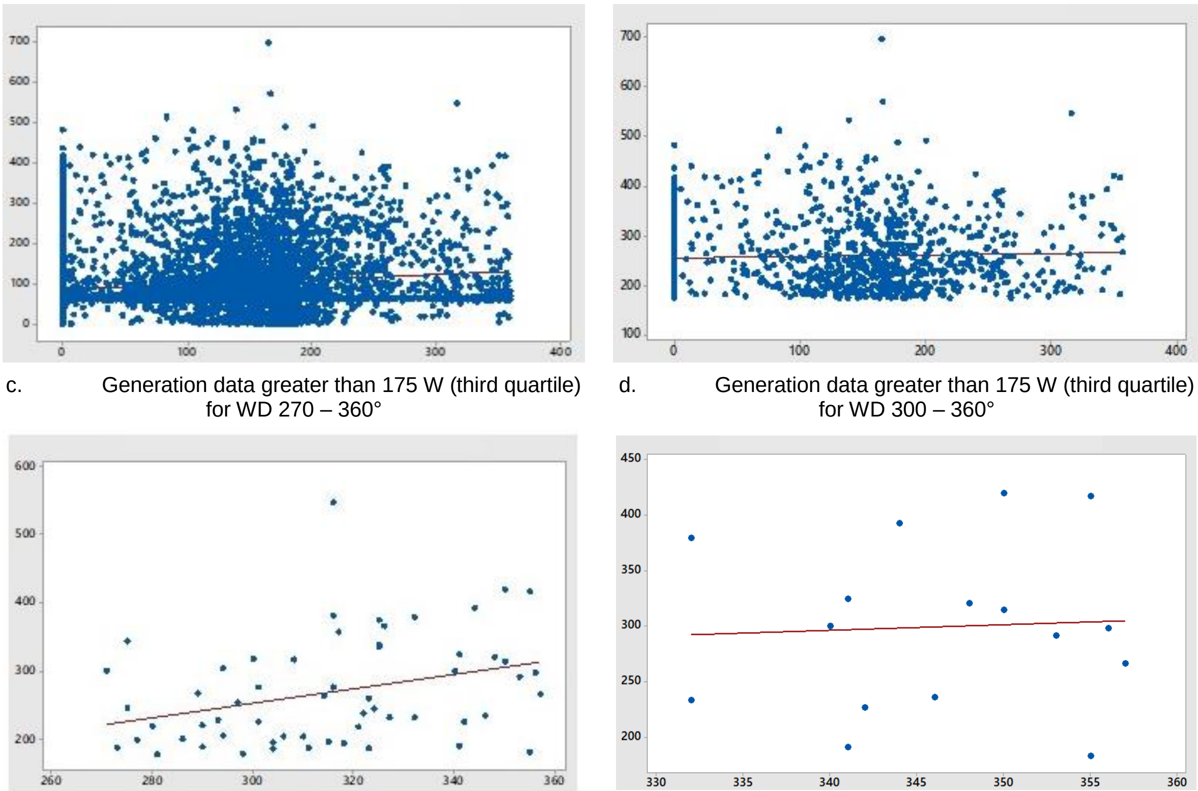

c. Generation data greater than 175 W (third quartile) for WD 270 – 360°

d. Generation data greater than 175 W (third quartile) for WD 300 – 360°

Figure 3 - Scatter charts with trend line.

Table 4 - Mean values (general data) of the analysed parameters.

GER (W)	PT (°C)	T (°C)	RH (%)	UV (mW/c)	WS (m/s)	WD (°)	AP (mmHg)
100.18	227.33	29.04	59.00	7.00	0.16	98.44	1,012.30

Table 5 - Correlations between generation and other parameters.

	PT	T	RH	UV	WS	WD	AP
Generation	0.442	0.371	-0.338	0.483	0.068	0.157	0.044
p-value	0.000	0.000	0.000	0.000	0.000	0.000	0.000

With the fractionation of the historical series of energy generation in subsamples, using the third quartile of the wind direction as a filter, that is, dividing 25% of the data of the largest generations into four quadrants of wind performance, where 0 to 90° constitute the first sample, between 90 and 180° the second sample, and so on, it is observed in Table 6 that the average power generation is 258.79 W between 0 and 90° (first quadrant), 257.36 W in the second quadrant, 257.47 W in the third quadrant and 270.00 W in the fourth quadrant, resulting in a slight increase in generation efficiency in the last quadrant in relation to the other quadrants.

After surveying the averages of electric energy generation in the third quartile in relation to each quadrant of wind direction, the range of analysis can be adjusted for the highest average of energy generations and, with that, it was identified that the wind direction between 330 and 360° has the highest average generation of the third quartile, with a value of 299.6 W (Table 7), resulting in an increase in energy generation efficiency of approximately 11% in relation to the average of the fourth quadrant.

Employing the correlations (Tables 8 to 12) between the values obtained by reading the meteorological elements and the generation

data and panel temperature, a more detailed observation of these data can be initiated.
It can be observed that, in general, the correlations between energy generation and wind direction, panel temperature and ultraviolet radiation provide more significant values concerning the other elements.

Table 6 - Mean values of parameters analysed in the third quartile in relation to wind direction.

a. Generation greater than 175 W and WD between 0 and 90°

Variable	N	N*	Average	SE average	Standard deviation	Minimum	Q1	Median	Q3	Maximum
Generation	465	0	258.79	3.07	66.22	175.07	205.90	244.70	296.13	513.47
PT	465	0	30,130	0.182	3,923	20,660	29,650	29,650	32,360	43,250
T	465	0	31,163	0.125	2,685	20,610	31,790	31,790	33,330	41,530
RH	465	0	51,829	0.438	9,434	30,240	50,970	50,970	51,175	86,800
UV	465	0	7.2224	0.0262	0.5640	6.0400	7.1400	7.1400	7,5500	9.9100
WS	465	0	0.0594	0.0064	0.1389	0.0000	0.0000	0.0000	0.1000	0.9100
WD	465	0	12.13	1.18	25.50	0.00	0.00	0.00	0.00	90.00
AP	465	0	1012.7	0.161	3.48	101.4	1013.5	1013.5	1015.4	1020.5

b. Generation greater than 175 W and WD between 90 and 180°

Variable	N	N*	Average	SE average	Standard deviation	Minimum	Q1	Median	Q3	Maximum
Generation	495	0	257.36	3.30	73.49	175.00	200.85	237.19	297.84	696.47
PT	495	0	29,923	0.206	4,583	16,770	26,980	29,410	32,160	44,180
T	495	0	30,514	0.143	3,172	17,240	28,560	30,710	32,450	39,920
RH	495	0	51,900	0.404	8,978	26,920	45,330	51,400	57,970	79,370
UV	495	0	7.2905	0.0259	0.5768	6.1300	6,9000	7,1800	7,6700	9,8700
WS	495	0	0.1737	0.0072	0.1612	0.0200	0.0500	0.1200	0.2400	0.8700
WD	495	0	148.32	1.14	25.34	90.00	129.00	152.00	170.00	180.00
AP	495	0	1013.3	0.158	3.51	1003.6	1011.0	1013.9	1015.8	1020.4

c. Generation greater than 175 W and WD between 180 and 270°

Variable	N	N*	Average	SE average	Standard deviation	Minimum	Q1	Median	Q3	Maximum
Generation	238	0	257.47	3.95	60.90	175.12	206.36	244.71	297.44	491.49
PT	238	0	29,350	0.262	4,049	16,770	26,488	29,155	31,595	40,330
T	238	0	30,673	0.221	3,413	17,240	28,212	31,140	33,245	37,570
RH	238	0	51,617	0.549	8,475	36,460	45,863	50,045	56,438	78,870
UV	238	0	7.2196	0.0325	0.5015	5.6400	6.9300	7.1400	7.5200	9.0200
WS	238	0	0.1441	0.0076	0.1181	0.0200	0.0500	0.11000	0.2000	0.5900
WD	238	0	215.95	1.79	27.64	180.00	191.00	212.00	241.25	270.00
AP	238	0	1011.5	0.244	3.76	1003.6	1008.3	1011.2	1013.9	1020.5

d. Generation greater than 175 W and WD between 270 and 360°

Variable	N	N*	Average	SE average	Standard deviation	Minimum	Q1	Median	Q3	Maximum
Generation	58	0	270.0	10.2	77.4	177.7	203.8	250.2	318.6	546.2
PT	58	0	31,868	0.568	4,323	23,270	29,260	31,050	34,255	45,860
T	58	0	32,664	0.416	3,166	25,250	31,248	32,475	34,487	42,290
RH	58	0	46.16	1.12	8.53	31.15	40.45	44.91	50.54	73.22
UV	58	0	7,4891	0.0733	0.5579	6,5700	7.0200	7.5300	7,8000	9.3400
WS	58	0	0.1895	0.0210	0.1602	0.0200	0.0700	0.1450	0.2775	0.7700
WD	58	0	315.57	3.21	24.45	271.00	296.25	316.00	334.00	357.00
AP	58	0	1011.6	0.545	4.15	1004.4	1007.6	1012.0	1014.8	1019.9

Table 7 - Mean values of parameters analysed in the third quartile in relation to wind direction between 330 and 360°.

Variable	N	N*	Average	SE average	Standard deviation	Minimum	Q1	Median	Q3	Maximum
Generation	16	0	299.6	18.8	75.3	182.7	233.8	299.1	365.7	419.7
PT	16	0	31,737	0.828	3,314	26,500	29,343	31,240	33,295	39,700
T	16	0	33,180	0.898	3,591	26,600	30,782	32,285	35,907	40,730
RH	16	0	46.09	2.45	9.81	34.62	39.17	06.43	52.23	72.64
UV	16	0	7,917	0.160	0.638	6,940	7,630	7,755	8,287	9,340
WS	16	0	0.2650	0.0542	0.2167	0.0200	0.1250	0.2100	0.4050	0.7700
WD	16	0	346.38	2.00	8.02	332.00	341.00	347.00	354.50	357.00
AP	16	0	1011.1	0.883	3.53	1004.4	1009.2	1012.0	1012.9	1016.4

In the third quadrant (Table 10), the highest correlation between ultraviolet radiation and power generation can be found, reaching a value of 0.401, considered moderate. There is still an inverse proportional relationship in relation to relative humidity of -0.313. Given these numerical factors, one can, empirically, have an impression of this being the quadrant

that presents the most positive results for the study.
However, when establishing a correlation by observing the concentration of data with higher generation values, it is identified that there is a range of coordinates in the northwest direction, 330 to 360° (Table 12), which presents average values of generation (299.6 W) that are higher (Figure 4).

Table 8 - Correlation of 1st wind direction quadrant (0 to 90°) and generation greater than 175 W.

	PT	T	RH	UV	WS	WD	AP
Generation	0.308	0.223	-0.284	0.308	0.180	0.184	-0.093
p-value	0.000	0.000	0.000	0.000	0.000	0.000	0.000

Table 9 - Correlation of 2nd wind direction quadrant (90 to 180°) and generation greater than 175 W.

	PT	T	RH	UV	WS	WD	AP
Generation	0.228	0.207	-0.181	0.292	0.063	-0.019	-0.096
p-value	0.000	0.000	0.000	0.000	0.162	0.674	0.032

Table 10 - Correlation of 3rd wind direction quadrant (180 to 270°) and generation greater than 175 W.

	PT	T	RH	UV	WS	WD	AP
Generation	0.397	0.315	-0.313	0.401	0.132	0.066	-0.132
p-value	0.000	0.000	0.000	0.000	0.043	0.314	0.041

Table 11 - Correlation of 4th wind direction quadrant (270 to 360°) and generation greater than 175 W.

	PT	T	RH	UV	WS	WD	AP
Generation	0.115	-0.018	0.077	0.253	0.082	0.333	-0.119
p-value	0.392	0.892	0.567	0.053	0.540	0.011	0.375

Table 12 - Correlations for wind direction (330 to 360°) and generation greater than 175 W.

	PT	T	RH	UV	WS	WD	AP
Generation	-0.112	-0.271	0.315	-0.231	-0.021	0.010	0.253
p-value	0.680	0.311	0.425	0.389	0.940	0.970	0.345

To make data analysis more accurate, it can be observed that, in addition to the wind direction between 330 and 360º, there is a punctual estimate for the highest average, the lower limit for the average generation estimate, in this wind direction interval, nearly exceeds the upper bound for the average generation estimates for all other quadrants. The statistical test in this range rejects equality with a p-value of 0.07, which is very close to 95% reliability.

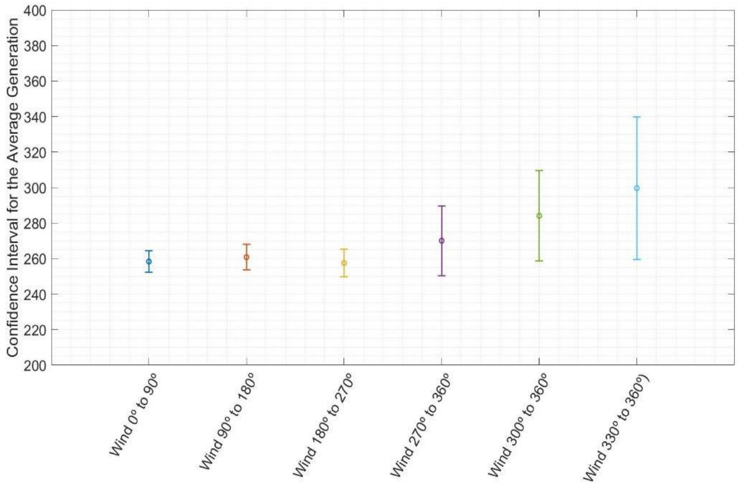

Figure 4 - Reliability Ratio for Energy Generation.

Thus, it can be observed that energy generation is a function of a composition of variables, which may differ in each region or location of installation of photovoltaic panels and, in this case in particular, higher generation occurs in wind directions between 330 and 360°, where the panel temperature, ambient temperature, ultraviolet radiation and wind speed are higher than in the other directions. Atmospheric pressure is maintained in all directions, and relative humidity is lower than in other directions.

According to Matin *et al.* (2020), the generation efficiency of photovoltaic cells is still relatively low and influenced by temperature and solar irradiance and, consequently, by meteorological elements.

Such specificity may be related to the characteristic geographic position of the observation site in the municipality of Itajaí, where the collector side of the photovoltaic panels is installed at 282° NW. The northwest wind is drier, originating from within the state of Santa Catarina, leaving the sky with less cloudiness and increasing the ultraviolet radiation, which falls within an optimal range for energy generation.

Climatic conditions play a crucial role in solar energy generation, as the excess or lack of certain phenomena can directly affect energy capture. A climate characterised by high humidity and a lack of wind can result in excessively hot conditions around solar cells, significantly impairing energy production. Additionally, the presence of moisture can lead to the formation of precipitation and clouds that cover and hinder the efficient absorption of solar radiation. The wind, in turn, is an essential element, as it has the role of moving air masses, displacing moisture and dispersing clouds. Furthermore, it plays a crucial role in cooling the PV system, thereby contributing to its overall efficiency and performance.

According to the sensitivity analysis conducted by LV *et al*. (2014), based on solar power generation measurement data in 2011, from a comprehensive perspective of daily and monthly power generation, the top five climate variables of importance are solar radiation time (i.e. solar radiation), speed wind, relative humidity, cloud cover and outside temperature.

The power generated by photovoltaic modules is linearly dependent on irradiance, except for small values of irradiance when the output power is zero. The efficiency of the photovoltaic plant not only strongly depends on the irradiance, but also depends on the module temperature (Chokmajirov *et al.*, 2006).

In this study, no significant variations were identified between the panel temperature and the ambient temperature (Table 6), including the average temperature of the panel around 1°C lower than the ambient temperature. This fact may be related to the location and position of the panel's installation, as the photovoltaic set is elevated above the roof, allowing for air circulation and convection on the panels.

According to Hamrouni *et al.* (2008), for several solar radiations ranging from 100 to 1000 W/m² and for a constant temperature equal to 25 °C, there is an increase in generation with an increase in radiation and a maximum global efficiency of the photovoltaic system for 300 W/m² of radiation.

According to research by Kaldellis *et al.* (2014), as wind speed increases, the working temperature of photovoltaic cells gradually approaches ambient temperature, which affects the efficiency of power generation. Thus, the photovoltaic conversion process, in addition to instantaneous solar radiation, also depends on the temperature of the modules. The module temperature, in turn, is influenced by climatic conditions, as well as by the technical characteristics of the photovoltaic panels.

Solar irradiance has the most significant impact on the output power of a photovoltaic system (Diaf et al., 2008). In addition to irradiance, weather conditions such as ambient temperature, along with several other factors (e.g. angle of incidence [AOI], dust, etc.) (Kaldellis *et al.*, 2012) can also affect the power output and energy production of a photovoltaic module. To this end, the module temperature is influenced by the ambient temperature, cloud patterns and wind speed (Buday, 2011), while the temperature change rate also depends on the PV material and frame position.

Normally, the impact of free convection is quite limited, while the radiation mechanism is dominant during low wind speed values (Kaldellis *et al.*, 2014).

The photovoltaic conversion process, in addition to instantaneous solar radiation, also depends on the temperature of the modules. The module temperature, in turn, depends on climatic conditions (such as ambient temperature, solar irradiation, and wind speed) and the technical characteristics of the photovoltaic panels (including material, type, assembly, and ventilation) (Kaldellis *et al.*, 2014).

For a better characterisation and prediction of photovoltaic module performance under a wide variety of climatic conditions, several detailed studies have been carried out (Jacques *et al.*, 2013; Armstrong *et al.*, 2010) and several models have been proposed, with most of them based on only in controlled indoor measurements (for example, controlling the wind flow over the panel surface with fans).

Parameters for improving the efficiency of clean energy generation

Calculation of gas emissions from the various generation sources

Based on the results of improving the efficiency of photovoltaic energy generation, it is possible to perceive the potential for reducing greenhouse gas (GHG) emissions from hydroelectric and thermoelectric plants, thereby enhancing the use of solar energy.

Tables 13 and 14 show the values of energy generation and emissions calculated using Equation 1, by type of energy generation and for each proposed scenario. In these scenarios, the values referring to energy related to wind, natural gas, and nuclear were kept constant, while energy from hydraulic and thermal power plants (biomass, coal, and oil) was reduced, and energy from solar sources was increased.

In the current scenario, there is a total gas emission of 28,609 x 10 ^{6} ton CO_{2eq}, while in the proposed scenarios 28,170; 27,592 and 27,078 x 10 ^{6} ton CO_{2eq} are generated, that is, a reduction of approximately 1,531 x 10 ^{6} ton CO_{2eq} in Scenario 3 compared to the current scenario, which results in a 5.3% reduction.

According to the IPCC special report (2021), it is crucial to reduce greenhouse gas (GHG) emissions by 45% by 2030, compared to 2010 levels, to limit the increase in global average temperature to 1.5°C above pre-industrial levels. This reduction is necessary to avoid more serious consequences of climate change.

Although a 5.3% reduction in emissions, related to the generation of electricity in Brazil, is not enough to generate a significant impact on the increase in global average temperature, it is one more factor to be considered for mitigating global warming, and it is fundamental to recognise that this phenomenon is complex and influenced by several factors. Therefore, in addition to this progress, a significantly greater effort is needed, in terms of electricity generation sources, to achieve the global warming mitigation targets established by the IPCC and prevent significant and irreversible impacts.

Table 13 - Energy generation for each scenario and each generation source.

	Power generation (MW)								
Scenario	**Hydraulics**	**Biomass**	**Wind**	**Natural gas**	**Oil**	**Coal**	**Nuclear**	**Solar**	**Total**
Current (2018)	104,587	14,776	14,448	13,134	10,015	3,612	1,970	1,641	164,187
1	103,766	14,448	14,448	13,134	9,851	3,283	1,970	3,283	
2	102,781	14,284	14,448	13,134	9,687	2,955	1,970	4,925	
3	101,795	14,120	14,448	13,134	9,522	2,626	1,970	6,567	

Table 14 - GHG emissions for each scenario.

	Emissions (x 10 ^{6} ton CO_{2eq})									
Scenarios	**Hydraulics**	**Biomass**	**Wind**	**Natural gas**	**Oil**	**Coal**	**Nuclear**	**Solar**	**Total**	**Reduction (%)**
Current (2018)	9,016	12	233	6,805	8,302	4,132	27	82	28,609	-
1	8,945	11	233	6,805	8,166	3,756	27	164	28,107	1.7
2	8,860	11	233	6,805	8,030	3,380	27	246	27,592	3.5
3	8,775	11	233	6,805	7,894	3,005	27	328	27,078	5.3

Calculation of fuel consumption reduction

Due to the reduction in energy generation from thermoelectric plants, there is a reduction in consumption (Table 15) of fuels (coal, oil and biomass), reaching a maximum reduction of 27% for coal and approximately 5% for oil and biomass.

Table 15 - Reductions in fuel used in thermoelectric plants.

	Fuel consumption (kg)				
Fuel	**Current scenario**	**Scene 1**	**Scenario 2**	**Scenario 3**	**Reduction (%) Scenario 3 x Current scenario**
Coal	1,242,795	1,129,814	1,016,832	903,851	27.3
Oil	2,549,874	2,508,072	2,466,271	2,424,470	4.9
Biomass	7,628,195	7,458,679	7,373,921	7,289,164	4.5

Calculation of reservoir area reduction by reducing generation in hydroelectric plants

By reducing the percentage of energy generation through hydraulic sources, biomass, oil and coal (Table 14), maintaining energy generation through wind, natural gas and nuclear sources and expanding energy generation through solar source, in addition to a reduction in CO_2 emissions from the generation itself, there is also a possibility of reducing emissions from the generation of CH_4 due to the anaerobic decomposition of organic matter present in the hydroelectric lakes (Barros *et al.*, 2021).

Zanoni *et al.* (2015) analysed the characteristics of the flooded soil and the CH_4 production that is produced at the bottom of the reservoirs by the anaerobic decomposition of the organic matter and emitted in the water-air interface, through bubbles or diffusion, demonstrating that the local factors of the flooding influence the amount of CH_4 produced.

According to some authors (Louis *et al.*, 2000; Pueyo *et al.*, 2011), the average methane emission rate in hydroelectric plants can vary from 20 to 300 mg of CH_4 /m² per day, depending on local conditions.

According to the method presented by Santos *et al.* (2008), CH_4 emission is 18.29 kg.km^{-2}.day^{-1}, which corresponds to an annual emission of 0.36 ton x 10^{6} in 55,000 km² of reservoir area, resulting in 2.06 ton x 10^{6} CO_{2eq} year, considering a CH_4 GWP of 21.

Considering GHG generation in Hydroelectric Power Plants for the total flooded area (E_{GHGatl}), for the current scenario, at 9,016 x 10^6 ton CO_{2eq} (Table 14) and the total reservoir area of 55,000 km², the GHG emission per km² (E_{GHG}) can be calculated using Equation 2.

$$E_{GHG\ at} = (E_{GHG}\ x\ A_{RES\ CUR})$$

$$9.016\ x\ 10^6 = (E_{GHG}\ x\ 55.000)$$

$$E_{GHG} = 163.927\ \frac{ton\ CO_{2eq}}{Km^2}$$

From the issuance of scenario 3 (8,775 x 10^6 ton CO_{2eq} - Table 14), the final area of the reservoir can then be calculated.

$$E_{GHG\ at} = (E_{GHG}\ x\ A_{RES\ SCEN3})$$

$$8.775\ x\ 10^6 = (163.927\ x\ A_{RES\ SCEN3})$$

$$A_{RES\ SCEN3} = 53.529{,}84\ km^2$$

And, through Equation 3, it is possible to calculate its consequent reduction in area (approximately 2.7%), due to the reduction in energy generation through hydroelectric plants.

$$R_{ARES} = (A_{RES\ CUR} - A_{RES\ SCEN3})$$

$$R_{ARES} = (55.000 - 53.529{,}84)$$

$$R_{ARES} = 1.470{,}16\ km^2$$

These equations are a simplified way of estimating the generation of greenhouse gases in hydroelectric power plants and, it is important to remember that the emission factor may vary according to the characteristics of each plant and that other factors may influence emissions, such as the type of vegetation removed during the construction of the reservoir and the type of soil present in the region.

According to the ANEEL, there are approximately 220 hydroelectric power plants in operation in Brazil, with a total installed capacity of more than 104 gigawatts (GW) as of 2022. The ANEEL provides detailed information about each of these plants, including the size of dams, the area flooded and the volume of water stored.

Through studies by the Ministry of Mines and Energy of Brazil, it is possible to verify that in the year 2020 there was a significant consumption of energy from hydroelectric plants, totalling 396,381 GWh (MME, 2022). The substantial amount of energy generated by hydroelectric plants underscores the importance of this sector in the national energy matrix, highlighting its crucial role in supplying electricity to the country.

However, it is worth remembering that the hydroelectric plants in operation in Brazil have a total area of dams of approximately 55,000 km² (ANEEL, 2022) and it is also worth noting that the size of dams of hydroelectric plants in Brazil is subject of debate and controversy due to the socio-environmental impacts that these undertakings cause. Several organisations and social movements have questioned the construction of large dams, arguing that they cause the loss of forest areas, the displacement of traditional communities, and the forced relocation of riverside populations (Fearnside, 2020).

Amaral *et al.* (2019) conducted an environmental assessment of hydroelectric power plants in Brazil, employing life cycle analysis and inventory methodologies. Based on this, the authors calculated greenhouse gas (GHG) emissions and other environmental impact categories, considering the plant's power density to differentiate emissions per km² of flooded area. The results indicated that power density was a significant factor in determining GHG emissions, with notable variations between the evaluated power plants. The study emphasised the importance of considering power density as a key factor in the environmental assessment of hydroelectric power plants. The estimation of greenhouse gas emissions associated with hydroelectric energy generation can be performed using a simplified equation that considers the plant's energy generation capacity, the reservoir area, and the emission factor.

The works by Miranda (2012) and Amaral (2019) address the assessment of the environmental performance of hydroelectric power plants, focusing on the analysis of greenhouse gas (GHG) emissions. Both studies employ the life cycle approach to assess GHG emissions throughout the life cycle of power plants, from construction to end of life.

While Miranda (2012) emphasises the importance of considering the plant's power density in assessing GHG emissions, Amaral (2019) utilises this concept to calculate GHG emissions per square kilometre of flooded area. This approach enables a more accurate assessment of the environmental performance of various hydroelectric plants, taking into account the unique characteristics of each project. By combining these approaches, it is possible to obtain a more comprehensive assessment of the environmental performance of hydroelectric plants.

In addition, it is essential to note that the National Electric Energy Agency (ANEEL), in its Annual Report on the Inspection of the Use of the Union's Heritage (2022), uses electricity generation capacity and the total area of dams in Brazil as references to estimate greenhouse gas emissions. This approach considers the diversity of existing plants and dams in the country, which have different operational characteristics and environmental impacts. However, it is important to point out that this methodology can be improved with the inclusion of specific emission factors for each plant, as proposed by Miranda and Amaral.

Final considerations

By analysing the influence of wind direction and speed, ambient temperature, relative humidity, atmospheric pressure, ultraviolet radiation and panel temperature on the efficiency of photovoltaic energy generation and its climate effect, it can be identified that:

- The efficiency of photovoltaic energy generation can be influenced by the composition of meteorological elements and panel temperature, and may vary in each region or location where photovoltaic panels are installed.
- In the specific case of this study, there is an average generation 11% higher in wind directions between 330 and 360°, since the collector face of the photovoltaic panels is installed at 282° NW and the northwest wind is a drier wind, coming from within the state of Santa Catarina, leaving the sky with less cloudiness, expanding ultraviolet radiation to within a range of excellent standards for energy generation.
- The proposition of scenarios with an increase in the percentage of energy generation by photovoltaic panels results in a reduction in greenhouse gas emissions of up to 5.3%.
- The reduction in energy generation through hydroelectric plants, proposed in the scenarios, allows for a 2.7% reduction in the area of the reservoirs.
- The reduction in energy generation through thermoelectric plants, proposed in the scenarios, makes it possible to reduce the consumption of coal, oil and biomass by 27.3%, 4.9% and 4.5%, respectively.

The study provides one more factor to consider for mitigating global warming, and it is essential to recognise that this phenomenon is complex and influenced by several components.

References

AMARAL, TR, NAVEIRA-COTTA, CP, NASSER, LS, BEZERRA, BS, SANTOS, AM, & LIMA, RP (2019). Environmental performance of hydropower plants: A Brazilian case study. *Journal of Cleaner Production, 232*, 751-763.

ANEEL. (2008). *Atlas of Electrical Energy.* National Electric Energy Agency, Brasília.

ANEEL. (2018). *Performance Report for Centrally Dispatched Thermoelectric Power Plants – Types IE Iiad.* National Electric Energy Agency, Brasília.

ANEEL. (2022). *Generation Information Bank.* National Electric Energy Agency, Brasília.

ARMSTRONG, S., & HURLEY, W. (2010). A thermal model for photovoltaic panels under varying atmospheric conditions. *Appl Therm Eng, 30*, 11-12.

BARROS, N.E. (2021). Greenhouse gas emissions from hydroelectric reservoirs: what knowledge do we have and what needs to be done? *Renewable and Sustainable Energy Reviews, 147*, 111-131.

BUDAY, M. (2011). *Measuring irradiance, temperature, Corkishe and angle of incidence effects on photovoltaic modules in Auburn Hills.* Michigan: University of Michigan.

CHOKMAVIROJ, S., WATTANAPONG, R., & SUCHART, Y. (2006). Performance of a 500 kWp Grid-Connected Photovoltaic System at Mae Hong Son Province, Thailand. *Renewable Energy, 31*, 19.

DIAF, S., NOTTON, G., BELHAMEL, M., HADDADI, M., & LOUCHE, A. (2008). Design and technoeconomical optimisation for hybrid PV/wind system under various meteorological conditions. *Applied Energy, 85*, 968-987.

FEARNSIDE, PM (2020). Large hydroelectric dams in Brazilian Amazonia: A flawed climate solution?. Environmental Science & Policy, 112, 215-225.

JACQUES, S; CALDEIRA, A; REN, Z; SCHELLMANNS, A; BATUT, N. Impact of the cell temperature on the energy efficiency of a single glass PV module: thermal modelling in steady-state and validation by experimental data. In: Proceedings of the international conference on renewable energies and power quality 2013 (ICREPQ'13), Bilbao, Spain.

HAMROUNI, N., JRAIDI, M., & CHÉRIF, A. (1995). Solar radiation and ambient temperature effects on the performance of a PV pumping system. *Revue des Energies Renouvelables* , pp. 95 – 106.

HANIFI, HP (2018). A Practical Optical and Electrical Model to Estimate the Power Losses and Quantification of Different Heat Sources in Silicon-Based PV Module. *Renewable Energy*, pp. 602-612.

KHOLOD, Yana et al. Excitation Energy Transfer Pathways in Light-harvesting Proteins: Modelling with PyFREC. Journal of Computational Chemistry, v. 39, no. 8, p. 438-449, 2018. Available at: https://onlinelibrary.wiley.com/doi/abs/10.1002/jcc.25101. Epub.

LOUIS, VL ST.; KELLY, CLA; DUCHEMIN, É.; RUDD, JWM; ROSENBERG, DM Reservoir surfaces as sources of greenhouse gases to the atmosphere: a global estimate. BioScience, v. 50, no. 9, p. 766-775, 2000.

HAYAT, MB, Ali, D., MONYAKE, KC, ALAGHA, L., & AHMED, N. (2019). Solar Energy: A Look into Power Generation, Challenges, and A Solar-Powered Future. *J. Energy Res.* , pp. 1049–1067.

IPCC. (2021). Climate Change 2021: The Physical Science Basis. Contribution of Working Group I to the Sixth Assessment Report of the Intergovernmental Panel on Climate Change. Cambridge: Intergovernmental Panel on Climate Change.

JAIN, Sachin, DHARA, Sumon, AGARWAL, Vivek. A Voltage-Zone Based Power Management Scheme With Seamless Power Transfer Between PV-Battery for OFF-Grid Stand-Alone System. IEEE Transactions on Industry Applications, v. 57, no. 1, p. 754-763, 2021. Available at: https://ieeexplore.ieee.org/document/9319219. Epub.

KALDELLIS, JK, KAVADIAS K., ZAFIRAKIS D. Experimental validation of the optimum photovoltaic panels' tilt angle for remote consumers. Renew Energy 2012; 46: 179 and 91.

KALDELLIS, JK; KAPSALI, M.; KAVADIAS, KA. Temperature and wind speed impact on the efficiency of PV installations. Experience obtained from outdoor measurements in Greece, Renewable Energy 66 (2014) 612–624.

LV, JWX; ZHU, H.; SONG, Y. The influence of meteorological factors on the photovoltaic daily generation (2014). DOI:10.13941/j.cnki.21-1469/tk.2014.10.001.

MATIN, MA et al. Bi(1-y)SmyFeO3 as potential photovoltaic materials. Bull Mater Sci, v. 43, p. 167, 2020. https://doi-org.ez130.

MIRANDA, MM (2012). Emission factor of greenhouse gases from electricity generation in Brazil: implications of applying the Life Cycle Assessment. 162p. Dissertation (Master). Engineering School of São Carlos. University of São Paulo. 2012.

MME - Ministry of Mines and Energy. National Energy Plan 2050. (2018). https://www.mme.gov.br/documents/10584/1102077/PNE+2050+-+vers%C3%A3o+final.pdf/3e3d0dbb-bf14-0c48-c287-0d4f3e33df44.

NAVNTOFT, LC, CRISTÓFALO, MP, CUCCORESE, S., DEFFERRARI, IR, & ROMERO, I. (2019). Distributed Solar Photovoltaic Generation Manual (1st revised ed.). Secretariat of the Government of Energy.

NEVES, A; BLONDEL, L; BRAND, K; HENDEL, B.S; RIVAS, CS; IANCU, A; MELICA, G; KOFFI, L.B; ZANCANELLA, P; KONA, A. Guide for presenting the results of the Covenant of Mayors for Climate and Energy, 2016, EUR 28160 PT, DOI: 10.2790/717311.

PUEYO, S.; FEARNSIDE, PM GREENHOUSE GAS EMISSIONS FROM HYDROELECTRIC RESERVOIRS: IMPLICATIONS OF A POWER LAW. Oecologia Australis 15(2): 199-212, June 2011 DOI:10.4257/oeco.2011.1502.02.

RAZA. A, Syed J, Muhammad Ali F, et al. Incidence of vitamin D Deficiency in Different Seasons in the Adult Karachi Population Presenting in the Medical Outpatient Department with Generalized Body Ache. Cureus, v. 11, no. 7, p. e5167, 2019. DOI: 10.7759/cureus.5167.

SANCHES, SR Meteorological Data Transmission System in Real Time for Marina Users' Cell Phones. Florianopolis: IFSC, 2020.

SANTOS, MA; ROSA, LP; MATVIENKO, B.; SANTOS, EO; D'ALMEIDA ROCHA, CHE; SIKAR, E.; SILVA, MB & JUNIOR, AMPB 2008. Greenhouse gas emissions from hydroelectric reservoirs. Oecologia Brasiliensis, 12: 116-129.

SOARES FILHO et al. Low Carbon Study for Brazil - Land Use, Land Use Change and Forests, 2010. International Bank for Reconstruction and Development.

WOLFE, Philip R. "What Is Photovoltaics?" In: The Solar Generation. 1st ed. Hoboken, NJ, USA: Wiley, 2018. p. 9-24.

ZANONI, Maria MV, Josiléia A. Zanatta, Jeferson Dieckow, Akemi Kan, and Carlos B. Reissmann. "Methane Emissions from Decomposition of Flooded Forestry Waste." Brazilian Journal of Agricultural and Environmental Engineering 19.2 (2015): 173-79.

RECyT
Year 27 / Nº 43 / 2025 /
DOI: https://doi.org/10.36995/j.recyt.2025.43.002

Wettability Device for Electronic Solder Alloys Using the Sessile Drop Method

Dispositivo de Humectabilidad para Aleaciones de Soldadura Electrónica Utilizando el Método de Gota Sésil

Dispositivo de Molhabilidade para Ligas e Soldagem Eletrônica Usando o Método de Gota Sésssil

Héricles R. O., Souza[1, *]; André C. C., Maciel[1]; Ariadne C. B., Farias[1]; Nádia S., Cosmo[1]; Maria A. P. S., Silva[1]

1- Instituto de Tecnologia. Universidade Federal do Pará. Belém, Pará, Brasil.
* E-mail: hericlesoliveira.ho@gmail.com

Received: 25/11/2023; Accepted: 20/11/2024

Abstract
In 2003, the RoHS (Restriction of Certain Hazardous Substances) Directive emerged in the European Union to restrict hazardous substances in electronics, prompting the search for alternatives to lead-based solder due to health concerns related to its toxicity. Soft solder, working at low temperatures (up to 450 °C), is essential in heat-sensitive electronic components. With the evolution of smart electronics, wettability (the ability of liquids to spread on solid surfaces) has become critical for the integration, power, miniaturization, and flexibility of electronics. However, the scarcity of affordable devices to test wettability limits research in this promising field. Addressing this need, an affordable device, costing around US$ 30.00, was developed to measure the wettability of low-temperature alloys. The construction was carried out by planning its structure and geometry through parametric 3D CAD (Computer Aided Design) modeling software. Then, the components were manufactured and assembled to conduct a wettability test. The device provided material dripping onto copper substrates, eliminating the need for prior contact. After six tests, the results revealed contact angles ranging from 139.08° to 147.93°, indicating partial wettability and low adhesion due to material drop caused by air resistance. This functional and affordable device can drive studies in the field, promoting research on lead-free solder and new materials for electronic components.

Keywords: lead-free, device development, wettability, sessile drop, electronic components.

Resumen
La Directiva RoHS (Restriction of Certain Hazardous Substances) surgió en la Unión Europea en el 2003 para restringir sustancias peligrosas en dispositivos electrónicos, impulsando la búsqueda de alternativas a la soldadura a base de plomo debido a preocupaciones de salud relacionadas con la toxicidad del plomo. La soldadura suave, al trabajar a bajas temperaturas (hasta 450 °C), es esencial en componentes electrónicos sensibles al calor. Con la evolución de la electrónica inteligente, la mojabilidad (la capacidad de los líquidos para extenderse sobre superficies sólidas) se ha vuelto crítica para la integración, potencia, miniaturización y flexibilidad de la electrónica. Sin embargo, la escasez de dispositivos asequibles para probar la humectabilidad limita la investigación en este campo prometedor. En respuesta a esta necesidad, se desarrolló un dispositivo asequible, con un costo de alrededor de US$ 30.00, para medir la humectabilidad de aleaciones de baja temperatura. La construcción se llevó a cabo planificando su estructura y geometría a través de un software modelador CAD (computer-aided design) paramétrico en 3D. Luego, los componentes se fabricaron y ensamblaron con el objetivo de realizar una prueba de mojabilidad. El dispositivo proporcionó goteo de material sobre sustratos de cobre, eliminando la necesidad de contacto previo. Después de seis pruebas, los resultados revelaron ángulos de contacto que oscilan entre 139,08° y 147,93°, indicando una mojabilidad parcial y baja adherencia debido a la caída del material causada por la resistencia del aire. Este dispositivo funcional y asequible puede impulsar estudios en el área, fomentando la investigación sobre soldadura sin plomo y nuevos materiales para componentes electrónicos.

Palabras claves: sin plomo, desarrollo de dispositivo, humectabilidad, gota sésil, componente electrónico.

Resumo
Em 2003, a Diretiva RoHS (Restriction of Certain Hazardous Substances) surgiu na União Europeia para restringir substâncias perigosas em eletrônicos, gerando a busca por alternativas à solda à base de chumbo devido a preocupações de saúde por conta da toxicidade do chumbo. A solda branda, por trabalhar em baixas temperaturas (até 450 °C), é essencial em componentes eletrônicos sensíveis ao calor. Com a evolução dos eletrônicos inteligentes, a molhabilidade (a capacidade de líquidos se espalharem em superfícies sólidas) tornou-se crítica para integração, potência, miniaturização e flexibilidade de eletrônicos. Entretanto, a escassez de dispositivos

acessíveis para testar a molhabilidade limita a pesquisa nesse campo promissor. Visando essa necessidade, um dispositivo acessível, custando cerca de US$ 30.00, foi desenvolvido para medir a molhabilidade de ligas de baixa temperatura. A construção foi feita a partir do planejamento de sua estrutura e geometria através de um software modelador CAD (computer-aided design) paramétrico em 3D, em seguida os componentes foram fabricados e montados com o objetivo da realização de um ensaio de molhabilidade, assim o dispositivo proporcionou o gotejamento do material em substratos de cobre, eliminando a necessidade de contato prévio. Após seis ensaios, os resultados revelaram ângulos de contato variando de 139,08° a 147,93°, apresentando molhabilidade parcial e baixa aderência por conta da queda do material devido à resistência do ar. Esse dispositivo funcional e acessível pode impulsionar estudos na área, promovendo pesquisas sobre solda branda sem chumbo e novos materiais para componentes eletrônicos.

Palavras-chave: livre de chumbo, desenvolvimento de dispositivo, molhabilidade, gota séssil, componentes eletrônicos.

1. Introduction

The United Nations (UN) has a clear position on lead (Pb): it is a toxic metal and can cause serious health problems. Anthropogenic activities, including industrialization, urbanization and mining have resulted in the redistribution of lead from the Earth's crust to the soil and the environment (THOMAS *et al*., 2022). "Although many countries have systematically banned or restricted its application, lead pollution has become a public health problem due to its non-biodegradable nature" (NIU *et al*., 2023). In 2003, the RoHS (Restriction of Certain Hazardous Substances) limited the use of certain hazardous substances in electrical and electronic equipment in EU members and disclosed a mechanism for additional restrictions in the future (PECHT *et al*., 2016). The RoHS originally came into effect on July 1, 2006, and later in 2011, the directive was modernized as RoHS-2. This provided deadlines for some exempt applications. It also mentioned the specific reasons for some exemptions that were essential to maintain. In 2015, the directive was revised again and further restricted some substances in electrical and electronic equipment. However, lead has proven to be hazardous to human health and the environment (PATIL and DABADE, 2019). From contact, lead has a half-life of about 30 days in the blood, after which it diffuses into soft tissues such as the kidneys, brain, and liver. Then, it is distributed to bones, teeth, and hair as lead phosphate (ENGWA *et al*., 2019). In the last 10 years, studies have shown detrimental effects on the environment and human health, with the use of many materials, including lead, being restricted and prohibited by the WEEE (Waste Electrical and Electronic Equipment) (CHENG *et al*., 2017). Still, according to Pecht *et al*. (2016), electronics manufacturers associated with excluded and exempt products often seek to preserve the use of lead-based parts and assembly processes, mainly due to the concerns regarding the long-term reliability of solder joints.

In electronics, soft soldering is a term commonly used to refer to low-temperature soldering, generally below 450°C, which is ideal for heat-sensitive electronic components, as it prevents damage to them. Thus, due to low cost, lower melting temperature, excellent mechanical and thermal properties, adequate wettability behavior and eutectic composition, Sn-Pb solders were widely used (JAFFERY *et al*., 2022). However, manufacturers have sought a new generation of lead-free solders, called Lead Free, to replace Sb-Pb solders as an alternative to this problem (ZHOU *et al*., 2023).

Liu *et al*. (2016) says that wettability is the ability of a liquid to spread over a solid surface and is measured by the contact angle. When the contact angle (θ) is small (less than 90°), the liquid tends to spread more, indicating high wettability. When the angle is large (greater than 90°) and wettability is low, the liquid tends to form droplets. According to Cosmo *et al*. (2022), wettability is an essential characteristic of the material to define weldability properties, especially in industries that use soft welding, as there is no casting between the filler alloy and the substrate. In recent years, the focus of studies about wettability testing has increased. This is associated with the use of new materials driven by the development of intelligent electronic equipment designed for high integration, power, miniaturization and folding (Kuang *et al*., 2022). Thus, due to the high cost and limited availability of the devices necessary to perform the wettability test, access to this technology is unfeasible in many places, which can hinder the development of promising research in this area. One of the most commonly used methods for analyzing the contact angle is the direct measurement of the tangent at the three-phase contact point using the sessile drop method (Figure 1) (HEBBAR *et al*., 2017).

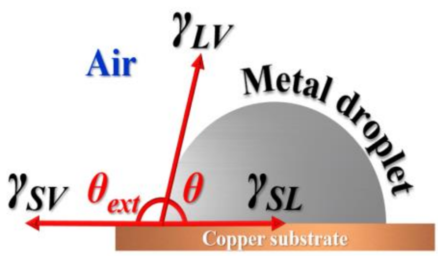

Figure 1. Diagram of contact angle (θ), external contact angle (θ_{ext}), interfacial tensions between solid-liquid (γ_{SL}), solid-vapor (γ_{SV}) and liquid-vapor (γ_{LV}) interfaces.

In Young's equation, the surface is considered ideal (i.e., flat, non-reactive, homogeneous, and non-porous) (Ebrahim *et al.*, 2021). In the present work, it is assumed that the surface under study is ideal. These ideal conditions serve as a reference for understanding the behavior of real surfaces, facilitating the development and optimization of materials and coatings in various practical applications in science and engineering. The relationship for the contact angle was defined by physicist Thomas Young (1773-1829) and is expressed in Equation 1 below:

$$cos\,cos\,(\theta) = \frac{\gamma_{SV} - \gamma_{SL}}{\gamma_{LV}} \tag{1}$$

γ_{SV} represents the surface energy between the solid and vapor (or air), while γ_{SL} denotes the surface energy between the solid and liquid. Additionally, γ_{LV} indicates the surface energy between the liquid and vapor (or air). The contact angle formed between the solid surface and the liquid is represented by θ. θ_{ext} refers to the external contact angle formed between the liquid surface and the vapor (or air). For contrast purposes, in some images, it is preferable to measure the θ_{ext} using the optical method of the sessile droplet so that it is possible to determine the θ (Equation 2).

$$\theta = 180° - \theta_{ext} \tag{2}$$

For Cosmo *et al*. (2022), this method consists of placing the material with the lowest melting point on the prepared surface of the solid substrate and heating the substrate until the material melts. However, some variations of this procedure are also used, such as dripping the material with a lower melting point onto the solid substrate at the desired temperature and avoiding prior contact with the materials, carried out by Sehirli *et al*. (2022).

The term *lead-free* refers to products or materials that do not contain lead. “For a long time, tin-lead alloys have been the main soldering materials in the field of electronic welding because of their good electrical conductivity, mechanical properties, and low cost” (GAN and NGAN, 2018; JIANG *et al*., 2019). The most commonly used alloy for microelectronics soldering is tin-lead eutectic, which is composed of approximately 63% Sn and 37% Pb (ŠURYOVÁ *et al*., 2020). Its melting point is around 183 °C, which prevents overheating of soldered electronic components (WERNICKI, 2023). However, due to restrictions on the use of this toxic metal, researchers around the world have carried out many studies on lead-free solder alloys. Tehrefore, tin-based (Sn-based) alloys are considered the most promising candidates to replace the traditional Sn-Pb solder alloy (LI Y. *et al*., 2020).

Two candidate alloys are Sn-2wt.%Sb, tested by Dias *et al*. (2015) and Rocha *et al*. (2018), and Sn-5.5wt.%Sb tested by Cosmo *et al*. (2022). The composition of these alloys has better resistance to room temperature, ductility, and greater microstructural stability when compared to Sn-Pb system alloys. Although the commercial Sn-37wt.%Pb alloy presented smaller angles than those of lead-free alloys, the difference is not significant, suggesting that Sb-containing alloys are potential substitutes for commercial lead-based alloys (COSMO *et al*., 2022).

Therefore, aiming to meet the study needs, the general objective of this work is the sizing, development, verification, and presentation of the costs of manufacturing a wettability analysis device for alloys up to 400 ºC. This device will use a variation of the sessile drop method that takes into account the free fall of the material. The development of this device aims to provide savings in the device purchasing value to enable future research in wettability with alternative lead-free alloys.

2. Materials and Methods

Various materials were used during the development of the device. Some of these materials are part of the device, while others helped in its creation. The distinction between these materials is important since the costs of developing the device will only include the materials and components that comprise it.

2.1. Device and Auxiliary Materials

Most of the materials that comprise the device were purchased, but some, such as the tiltable stand and the substrate platform, were reused (Figure 2).

Figure 2. Materials that integrate the wettability device.

Next, Figure 3 shows the auxiliary materials that belong to the laboratory where the device was developed, and for this reason, their purchasing values will not be counted.

Figure 3. Materials used during the development of the wettability device.

2.2. Development Methodology

2.2.1. Making the Device Support

Some of the requirements for selecting and manufacturing the bases of this wettability device are the type of material, inclination, stability, size, and mobility. Taking these aspects into account, two components within the laboratory that met these characteristics were unusable, but they were reused for the development of the device. Both components belonged to damaged laboratory microscopes. One of these was the adjustable base made of aluminum, which has a melting point of 660 °C and was of a suitable size for mobility. Moreover, the substrate structure has an adjustable height, which facilitates the determination of the height at which the liquid drop falls. Therefore, the substrate platform was attached to the front of the adjustable stand and fixed by screws, forming a single structure. Furthermore, some holes were made in the adjustable base for securing screws to the ceramic piece and substrate platform and for passing the power cable, shown in the red circles in Figure 4.

Figure 4. Union of the manufactured support.

Inserting the power cable into the back of the apparatus prevents the wires from being affected by the heat of the test and ensures they remain firm with the help of the clamp.

2.2.2. Production of the Ceramic Piece and its Components

The objective of the ceramic part is to concentrate the heat emitted from the test in itself, preventing the heat from being dissipated from the system. Therefore, to obtain the model of the part, © FreeCAD (3D parametric CAD—computer-aided design and modeling software) in Figure 5a was used. Through the design of the part, additive manufacturing was used to obtain a 3D printed mold, thus making it possible to develop the established dimensions and desired geometry. Figure 5b shows the mold model developed and printed in 3D.

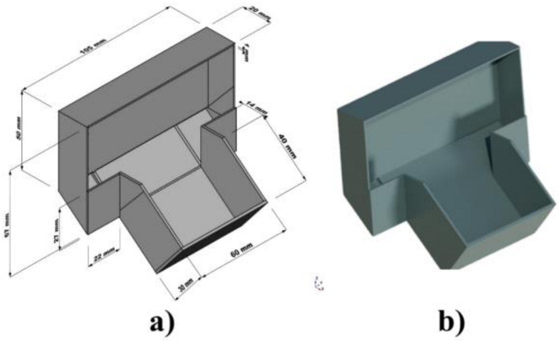

Figure 5. a) Mold model design and b) 3D mold printing.

In the next stage, the composition materials of the ceramic piece were used to obtain the final mass of the piece. To obtain a piece that was highly resistant to high temperatures, the recommendation on the packaging of the refractory mass was followed. A proportion of 5:1:1 (refractory: cement: sand) was recommended for intermediate mass, consistent Pivinskii's (2021) findings on the reduction of mixtures to increase resistance to high temperatures. However, clay was also included in the intermediate mass in a ratio of 2:1 (intermediate-mass: clay), as it can be molded easily due to its high plasticity, presenting structural resistance after firing at high temperatures (ALMEIDA *et al.*, 2015). Furthermore, after obtaining the final mass, a ratio of 1:5 (water: final mass) was used to obtain the final mixture. The next step consisted of depositing the final mixture into the mold and waiting 24 hours for pre-curing. After that, the piece was removed from the mold and placed in an oven (Figure 6a) at 150 °C for 30 minutes to bake and dehumidify the piece. Then, with the piece prepared, roughing was carried out in the frontal region to open a channel (Figure 6b), this being the place where the resistance that will emit heat will be deposited. In addition, holes were made for the screws that will fix the piece to the support. Finally, the aluminum sheet was made to suspend the metal that will be cast, covering the front part of the ceramic piece (Figures 6c, 6d, and 6e). The complete production is shown in Figure 6.

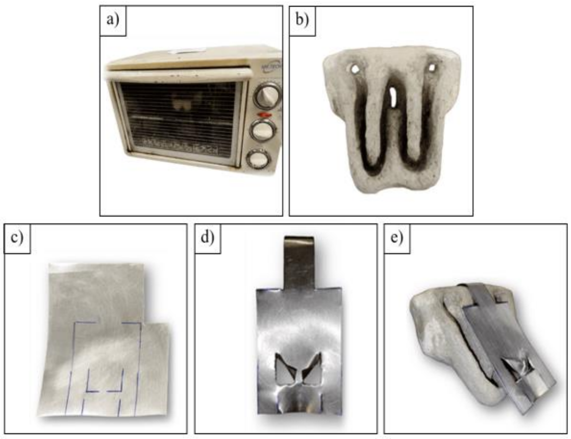

Figure 6. a) ceramic piece in the oven; b) front roughing; c) drawing for aluminum sheet cutting; d) cut aluminum sheet, and e) final result.

The resistance channel is relatively deep. Therefore, the aluminum sheet will not come into direct contact with the resistance, thus avoiding a short circuit in the system.

2.2.3. Device Assembly

With all the device components made and prepared, the next step consisted of assembling the device, as shown below:

1) Initially, the power cables were inserted into the holes designed to support the device, and they were tied to the base with a cable so that they would not come loose.

2) The electrical resistance was fitted into the channel (in the lower front part of the piece) and its two ends were connected to each of the screws (in the upper front part of the part ends). This connection aims to pass electrical current through the resistance, thus heating it due to the Joule effect, to induce heat in the experiment.

3) The ceramic piece was attached to the base and fixed using a screw and a nut (in the middle of the piece);

4) The stripped ends of the power cable were wrapped around the two screws (on the upper back of the ends of the piece) and were firmly tightened between the nuts and washers;

5) The aluminum sheet overlaps the ceramic piece (on the front of the piece) so that it is heated by the heat from the electrical resistance through conduction.

6) Finally, the current controller was coupled to the device's power cable so that it was possible to control the power of the electrical resistance. Therefore, the assembled device can be seen in Figure 7, which displays several viewing perspectives.

Figure 7. Display of the developed wettability device (without aluminum sheet) from various perspectives.

In Figure 7 above, the device is shown without the aluminum sheet, allowing for an analysis of its interior. As noted, the device was rigid, stable, and functional, ready to perform the six planned tests. However, the copper substrates and the specimens to be tested still needed to be prepared.

2.2.4. Preparation of Copper Substrates and Test Specimens

Considering the importance of the substrate parameters for carrying out the test, the surface must come close to the ideal model proposed by Young, which must be clean and as smooth as possible. Thus, Figure 8 shows the steps that were followed to obtain the copper substrates and the alloy test specimens used for the test.

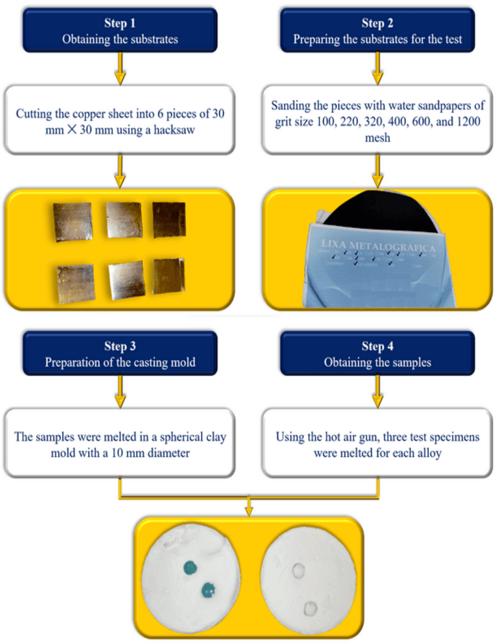

Figure 8. Steps for obtaining and preparing copper substrates for testing and test specimens.

As mentioned before, two alloys will be used to compare the test angles, Sn-5.5wt.%Sb and Sn-37wt.%Pb, with three test specimens for each alloy.

2.2.5. Carrying out the Wettability Test

After assembling the device and preparing the copper substrates and test specimens, it was possible to carry out wettability tests using the developed device. Thus, the test followed these steps:

1) Firstly, because one of the alloys contains lead in its composition, PPE (Personal Protective Equipment) such as masks, gloves, boots, and glasses were used to avoid contact with the toxic metal.

2) Each of the six specimens to be tested was placed on the aluminum sheet, one for each test. Then, the sheet was superimposed on the ceramic piece to transmit heat to the specimen.

3) The copper substrate was leveled at approximately 180° with the aid of the spirit level so that there was no difference caused by unevenness. In addition, the distance of the lower edge of the aluminum sheet was adjusted to 1 cm to try to prevent the liquid drop from being significantly affected by the effect of air resistance and from solidifying during the fall.

4) The pyrometer was configured and fixed on a tripod and positioned to measure the temperature of the contact line between the test piece and the aluminum sheet.

5) Since there is still no place for thermal insulation of the device, the test environment was controlled to avoid air currents near the device during the experiment, thus avoiding changes in results due to temperature variation.

6) The device's power cable was connected to the current controller to control the resistance power in a 110 V socket.

7) With the current controller, the resistance power was increased, thus increasing the heat emitted to the aluminum sheet, which consequently increased the temperature of the test piece.

8)The drop of the test piece on the copper substrate had a distance of 1 cm and was recorded by a cell phone camera to observe the way the drop fell and its adhesion to the copper substrate. Moreover, the aluminum sheet was readapted not only to heat the metal to be melted but also to heat the copper substrate by conduction, thus facilitating the union of the droplet with the substrate. Figure 9 shows a schematic of the device and the droplet as it falls onto the substrate.

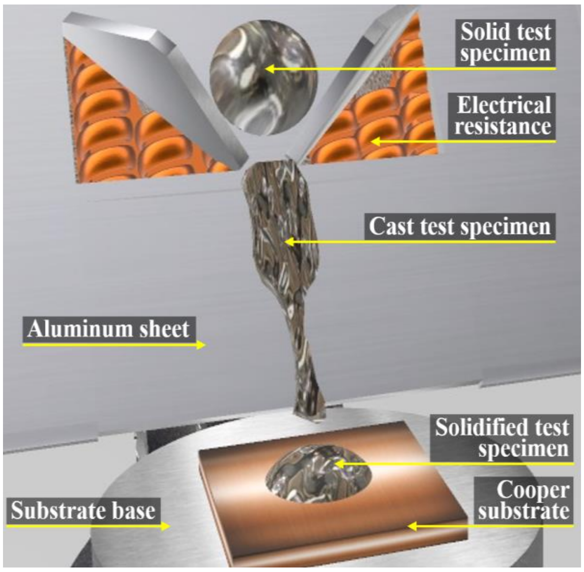

Figure 9. Schematic of the device showing the droplet falling onto the substrate.

Finally, measurements of the external contact angles (θ_{ext}) were carried out using the optical sessile droplet method. Three stereoscope images of the test specimen were taken to determine the average of the angles, standard deviations, and coefficients of variation, as calculated by Equations 3, 4, and 5, respectively.

$$\underline{\theta} = \frac{\sum \quad \theta_i}{n} \tag{3}$$

$$s = \sqrt[2]{\left(\frac{\sum \quad (\theta_i - \underline{\theta})^2}{n-1}\right)} \tag{4}$$

$$CV = \frac{s}{\underline{\theta}} \times 100\% \tag{5}$$

Hence, it is possible to check through these equations the average reliability of the contact angle measured, since the standard deviation and coefficient of variation are measures that allow the analysis of data dispersion. That is, they are used to measure the average dispersion around the average arithmetic.

3. Results

3.1. Measurement of the Developed Wettability Device

The equipment weighs approximately 1.2 kg and its dimensions are 34.0 cm in height and 8.0 cm in width. It has a tilt of 45, and the liquid material is suspended at a distance of 1.0 cm from the copper platform (which can be altered by varying the height of the copper substrate). The aluminum sheet was changed twice during the tests, meaning one sheet for every three tests of each alloy. The device is shown in Figure 10.

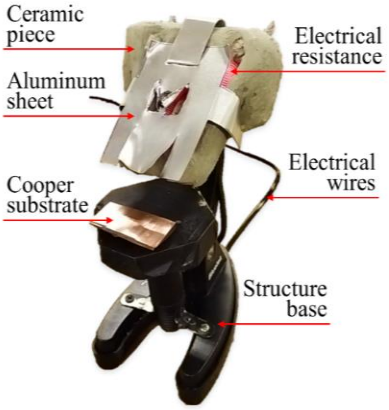

Figure 10. The developed wettability device.

To carry out the tests, it was necessary to wait for the copper substrates to reach a temperature of 50 °C so that a good union between the metals could occur. Additionally, using the Optical Pyrometer, it was noted that the maximum temperature the device reaches is 650 °C. However, for safety reasons, the device will be operated up to a temperature of 400°C, representing the ideal temperature for the project. Hence, the burning of the electrical resistance is avoided. The sequence illustrates the transformation of a solid droplet into a liquid flowing over the heated aluminum foil (Figure 11).

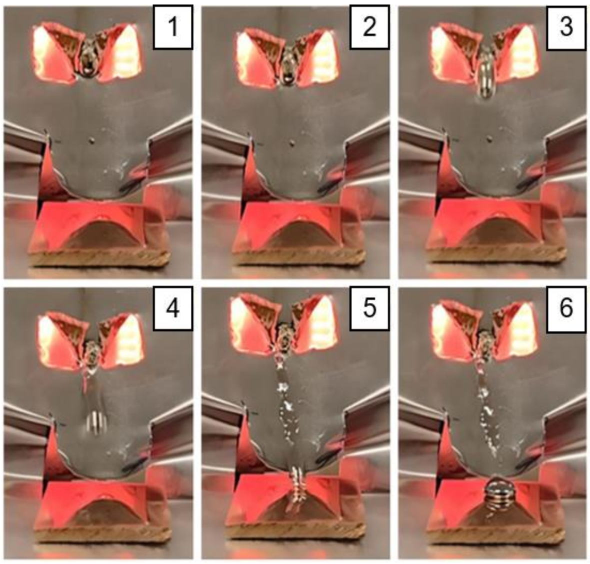

Figure 11. Recording the droplet falling on the copper substrate.

In the first stage, the solid droplet is at the top, maintaining its shape. In the second, liquefaction begins, making the surface shiny. In the third stage, the droplet starts to descend due to gravity, elongating as it falls. In the fourth, it is midway down, with the liquid flowing to the bottom. In the fifth stage, the droplet reaches the tip of the fall and is about to detach. Finally, in the sixth stage, the droplet is released, and it is deposited onto the copper substrate, spreading out upon contact.

3.2. Measurements of the Contact Angle and External Contact Angle

After measuring the wettability device and validating it after carrying out the tests, the test specimens were identified and grouped as shown in Figure 12.

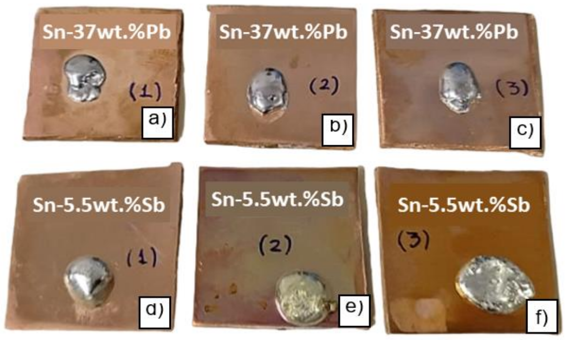

Figure 12. a), b), c) 1st, 2nd and 3rd test specimen of lead alloy; d), e), f) 1st, 2nd and 3rd test specimen of lead-free alloy.

During the testing of Sn-37wt.%Pb alloy specimens, it was observed that the droplets tended to form with one end wetting the substrate in a circular shape, while the other end displayed irregularities. This occurs as the droplet falls, since the contact area between the aluminum plate and the liquid droplet decreases, reducing heat transfer between them. This results in the droplet solidifying in midair due to air resistance. Additionally, similar characteristics were observed during testing of the Sn-5.5wt.%Sb alloy, as it has a liquidus-to-solidus temperature difference of only 2 °C. The external contact angles of both alloys showed partial wettability on the copper substrates and were subsequently measured using the ImageView software in the stereoscope. An example of the measurement is shown in Figure 13.

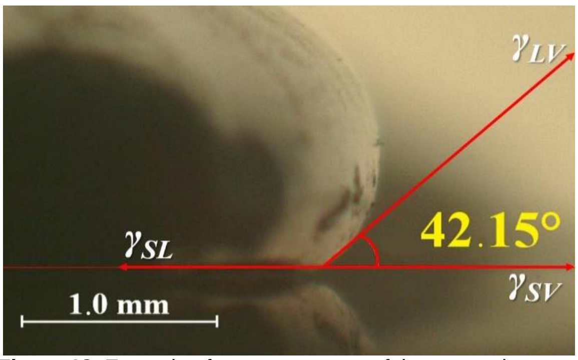

Figure 13. Example of a measurement of the external contact angle (θ_{ext}) of test specimens.

Furthermore, to maintain stability when taking images with the stereoscope, the specimens were attached to a support base. Each of the two alloys was tested three times, with three external contact angles measured for each specimen. Table 1 shows the contact angles obtained for the three Sn-37wt.%Pb alloy specimens (Equation 2), as well as their averages, standard deviations, and coefficients of variation.

Table 1. Contact angles obtained from the three test specimens of the Sn-37wt.%Sb alloy.

Test Specimen	Contact angle 1, θ_1 (°)	Contact angle 2, θ_2 (°)	Contact angle 3, θ_3 (°)	Average, $\bar{\theta}$ (°)	Standard deviation, s	Coefficient of variation, CV (%)
1	137.85	139.95	140.60	139.47	1.87	3.49
2	142.57	143.19	146.16	143.97	2.23	4.97
3	144.84	146.85	147.82	146.50	1.94	3.75

Thus, it can be observed that the maximum values of standard deviation and coefficient of variation are 2.23 and 4.97%, respectively. The same procedure was then performed for the three Sn-5.5wt.%Sb alloy specimens shown in Table 2, which presents the obtained contact angles, as well as their averages, standard deviations, and coefficients of variation.

Table 2. Contact angles obtained from the three test specimens of the Sn-5.5wt.%Sb alloy.

Test Specimen	Contact angle 1, θ_1 (°)	Contact angle 2, θ_2 (°)	Contact angle 3, θ_3 (°)	Average, $\bar{\theta}$ (°)	Standard deviation, s	Coefficient of variation, CV (%)
1	143.34	145.78	146.94	145.35	2.34	1.61
2	146.91	147.38	149.51	147.93	1.61	1.09
3	137.52	139.78	139.95	139.08	1.82	1.31

Therefore, the maximum values of standard deviation and coefficient of variation are 2.34 and 1.61%, respectively. The higher coefficient of variation (CV) values of 4.97% and 1.61% indicate low variability relative to the mean, suggesting that both samples have consistent data with little dispersion. Hence, the average contact angles obtained in Tables 1 and 2 are plotted in Graph 1.

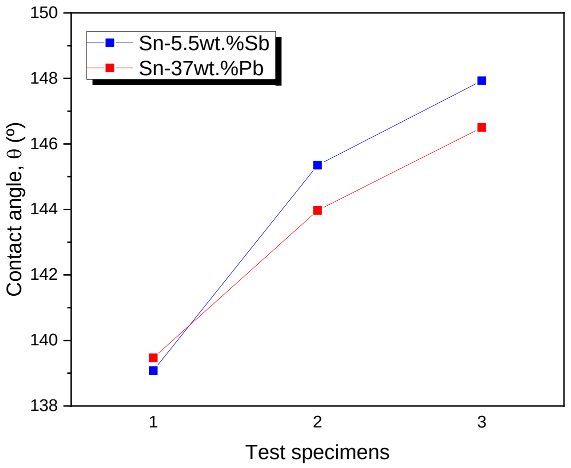

Graph 1. Average contact angles obtained from test specimens of Sn-37wt.%Pb and Sn-5.5wt.%Sb alloys.

From the graph, it can be observed that the wettability of the Sn-37%Pb alloy is better than that of the Sn-5.5%Sb alloy, as it showed lower contact angles in specimens 2 and 3, with a difference of almost 1% for each of these specimens. However, in specimen 1, the Sn-5.5%Sb alloy presented a contact angle 0.27% lower than that of the commercial lead alloy. Additionally, this observation is similar to the findings in the study by Cosmo *et al*. (2022). In that study, one out of four tested specimens also showed a lower contact angle for the Sn-5.5%Sb alloy than the commercial lead alloy, further highlighting Tin-Antimony as a promising material for lead-free alloys. Furthermore, it was found that the contact angles of the specimens in this study are approximately 7.9% lower than those reported by Cosmo *et al*. (2022). This difference can be attributed to the material falling onto the solid substrate due to gravity, which increases spreading and decreases the contact angles, an effect that did not occur in Cosmo *et al*. (2022) due to their use of the conventional sessile drop method. In contrast, some specimens in Figure 12 detached easily, which is an indication of non-adhesion as a result of insufficient heat transfer between the materials. In this case, both the copper substrate was not at the ideal temperature to create adhesion with the drop, and the drop itself lost heat during its fall, thereby preventing intermetallic compound formation for a strong bond.

3.3. Development Cost of the Device

The device was developed with the help of some materials and components already existing in the laboratory, but others were acquired for the project. Therefore, only the materials that make up the device will be included in the cost calculation. Hence, such materials and their purchasing values are shown in Table 3.

Table 3. Cost of the developed wettability device.

COMPONENTS / MATERIALS	UNITS	PRICE
500 g of clay	1	US$ 1.50
500 g of cement	1	US$ 0.10
500 g refractory dough	1	US$ 0.28
Nylon cable tie	1	US$ 0.03
2 m power cable	1	US$ 5.65
Current controller	1	US$ 9.79
Aluminum sheet 0.4 mm x 20 cm x 1 m	1	US$ 3.40
Bubble level	1	US$ 3.33
Screws, nuts, and washers 3/16" x 3/4"	2	US$ 3.39
Electrical resistance 1000 W	1	US$ 2.00
		TOTAL
		US$ 29.47

Thus, the developed device was able to perform the 6 planned tests without any issues related to functionality or durability. However, due to residue formed along the path followed by the droplet, the aluminum sheet used must be sanded or replaced when different materials are tested. The average cost of a wettability measurement device can vary considerably, depending on its precision and functionalities. In general, the price of basic wettability measurement equipment can range from about US$ 20,000 to US$ 50,000. Compared to these commercially available devices, the developed device, costing less than US$ 30.00, lacks features such as a high-resolution camera, thermal insulation, or real-time data acquisition. However, the results it produced were of great value for the research.

4. Conclusions

A small-sized and low-cost device was successfully developed, showing promise in terms of accessibility and portability, although it may lack some functionalities compared to market devices. Nevertheless, it proved to be valuable for research, undergoing tests with Sn-37wt.% Pb and Sn-5.5wt.%Sb alloys. In these experiments, patterns and trends in the wettability properties of the mentioned alloys were identified. Early solidification of sessile drops due to heat loss during the fall resulted in different wettability modes at the ends, suggesting the potential for process improvement by reducing substrate roughness or shortening the fall distance. Measurement and data processing procedures were accurate and reliable, with wettability angles calculated based on Young's equation and using the contact angle measurement technique. The values of mean, standard deviation, and coefficient of variation were consistent, indicating reliable results, and the understanding of the wettability behavior of lead-free alloys provides valuable insights for the development of new materials. This can lead to the creation of more efficient, durable, and environmentally friendly alloys for use in electronic components. From the promising results obtained in the wettability test, there is an indication that these alloys may meet environmental and joint reliability requirements, contributing to regulatory compliance. The device was effective in investigating the interaction between low-melting alloys and a copper substrate, especially in the analysis of material drop due to gravity. This resulted in an increase in spreading and contact angles but a decrease in joint adhesion, without the formation of intermetallic compounds between the materials. This study serves as a stimulus for future improvements and further research in the academic field, with the potential to significantly contribute to advancing knowledge about the wettability behavior of low-melting alloys.

5. References

Almeida, P. H. S., Franco, J. de M., & Tavares, C. R. G. (2015). Influência do tipo de argila no processo de solidificação/estabilização de lodo têxtil. *Cerâmica*, *61*(357), 137–144. https://doi.org/10.1590/0366-69132015613571870

Cheng, S., Huang, C.-M., & Pecht, M. (2017). A review of lead-free solders for electronics applications. *Microelectronics Reliability*, *75*, 77–95. https://doi.org/https://doi.org/10.1016/j.microrel.2017.06.016

Cosmo, N. S., Brabo, C. A. da S., Mesquita, S. Q., Costa, T. A. P. de S., da Rocha, O. F. L., & da Silva, M. A. P. de S. (2022). Análise Comparativa do Ângulo de Molhabilidade em uma Liga Livre de Chumbo Sn-2%Sb / Comparative Analysis of the Wetting Angle in a Lead-free Sn-2.0wt%Sb Alloy. *Brazilian Journal of Development*, *8*(2), 13655–13666. https://doi.org/10.34117/bjdv8n2-343

Dias, M., Costa, T., Rocha, O., Spinelli, J. E., Cheung, N., & Garcia, A. (2015). Interconnection of thermal parameters, microstructure, and mechanical properties in directionally solidified Sn–Sb lead-free solder alloys. *Materials Characterization*, *106*, 52–61. https://doi.org/https://doi.org/10.1016/j.matchar.2015.05.015

Ebrahim Nataj, Z., Kazemi, A. S., & Abdi, Y. (2021). Surface effects and wettability measurement considerations in fluorinated carbon nanotubes. *Applied Physics A, 127*(11), 874. https://doi.org/10.1007/s00339-021-05029-z

Engwa, G. A., Ferdinand, P. U., Nwalo, F. N., & Unachukwu, M. N. (2019). Mechanism and Health Effects of Heavy Metal Toxicity in Humans. In O. Karcioglu & B. Arslan (Eds.), *Poisoning in the Modern World*. IntechOpen. https://doi.org/10.5772/intechopen.82511

Gan, K. F., & Ngan, A. H. W. (2018). The unusual size effect of eutectic Sn/Pb alloys in the micro regime: Experiments and modeling. *Acta Materialia*, *151*, 282–292. https://doi.org/https://doi.org/10.1016/j.actamat.2018.04.005

Hebbar, R. S., Isloor, A. M., & Ismail, A. F. (2017). Chapter 12 - Contact Angle Measurements. In N. Hilal, A. F. Ismail, T. Matsuura, & D. Oatley-Radcliffe (Eds.), *Membrane Characterization* (pp. 219–255). Elsevier. https://doi.org/https://doi.org/10.1016/B978-0-444-63776-5.00012-7

Jaffery, S. H. A., Sabri, M. F. M., Rozali, S., Hasan, S. W., Mahdavifard, M. H., AL-Zubiady, D. A. S., &Ravuri, B. R. (2022). Oxidation and wetting characteristics of lead-free Sn-0.7Cu solder alloys with the addition of Fe and Bi. *Microelectronics Reliability*, *139*, 114802. https://doi.org/https://doi.org/10.1016/j.microrel.2022.114802

Jiang, N., Zhang, L., Liu, Z.-Q., Sun, L., Long, W.-M., He, P., Xiong, M.-Y., & Zhao, M. (2019). Reliability issues of lead-free solder joints in electronic devices. *Science and Technology of Advanced Materials*, *20*(1), 876–901. https://doi.org/10.1080/14686996.2019.1640072

Kuang, H., Wu, B., Wang, J., Fu, J., Feng, Y., Yu, C., Wang, Z., Zhang, J., & Ji, Y. (2022). Wettability and thermal contact resistance of thermal interface material composited by gallium-based liquid metal on copper foam. *International Journal of Heat and Mass Transfer*, *199*, 123444. https://doi.org/https://doi.org/10.1016/j.ijheatmasstransfer.2022.123444

Li, Y., Chen, C., Yi, R., & Ouyang, Y. (2020). Review: Special brazing and soldering. *Journal of Manufacturing Processes*, *60*, 608–635. https://doi.org/https://doi.org/10.1016/j.jmapro.2020.10.049

Liu, G., Du, K., & Wang, K. (2016). Surface wettability of TiO2 nanotube arrays prepared by electrochemical anodization. *Applied Surface Science*, 388, 313–320. https://doi.org/10.1016/j.apsusc.2016.01.010

Niu, C., Dong, M., &Niu, Y. (2023). Lead toxicity and potential therapeutic effect of plant-derived polyphenols. *Phytomedicine*, *114*, 154789. https://doi.org/https://doi.org/10.1016/j.phymed.2023.154789

Patil, P. S., & Dabade, U. A. (2019). Selection of bearing material to comply RoHS regulations as per EU directive: A review. *Materials Today: Proceedings*, *19*, 528–531. https://doi.org/https://doi.org/10.1016/j.matpr.2019.07.648

Pecht, M., Shibutani, T., & Wu, L. (2016). A reliability assessment guide for the transition planning to lead-free electronics for companies whose products are RoHS exempted or excluded. *MicroelectronicsReliability*, *62*, 113–123. https://doi.org/10.1016/j.microrel.2016.03.020

Pivinskii, Y. E. (2021). Cement-Free Refractory Concretes. Part 7. Concrete Mix Properties and their Grain Size Distribution. *Refract Ind Ceram* *62*, 32–40. https://doi.org/10.1007/s11148-021-00556-x

Rocha, O. L., Costa, T. A., Dias, M., & Garcia, A. (2018). Cellular/dendritic transition, dendritic growth, and microhardness in directionally solidified monophasic Sn-2%Sb alloy. *Transactions of Nonferrous Metals Society of China*, *28*(8), 1679–1686. https://doi.org/10.1016/S1003-6326(18)64811-3

Sehirli, E., Erer, A. M., &Turan, M. K. (2022). A new approach for measuring the wetting angles of lead-free solder alloys from digital images. *Engineering Science and Technology, an International Journal*, *36*, 101279. https://doi.org/https://doi.org/10.1016/j.jestch.2022.101279

Šuryová, D., Kostolný, I., &Koleňák, R. (2020). Properties and application of Zn-based solders. *International Journal of Scientific and Technical Research in Engineering (IJSTRE) Www.Ijstre.Com*, *5*. www.ijstre.com

Thomas, O., leBot, B., Verrey, D., Durand, S., Harpet, C., Froment, A., &Jégou, B. (2022). High lead level in the Alps in XIXth century, learning from the analysis of 138 historical hair stands. *Chemosphere*, *286*, 131658. https://doi.org/https://doi.org/10.1016/j.chemosphere.2021.131658

Wernicki, E., Shu, Y., Fratto, E., Gao, F., Morose, G., Lucas, B., Yang, Z., &Gu, Z. (2023). Preparation and characterization of nano-solder paste with high nanoparticle loading and their thermal and printing properties. *Materials Chemistry and Physics*, *297*, 127399. https://doi.org/https://doi.org/10.1016/j.matchemphys.2023.127399

Zhou, Z., Chen, J., Yu, C., Wang, Y., & Zhang, Y. (2023). Failure Analysis of Printed Circuit Board Solder Joint under Thermal Shock. *Coatings*, *13*(3). https://doi.org/10.3390/coatings13030572

RECyT
Year 27 / Nº 43 / 2025 /
DOI: https://doi.org/10.36995/j.recyt.2025.43.003

Comparison of sensory shelf-life estimation of a beverage assessed in two locations

Comparación de la estimación de vida útil sensorial de una bebida en dos emplazamientos

Eliana, Elizagoyen[1, 2, *]; Fernanda, Gugole Ottaviano[1, 3]; Soledad, Arce[1, 2]; Lorena, Garitta[1, 2]

1- Departamento de Evaluación Sensorial de Alimentos (DESA). Instituto Superior Experimental de Tecnología Alimentaria (ISETA). Buenos Aires, Argentina.
2- Consejo Nacional de Investigaciones Científicas y Técnicas (CONICET). Godoy Cruz 2290, CABA, Argentina.
3- Comisión de Investigaciones Científicas (CIC). Buenos Aires, Argentina.
* E-mail: eliana@desa.edu.ar

Received: 31/10/2023; Accepted: 28/02/2025

Abstract
Sensory Shelf-Life (SSL) estimation of a product consists of the sensory evaluation of a set of samples with different storage times, in which the test location plays an important role. The test location not only defines how the product is sampled and perceived, but it can also lead to different results with a given set of samples and consumers. This study compared the SSL estimation affected by two test locations: Central Location Test (CLT) and Home Use Test (HUT). Lemon-flavoured juice was used as a case study.
In the CLT, 112 consumers tested 50 ml of the sample (a small serving), whereas in the HUT, 300 consumers received a whole sealed bottle and tasted their regular consumption serving. In both cases, consumers were asked to express a decision of acceptance or rejection ("Would you normally consume this product? Yes or No"). Data was analysed using survival analysis statistics. No significant differences were found when estimating SSL in HUT and CLT.
This may be considered as the starting point for future investigations that can certainly confirm that the estimation of the SSL can be carried out by means of a conventional test, in CLT, considering its advantages in terms of cost and time invested.

Keywords: sensory shelf-life, Central Location Test, Home Use Test, survival analysis, censored data.

Resumen
La estimación de la Vida Útil Sensorial (VUS) de un producto consiste en la evaluación de un conjunto de muestras con diferentes tiempos de almacenamiento en la que el emplazamiento cumple un papel importante. Se pueden obtener diferentes resultados en diferentes emplazamientos con un conjunto de muestras y consumidores determinados. En este estudio se comparó la VUS evaluada en dos emplazamientos: Prueba de Ubicación Central (CLT) y Prueba de Uso Doméstico (HUT). Se utilizó agua saborizada como caso de estudio.
En la CLT, 112 consumidores probaron 50 ml de muestra (una porción) y, en la HUT, 300 consumidores recibieron una botella cerrada y degustaron su porción habitual de consumo. En ambos casos, se pidió a los consumidores que expresaran una decisión de aceptación o rechazo. Los datos se analizaron mediante estadísticas de supervivencia. No se encontraron diferencias significativas al estimar la VUS en la HUT y la CLT.
Esto puede considerarse el inicio de futuras investigaciones que permitan establecer con certeza que la estimación de la VUS puede realizarse mediante el empleo del test convencional, en la CLT, con la ventaja que ello conlleva en cuanto a coste y tiempo invertido.

Palabras clave: vida útil sensorial, Prueba de Ubicación Central, Prueba de Uso Doméstico, análisis de supervivencia, datos censurados.

1. Introduction

Sensory Shelf-Life (SSL) estimation of a food product consists of evaluating the sensory characteristics of a set of samples with different storage times [1]. Survival analysis has become one of the most popular methodologies for SSL estimation, focusing on the risk of consumer rejection rather than on product deterioration [2;3;4]. Experimental work is relatively simple: a group of consumers tasted samples with different storage times or levels of sensory defect and answered whether they accepted or rejected them. This decision was in line with typical consumer behaviour when dealing with a food product nearing the end of its SSL or approaching intolerable sensory limits [5].

Sensory studies with consumers can be carried out in different locations and, according to that, environmental conditions are different as well as the way in which tested samples are presented to consumers [6].

In standardised situation tests, such as Central Location Tests (CLTs) and laboratory studies, a consumer tastes a small serving of a product, for example, a quarter of an *alfajor* [7], 50 g of yoghurt [8;4] or a slice of tomato [9]. In a SSL study, consumers have to taste six or seven samples with different storage times under standardised consumption conditions [10;6]; in this way, they can taste three of them, take a break and drink some water as a palate cleanser, and then proceed to taste the remaining three samples. This is one of the most popular (or common) methods. These kinds of tests are usually performed in a university classroom, a shopping centre or a sensory analysis laboratory, among other facilities. The main disadvantage is that standardised preparation procedures and product handling protocols might not necessarily mimic consumer behaviour and experience at home, i.e., they might differ from natural consumption situations [6].

In contrast, real environments (such as Home Use Tests or HUTs) constitute another possibility. In this case, consumers receive a whole sealed product, then they prepare it in their own way, choose the moment and taste a regular consumption serving. For example, a pizza [11] or a chocolate bar [12]. The product is prepared and/or consumed under natural conditions, facilitating information collection over repeated consumption of the product rather than a first impression only. The advantage is that this approach allows for gathering more information regarding the product in general [6].

It should be noted that none of the examples mentioned above, about whole sealed products evaluated in HUTs, correspond to SSL studies. Some studies on SSL have only evaluated the effect of context or environment using the evoked context methodology [13; 14]. That is, although the influence of context has been studied, consumers did not taste the whole product in a real consumption environment or in the natural way they generally would. Elizagoyen *et al*. (2017) [15] studied the behaviour of consumers considering two different occasions: purchase and home consumption. In this latter study, survival analysis statistics were applied to estimate the optimal ripening indexes of bananas based on hue-angle measurements, revealing that purchase occasions were lower than consumption occasions for home. Using a model based on survival analysis statistics, Sosa *et al*. (2008) [16] compared the optimal salt concentration in French-type bread both in HUTs and CLTs.

No studies have been conducted to determine whether differences exist in the SSL estimation when a consumer tastes a small serving of a product in a CLT versus a regular serving in a HUT. Therefore, this was the objective of the present study.

2. Materials and methods

2.1 Samples

From a batch of fresh samples kept at a cooling temperature, each of them was stored in a chamber at 24 °C and exposed to 12 hours of light a day with daylight-type fluorescent lamps to simulate bottle conditions on supermarket shelves.

Three fresh batches were used to ensure that all conditions originated from fresh samples. One batch was used at the beginning of the trial (from which times T6, T5, T4 and T3 were taken), another one in the middle of the trial (from which times T2 and T1 were taken) and a final batch which corresponded to T0 or the fresh sample.

Each time the fresh sample was replaced, a panel of trained evaluators and assessors performed a triangle test under the guidelines of ISO 4120 [17]

(Sensory analysis. Methodology. Triangle test.) for similarity tests, ensuring there were no variations in the different batches.
Storage times for both tests (small serving in a CLT and regular serving in a HUT) are presented in Table 1.

Table 1. Storage times for each sample of the corresponding lemon-flavoured juice.

Storage time (days)	Sample
0	T0
90	T1
150	T2
210	T3
240	T4
270	T5
300	T6

2.2 Methodology

Following the guidelines proposed by Hough (2010) [6] for SSL estimation, the employed methodologies were different for a small serving evaluated in a CLT in comparison with a regular serving evaluated in a HUT, as described below:

a) To evaluate a small serving in a CLT: this test was conducted in the Instituto Superior Experimental de Tecnología Alimentaria (from Spanish, Higher Experimental Institute of Food Technology or ISETA), equipped with individual booths, daylight type fluorescent lamps, air extractors, and controlled temperature. 112 frequent consumers of lemon-flavoured drinks were recruited [18], whose average age was between 18 and 60 years old and who were from Nueve de Julio city.

Consumers evaluated 7 samples corresponding to 7 storage times (Table 1). 50 ml of each sample was served at 12 ± 2 °C in plastic cups with a maximum capacity of 70 ml and coded with a three-digit number. For each sample, consumers were asked to express a decision of acceptance or rejection (“Would you normally consume this product? Yes or No”).

The presentation order of the samples was balanced over consumers.

b) To evaluate a regular serving in a HUT: this test was conducted at the home in a real consumption environment. We used the methodology developed by Araneda *et al*. (2008) [19]. Following the guidelines of Libertino *et al*. (2011) [20], 300 consumers with the same consumption and sociodemographic characteristics as in the CLT participated in the test, and they also had to answer (“Would you normally consume this product? Yes or No”). For each sample or experimental unit, they were divided into 6 groups of 50 consumers (from T1 to T6 in Table 1). Each group was composed of different individuals, and participants in the HUT did not participate in the CLT. This type of data is known as Current-Status Data (CSD) in survival analysis statistics [21]. In contrast to conventional designs, where consumers evaluate the fresh sample and, if they accept it, proceed to further evaluations; CSD designs do not require consumers to evaluate the fresh sample, because no further evaluation of the samples will occur. The premise of the design is that each consumer evaluates a single sample. Thus, if they reject the sample, we already know they are not eligible for a task that will not be required of them [20].

Each consumer received a sealed 500 ml bottle of lemon-flavoured juice, without a commercial label and coded with a three-digit number. They were instructed to consume as much as they normally would, at the temperature they normally prefer, at the time they want and accompanied by the food of their choice.

Ethics statement: this study was approved by the Ethics Committee of the Higher Experimental Institute of Food Technology (ISETA), and informed consent was obtained from each subject prior to their participation.

2.3 Statistical analysis

To estimate the SSL of a product, the first step is to obtain censored data based on participants’ acceptance or rejection of the question: “Would you normally consume this product? Yes, or No?” [6].

As it was explained in Section 2.2, the methodology employed for evaluations in CLTs and HUTs was different and, for this reason, data treatment to collect censored data is also different. The procedure used in each case is described below. In a CLT, the conventional methodology was applied, following the same model as the one developed by Hough (2010) [6]. It is then assumed that a random variable T represents the storage time at which the consumer rejects the sample. Thus, the rejection function can be defined as the probability of a consumer to reject a product before time *t*, to be precise, F(t)= P (T ≤ t).

The moment at which the consumer rejects a sample depends on the product storage time. However, since the exact time of rejection is not directly observed, the results are considered as censored times [22]. For instance, data from 3 consumers are presented in Table 2 to illustrate the different types of censoring.

Table 2. Examples of censored data obtained using the conventional methodology (small serving in the CLT).

Consumer	Storage time (days)							Censoring
	0	90	150	210	240	270	300	
1	Yes	Yes	Yes	Yes	No	No	No	**interval: 210 – 240**
2	Yes	Yes	Yes	Yes	Yes	Yes	Yes	**right: > 300**
3	Yes	No	Yes	Yes	No	No	No	**left: ≤240**

Yes/No: answer to the question "Would you normally consume this product? Yes or No"

In the case of *Consumer 1,* the data are interval-censored because the precise storage time (between 210 days and 240 days) at which the consumer would begin to reject the product is not known. For *Consumer 2,* rejection is assumed to occur in a storage time after than 300 days, resulting in right-censored data. In the matter of *Consumer 3,* their data was considered left-censored. This constitutes a special case of interval-censoring with the lower bound being equal to Time=0. On this occasion, it could be interpreted as T≤ 90 days or T ≤ 240 days, and we have considered the latter option.

The likelihood function (Equation 1), used to estimate the rejection function [24], is a mathematical expression that represents the joint probability of obtaining the observed data from the consumers in the study, expressed as a function of the unknown parameters of the model being considered.

$$\boldsymbol{L} = \coprod_{i\varepsilon R}(\boldsymbol{1} - \boldsymbol{F}(\boldsymbol{r_i}))\prod_{i\varepsilon L}\boldsymbol{F}(\boldsymbol{l})\prod_{i\varepsilon I}(\boldsymbol{F}(\boldsymbol{r_i}) - \boldsymbol{F}(\boldsymbol{l_i}))$$
(Equation 1)

R represents the set of right-censored observations ($\boldsymbol{r_i}$ corresponds to each right-censored observation), while ***L*** is the set of left-censored observations ($\boldsymbol{l_i}$ corresponds to each left-censored observation), and ***I*** represents the set of interval-censored observations. This equation illustrates how each type of censored data contributes differently to the likelihood functions.

As for the HUT, each consumer tasted a single sample corresponding to a single storage time (CSD). As an example, Table 3 illustrates the different types of censored data.

Table 3. Censored data obtained from the CSD methodology (regular serving in the HUT).

Consumer	Storage time (days)	Answer	Censoring
1	90	Yes	**right**
2	90	Yes	**right**
3	90	Yes	**right**
…	…	…	**…**
151	240	No	**left**
152	240	Yes	**right**
153	240	No	**left**
…	…	…	**…**
348	300	No	**left**
349	300	No	**left**
350	300	No	**left**

Yes/No: answer to the question "Would you normally consume this product? Yes or No"

When consumers taste a sample, there are two alternatives: 1) They accept it, which means their data is right-censored. In other words, consumers´ rejection time exceeds the duration or intensity of the tasted sample. 2) They reject it, which means their data is left-censored. Specifically, consumers´ rejection time is lower than the duration or intensity of the tasted sample.

As was previously explained, in HUTs, there is no interval censoring and, therefore, the likelihood function is:

$$\boldsymbol{L} = \prod_{i\varepsilon R}(\boldsymbol{1} - \boldsymbol{F}(\boldsymbol{r_i})\ \prod_{i\varepsilon L}(\boldsymbol{F}(\boldsymbol{l_i}))$$ **(Equation 2)**

R represents the set of right-censored observations ($\boldsymbol{r_i}$ corresponds to each right-censored observation) while ***L*** represents the set of left-censored observations ($\boldsymbol{l_i}$ correspond to each left-censored observation).

Once censored data for both locations were obtained, they were grouped or stacked to continue with the survival analysis. An example of the censored data from both methodologies is presented schematically in Table 4.

Table 4. Censored data from both locations (CLT and HUT).

Consumer	Tlow	Thigh	Cens	Location
1	210	240	interval	CLT
2	300	300	right	CLT
3	240	240	left	CLT
…	…	…	…	…
1	240	240	left	HUT
2	240	240	right	HUT
3	240	240	left	HUT

Column headings: consumer: identification of consumer within each group; tlow: low time interval (days); thigh: high time interval (days); cens: type de censoring; location: CLT or HUT

Survival times are typically not normally distributed; instead, their distribution is often right-skewed. In such cases, a log-linear model is employed:

$$\boldsymbol{ln(t) = \mu + \sigma W} \qquad \textbf{(Equation 3)}$$

Where $\boldsymbol{W}$ is the error distribution.
If the Weibull distribution is chosen for $\boldsymbol{t}$, the rejection function is defined as:

$$\boldsymbol{F(t) = exp\left[- exp\left(\frac{\ln(t) - \mu}{\sigma}\right)\right]} \qquad \textbf{(Equation 4)}$$

where, $\boldsymbol{exp[-exp]}$ represents the rejection of the extreme value distribution, and $\boldsymbol{\mu}$ and $\boldsymbol{\sigma}$ represent the model parameters.
To determine whether the employed testing location (CLT or HUT) influenced the SSL estimation, the following log-linear regression model with covariates was applied [25]:

$$\boldsymbol{ln(t) = \mu + \sigma W = \beta_0 + \beta_1 Z + \sigma W} \qquad \textbf{(Equation 5)}$$

Where $\boldsymbol{t}$ represents the storage time at which a consumer rejects a sample; $\boldsymbol{\beta_0}$ and $\boldsymbol{\beta_1}$ correspond to the regression coefficients; $\boldsymbol{Z}$ represents the covariate indicating the location: 1 HUT and 0 CLT; $\boldsymbol{\sigma}$ correspond to the shape parameter, which does not depend on the covariates; and $\boldsymbol{W}$ represents the error distribution.
If the Weibull distribution is chosen for $\boldsymbol{t}$, the rejection function is defined as:

$$\boldsymbol{F(t) = exp\left[- exp\left(\frac{\ln(t) - \beta_0 + \beta_1 Z}{\sigma}\right)\right]} \qquad \textbf{(Equation 6)}$$

The parameters of the log-linear model were estimated by maximising the likelihood function. Klein and Moeschberger (1997) [22] and Lindsey (1998) [26] present a complete discussion of different distributions.
To define the model that best fits the experimental data, different distributions were considered, and the log-likelihood criterion was used [6].
Survival analysis was performed using TIBCO Spotfire® S+ software (TIBCO Inc., Seattle, WA). After statistical analysis, an SSL value must be recommended, and this implies selecting an adequate percent rejection. Some authors adopted rejection levels of 25% or 50%, depending on the product [8]. This means that if a consumer tastes a product with a storage time corresponding to a 50% rejection probability, it has a 50% likelihood of being rejected by the consumer. This is consistent with other studies and international sensory analysis standards [27;28;17], which establish criteria for determining when the proportion of the population able to detect a difference is considered significant [6]. In this study, a 50% rejection threshold was adopted for SSL estimation.

3. Results and discussion

Data was best adjusted by the Weibull distribution. The location covariate was not significant, resulting in a value of p = 77%. Thus, the model without the covariate was adopted (Equation 4), whose parameters were: μ = 6.02 and σ= 0.63. These parameters were used to graph the percentage of rejection versus storage time, shown in Figure 1.

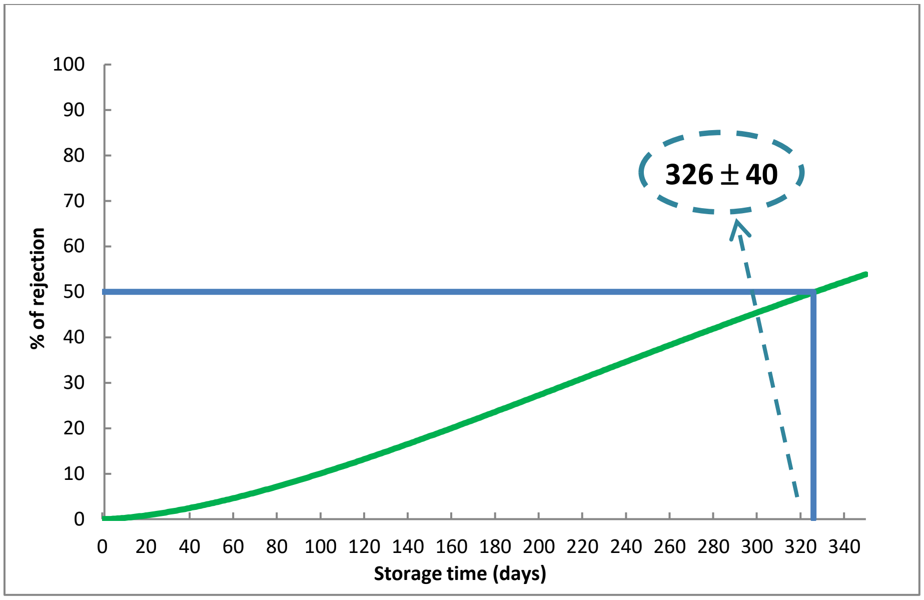

Figure 1. Percentage of rejection versus storage time.

The estimated SSL value corresponding to 50% consumers' rejection, with their 95% confidence interval, was equal to 326 ± 40 days.

This is particularly relevant, as it provides the certainty that for this type of product, self-life can be estimated by performing conventional laboratory testing, offering advantages in terms of cost and time efficiency. However, it should be noted that standardised preparation procedures and product handling protocols in the laboratory differ from those in a natural consumption situation [6].

The SSL estimation results obtained in this study have exhibited a different behaviour from those reported in previous studies. For example, Ares *et al*. (2008) [13] used survival analysis statistics to study the influence of evoked context on the SSL of minimally processed lettuce. They found that the SSL associated with the purchase occasion was lower than that for the in-home consumption occasion. Giménez *et al*. (2015) [14] also employed survival analysis to study the effect of evoked context (consumption at home and purchase at supermarkets). The shelf-lives estimated on consumers' rejection when purchasing were shorter than those estimated based on rejection to consume. This rejection of products with different storage times or a sensory defect intensity is noteworthy and should be considered in future SSL studies. It is important to note that the referenced studies employed an evoked context methodology for evaluation, instead of the real consumption situation that was used in this study. Having said this, it would be valuable to repeat these methodologies with both similar and non-similar products as a way of validating this research.

4. Conclusion

In this study, no significant differences were found at evaluating a small serving of lemon-flavoured juice in a CLT versus a HUT. Therefore, SSL studies applying survival analysis could be carried out using either of the two methodologies. However, employing the conventional test, in CLT (which offers advantages in terms of cost and time efficiency), appears to be the recommended approach for determining SSL in consumers.

Further research should be carried out to confirm the findings of the present study with other products, while considering other factors for future studies, such as consumer age, different expiration dates, and differences between packaged and unpackaged products. It may also be of interest to replicate this study using a single environment (laboratory) to investigate the effect of the sample serving on SSL estimation under controlled conditions.

Nomenclature

SSL: Sensory Shelf-Life
CLT: Central Location Test

HUT: Home Use Test
CSD: Current-Status Data

Acknowledgments
The authors are grateful to Dr. G. Hough for his selfless help in the statistical analysis of data.

References

[1] Bishop, J.R. & White. C.H. (1986). Assessment of dairy product quality and potential shelf-life – A review. Journal of Protection, 49, 739-753. DOI: https://doi.org/10.4315/0362-028X-49.9.739.

[2] Giménez, A., Ares, F., & Ares, G. (2012). Sensory shelf-life estimation: A review of current methodological approaches. Food Research International, 49, 311-325. DOI: https://doi.org/10.1016/j.foodres.2012.07.008.

[3] Hough, G., Garitta, L. & Sanchez, R. (2004). Determination of consumer acceptance limits to sensory defects using survival analysis. Food Quality and Preference, 15, 729-734. DOI: 10.1016/j.foodqual.2004.02.006.

[4] Hough, G., Langohr, K., Gómez, G., & Curia, A. (2003). Survival analysis applied to sensory shelf-life of foods. Journal of Food Science, 68 (1), 359-362. DOI: https://doi.org/10.1111/j.1365-2621.2003.tb14165.x.

[5] Garitta, L., Langohr, K., Gómez, G., Hough, G. & Beeren, C. (2015). Sensory cut-off point obtained from survival analysis statistics. Food Quality and Preference, 43, 135-140. DOI: https://doi.org/10.1016/j.foodqual.2015.02.012.

[6] Hough, G. (2010). Sensory Shelf-Life Estimation of Food Products (1st ed.). CRC Press. DOI: https://doi.org/10.1201/9781420092943.

[7] Gámbaro, A., Giménez, A., Varela, P., Garitta, L. & Hough, G. (2004). Sensory shelf-life estimation of an Alfajor by survival analysis. Journal of Sensory Studies. 19, 500-509. DOI: http://10.1111/j.1745-459X.2004.050704.x

[8] Curia, A., Aguerrido, M., Langohr, K. & Hough, G. (2005). Survival Analysis Applied to Sensory Shelf Life of Yogurts–I: Argentine Formulations. Journal of Food Science, 70, 442-445. DOI: http://dx.doi.org/10.1111/j.1365-2621.2005.tb11489.x.

[9] Garitta, L., Hough, G. & Hulshof, E. (2008). Determining optimum ripening time of fruits applying survival analysis statistics to consumer data. Food Quality and Preference. 19, 747-752. DOI: http://10.1016/j.foodqual.2008.03.003.

[10] Boutrolle, I., Delarue, J., Arranz, D., Rogeaux, M. & Köster, E. (2007). Central location test vs. home use test: Contrasting results depending on product type. Food Quality and Preference 18, 3. DOI: http://dx.doi.org/10.1016/j.foodqual.2006.06.003.

[11] Ratanatriwong, P., Suk Yeung, M., Jusup, C. & Matrid, N. (2006). Comparison of Consumer Acceptances of Frozen Pizzas Assessed at Central Location Test (CLT) vs Home Use Test (HUT). Natural Science 40, (5): 197-202.

[12] Karin, W.; Annika, A.; Anna, S. 2015. Exploring differences between central located test and home use test in a living lab context. International Journal of Consumer Studies 39: 230-238.

[13] Ares, G., Giménez, A., & Gámbaro, A. (2008). Sensory shelf-life estimation of minimally processed lettuce considering two stages of consumers` decision-making process. ScienceDirect, 50, 529-535. DOI: https://doi.org/10.1016/j.appet.2007.11.002.

[14] Giménez, A., Gagliardi, A., & Ares, G. (2015). Influence of evoked contexts on consumers' rejection of two products: Implications for shelf-life estimation. Food Research International, 76, (3), 527-531. DOI: https://doi.org/10.1016/j.foodres.2015.06.041.

[15] Elizagoyen, E.S., Hough, G., Garitta, L. Fiszman, S. & Vasquez, J. (2017). Consumer's expectation of changes in fruit based on their sensory properties at purchase. The case of banana (Musa Cavendish) appearance evaluated on two occasions: Purchase and home consumption. Journal of sensory studies, 32, 4. DOI: https://doi.org/10.1111/joss.12278.

[16] Sosa, M., Flores, A., Hough, G., Apro, N., Ferreyra, V. & Orbea, M. M. (2008). Optimum Level of Salt in French-Type Bread. Influence of Income Status, Salt Level in Daily Bread Consumption, and Test Location. Journal of Food Science, 73 (8). S392-S397. DOI: https://doi.org/10.1111/j.1750-3841.2008.00898.x.

[17] ISO Standard 4120 (2004). Sensory analysis – Methodology – Triangle test. Geneva: International Standard Organization.

[18] Hough, G., Calle, M. L., Serrat, C., & Curia, A. (2007). Number of consumers necessary for shelf-

life estimations based on survival analysis statistics". Food Quality and Preference, 18, 771-775. DOI: https://doi.org/doi:10.1016/j.foodqual.2007.01.003.

[19] Araneda, M., Hough, G. & Wittig De Penna, E. (2008). Current-status survival analysis methodology applied to estimating sensory shelf life of ready-to-eat lettuce (Lactuca sativa). Journal of Sensory Studies: 23, 162–170. https://doi.org/10.1111/j.1745-459X.2007.00140.x

[20] Libertino, L.; López Osornio, M. & Hough, G. 2011. Number of consumers necessary for survival analysis estimations based on each consumer evaluating a single sample. DOI:10.1016/j.foodqual.2010.06.006

[21] Shiboski, C. (1998). Generalized additive models for current status data. Lifetime. Data analysis, 4: 29-50. DOI: https://doi.org/10.1023/a:1009652024999.

[22] Klein, J.P. & Moeschberger, S. (1997) Survival Analysis: Techniques for Censored and Truncated Data. Springer, Berlin. DOI: https://doi.org/10.1007/978-1-4757-2728-9.

[24] Garitta, L.; Hough, G. & Sanchez, R. 2004. Sensory shelf life of dulce de leche. Journal of Dairy Science, 87: 1601-1607. DOI: https://doi.org/10.3168/jds.S0022-0302(04)73314-7.

[25] Meeker, W.Q. & Escobar, L.A. (1998). Statical methods for reliability data. New York, USA: John Wiley y Sons.

[26] Lindsey, J.K. (1998). A study of interval censoring in parametric regression models. Lifetime Data Analysis, 4, 329-354.

[27] ATSM Standard E1432-04. 2006. Standard practice for defining and calculating in individual and group sensory threshold from forced-choice data sets of intermediate size. West Conshohocken, PA: American Society for Testing and Material.

[28] ISO Standard 13301 (2002). Sensory analysis – Methodology – General guidance for measuring odour, flavor and taste detection thresholds by a three-alternative forced-choiced (3-AFC) procedure. Geneva: International Standard Organization.

RECyT
Year 27 / Nº 43 / 2025 /
DOI: https://doi.org/10.36995/j.recyt.2025.43.004

Effect of operating parameters on air drying potential in a prototype dryer with heat pump

Efecto de los parámetros de funcionamiento sobre el potencial de secado del aire en un prototipo de secador con bomba de calor

Efeito dos parâmetros operacionais no potencial de secagem do ar em um protótipo de secador com bomba de calor

Rodrigo, Aparecido Jordan[1]; Fabricio, Correia de Oliveira[2, *]; Anamari, Viegas de Araújo Motomiya[1]; João, Pedro Jordan[3]; Rodrigo, Couto Santos[1]; Valdiney, Cambuy Siqueira[1]; Elton, Aparecido Siqueira Martins[1]

1- Universidade Federal da Grande Dourados. Brasil.
2- Universidade Tecnológica Federal do Paraná (UTFPR). Brasil.
3- Universidade Estadual do Oeste do Paraná (UNIOESTE). Brasil.

* E-mail: fcoliveira@utfpr.edu.br

Received: 20/08/2024; Accepted: 20/03/2025

Abstract
In low temperature drying, relative humidity —which expresses the relationship between air vapour pressure and saturation pressure at the same temperature— is the parameter with the greatest influence on the drying rate, as mass exchange is directly related to the vapour pressure difference between the product and the air. This study aimed to evaluate the effects of operating parameters on relative humidity values in a prototype system based on heat pump technology. This system was developed for low-temperature drying, cooling, and the control of air psychrometric conditions for post-harvest storage and preservation of agricultural products. The data was evaluated using a completely randomized design with five replications. Two drying temperatures were employed: 25 °C and 30 ºC. As for the air blower, rotations of 20, 25, 30, 35, 45 and 60 Hz were used. Regarding the refrigeration compressor, rotations of 30, 35, 40, 45 and 50 Hz were used. The results showed that both compressor and blower rotations had highly significant effects. On the other hand, relative humidity values tended to decrease as compressor rotation increased, whereas they increased with higher blower rotation.

Keywords: low temperature, relative humidity, cooling, evaporation temperature.

Resumen
En el secado a baja temperatura, la humedad relativa (que expresa la relación entre la presión de vapor del aire y la presión de saturación a la misma temperatura) es el parámetro que más influye en la velocidad del proceso, ya que el intercambio de masa está directamente relacionado con la diferencia de presión de vapor entre el producto y el aire. El objetivo de este trabajo fue evaluar los efectos de los parámetros de operación sobre los valores de humedad relativa en un prototipo de sistema basado en la tecnología de bomba de calor. Este sistema se desarrolló para el secado a baja temperatura, enfriamiento y control de las condiciones psicrométricas del aire para el almacenamiento poscosecha y conservación de productos agrícolas. Los datos se evaluaron mediante un diseño completamente aleatorizado con cinco repeticiones. Se utilizaron dos temperaturas de secado: 25 °C y 30 °C. Se utilizaron rotaciones del soplador de aire de 20, 25, 30, 35, 45 y 60 Hz. En cuanto al compresor de refrigeración se utilizaron rotaciones de 30, 35, 40, 45 y 50 Hz. Los resultados mostraron que tanto la rotación del compresor como la del soplador tenían efectos muy significativos. Mientras que los valores de humedad relativa tendían a disminuir al aumentar la rotación del compresor, ocurría lo contrario al aumentar la rotación del soplador.

Palabras claves: baja temperatura, humedad relativa, enfriamiento, temperatura de evaporación.

Resumo
Na secagem a baixa temperatura, a umidade relativa, que expressa a relação entre a pressão de vapor do ar e a pressão de saturação na mesma temperatura, é o parâmetro de maior influência na velocidade do processo, uma vez que a troca de massa está diretamente relacionada à diferença de pressão de vapor entre o produto e o ar. O objetivo deste trabalho foi avaliar os efeitos dos parâmetros operacionais sobre os valores de umidade relativa em um protótipo de sistema baseado na tecnologia de bomba de calor, desenvolvido para secagem a baixa temperatura, resfriamento e controle das condições psicrométricas do ar para armazenamento e conservação pós-colheita de produtos agrícolas. Os dados foram avaliados utilizando um delineamento inteiramente casualizado com cinco repetições. Foram utilizadas duas temperaturas de secagem: 25 ºC e 30 ºC. Para o insuflador de ar,

foram utilizadas as rotações de 20, 25, 30, 35, 45 e 60 Hz. Para o compressor de refrigeração, foram utilizadas rotações de 30, 35, 40, 45 e 50 Hz. Os resultados mostraram que tanto a rotação do compressor como a do insuflador tiveram efeitos altamente significativos. Enquanto os valores de umidade relativa tendem a diminuir com o aumento da rotação do compressor, o oposto acontece com o aumento da rotação do insuflador.

Palavras-chave: baixa temperatura, umidade relativa, resfriamento, temperatura de evaporação.

Introduction

The search for more efficient technologies to reduce losses, improve product quality and, equally importantly, address the environmental issue of mitigating carbon emissions is becoming increasingly important nowadays [1].

In the agricultural sector, a major consumer of energy with a large share of non-renewable sources [2], this cannot be any different. While in rural areas agricultural machinery operates practically on its own, other sectors have seen little progress, for example, the drying of agricultural products in Brazil, which is still predominantly performed using direct-burning dryers, with firewood being the most commonly used fuel [3].

In addition to product contamination with toxic and cancerous residues from direct burning [4, 5], this process also leads to the emission of greenhouse gases [6], environmental issues related to the sourcing of the wood used [7], socio-economic concerns related to land-use changes for energy crops [8]. Moreover, the combustion process in an environment laden with particulates also poses the risk of accidents related to explosions [9]. In Brazil, in recent years, there has been an increase in the number of accidents in post-harvest processing and storage units for agricultural products due to the expansion of grain production [10].

Another characteristic of wood-fired dryers is their operation with high drying temperatures, which not only increase the occurrence of physical damage [11], but also cause nutritional and sensory losses in the products [12, 13]. These factors result in storage problems and reduced market value due to loss of quality [14, 15].

In this context, heat pumps are an interesting option which make rational use of the energy, generating a thermal effect that is many times greater, as they do not convert electrical energy directly into heat, but rather transfer heat from a low-temperature source to a high-temperature source [13].

Brazil has an exceptionally clean electricity matrix, with over 87% currently sourced from renewable sources [16]. This share is continuously growing, particularly with the expansion of photovoltaic energy following the approval of laws regulating distributed generation [17]. Such regulations create a compensation system where electricity surplus can momentarily be injected into the grid and retrieved for later use, creating an even more favourable environment for the adoption of cleaner technologies, such as heat pumps.

Heat pumps stand out as very efficient equipment [18]. In addition to being environmentally friendly, as they do not use fossil fuels but high-quality energy, they are attractive for studies in drying since they offer the advantage of multiple operating controls over temperature and relative humidity. The ecological advantage of using heat pumps in drying processes lies not only in their high efficiency, but also in the precise control of temperature and relative humidity [19, 20].

While, on the one hand, reducing the temperature is beneficial for maintaining product quality [21, 22, 23, 24, 25, 26], it can also greatly extend drying time, potentially having a negative impact due to the increased energy consumption with both economic and environmental implications [27].

Therefore, in order to obtain optimal results, low-temperature drying must be performed within a brief period [28]. Unlike high temperature drying, where temperature is the determining factor in time, in low temperature drying, relative humidity is the determining factor. Therefore, the lower its value, the greater the drying potential and the shorter the as well as the less energy consumption [13].

The air supply with low relative humidity values, even at low temperatures, is another advantageous aspect of using heat pumps in drying [29]. In contrast with conventional dryers, where the air only undergoes sensible heating, heat pumps first cool the air together with a process of dehumidification and reduce its vapour pressure, then reheat it [30, 31]. In this way, low humidity values can even be obtained at low temperatures.

Another advantage of heat pumps is the possibility of full automation of all operations [32]. Being aware of how the operating parameters affect the air outlet conditions, especially the relative humidity, is important when implementing more efficient control logic. In this context, this work aimed to analyse the operation of a prototype dryer and psychrometric controller for agricultural product storage conditions based on heat pump technology, focusing on the behaviour of relative humidity as a function of the main operating parameters (compressor speed and air blower speed).

Materials and methods

The equipment used in this study, named SIARCOMPAG (Autonomous System for Cooling and Psychrometric Control of Grain Storage Conditions), is a prototype developed to modulate the psychrometric conditions of the air used in drying and post-harvest conservation of agricultural products. Its operation focuses on modulating the temperature and relative humidity of the air [33].

Constructed with pump technology, as depicted in Figures 1 and 2, the SIARCOMPAG system features an air treatment duct. Within this section, the evaporator, secondary condenser, and fan (referred to as the air blower) are located. The refrigeration compressor and primary condenser are positioned below this duct, together with their corresponding blower. Furthermore, the system is equipped with an isothermal humidifier, which has the function of incrementing both the absolute and relative humidity of the air under particular conditions. Notably, increasing the water content of the processed product is necessary only in specific use cases. Nonetheless, this action is not required when the system operates in its drying mode.

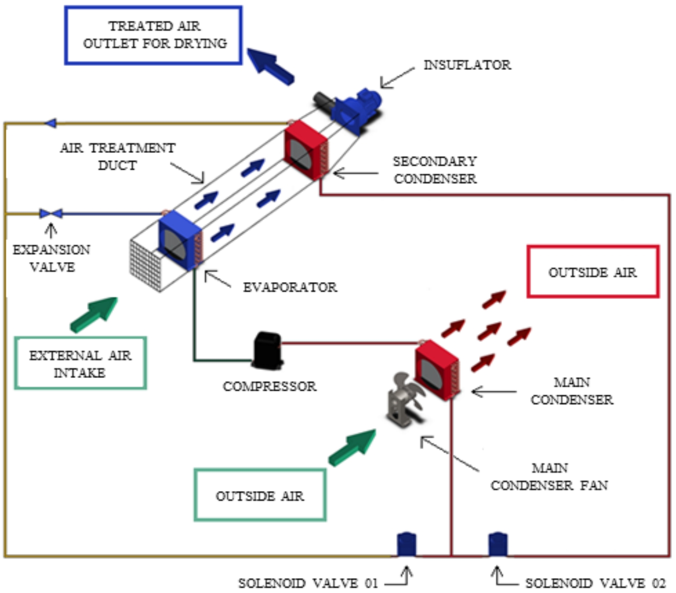

Figure 1: schematic diagram of the SIARCOMPAG.

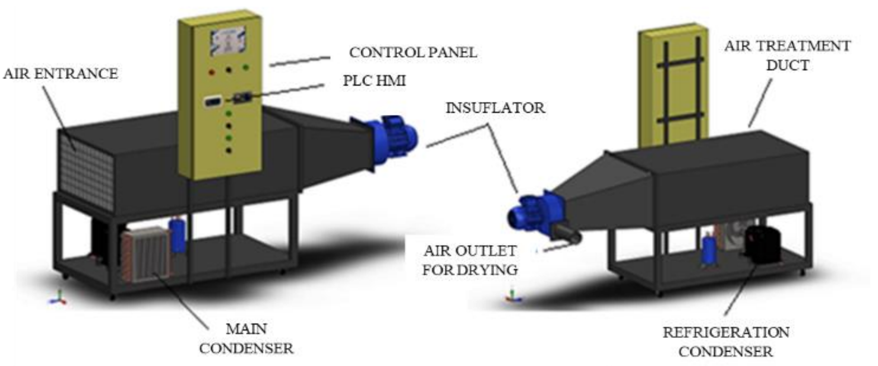

Figure 2: perspective view of the SIARCOMPAG.

The SIARCOMPAG system offers different operating modes: fully automatic, semi-automatic and fully manual. These modes can be selected and adapted based on programmable logic controller (PLC) settings through the human-machine interface (HMI). When operating in fully automatic mode, users can enter specific parameters into the HMI, including product type, desired temperature, and desired humidity of the final product. When operating in this mode, the PLC autonomously manages operating conditions by referencing equilibrium humidity equations, using PID (Proportional Integral Derivative) logic.

As for manual mode, operators are required to manually configure operational settings for each component: compressor rotation, blower rotation, auxiliary condenser activation, and main condenser fan rotation. Alternately, semi-automatic mode allows for a combination of manual and automatic adjustments. For instance, some conditions are automated, like outlet temperature, while others can be manually set.

When the system operates in drying mode, the outlet air temperature is maintained by adjusting the heat flow between the primary and secondary condensers. This is done by adjusting the rotation of the main condenser fan. Since both condensers are positioned in a sequence within the cooling circuit (an arrangement managed by the solenoid valves as depicted in Figure 1), varying the rotation of the main condenser fan adjusts the heat rejected by the secondary condenser, consequently altering the drying air temperature.

For our experiments, the system was set to semi-automatic mode: the outlet air temperature was controlled automatically, but the compressor and blower rotations were adjusted manually. In this configuration, the PLC automatically regulates the rotation of the main condenser fan to regulate the heat flow to the secondary condenser.

The drying temperatures chosen for the tests were inspired by a previous study [15], which found a correlation between drying temperature, relative humidity and drying time, revealing a direct proportionality between drying time and relative humidity. Therefore, in our study, we opted for temperatures of 25 ºC and 30 ºC, at which the relative humidity values significantly reduced the drying time.

The refrigeration compressor (Elgin model CR18K6TF5) was set to operate at rotations or frequencies of 30, 35, 40, 45, and 50 Hz. The air blower (Ventbras model SV100) was adjusted to rotations of 20, 25, 30, 35, 45, and 60 Hz. Maximums were limited to not exceeding the device’s designated factory specifications. The compressor's minimum rotation was guided by manufacturer guidelines, particularly to ensure proper lubrication. The lower limit of the blower was set to prevent evaporator blockage due to potential freezing, which could be caused by an insufficient airflow rate.

Temperature and relative humidity values at the air inlet (Ent), between the evaporator and the secondary condenser (Meio), and at the air blower outlet (Saida) were supplied using the RHT sensors integrated in the SIARCOMPAG system (Figure 3), These sensors provide data on air conditions to the PLC, enabling the automatic adjustment of operating parameters.. This information can be accessed via a specific HMI (human-machine interface) screen (Figure 4).

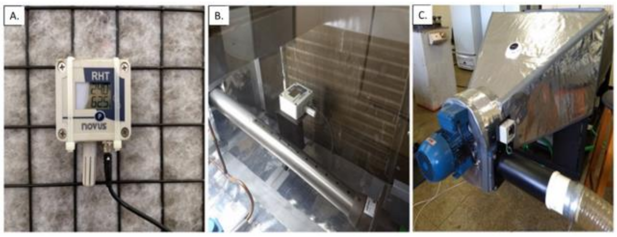

Figure 3: sensor locations: (A) RHT sensors at the entry, (B) sensor between the evaporator and secondary condenser, and (C) sensor at the air blower outlet.

Figure 4: human-machine interface screen with temperature and relative humidity data: input (Ent), midpoint (Meio) and output (Saida).

Evaporation temperatures and opening rates were supplied by the electronic expansion valve controller, which is assembled in the control panel of the psychrometric controller (Figure 5). This controller allows a highly accurate adjustment of the superheat temperature at the evaporator outlet, which facilitates operation with a practically constant evaporation temperature in each condition during the tests.

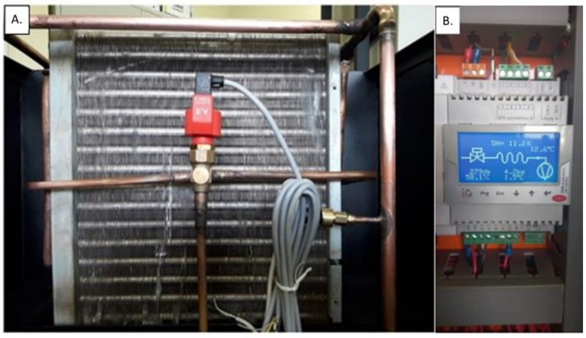

Figure 5: electronic expansion valve Carel model E^2V (A) and its corresponding controller Carel model EVD (B).

In tests where compressor rotation was adjusted, blower rotation was consistently set to its nominal value. Similarly, when blower rotation was modified, compressor rotation remained fixed at its nominal rate. For both cases, nominal rotations were equated to the maximum value employed during testing, which stood at 60 Hz.

For each setting condition, once parameters were adjusted, a stabilisation period for the equipment was observed, which ranged between 10 and 15 minutes. Upon stabilisation, measurements were taken and, to do so, each condition was subjected to five repetitions conducted at 2-minute intervals, totalling a 10-minute duration for each test.

Graphic presentations were employed to streamline the analysis, focusing on output conditions (relative humidity and temperature values) as a function of operating parameters (compressor and blower rotations).

Statistical evaluations were conducted using R statistical software, version 4.0.2 [34], based on a completely randomized design with five replications per assay. Data underwent tests to measure normality (Shapiro-Wilk test) and variance homoscedasticity (Bartlett test). After verifying these facts for each test, a variance analysis (ANOVA) was executed, gauging significance with the F test ($p \leq 0.01$).

When F values were deemed significant, data were subjected to regression analysis, evaluating both linear and polynomial models ($p \leq 0.01$). Best-fitting equations were selected based on the significance of model coefficients together with the optimal determination coefficients (R^2). As already mentioned [35], these statistical estimators effectively outline the structure of spatial dependence, which is influenced by the variables under analysis, as well as the shape and volume of the samples.

Results and discussion

Table 1 provides a summary of the variance analysis for output relative humidity values, considering both blower and compressor rotation. F-values are highly significant ($p \leq 0.01$) for both factors, indicating statistically distinct group means. The coefficient of variation (CV) is notably low, under 1%, reflecting strong experimental control and consistent data repeatability. As highlighted by Singh *et al*. [36], in agricultural research, it is preferable for CV values to be below 10%.

Table 1: F-values of the variance analysis (ANOVA) for average output relative humidity as a function of the blower and compressor rotations.

		Blower rotation			Compressor rotation	
		Drying temp. 25 °C	Drying temp. 30 °C		Drying temp. 25 °C	Drying temp. 30 °C
SV	DF	Mean squares		DF	Mean squares	
Rotation	5	114.925**	189.056**	4	50.431**	14.5536**
Error	24	0.053	0.014	20	0.049	0.0038
CV (%)		1.02	0.57		0.61	0.23

**: significant at $p \leq 0.01$ for the F-test; SV: sources of variation; DF: degrees of freedom; CV: coefficient of variation.

Figure 6 shows the air conditions at the psychrometric controller inlet, representing the average temperature and relative humidity values during the tests.

Figure 7 illustrates the behaviour of the average evaporation temperature in relation to blower rotation (A) and compressor rotation (B) at drying temperatures of 25 ºC and 30 ºC. The evaporation temperature was notably influenced by these parameters. In particular, the temperature showed a direct proportionality regarding blower rotation and an inverse proportionality regarding compressor rotation.

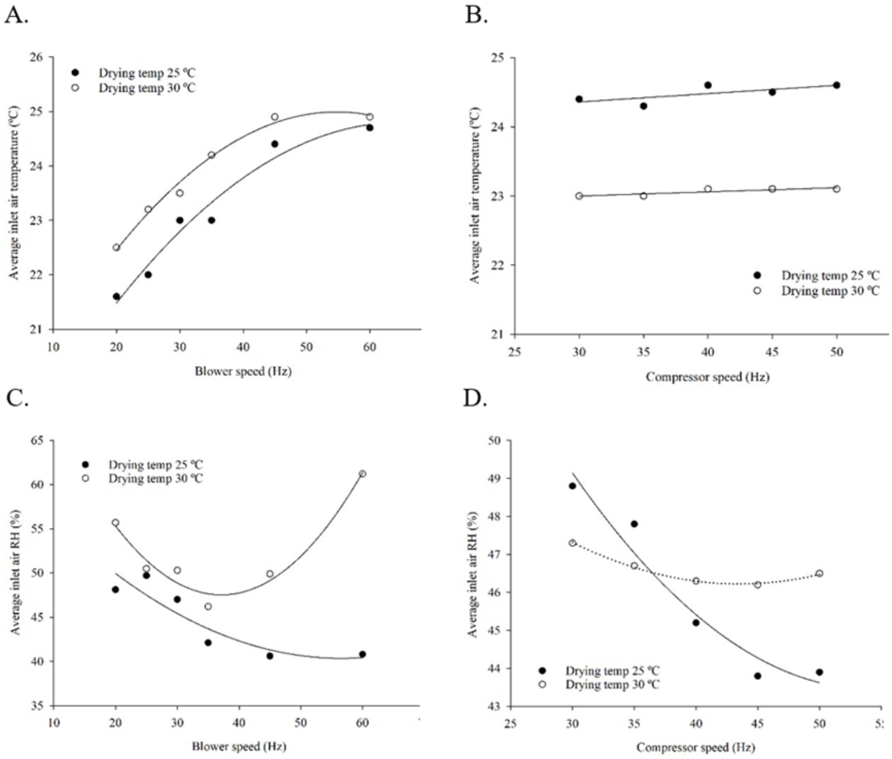

Figure 6: air conditions at the psychrometric controller inlet during tests: (A) average temperature with varied blower rotation, (B) average temperature with varied compressor rotation, (C) average relative humidity with varied blower rotation, and (D) average relative humidity with varied compressor speed.

The trend observed in the evaporation temperature in relation to the blower rotation can be attributed to the heat exchange in the evaporator and the capacity of the refrigeration system. Given that the compressor rotation remained constant, any variation in the air flow produced a change in the temperature of the evaporator outlet. This, in turn, prompted the expansion valve to avoid superheating by regulating the flow of refrigerant fluid within the evaporator. Consequently, this process altered the evaporation temperature to optimise the heat exchange process. As highlighted in a study by Wang *et al*. [37], optimizing heat exchange is crucial for heat pump systems, emphasizing the high efficiency of the dryer.

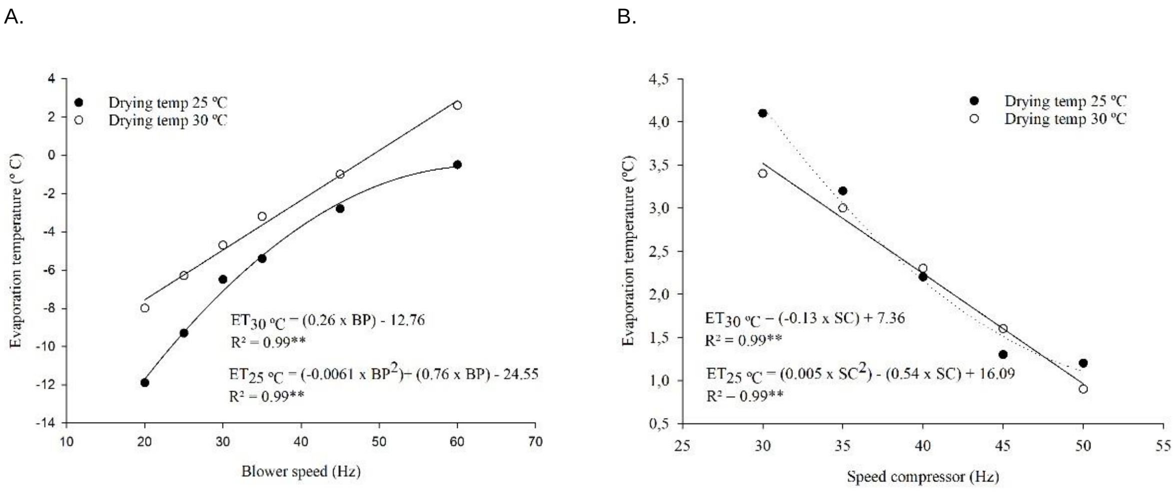

Figure 7: average evaporation temperature as a function of blower speed variation with a compressor speed fixed of 60 Hz (A) and compressor speed variation (B) with a blower speed fixed of 60 Hz.

The differences in behaviour (linear with 30 °C and second order with 25 °C) for the evaporation temperature observed in Figure 7 may be related to the difference in condensation pressure (Figure 8A), which affected the opening rate of the expansion valve (Figure 8B). The increase in drying temperature implies an increase in condensation temperature and, consequently, in condensation pressure, due to the reduction in the main condenser fan rotation to increase the heat flow that is rejected into the air in the secondary condenser.

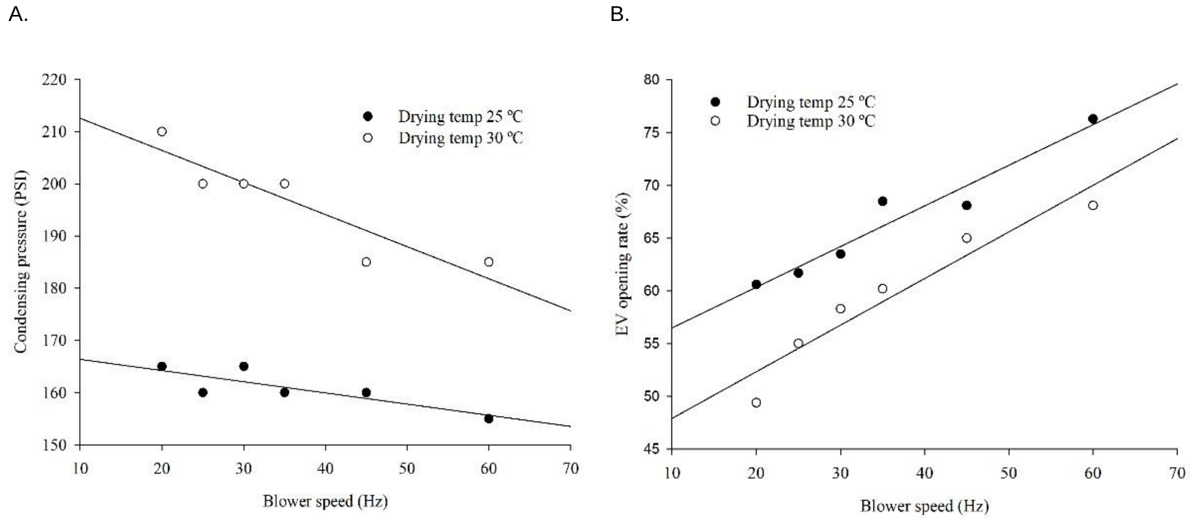

Figure 8: changes in condensing pressure (A) and expansion valve opening rate (B) as a function of varying blower rotation with compressor rotation fixed at 60 Hz.

As blower rotation increased, there was a noticeable decline in condensation pressure. This is attributed to a greater volume of air moving through the secondary condenser, enhancing the heat exchange process. Patel [38] highlighted the importance of this aspect, noting that refrigeration system performance relies significantly on efficient heat exchange, with its energy efficiency intricately linked to the pressure within the condenser.

The increase in drying temperature is achieved by reducing heat exchange in the primary condenser through a decrease in its fan speed, which in turn increases heat rejection in the secondary condenser. As the secondary condenser has a smaller capacity than the primary one, this explains the observed differences in pressure, the opening rate of the expansion valve and the slight variation in the slope inclination between the adjusted lines.

When examining the effects of changes in compressor rotation (Figure 7A), the trends in evaporation temperature appeared to be strongly associated with fluctuations in the refrigerant flow, which is controlled by the compressor. This relationship then affected the degree of opening of the expansion valve (Figure 9A). Inlet conditions during these tests were both smaller and more stable (Figures 6C and 6D). Additionally, changes in compressor rotation affected condensation pressure (Figure 9B). However, this influence was less pronounced on the opening rate of the expansion valve when the drying temperature was kept constant and only the blower rotation was varied.

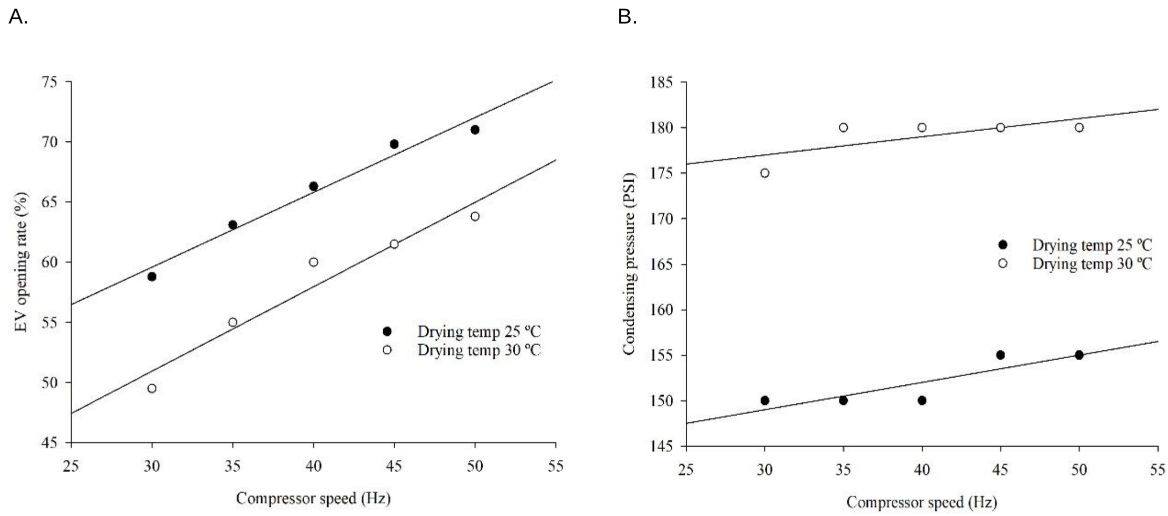

Figure 9: changes in condensing pressure (A) and expansion valve opening rate (B) as a function of varying compressor rotation with blower rotation fixed at 60 Hz.

A significant observation across both scenarios (altering blower rotation and adjusting compressor rotation) was that the opening rate of the expansion valve was higher when setting the drying temperature to 25 ºC. This trend can be attributed to the lower condensation pressure since the flow of refrigerant fluid is inherently dependent on the pressure difference between the condensation and evaporation stages. A reduced pressure difference requires the expansion valve to open further in order to maintain balanced flow.

Salazar-Hincapié et al. [18] assessed a heat pump for dehydrating aromatic herbs. They noticed that a decrease in condensation pressure was accompanied by a drop in evaporation temperature. Moreover, they further observed that an increase in condensation pressure in one of their tests resulted in greater compression work, related to the gap between the pressures during condensation and evaporation.

The variance analysis of the output relative humidity values, based on both blower and compressor rotations, showed significant results for the two assessed temperatures (Table 1). The low coefficient of variation in the results indicates an elevated level of experimental control and consistency.

Following the same trend as the evaporation temperature, the relative humidity of the air leaving the psychrometric controller tended to increase with higher blower rotation (Figure 10A) and to decrease as the compressor rotation increased (Figure 10B). This is because relative humidity values are directly related to evaporation temperature values (Figures 11 and 12) due to the cooling process with dehumidification, which takes place in the evaporator. As a consequence, the greater the cooling below the dew point, the lower the relative humidity of the air in the reheating process (outlet). Once again, the influence of compressor rotation on the pressure differential across the expansion valve becomes evident, resulting in models with different behaviour for the drying temperatures of 25 ºC and 30 ºC (Figure 10B).

A. B.

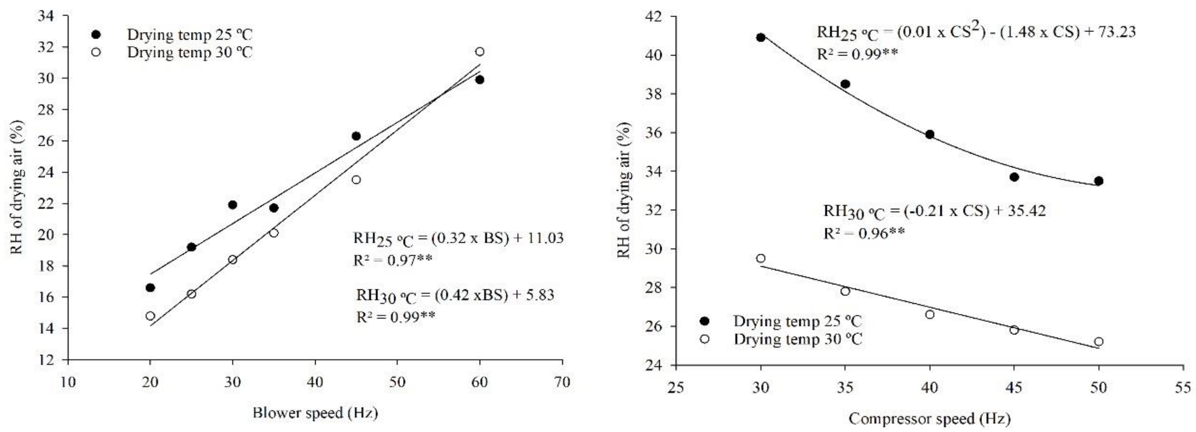

Figure 10: average output relative humidity as a function of varying blower rotation (A) at a fixed compressor rotation of 60 Hz, and (B) varying compressor rotation at a fixed blower rotation of 60 Hz.

Minimum observed values for relative humidity were 16.6% at a drying temperature of 25 ºC and 14.8% at 30 ºC. These values were observed at the lowest blower rotation while the compressor maintained a consistent rotation (Figure 10A). In a study by Aktas *et al*. [29], they achieved around 18% of relative humidity at a 36 ºC drying temperature using a recirculating heat pump dryer. Salehi [39] recorded 16% of relative humidity at 40 ºC-45 ºC during their fruit drying experiment with a heat pump. Meanwhile, Escalona *et al*. [40] recommended a minimum relative humidity of 12% for mild drying conditions at a drying temperature of 30 °C using a heat pump.

At 25 ºC, maximum values for relative humidity (40.9%) were obtained at the slowest compressor speed using a steady blower speed (Figure 10B). Meanwhile, at 30 ºC, the peak relative humidity (31.7%) was recorded at the highest blower speed with the compressor speed remaining unchanged (Figure 10A). Zlatanović *et al*. [41] reported 30% of relative humidity at 35 ºC while drying several items, including potatoes, apples, and bananas, with a heat pump. Similarly, Getahun *et al*. [42] reported approximately 35% of humidity at 50 ºC during their drying experiments with chilli peppers.

A. B.

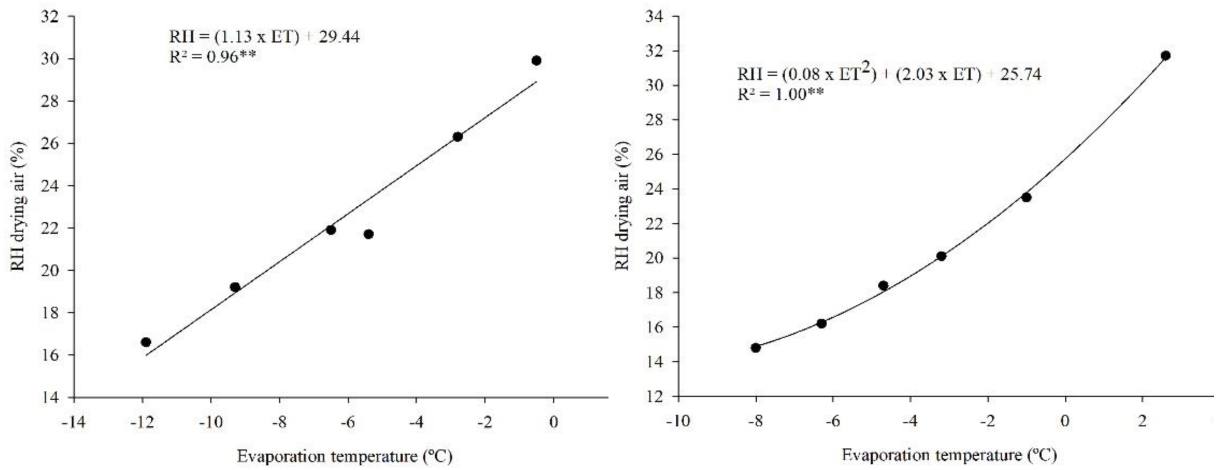

Figure 11: average relative humidity based on the evaporation temperature obtained during tests with a varying blower rotation and a fixed compressor rotation of 60 Hz: (A) drying at 25 ºC and (B) drying at 30 ºC.

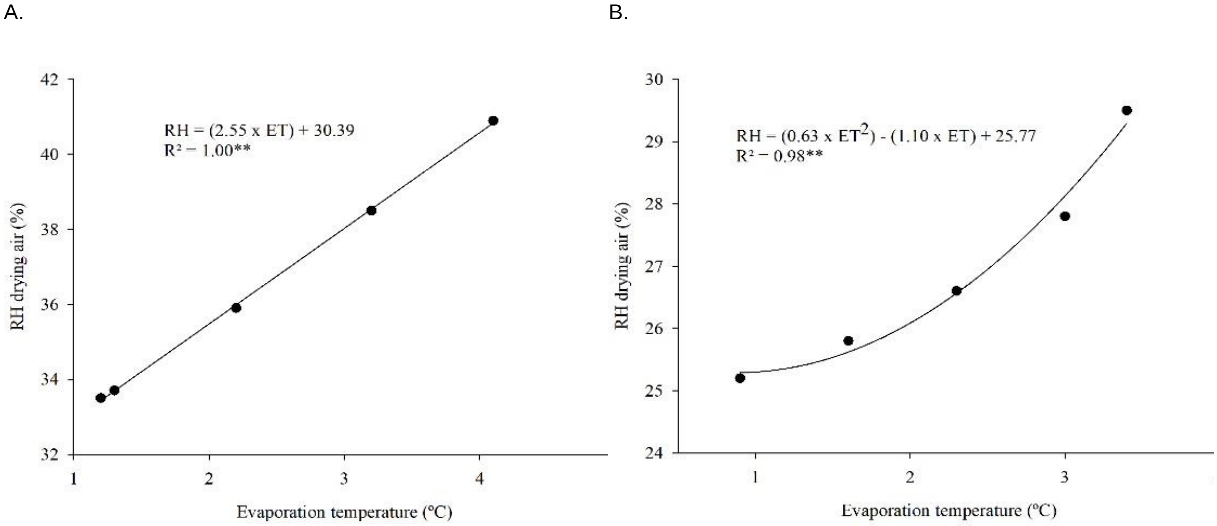

Figure 12: average relative humidity based on the evaporation temperature obtained during tests with a varying compressor rotation and a fixed blower rotation of 60 Hz: (A) drying at 25 ºC and (B) drying at 30 ºC.

The gap in relative humidity values between the two drying temperatures was more pronounced when adjusting the compressor rotation, despite only minimal variations in evaporation temperatures (Figure 7B). This suggests that the dehumidification effect associated with elevated evaporation temperatures (Figure 11) is less pronounced, implying that the primary factor in reducing relative humidity is the heating phase.

In contrast, when adjusting the blower rotation, the gap in relative humidity values between drying temperatures was narrower. Lower evaporation temperatures during the drying process of 25 ºC (Figure 10) amplified dehumidification, compensating for the decrease in relative humidity attributed to heating.

According to Zhang *et al*. [31], an increase in evaporation temperature led to a reduced drying rate, primarily due to diminished air dehumidification efficiency at higher evaporation temperatures. Mołczan & Cyklis [43] explored the effect of evaporation temperature on specific drying rates, discovering that a 10 ºC decrease in evaporation temperature enhanced water removal by more than four times, shifting from 0.44 kg kW h^{-1} to 1.90 kg kW h^{-1}.

Furthermore, Salazar-Hincapié *et al*. [18] detected challenges with ice formation in the evaporator at particularly low evaporation temperatures, which triggered heat transfer difficulties by altering the convective coefficients. Indeed, evaporator freezing is a significant issue; not only does the insulating nature of ice reduce thermal exchange, but it can also obstruct airflow.

In this study, ice buildup in the evaporator became apparent when the blower rotation dropped to 35 Hz. This accumulation hampered the heat transfer and widened the gap between the evaporator outlet and the evaporation temperature (Figure 13).

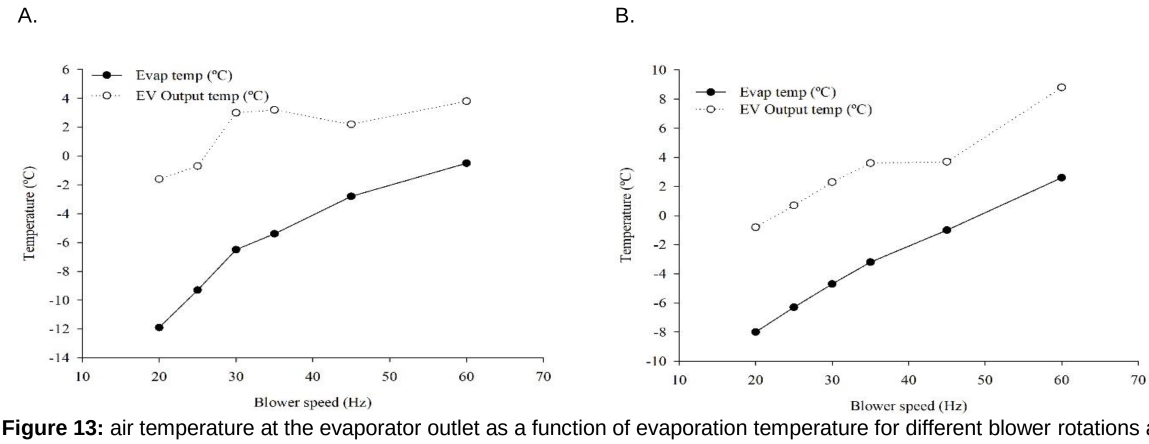

Figure 13: air temperature at the evaporator outlet as a function of evaporation temperature for different blower rotations and a fixed compressor rotation of 60 Hz: A) drying at 25 ºC and B) drying at 30 ºC.

Ice formation on the surface of the evaporator, which is more pronounced at 25 ºC (Figure 12), is a factor that may also have contributed to the differences in the slope of the adjusted lines for the linear functions, as well as to variations observed in the adjusted models (linear or quadratic).

For drying at 25 ºC (Figure 13A), assuming no ice formation and that the outlet air temperature follows the trend set by the evaporation temperature up to a blower rotation of 45 Hz, the predicted evaporator exit air temperature would be around -7 ºC with a rotation of 20 Hz. Nevertheless, due to the disruptive effect of ice on heat exchange, the actual exit temperature at this rotation was recorded as -1.7 ºC.

By modelling a scenario with an evaporator outlet air temperature of -7 ºC and then reheating it to 25 ºC, a simulation using the Grapsi v.8.1.1 software predicted an exit relative humidity of 11%. This value is considerably lower than the 16.6% observed under real conditions where ice formation occurred.

To enhance air cooling and mitigate issues related to evaporator freezing, one potential solution could be the implementation of a multi-stage cooling system. This approach could involve using a heat pump system equipped with multiple evaporators, as suggested by Du & Long [44]. By employing this strategy, the majority of the moisture in the air would be removed in the first stage, with the initial evaporator operating at a positive temperature. Subsequently, the temperature could be further reduced in the second stage with the secondary evaporator operating at sub-zero temperatures. This sequential process would not only improve the cooling efficiency but also significantly reduce the probability of ice formation.

Conclusions

1. Varying compressor and blower rotations, even with a constant drying temperature, resulted in a variation of almost 40% in relative humidity values of the outlet air.
2. Increasing the compressor rotation from 30 Hz to 50 Hz produced a reduction of nearly 20% in the relative humidity values, whereas increasing the blower speed from 20 Hz to 60 Hz led to an approximate 50% increase. Therefore, lower blower rotations and higher compressor rotations help to reduce relative humidity values and, consequently, increase the drying potential of the air.
3. Varying the blower rotation implied a greater variation in relative humidity values, due to an existing correlation between relative humidity and evaporation temperature — lower evaporation temperatures resulted in lower relative humidity values. Consequently, the reduction in air flow produced a decrease in evaporation temperature values.
4. Decreasing temperature and air flow rate, combined with an increasing compressor rotation (that is to say, a greater mass flow of refrigerant), produced more efficient heat exchange, ensuring that the air is cooled below the dew point. The greater the degree of cooling below the dew point, the more water is removed, resulting in lower absolute humidity and lower vapour pressure. As a result, after the reheating stage, the relative humidity of the air is reduced, thereby enhancing its drying potential at the same temperature.
5. On the other hand, reducing the blower rotation below 35 Hz caused the evaporation temperature to drop below 0 °C, leading to ice formation and accumulation in the evaporator. This consequence interfered with the downward behaviour of the relative humidity values of the drying air.

Acknowledgments

We express our deep gratitude to the *Programa de Pós-Graduação em Engenharia Agrícola* at the *Universidade Federal da Grande Dourados* (PGEA/UFGD). We extend our sincere gratitude to the Coordenação de Aperfeiçoamento de Pessoal de Nível Superior (CAPES—Finance Code: PDPG 155 and 16/2022) for their financial support. We would also like to thank the team at STTA for their valuable feedback and review of the definitive version of this article.

Reference

1. **Rawat, A., Kumar, D., & Khati, B. S**. (2024). *A review on climate change impacts, models, and its consequences on different sectors: A systematic approach*. Journal of Water and Climate Change, 15(1), 104-126. https://doi.org/10.2166/wcc.2023.536
2. **Guimarães, G.; Arcanjo, A.** *Os benefícios da energia solar em propriedades rurais*. 2019. SolarVolt Energia. [SolarVolt]. Disponível em:

https://www.solarvoltenergia.com.br/blog/energia-solar-em-propriedades-rurais/. Acesso em: 8 ago. 2023.
3. **Cortez, L. A. B., Lora, E. E. S., Gomez, E. O.**, 2008. *Biomassa para energia*. Campinas, SP: Editora UNICAMP.
4. **Lima, R. F., Dionello, R. G., Peralba, M. C. R., Barrionuevo, S., Radunz, L. L., Reichert Júnior, F. W.**, 2017. *PAHs in corn grains submitted to drying with firewood*. Food Chemistry. 215, 165–170.
5. **Resende, O.; Costa, E. R.; Quequeto, W. D.; Costa, L. M.; Oliveira, D. E. C.; Tfouni, S. A. V.; Gomes, F. M. L.; Quirino, J. R.; Lima, R. R.** *Quality of corn grains subjected to drying using direct-fired furnace fed with eucalyptus chips and firewood*. Food Sci. Technol, Campinas, v42, e55820, 2022. https://doi.org/10.1590/fst.55820.
6. **Bilandzija, N.; Voca, N.; Jelcic, B.; Jurisic, V.; Grubor, M.; Kricka, T.** 2018. *Evaluation of Croatian agricultural solid biomass energy potential*. Renewable and Sustainable Energy Reviews 93, 225–230.
7. **Seiffert, M. E. B.** *Mercado de Carbono e Protocolo de Quioto: Oportunidades de negócio na busca da sustentabilidade.* 2. ed. São Paulo: Atlas, 2013.
8. **Lourenzani, W. L.; Caldas, M. M.** *Mudanças no uso da terra decorrentes da expansão da cultura da cana-de-açúcar na região oeste do estado de São Paulo*. Ciência Rural, Santa Maria, v.44, n.11, p.1980-987, nov, 2014. https://doi.org/10.1590/0103-8478cr20140186 .
9. **Zaperllon, L. E.; Morejon, C. F. M.** *Estudo prospectivo dos incêndios e explosões em unidades industriais de beneficiamento e armazenamento de grãos no estado do Paraná*. Revista Científica do Corpo de Bombeiros Militar de Pernambuco. Vol.04 Nº11 - Edição Especial XVIII SENABOM, novembro de 2018. http://dx.doi.org/10.17648/2359-4837/flammae.v4n11.p155-169.
10. **Ferreira, R. A.; Martinazzo, A. P.** *Levantamento de acidentes de trabalho em unidades armazenadoras brasileiras no período de 2011/2021*. Revista Thêma et Scientia – Vol. 13, no 1, jan/jun 2023.
11. **Mabasso, G. A.; Siqueira, V. C.; Resende, O.; Quequeto, W. D.; Goneli, A. L. D.; Martins, E. A. S.; Takagi, A. D. A.** *Mechanical properties and integrity of stored corn grains after continuous and intermittent drying*. Food Sci. Technol, Campinas, 43, e21323, 2023. Food Sci. Technol, Campinas, 43, e21323, 2023. https://doi.org/10.5327/fst.21323.
12. **Schiavon, R. A.; Castro, L. K.; Borges, G. B.; Nogueira, I. S.; Silva, R. V.** *Efeito da temperatura de secagem sobre a qualidade dos grãos de soja*. Anais da VII Conferência Brasileira de Pós-colheita e X Simpósio Paranaense de Pós-colheita de grãos. 16 a 18 de outubro de 2018. Londina-PR. Disponível em: https://eventos.abrapos.org.br/anais/paperfile/910_20181103_02-43-42_832.pdf. Acesso em: 12 jul 2024.
13. **Jordan, R. A., Siqueira, V. C., Quequeto, W. D., Cavalcanti-Mata, M. E. R. M., Hoscher, R. H., Mabasso, G. A., Battilani, M., Oliveira, F. C. de, Martins, E. A. S. & Freitas, R. L.** (2020). *Consumo específico de energia na secagem de café com sistema de aquecimento resistivo e bomba de calor*. Research, Society and Development, 9(9), e303997297-e303997297. doi: 10.33448/rsd-v9i9.7297
14. **Alves, G. E., Borém, F. M., Isquierdo, E. P., Siqueira, V. C., Cirillo, M. A., Pinto, A. C. F.** (2017). *Physiological and sensorial quality of Arabica coffee subjected to different temperatures and drying airflows*. Acta Scientiarum. Agronomy, 39(2), 225-233.
15. **Borém, F. M.; Isquierdo, E. P.; Alves, G. E.; Ribeiro, D. E.; Siqueira, V. C.; Taveira, J. H. Da. S.** *Quality of natural coffee dried under different temperatures and drying rates*. Coffee Science, v.13, n.2, p.159-167, 2018. http://dx.doi.org/10.25186/cs.v13i2.1410
16. **EPE [Empresa de Pesquisa Energética]**. *Balanço Energético Nacional (BEN) 2024/Relatório síntese: Ano base 2023*. Disponível em https://www.epe.gov.br/sites-pt/publicacoes-dados-abertos/publicacoes/PublicacoesArquivos/publicacao-819/topico-715/BEN_S%C3%ADntese_2024.pdf. Acesso em: jun/2024.
17. **BRASIL**. *LEI No 14.300, DE 6 DE JANEIRO DE 2022 - DOU - Imprensa Nacional*. 6 jan. 2022. Portal da Imprensa Nacional do Brasil. Diário Oficial da União. Disponível em: https://in.gov.br/en/web/dou/-

/lei-n-14.300-de-6-de-janeiro-de-2022-372467821. Acesso em: 28 ago. 2023. (Brasília, DF).

18. Salazar-Hincapié, A.; Delgado-Mejía, A; Romero-Maya, A. F.; Duque-Grisales, E. *Experimental assessment of the thermal performance of a heat pump dryer system based on the variations in compressor discharge pressure on oregano drying*. Energies, v.13, p.6333, 2020. https://doi.org/10.3390/en13236333

19. Budžaki, S.; Leko, J.; Jovanović, K.; Viszmeg, J.; Koški, I. *Air Source Heat Pump Assisted Drying for Food Applications*. Croatian Journal of Food Science and Technology, v.11, p.122-130, 2019. https://doi.org/10.17508/CJFST.2019.11.1.18

20. Loemba, A. B. T.; Kichonge, B.; Kivevele, T. *Comprehensive assessment of heat pump dryers for drying agricultural products*. Energy Science & Engineering, v.11, n.8, p.2985-3014, 2023. https://doi.org/10.1002/ese3.1326

21. Montoya-Ballesteros, L. C.; González-León, A.; Martínez-Núnez, Y. J.; Robles-Burgueno, M. R.; García-Alvarado, M. A.; Rodríguez-Jimenes, G. C. *Impact of open sun drying and hot air drying on capsaicin, capsanthin, and ascorbic acid content in chiltepin (Capsicum annuum L. var. glabriusculum)*. Revista Mexicana de Ingeniera Quimica, v.16, p.813-825, 2017.

22. Verruck, S.; Prudencio, E. S.; da Silveira, S. M. *Compostos bioativos com capacidade antioxidante e antimicrobiana em frutas.* Revista CSBEA, v.4, n.1, p.111-124, 2018. https://doi.org/10.5965/24473650412018111

23. Gasecka M.; Siwulski M.; Magdziak Z.; Budzynska S.; Stuper-Szablewska K.; Niedzielski P.; Mleczek, M. *The effect of drying temperature on bioactive compounds and antioxidant activity of Leccinum scabrum (Bull.) Gray and Hericium erinaceus (Bull.) Pers*. Journal of Food Science and Technology, v.57, n.2, p.513-525, 2020. https://doi.org/10.1007/s13197-019-04081-1

24. Ashok, K. M.; Rajakarunakaran, S.; Kumaresan, G. *Performance Evaluation of Heat Pump Dryer in Specific Moisture Evaporation Rate for Various Herbal Leaves*. International Journal of Engineering Research & Technology (IJERT), v.10, n.7, p.616-620, 2021.

25. Gou, M.; Bi, J.; Chen, Q.; Wu, X.; Fauconnier, M-L.; Qiao, Y. *Advances and Perspectives in Fruits and Vegetables Flavor Based on Molecular Sensory Science*. Food Reviews International, v.39, p.3066-3079, 2021 https://doi.org/10.1080/87559129.2021.2005088

26. Xu, L.; Zang, E.; Sun, S.; Li, M. *Main flavor compounds and molecular regulation mechanisms in fruits and vegetables*. Critical Reviews in Food Science and Nutrition, p.1-2, 2022. https://doi.org/10.1080/10408398.2022.2097195

27. Tajudin, N. H. A.; Ang, W. L.; Tasirin, S. M.; Rosli, M. I. *Process variables optimization for heat pump drying of roselle calyx by using response surface methodology*. Jurnal Kejuruteraan, v.33, n.4, p.903-914, 2021. https://doi.org/10.17576/jkukm-2021-33(4)-13

28. ElGamal, R.; Song, C.; Rayan, A. M.; Liu, C.; Al-Rejaie, S.; ElMasry, G. *Thermal Degradation of Bioactive Compounds during Drying Process of Horticultural and Agronomic Products: A Comprehensive Overview*. Agronomy, v.13, n.6, p.1580. https://doi.org/10.3390/agronomy13061580

29. Aktaş, M.; Taşeri, L.; Şevik, S.; Gülcü, M.; Uysal Seçkin, G.; Dolgun, E. C. *Heat pump drying of grape pomace: Performance and product quality analysis*. Drying Technology, v.37, n.14, p.1766-1779, 2019. https://doi.org/10.1080/07373937.2018.1536983

30. Uthpala, T. G. G.; Navaratne, S. B.; Thibbotuwawa, A. *Review on low-temperature heat pump drying applications in food industry: Cooling with dehumidification drying method*. Jouranl of Food Process Engineering, v.43, p.e13502, 2020. https://doi.org/10.1111/jfpe.13502

31. Zhang, T.; Yan, Z. W.; Wang, L.Y.; Zheng, W.J.; Wu, Q.; Meng, Q. L. *Theoretical analysis and experimental study on a low-temperature heat pump sludge drying system*. Energy, v.214, p.118985, 2021. https://doi.org/10.1016/j.energy.2020.118985

32. Liu, Y., Zhao, K., Jiu, M., & Zhang, Y. (2017). *Design and drying technology research of heat pump Lentinula edodes* *drying room*. Procedia Engineering, 205(1), 983-988.

33. Jordan, R. A.; Siqueira, V. C.; Cavalcanti-Mata, M. E. R. M.; Hoscher, R. H.; Mabasso, G. A.; Quequeto, W. D.; Battilani, M.; Freitas, R. L.; Oliveira, F. C.; Martins, E. A. S. *Qualidade sensorial do café submetido a secagem a baixa temperatura e a frio com emprego de um sistema baseado em tecnologia de bomba de calor*. Research, Society and Development, v.9, n.11, p.e59791110302, 2020. https://doi.org/10.33448/rsd-v9i11.10302

34. R Core Team. *R: A language and environment for statistical computing. Vienna: R Foundation for Statistical Computing*, 2017. Available on: <https://www.r-project.org/>. Accessed on: Set. 2023.

35. Silva, N. C. D.; Santos, R. C.; Zucca, R.; Geisenhoff, L. O.; Cesca, R. S.; Lovatto, J. *Enthalpy thematic map interpolated with spline method for management of broiler chicken production*. Revista Brasileira de Engenharia Agrícola e Ambiental, v.24, p.431-436. https://doi.org/10.1590/1807-1929/agriambi.v24n7p431-436

36. Singh, A.; Sharma, J.; Paichha, M.; Chakrabarti, R., 2020. *Achyranthes aspera (prickly chaff flower) leaves- and seeds-supplemented diets regulate growth, innate immunity, and oxidative stress in Aeromonas hydrophila-challenged Labeo rohita*. J. Appl. Aquacult., 32 (3): 250-267

37. Wang, C.; Gao, Y.; Dai, Z.; Wu, D.; Huang, Z.; Zhang, X.; Jiang, L. *Experimental investigation and performance evaluation on a direct expansion solar-air source heat pump system*. International Journal of Refrigeration, v.145, p.168-176, 2023. https://doi.org/10.1016/j.ijrefrig.2022.08.030

38. Patel, A. *Enhancing Heat Transfer Efficiency in Solar Thermal Systems Using Advanced Heat Exchangers*. Multidisciplinary International Journal of Research and Development (MIJRD), v.2. n.06, p.31-51, 2023. https://www.mijrd.com/papers/v2/i6/MIJRDV2I60003.pdf

39. Salehi, F. *Recent applications of heat pump dryer for drying of fruit crops: A review*. International Journal of Fruit Science, v.21, n.1, p.546-555, 2021. https://doi.org/10.1080/15538362.2021.1911746

40. Escalona, A.; Cuevas, C.; Salazar, L.; Hernandez, V. *Modelling of heat pump drying system powered by a hybrid PV-wind-battery plant for slow-drying hardwoods*. Energy for Sustainable Development, v.76, p.101282, 2023. https://doi.org/10.1016/j.esd.2023.101282

41. Zlatanović, I.; Komatina, M.; Antonijević, D. *Experimental investigation of the efficiency of heat pump drying system with full air recirculation*, Journal of Food Process Engineering, v.40, n.2, 2017. https://doi.org/10.1111/jfpe.12386

42. Getahun, E.; Delele, M. A.; Gabbiye, N.; Fanta, S. W.; Vanierschot, M. *Studying the drying characteristics and quality attributes of chili pepper at different maturity stages: experimental and mechanistic model*. Case Studies in Thermal Engineering, v.26, p.101052, 2021. https://doi.org/10.1016/j.csite.2021.101052

43. Mołczan, T.; Cyklis, P. *Impact of the evaporation temperature on the air-drying rate for a finned heat exchanger*. Energies, v.16, n.5, p.2132, 2023. https://doi.org/10.3390/en16052132

44. Du, A.; Long, J. *Heating performance of a novel two-stage evaporator air-source heat-pump for drying applications*. Dry Technol, v.40, p.1356-1368, 2022. https://doi.org/10.1080/07373937.2020.1869036

RECyT
Year 27 / Nº 43 / 2025 /
DOI: https://doi.org/10.36995/j.recyt.2025.43.005

Influence of density models on the numerical modeling of natural convection near the water density-inversion point during transient conjugate heat transfer

Influencia del modelo de densidad en el modelado numérico de convección natural cercano al punto de inversión de densidad del agua durante la transferencia de calor conjugado transitoria

Carlos A., Schvezov[1, *]; Alejandro R., Lespinard[2]; Mario R., Rosenberger[1]

1- Instituto de Materiales de Misiones (IMAM), CONICET. Facultad de Ciencias Exactas, Químicas y Naturales. Universidad Nacional de Misiones (UNaM). Felix de Azara 1552 (3300), Posadas, Misiones, Argentina.
2- Instituto Multidisciplinario de Investigación y Transferencia Agroalimentaria y Biotecnología (IMITAB), CONICET. Instituto de Ciencias Básicas y Aplicadas. Universidad Nacional de Villa María. Av. Arturo Jauretche 1555, (5900), Villa María, Córdoba, Argentina.
* E-mail: cschvezov@fceqyn.unam.edu.ar

Received: 02/12/2024; Accepted: 28/04/2025

Abstract
Pasteurization of dairy products using the low temperature, long time (LTLT) method is a simple and cost-effective heat treatment that requires minimal investment, making it suitable for small-scale milk production. However, the cooling stage of pasteurization is often overlooked and rarely considered in process design. This study aims to evaluate heat transfer during the cooling phase of a batch pasteurization process, modeled as two concentric, vertically enclosed cylinders filled with water. For the experiment, the outer enclosure was maintained between 2 ºC and 4 ºC —close to the water density inversion temperature (3.98 ºC)—while the inner enclosure ranged from 63 ºC to 4 ºC. The process was simulated using conjugate heat transfer solvers within the OpenFOAM Finite Volume Method framework. Various water density models were analyzed, compared, and validated against experimental data. Models lacking a density inversion point to accurately simulate this process underestimated the time required for the inner enclosure to reach the final temperature (4 ºC).

Keywords: Conjugate heat transfer; Density-inversion; Finite volume method; Natural convection; Computational fluid dynamics.

Resumen
La pasteurización de productos lácteos mediante el método de baja temperatura y tiempo prolongado es un tratamiento térmico simple y eficaz que requiere de baja inversión, siendo atractivo para la producción de leche a baja escala. Sin embargo, en su diseño del proceso el período de enfriamiento de la pasteurización a menudo no es considerado. El objetivo de este trabajo fue evaluar la transferencia de calor entre dos cilindros cerrados verticales concéntricos llenos de agua durante el proceso de enfriamiento de un tratamiento térmico discontinuo. Para este proceso, la temperatura del recinto exterior osciló entre 2 ºC y 4 ºC, cerca de la temperatura de inversión de la densidad del agua (3,98 ºC), mientras que la temperatura del recinto interno osciló entre 63 y 4 C. Esto se simuló utilizando el método de volumen finito del sofware OpenFOAM mediante algoritmos para transferencia de calor conjugados. Se analizaron, compararon y validaron el uso diferentes modelos de densidad del agua para la simulación con datos experimentales. Los modelos de densidad que no tenían punto de inversión no pudieron modelar este proceso con precisión y subestimaron el tiempo que requiere el recinto interior para alcanzar la temperatura final (4 ºC).

Palabras claves: Transferencia de calor conjugado; Inversión de densidad; Método de volumen finito; Convección natural; Fluidodinámica computacional.

1. Introduction

Long-time low-temperature (LTLT) milk pasteurization is a traditional, simple and effective heat treatment used to reduce mesophilic bacteria populations and eliminate pathogenic microorganisms, thereby enhancing the shelf-life and ensuring consumer safety [1]. The method involves rapidly heating the dairy product to 63 °C, maintaining this temperature for 30 minutes, and subsequently cooling the product quickly. However, in settings involving small-scale regional production, limited technical expertise, or restricted access to modern equipment and utilities, a slight modification of the conventional LTLT method can simplify the process. One of the most practical and hygienic adaptations is to pasteurize pre-packaged dairy products, thus minimizing the risk of post pasteurization contamination during or after packaging [2]. An alternative method is pot pasteurization; however, Dumaslisle, P. et al. (2005) [3] reported that *Escherichia coli* and other bacteria may survive this form of heat treatment. Beyond milk, the LTLT method has also been applied successfully to other food products, including raspberry pulp [4] and crushed tomato [5].

There is limited information available on the cooling stage of LTLT pasteurization for dairy products, as most research has primarily focused on the heating process [5]. According to regional regulations such as the Argentine Food Code [6], the cooling process should be as brief as possible to prevent nutrient degradation, and the final temperature of the dairy product must be at or below 5 ºC (278.15 K). The cooling period is crucial for the product quality, as prolonged cooling can lead to increased nutrient loss and subsequent decline in product quality. Additionally, because microbial inactivation continues during cooling, the thermal profile and its evolution should be considered in the calculation of total pasteurization lethality and F-value. Despite this, the current lethality calculations typically account only for the come-up and holding phases of batch thermal processing. However, in some cases, the cooling phase significantly contributes to the total lethality and should be included in process design considerations to avoid unnecessary overprocessing and degradation of food quality. [5].

The simplest cooling method initially proposed involves immersing the dairy sachet in a water-ice bath under free convection conditions [2]. However, this approach overlooks a key thermodynamic characteristic of water: its density-inversion point near 3.98 ºC. At this temperature, water reaches its maximum density and its volumetric expansion coefficient approaches zero, effectively reversing the direction of the buoyancy force. This inversion significantly hinders heat transfer by free convection when the fluid temperature approaches this point. Specifically, below 3.98 °C, a decrease in temperature leads to a decrease in density, causing the buoyant force to act upward. Conversely, above 3.98 °C, a temperature decrease results in an increase in density, producing a downward buoyant force. At exactly 3.98 °C, the buoyant force is approximately null due to the maximum density of the water. This unique behavior is often neglected in standard buoyancy models used to simulate free convection, despite the fact that buoyancy—driven by local temperature differences— is the primary force driving fluid motion in these scenarios. Therefore, it is essential that density models used in numerical simulations accurately capture the behavior of buoyant forces within the relevant temperature range.

Heat transfer and fluid dynamics in natural convection involving water near its density-inversion point have been extensively studied, particularly in the context of enclosed square cavity. Quintino et al. (2017) [7] reviewed research spanning from 1964 to 2015, highlighting both experimental and numerical studies. These studies commonly involve square cavities oriented at various angles, with opposing hot and cold vertical walls. However, relatively few investigations have examined configurations where the cold surface at the bottom —cases which are particularly relevant for understanding the effects of penetrative convection [8-9]. Most studies adopt simplified water density models, such as the second-degree polynomial proposed by Debbler [10], the potential model by Gebhart & Mollendorf [11], or a fitted fourth-degree polynomial. These models typically span different temperature ranges of 0 – 8 ºC, 0 – 20 ºC and 0 – 40 ºC, respectively.

Other heat transfer studies on natural convection near the anomalous density point of water have investigated a variety of geometrical configurations. These include convection around a horizontal cylinder enclosed in a rectangular cavity [12], within elliptical enclosures [13-14], in eccentric horizontal cylindrical annuli [15], in general annular enclosures [16], in concentric vertical cylinders of different heights [17], and in both concentric and eccentric cylindrical configurations [18-19]. These studies primarily focus on buoyancy-driven flow patterns influenced by the water density-inversion phenomenon, or are applied to processes involving water fusion [20-21].

Additionally, several authors have investigated buoyant heat transfer in enclosed containers containing bluff or internal bodies of various shapes and positions, without strict temperature limitations. A comprehensive review of studies involving enclosed square cavities was presented by Pandey et al. (2019) [22]. Laminar natural convection from heated bodies of different geometries in cubic or spherical enclosures has been examined both numerically and experimentally by Teertstra et al. (2004) [23], Kumar and Mahapatra, 2023 [24] explored natural convection inside a partially open enclosure with a cylindrical obstacle. Heat convection inside a cubic cavity with various heat sources has been studied numerically by Gibanov & Sheremet (2018) [25] and experimentally by Zhan et al. (2019) [26], with a focus on electronic heat dissipation. Furthermore, Priam et al, 2021 [27] provided an example of conjugate natural convection between two fluids.

In standard texts on process engineering and heat transfer, the phenomenon of anomalous density inversion in water is rarely discussed in detail. These references typically apply the Boussinesq approximation [28-30] to model free convection, assuming small density variations and treating them as a linear function of temperature. This is done using a reference temperature and the corresponding volumetric thermal expansion coefficient. However, in the cooling of dairy products where the initial and final product temperatures are 63º C and 5º C, respectively, and the cooling bath temperatures ranges from 0º C and 10º C, this simplification becomes inadequate. Near 3.98º C—where water reaches its maximum density—the volumetric expansion coefficient approaches zero. As a result, the linear approximation fails to accurately capture the non-monotonic behavior of water density, and thus does not adequately represent the heat transfer and fluid dynamics of the system under study.

Based on the considerations above, the aim of this work was to compare buoyancy-driven heat transfer models under free convection during batch LTLT pasteurization using the Finite Volume Method (FVM) and the OpenFOAM v10 multiregion solver. Specifically, the study examined how the choice of density model affects fluid dynamics and heat transfer predictions, particularly in scenarios where the temperature range includes the water density-inversion point. In such cases, inaccurate modeling may lead to erroneous estimations of cooling time or even incorrect conclusions about whether the final target temperature is attainable within design constraints. This, in turn, has implications for the development of accurate industrial control systems. To address this, several density models were evaluated: polynomial functions of temperature (fifth-, third-, second-, and linear-orders) and Boussinesq approximations calculated at different representative temperatures (process average, bath average, and with negative thermal expansion). All other thermophysical properties were modeled as temperature-dependent. The numerical results were validated and compared against experimental data to assess the accuracy of each approach.

2. Materials and Methods

For the analysis conducted in this study, the cooling process was simulated using a single dairy sachet submerged in a water and ice bath contained within a cylindrical enclosure. The sachet was positioned at the axial center of the system. Dynamic simulations were performed using the Finite Volume Method implemented in OpenFOAM v10. The FVM is a numerical technique for solving systems of partial differential equations, enabling the computation of time dependent temperature and velocity vector fields throughout the analyzed volume. This approach contrasts with classical design methods, which typically solve simplified systems of ordinary differential equations (ODEs) and assume spatially homogeneous temperatures. For the purpose of this study, the dairy product was modeled using the thermophysical properties of water. The simulations were evaluated at 30, 60, 120, 360, 600, 900, 1200, 1800, 3000, 3600, and 4000 seconds.

The model was solved using OpenFOAM's multiregion heat transfer solver, *chtMultiRegionFoam*, employing a mixed Euler and Crank-Nicolson time integration scheme with linear interpolation for cell values [31]. The dynamic system was resolved using the PISO (Pressure Implicit with Splitting of Operator) algorithm [32]. Simulations incorporated either fitted density models—expressed as polynomial functions of temperature—or the Boussinesq approximation. The fitted density models were selected and compared based on data from chemical engineering literature.

To determine an appropriate mesh resolution for the FVM simulations, a mesh sensitivity analysis was conducted using a simplified benchmark system: a square cavity with isothermal lateral walls, with the left wall maintained at 283 K and the right wall at 273 K. The resulting velocity and temperature were compared with published data by

Michalek et al. (2005) [33] and Phu & Nguyen (2020) [34] (See appendix A).

2.1. Governing equations

The governing equations used to model natural convection heat transfer between two enclosed fluids were the continuity equation (Eq. 1), the momentum conservation equation (Eq. 2) and the energy conservation equation (Eq. 3). These equations are presented in the form implemented by the OpenFOAM solver. The fluid was assumed to be incompressible, Newtonian, and the flow was considered laminar.

$$\frac{\partial \rho}{\partial t} + \nabla \cdot (\rho u) = 0 \quad (1)$$

$$\frac{\partial (\rho u)}{\partial t} + \nabla \cdot (\rho u u) = -\nabla p + \nabla \cdot (\mu \nabla u) + \nabla \cdot [\mu (\nabla u)^T] - \frac{2}{3}\mu \nabla (\nabla \cdot u) + \rho g \quad (2)$$

$$\frac{\partial (\rho h)}{\partial t} + \nabla \cdot (\rho u h) + \frac{\partial (\rho K)}{\partial t} + \nabla \cdot (\rho u K) - \frac{\partial p}{\partial t} = \nabla \cdot (\frac{\kappa}{Cp} \nabla h) + \rho u \cdot g \quad (3)$$

where ρ is the fluid density; u is the velocity; t is time; p is the pressure; h is the specific enthalpy, calculated as the integral of the specific heat with respect to fluid temperature; K is the kinetic energy, calculated as half the square of the modulus of u; κ is the thermal conductivity and Cp is the specific heat at a constant temperature.

For this analysis, two models for density were proposed. The first represents density as a polynomial function of temperature (detailed in the next section). The second applies the Boussinesq approximation, defined as:

$$\rho = \rho_0 (1 - \beta (T - T_0)) \quad (4)$$

where β is the thermal expansion coefficient, T_0 is a reference temperature and ρ_0 is the density at the reference temperature.

The temperature dependence of specific heat, dynamic viscosity, and thermal conductivity for water was defined using polynomial equations of third (Eq. 5), fourth (Eq. 6) and second (Eq. 7) degree respectively. The specific heat equation was derived from data in *Fundamentals of Thermal-Fluid Sciences* by Çengel [30]. The viscosity equation was fitted using values derived from *Yaws' Chemical Properties Handbook* [35], within the range 273-500 K. This fitting approach was used to avoid the instabilities that arise when using high-degree polynomials outside their valid temperature range in simulations involving heating processes.

$$Cp = 1112.6 - 60.801T + 0.17589T^2 - 1.9800x10^{-4}T^3 \quad (5)$$

$$\mu = 0.101358 - 9.72703x10^{-4}T + 3.50981x10^{-6}T^2 - 5.62246x10^{-9}T^3 + 3.36814x10^{-12}T^4 \quad (6)$$

$$\kappa = -0.2758 + 4.6120x10^{-3}T - 5.5391x10^{-6}T^2 \quad (7)$$

2.2. Water density models

The values of water density as a function of temperature were taken from Kohlrausch (1986) [36]. In the temperature range from 0 ºC (273.15 K) to 63 ºC (336.15 K), the water density was fitted using a fifth-degree polynomial (P5), which served as the most accurate model to represent density (P5) (Eq. 8). Other models used for comparison were a cubic (P3) (Eq. 9), a quadratic (P2) (Eq.10) and a linear (P1) degree (Eq. 11) polynomial function. These were fitted over the same range as the fifth-degree function, except for the linear model, which was fitted between 0 and 20 ºC, to obtain a more balanced approximation.

$$\rho = -6609.06 + 110.511T - 0.645635T^2 + 0.00190264T^3 - 2.83014x10^{-6}T^4 + 1.69231x10^{-9}T^5 \quad (8)$$

$$\rho = 86.0224 + 8.19908T - 0.0234154T^2 + 2.06746x10^{-5}T^3 \quad (9)$$

$$\rho = 708.399 + 2.17349T - 0.00404582T^2 \quad (10)$$

$$\rho = 1098.57 - 0.347789T \quad (11)$$

Another model applied to buoyant heat transfer used was the Boussinesq approximation, as described in Eq. 4. For this approximation, three alternatives were evaluated: one at the process average temperature of 31 ºC (304.15 K) (B304), a second one at the bath average temperature of 4 ºC (277.15 K) (B277), close to the point of maximum water density, and a third at 1 ºC (274.15 K) (B274), where volumetric expansion becomes negative. The corresponding values of volumetric expansion used were 3.03 x 10^{-4}, 0.003 x 10^{-4} and -0.5 x 10^{-4} K^{-1}, and the reference densities were 994.03, 999.97 and 999.85 kg m^{-3}, respectively.

2.3. Pasteurizer

The cooling phase of pasteurization was simulated in an insulated cylindrical container filled with an ice-water bath. The container had a height of 0.15 m and a radius of 0.125

m. A single hot dairy sachet, modeled as a right circular cylinder, was placed at the center of the container, maintaining a 9-mm clearance from the bottom surface to allow fluid circulation underneath. The dairy sachet contained 500 cm^3 of fluid and was modeled as a cylinder with a height of 0.115 m and a radius of 0.0374 m. For the purpose of this study, the fluid within the sachet was assumed to exhibit the thermophysical properties of water.
The dynamic simulation was carried out using the FVM implemented in the OpenFOAM v10 software package [31].

2.3.1. Geometry and mesh

The simulation domain consisted of two concentric cylinders: the outer cylinder, representing the ice-water bath, measured 0.15 m in height and 0.125 m in radius, while the inner cylinder, representing the dairy sachet, measured 0.115 m in height and 0.0374 m in radius. The inner cylinder was positioned concentrically and elevated 9 mm above the bottom surface of the outer container.
The computational domain was divided into two thermally interacting regions: the dairy sachet and the surrounding water bath. These regions exchanged heat, but not mass. The bath region was assumed to be entirely liquid water. Since ice naturally floats on water, the influence of the ice was represented via an upper Robin boundary condition.

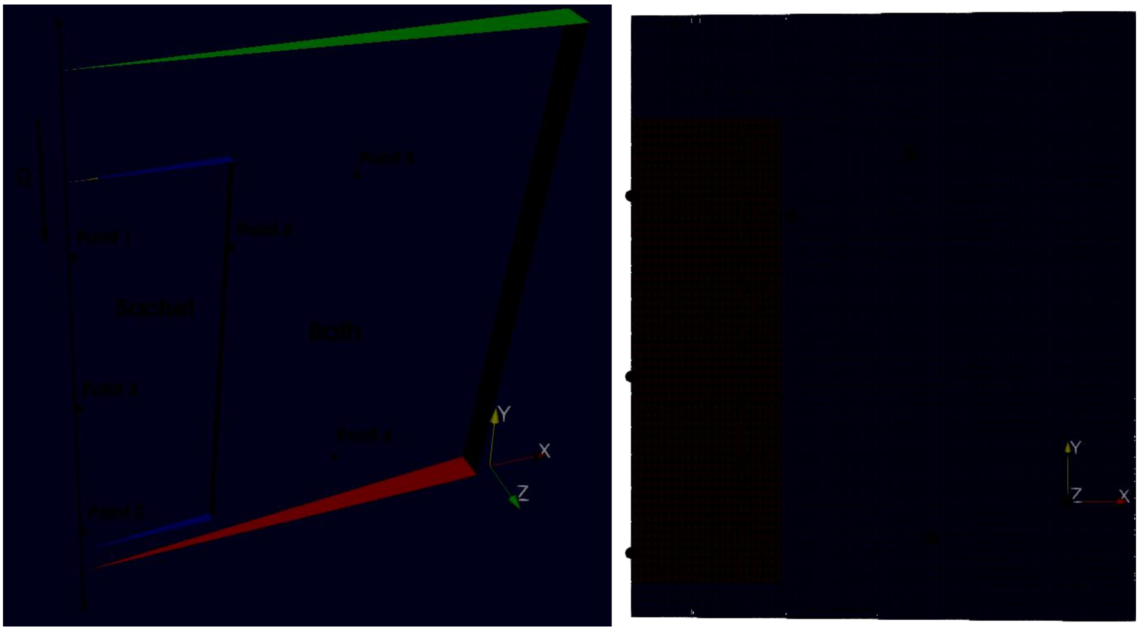

Fig. 1. Boundary conditions and measurement points (left), and structured mesh of the computational domain (right). Bath region (blue) and sachet region (red), and temperature measurement locations (black points).

An axial symmetry was applied; simplifying the problem to a two-dimensional mesh, using the OpenFOAM *wedge* patch. The computational domain was discretized into 6860 structured square cells, of which 5618 belonged to the bath region (Fig. 1b, yellow) and 1242 to the sachet region (Fig. 1b, red). To achieve this configuration, 70 vertical cells and 98 radial cells were defined, with a radial expansion of 0.5, producing a progressively finer mesh near the sachet (see Fig. 1b). This mesh design was informed by the cavity model analysis, using an equivalent average cell size to ensure consistent resolution.
Time steps were variable, adjusted to maintain a Courant Number [31] of up to 0.5 during the first 40 seconds of simulation and up to 1.0 thereafter. A mixed Crank-Nicolson and Euler time integration scheme [31] was applied, with weighting coefficient of 0.9.

2.3.2. Boundary conditions

Ice was modeled as an upper Robin boundary condition, with a fixed normal temperature gradient of 120 K m^{-1}, representing the removal of heat due to the enthalpy of melting, and a fixed temperature value of 273.15 K. In this simulation, ice was not modeled as a separate region, and the resulting meltwater was not considered.
A total pressure of 100 kPa was imposed throughout the domain, with the static pressure calculated as:

$$p = p_0 - 0.5|u|^2 \qquad (12)$$

where p_0 is the total pressure and u is the velocity vector. The bottom and external walls of the bath were considered to be adiabatic (insulated). All walls were assigned a no-slip condition, except for the upper Robin boundary, where a slip condition was applied. At the interface between the sachet and the bath, a baffle condition was used with no added thermal resistance, along with a no-slip condition. Heat transfer across the interface was modeled using OpenFOAM's *turbulentTemperatureCoupledBaffleMixed* boundary condition. In this condition, face temperature is evaluated as:

$$T_{\text{face}} = T_1 * \left(\frac{\kappa_1 \Delta_1}{\kappa_1 \Delta_1 + \kappa_2 \Delta_2}\right) + T_2 \left(\frac{\kappa_2 \Delta_2}{\kappa_1 \Delta_1 + \kappa_2 \Delta_2}\right) \quad (13)$$

where the subscripts 1 and 2 refer to the cells of each region, κ is the thermal conductivity, and Δ is the distance from the cell center to the interface. This expression is derived under the assumption of temperature continuity and equal heat flux across the interface.

Due to numerical instabilities caused by heat transfer between two enclosed fluid regions—especially near the beginning of the simulation when the velocity-pressure coupling diverges—four pressure-relief faces were defined at the top center of the sachet interface. These faces had a total radius of 7 mm and were assigned a fixed total pressure of 100 kPa using Equation 12 (see Fig. 1; yellow surface).

The initial conditions were set to 336 K (63 ºC) for the sachet and 275 K (2 ºC) for the bath.

2.3.3. Experimental validation

An experimental setup was developed to obtain temperature profiles for validating the simulation results. Six type-K thermocouples were used: three were inserted along the central vertical axis of the dairy sachet at different heights, and the remaining three were positioned to monitor the temperature of the bath.

A 500-cm³ sachet of raw milk, with a height of 0.115 m, was preheated to 336 K and then submerged within a 6.8-cm³ ice-water bath, with a radius of 0.125 m and an average initial temperature of 2 ºC. Ice was added to maintain thermal conditions, and measurements were recorded until complete melting of the ice. These experimental data were subsequently compared with the simulation results for validation purposes.

3. Results and Discussion

3.1. Comparison of the density models

Figure 2 presents the fitted density models alongside data collected by Kohlrausch [36] and the CRC Handbook [37]. Among the models, only the cubic and fifth-degree polynomials exhibit a maximum density value. According to Kohlrausch's data, the maximum water density is 999.973 kg m^{-3} at 277.05 K, while the CRC Handbook reports a maximum of 999.9749 kg m^{-3} between 277.05 and 277.15 K. In the present study, the maximum values for the cubic and fifth-degree models were 999.952 kg m^{-3} at 275.88 K and 999.969 kg m^{-3} at 277.10 K, respectively. Thus, the fifth-degree polynomial provides a more accurate estimate of the density peak. Furthermore, the average relative error of the fifth-degree model compared with the Kohlrausch and CRC data was 3.6 x 10^{-6} and 1.7 x 10^{-6}, respectively, while the cubic model showed errors of 3.3 x 10^{-5} and 4.1 x 10^{-5}, respectively.

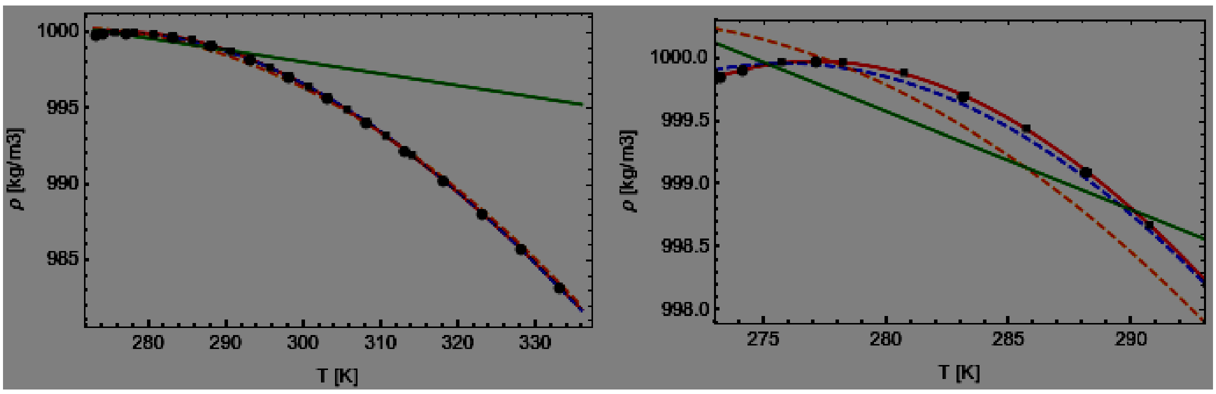

Fig. 2. Comparison between modeled water density as a function of temperature (lines) and collected reference data (points). Models include fifth-degree (red), third-degree (blue), second-degree (orange), and linear (green) polynomial fits, data from Kohlrausch [36] (circles) and CRC Handbook [37] (square).

Several handbooks and educational textbooks were reviewed regarding the treatment of water's anomalous density behavior. Kreith's *Principles of Heat Transfer*

[28] provides tabulated data (Table 13) for the properties of liquid water at saturation pressure in 5 K increments. These data include a density inversion point and a negative coefficient of thermal expansion. In contrast, Holman's *Heat Transfer* [29] contains only tabulated values (Table A.9), which do not reflect any density inversion; it also includes Rayleigh number values per cubic meter and per degree Celsius with no negative entries.

Typically, the density of a pure substance is usually modeled using the Rackett equation or a modified version. A model for water density using a modified Rackett equation (Eq. 14) is available in Yaws' *Chemical Properties Handbook* [35]. However, this equation does not feature a mathematical maximum and therefore cannot represent the density inversion of water. Thus, it is unsuitable for modeling free convection heat transfer at low temperatures.

$$\ln(\rho) = \ln(347.1) + (-(1-\frac{T}{647.096})^{0.28571})\ln(0.274)$$
(14)

On the other hand, Perry's *Chemical Engineers' Handbook* [38] provides two models for water density: one valid from 273.16 K to 647.096 K, and another from 273.16 K to 353.15 K. These are given in Eqs. 15 and 17, respectively.

$$\rho=(17.863 + 58.606\tau^{0.35} - 95.396\tau^{2/3} + 213.89\tau - 141.56\tau^{4/3})x18.015 \quad (15)$$

$$\tau=(1-\frac{T}{647.096K});T=[273.16;647.096]K \quad (16)$$

$$\rho=(-13.851 + 0.64038T - 0.00191T^2 + 1.8211x10^{-6}T^3) * 18.015;T=[273.16;353.15]K \quad (17)$$

Only the second model (Eq. 17) exhibits a maximum value at 278.83 K with a density of 1003.23 kg m^{-3}, which is 1 K higher and 3 kg m-^{3} greater than the experimental value of 999.973 kg m^{-3} at 277.05 K reported by Kohlrausch. While this discrepancy may be acceptable for modeling natural convection with a cubic approximation, the overestimation is evident in Figure 4 (off by 3 kg m^{-1}). As with other references, Perry's Handbook also includes tabulated values of saturated liquid water properties at 2 K intervals.

3.2. Comparison between simulations with different density models

Figure 3a displays the volume-averaged temperature of the bath as a function of simulation time. At 4000 seconds, the maximum temperature difference between models is approximately 6 K, with the lowest temperature of around 273 K predicted by the B304 model and the highest temperature of around 279 K predicted by the B274 model. Additionally, the temperature profiles of the linear and quadratic models are nearly identical. The linear and B304 models also show similar temperature trends.

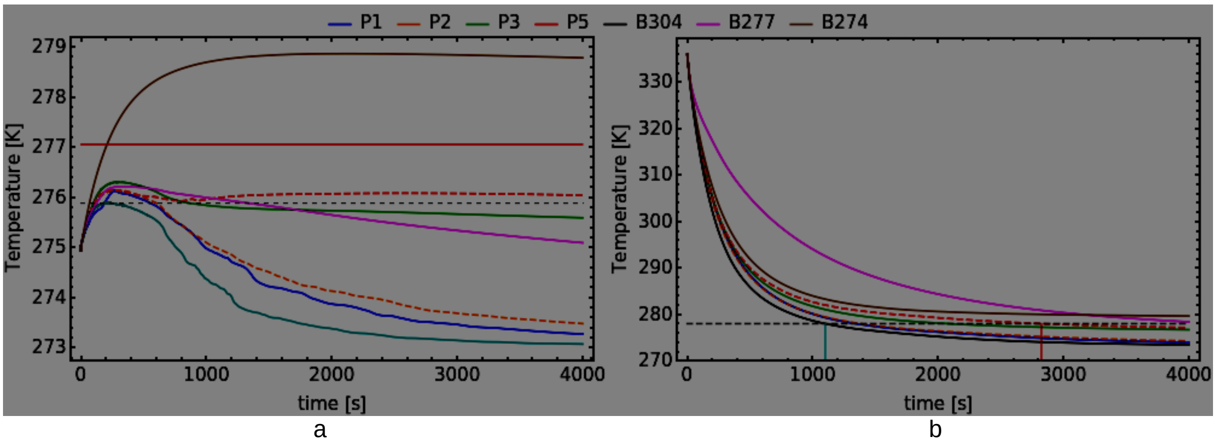

Fig. 3. a) Volume-averaged temperature of the bath as a function of simulation time. b) Volume-averaged temperature of the sachet as a function of simulation time.

Figure 3b shows the volume-averaged temperature profile of the fluid inside the sachet. It can be observed that the B304 model results in the fastest cooling rate, reaching 278 K at 1100 s, whereas the more accurate fifth-degree model reaches the same temperature at 2824 s. In contrast, the B277 and B274 models do not reach the target temperature within the simulated time frame.

Furthermore, the average temperatures of both regions in the linear and quadratic models are nearly similar. The profiles of the average temperature within the bath for the linear and B304 models are also very similar, although the B304 model exhibits a greater cooling rate. The model showing the highest thermal inertia is B277, as its expansion coefficient is close to zero, which leads to lower convective flow velocities.

For the cubic and fifth-degree models, the bath temperature remains around 275.5 K and 276 K, respectively, for most of the simulation. This behavior is attributed to the density inversion points at 275.88 K and 277.1 K, respectively. Thus, both models—characterized by anomalous density behavior— show similar temperature profiles, with slight differences due to variations in the location of their maximum density points.

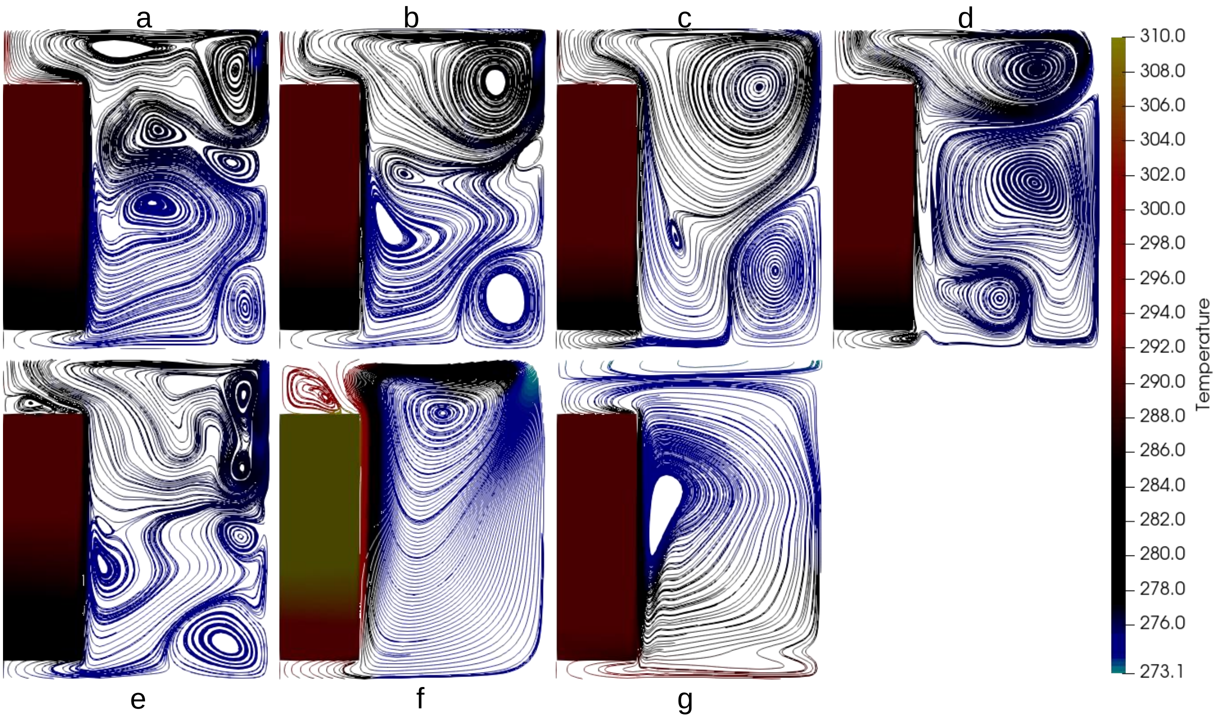

Fig. 4. Streamlines in the bath, colored by temperature, and temperature field within the sachet, at 360 s. a) linear, b) quadratic, c) cubic, d) fifth-degree, e) B304, f) B277 and g) B274.

Figures 4 and 5 display the bath streamlines colored by temperature alongside the temperature gradient within the sachet. These visualizations can be analyzed in conjunction with Figure 6, which shows the bath streamlines colored by the magnitude of the flow velocity. As indicated in Figure 3b, the Boussinesq models B277 and B274 do not reach the target temperature of approximately 278 K, suggesting that the overall heat transfer and flow velocities in these models—visible on Figure 6f and 6g— are lower compared to the other models.

The streamlines shown in Figure 6 help explain the subsequent results. The B277 and B274 models exhibit reduced buoyancy due to the lower absolute values of the volumetric expansion coefficient. In the case of B277, this coefficient is nearly zero, resulting in the slowest overall heat transfer among all models, as illustrated by the velocity scale in Figure 6f. Conversely, the B274 model, which has a negative volumetric expansion coefficient evaluated at 274 K, experiences inverse buoyancy throughout the process. As the temperature rises, the density also increases, causing the warmer fluid to sink and producing a descending temperature gradient. As a result, with the coldest region located at the top of the domain, heat transfer through the upper cold surface occurs primarily via conduction. This leads to lower flow velocities and the stratification of the fluid, as evident in the streamlines and a temperature gradient shown in Figures 5g and 6g.

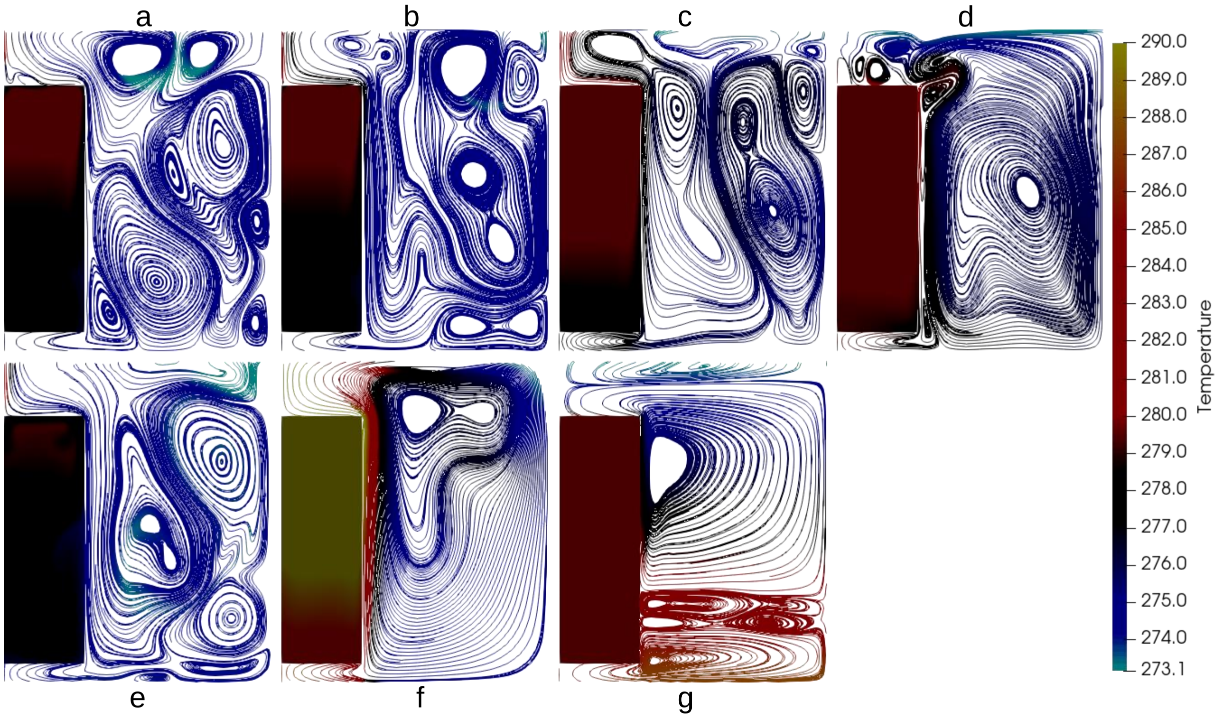

Fig. 5. Streamlines in the bath, colored by temperature, and temperature field within the sachet, at 1200 s. a) linear, b) quadratic, c) cubic, d) fifth-degree, e) B304, f) B277 and g) B274.

Another observation from the streamlines at 1200 s (Figs. 5 and 6,) for the B304 model is that, despite having the lowest average temperature (274.02 K) and a small temperature difference between the cold and hot surfaces, it exhibits the highest fluid velocity. This suggests that, in this case, evaluating fluid properties at the average process temperature is not appropriate for this model—a discrepancy also reflected in the experimental validation. As observed previously, the streamlines indicate reduced diffusion in models with a low thermal expansion coefficient. Nevertheless, the fluid velocity in the B304 model remains the highest among all models analyzed.

The streamlines shown in Figure 5 at 360 s, indicate that the models generally exhibit similar flow patterns, with the exception of those using a low and constant absolute value for the thermal expansion coefficient (B277 and B274). This similarity across models may be attributed to the predominance of local buoyant effects near the sachet wall, which drive the flow regardless of whether the average bath temperature is above or below the density inversion point. Notably, even in the B277 model, where the thermal expansion coefficient is nearly zero and buoyancy acts in the opposite direction, localized buoyant forces still influence the flow near the sachet interface.

Local heat transfer for the seven density models were obtained using OpenFOAM's *wallHeatTransfer postProcess* command. The results, shown in Figure 7, illustrate that at 360 s (Fig. 7a), all models follow a similar overall trend. The B274 model shows notably lower heat transfer along the bottom surface of the sachet. On the lateral wall, heat transfer generally increases with height in all models, with the exception of the B277 model, which maintains a nearly constant value of approximately 3300 W m^{-2}. Conversely, on the upper wall, heat transfer decreases across all models.

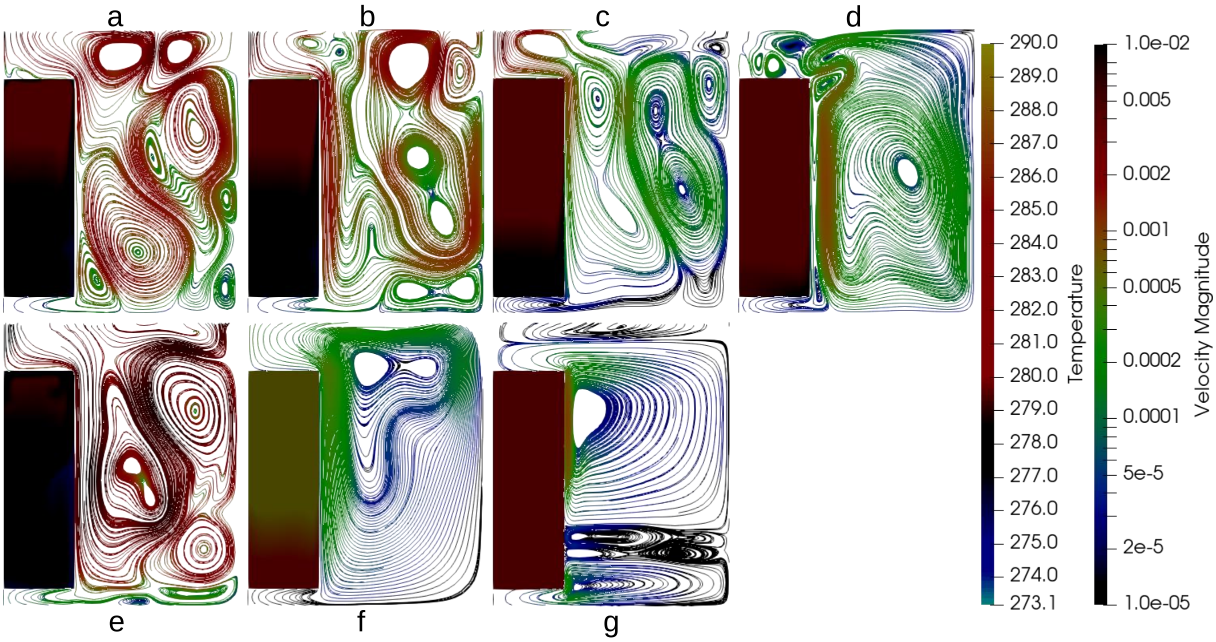

Fig. 6. Streamlines in the bath region colored by the magnitude of flow velocity and temperature field of the sachet, at 1200 s. a) linear, b) quadratic, c) cubic, d) fifth-degree, e) B304, f) B277 and g) B274.

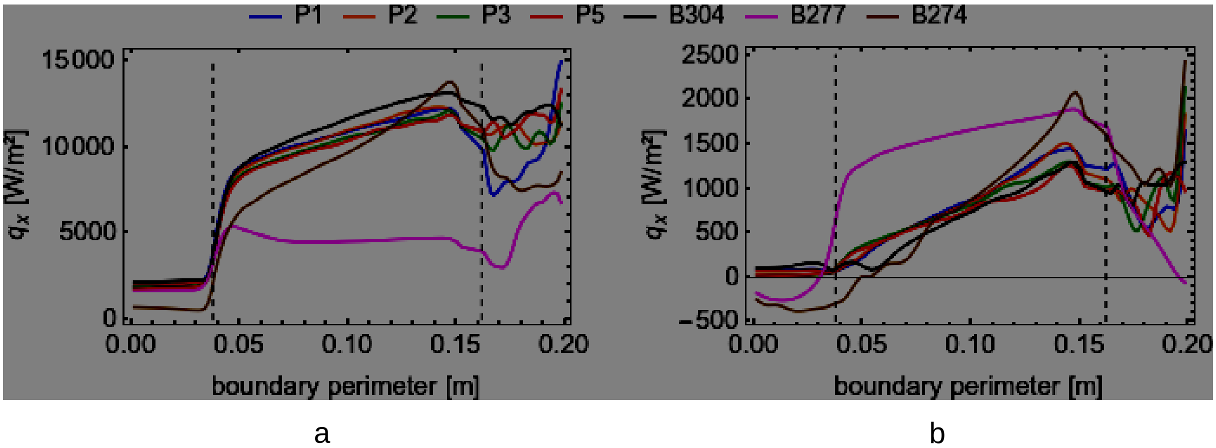

Fig. 7. Local heat transfer along the sachet-bath interface, from bottom to top, at a) 360 s; b) 1200 s and c) 3600 s. Vertical dashed lines indicate the interface vertices, dividing the interface into three regions: bottom, lateral, and top. Positive values represent heat flow from the sachet to the bath; negative values indicate the opposite.

As the simulation progresses to 1200 s (Fig. 7b), reverse heat transfer—from the bath to the product—occurs at the bottom wall of the sachet models with a low thermal expansion coefficient. This effect is primarily is due to thermal stratification within the bath and heat accumulation near its lower region, particularly in the B274 model. Moreover, the sachet is modeled using the fifth-degree density formulation, which causes its lower portion to reach the lowest temperature, thereby generating a reverse temperature gradient. In the case of the b277 model, the reduced circulation velocity leads to similar heat buildup below the sachet, as evidenced by the streamlines (Fig. 6). In contrast, the remaining models show a general decrease in heat transfer, attributed to a diminishing temperature gradient.

3.3. Experimental validation

A comparison between the experimental temperature measurements and the fifth-degree simulation results at three locations inside the sachet (points 1, 2 and 3) is presented in Fig. 8a and detailed in Table 1. Overall, the simulation results show good agreement with the simulation and the experimental data, with average absolute errors of 0.788 K, 1.346 K and 1.324 K for points 1, 2 and 3 respectively. A 95th percentile of the error of 2.127 K, 4.920 K and 2.853 K for the same points, with point 2 showing the largest deviation—primarily during the first 100 seconds. This discrepancy may be attributed to an electrical short circuit in the sensor, movement of the sachet or the thermocouple within the bath, or experimental limitations, such as the opacity of milk, which made visual confirmation inside the sachet impossible. Additionally, Fig. 8a shows a temperature inversion at 2550 s in the simulated data, with point 3 registering the highest temperature and point 1 the lowest.

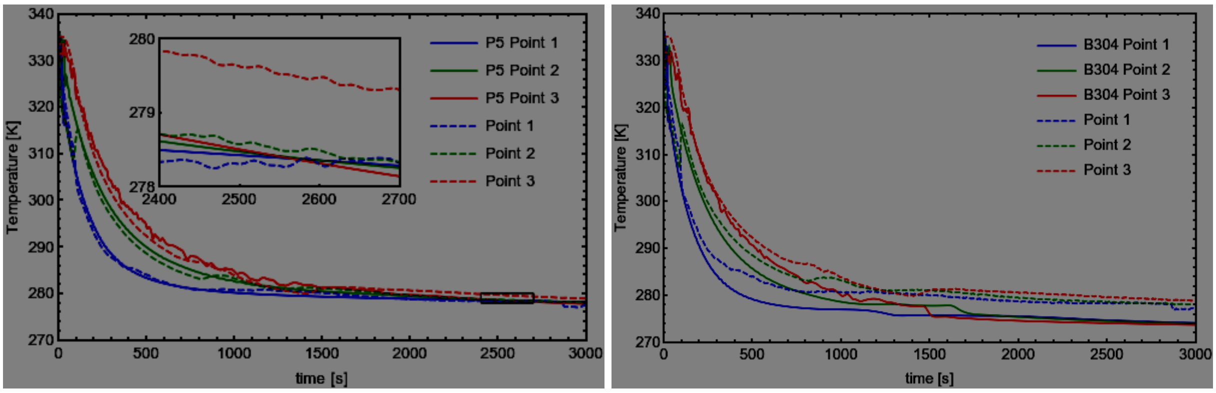

a) b)

Fig. 8. a) Comparison between temperature profiles predicted using a fifth-degree density model and experimental data at three locations (points 1, 2 and 3) within the sachet region. b) Comparison between temperature profiles predicted using a Boussinesq approximation evaluated at 304 K and experimental data at three locations (points 1, 2 and 3) in the sachet region.

As for the other simulations, a comparison between experimental data and the B304 model is shown in Fig. 8b, which demonstrates that this model does not adequately estimate the temperature profile of the process. The simulated temperature begins to deviate from the experimental data after approximately 300 seconds. At 2000 seconds, the simulated temperatures are 3.204 K, 4.120 K and 6.044 K lower than the measured values at points 1,2 and 3, respectively. The average absolute error for these points were 3.911 K, 3.467 K and 2.989 K, respectively, while the 95th percentile errors were 4.931 K, 4.920 K and 6.062 K respectively.

On the other hand, the cubic density model also showed good overall agreement with the experimental data, with average absolute errors of 1.572 K, 1.685 K and 1.288 K for each point. The corresponding 95th percentile errors were 2.204 K, 4.920 K and 2.863 K. The quadratic model yielded higher average absolute errors of 2.660 K, 2.308 K and 1.353 K for each point, with 95th percentile errors of 3.498 K, 4.920 K and 2.897 K, respectively. Additionally, the quadratic model underestimated the final temperature by 3.0 K, 3.7 K and 4.69 K for points 1, 2 and 3, whereas the cubic model underestimated by 0.476 K, 1.291 K and 2.290 K, respectively.

Table 1. Model comparison with experimental data at each measured point. See Figure 1.

	Model	Measured point					
		1	2	3	4	5	6
Average absolute error [K]	P5	0.79	1.35	1.32	1.31	0.65	1.48
	P3	1.57	1.69	1.29	1.76	0.61	0.63
	P2	2.66	2.31	1.35	2.03	1.24	1.67
	B304	3.91	3.47	2.99	2.93	1.76	4.36
95th Percentile of the error [K]	P5	2.13	4.92	2.85	1.81	1.19	1.77
	P3	2.20	4.92	2.86	2.53	1.19	1.42
	P2	3.50	4.92	2.90	3.83	2.67	2.94
	B304	4.93	4.92	6.06	4.66	3.46	6.29
Temperature deviation [K] at 3000 s (experiments minus simulations)	P5	-0.08	-0.57	-1.53	-0.39	-2.30	1.96
	P3	-0.48	-1.29	-2.29	-1.52	-2.12	1.90
	P2	-3.00	-3.70	-4.69	-3.81	-4.44	-0.61
	B304	-4.02	-4.56	-5.45	-4.26	-4.92	-1.25

Similarly, in the bath region, a comparison between the temperatures predicted by the fifth-degree and cubic density models and the experimental temperatures at three points (points 4, 5 and 6) is shown in Figure 9a and 9b, respectively, and detailed in Table 1. The average absolute errors for points 4, 5 and 6 were 1.31 K, 0.653 K and 1.476 K, respectively, while the 95th percentile errors were 1.813 K, 1.186 K and 1.774 K. The discrepancies between the experimental and simulated results may be attributed to simplifications in the geometry—such as modeling the sachet as a perfect cylinder—and the omission of air in the headspace, as well as a possible deviation of the sachet's vertical axis. For points 4 and 5, the simulation slightly underestimated the experimental temperatures; at 3000 s, both models predicted temperatures 1.45 K lower than the experimental values. This discrepancy may result from low insulation in the experimental setup's lateral walls and the fixed gradient used in the model's top boundary condition. In the case of point 6, deviations could stem from minor thermocouple movement, misalignment of the sachet axis, and the assumption of laminar flow in the simulation.

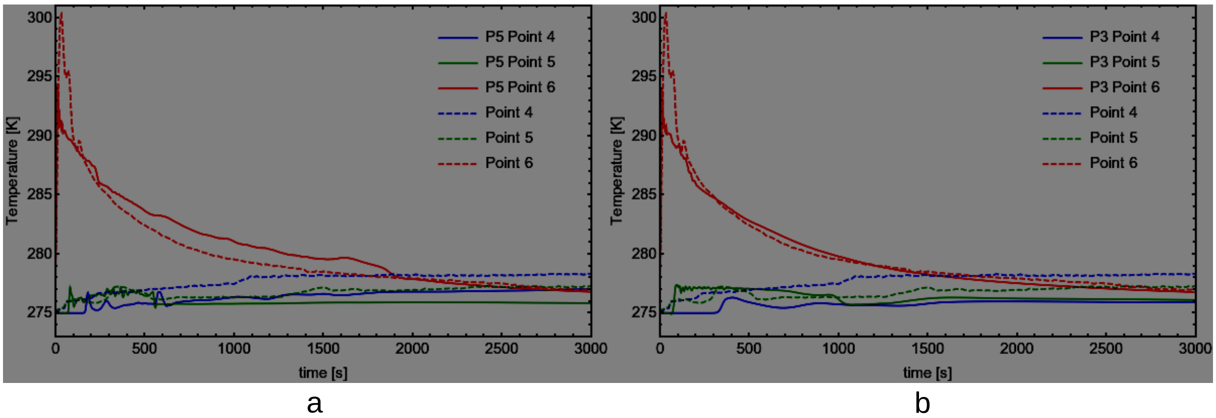

Fig. 9. a) Comparison between temperature profiles predicted with a fifth-degree density model and experimental temperature profiles at three locations (points 4, 5 and 6) in the bath region. b) Comparison between temperature profiles predicted with a cubic density model and experimental temperature profiles at three locations (points 4, 5 and 6) in the bath region.

Nevertheless, the predicted temperature showed overall good agreement with the experimental data, and the temperature trends were consistent. As point 2 is located below point 4, it consistently exhibited a higher temperature, supporting the choice of a density model that includes a density-inversion point for accurately capturing buoyancy-driven heat transfer in the bath. Lastly, point 6 lies within the boundary layer, where a sudden temperature increase is expected; however, the model responds more slowly and fails to capture such rapid transitions.

4. Conclusions

The performance of seven density models—linear, second-degree, third-degree, fifth-degree, B304, B277, and B274—was evaluated over a temperature range of 273 K to 336 K to represent the cooling process near water's density inversion point using a finite volume method. The following conclusions were drawn.

Density models that incorporate a density inversion point—such as the fifth-degree and cubic models presented in this study—proved to be the most accurate in reproducing the experimental results from the pasteurization process. This was consistently validated throughout the simulations. In contrast, the other models failed to accurately predict the final temperatures and the time required to reach them. These findings highlight the critical importance of selecting an appropriate density model that accurately represents fluid behavior across the full temperature range of the simulated process—an aspect often overlooked in some textbooks and handbooks, many of which rely on models lacking a density inversion point. Additionally, this work provided streamlines and temperature profiles for natural convection heat transfer in a cylindrical enclosure with a blunt concentric cylinder filled with fluid.

When the cold plate was positioned at the top, some models—such as linear and quadratic polynomials, as well as the Boussinesq approximation evaluated at 304 K (B304)—

resulted in faster cooling of the pasteurized product. In contrast, other models—including the cubic and fifth-degree polynomials, the Boussinesq approximation at 277 K (B277), and at 274 K (B274)—exhibited delayed cooling due to reduced flow velocity and pronounced stratification effects.
In conclusion, modeling and simulating heat transfer and fluid dynamics in scenarios where the density inversion point lies within the temperature range underscores the importance of selecting appropriate density models—particularly when buoyancy is the primary driving force in the system.

Acknowledgment

This study was completed as part of the *Doctorado en Ciencias Aplicadas*. Universidad Nacional de Misiones, Facultad de Ciencias Exactas, Químicas y Naturales. The author, Carlos Schvezov, acknowledges the Consejo Nacional de Investigaciones Científicas y Técnicas for the scholarship support.

References

1. P. Fellows, *Food Processing Technology: Principles and Practice, Chapter 11: Pasteurisation*. 4th ed., Woodhead Publishing, 2017, p 563.
2. A.M. Martinez, M.R. Rosenberger, Modelado Numérico de Pasteurización Artesanal de Leche y Jugos Naturales, Mecánica Computacional Vol XXXII, (2013) 2485-2501.
3. P. Dumalisile, R.C. Witthuhn, R.J. Britz, Impact of Different Pasteurization Temperatures on the Survival of Microbial Contaminants Isolated from Pasteurized Milk. *Int. J. of Dairy Technol.*, vol. 58, no. 2, May 2005, pp. 74–82. https://doi.org/10.1111/j.1471-0307.2005.00189.x.
4. E.E. Badin, P.E.D. Augusto, R.A. Quevedo-Leon, A. Ibarz, P.D. Ribotta, A.R. Lespinard, *Raspberry Pulp Pasteurization: Computational Fluid Dynamics Modeling and Experimental Validation of Color and Bioactive Compound Retention. J. of Food Process Eng.*, vol. 46, no. 1, Nov. 2022, p. e14168. https://doi.org/10.1111/jfpe.14168.
5. E.E. Badin, M.M. Mercatante, R.H. Mascheroni, R.A. Quevedo-Leon, A. Ibarz, P.D. Ribotta, A.R. Lespinard, Effect of Pasteurization on Color, Ascorbic Acid and Lycopene of Crushed Tomato: A Computational Study with Experimental Validation, *J. of Food Eng.*, vol. 337, Jan. 2023, p. 111218. https://doi.org/10.1016/j.jfoodeng.2022.111218.
6. Código Alimentario Argentino – Capítulo VIII: Alimentos Lácteos. Art. 558.
7. A. Quintino, E. Ricci, S. Grignaffini, M. Corcione, Heat Transfer Correlations for Natural Convection in Inclined Enclosures Filled with Water around Its Density-Inversion Point, *Int. J. of Thermal Sc.*, vol. 116, June 2017, pp. 310–19. https://doi.org/10.1016/j.ijthermalsci.2017.03.008.
8. M. Corcione, A. Quintino, Penetrative convection of water in cavities cooled from below, Comput. and Fluids, vol 123, Dec. 2015, pp 1-9. https://doi.org/10.1016/j.compfluid.2015.09.003.
9. C. Cianfrini, M. Corcione, E. Habib, A. Quintino, Natural Convection of Water Near 4°C in a Bottom-Cooled Enclosure, *Energy Procedia*, vol. 82, Dec. 2015, pp. 322–27. https://doi.org/10.1016/j.egypro.2015.12.040.
10. W.R. Debler, On the Analogy between Thermal and Rotational Hydrodynamic Stability, *Journal of Fluid Mechanics*, vol. 24, no. 1, Jan. 1966, pp. 165–76. *Cambridge University Press*, https://doi.org/10.1017/S0022112066000569.
11. B. Gebhart, J.C. Joseph, A New Density Relation for Pure and Saline Water, *Deep Sea Research*, vol. 24, no. 9, Sept. 1977, pp. 831–48. https://doi.org/10.1016/0146-6291(77)90475-1
12. K. Sasaguchi, K. Kuwabara, K. Kusano, H. Kitagawa, Transient Cooling of Water around a Cylinder in a Rectangular Cavity—a Numerical Analysis of the Effect of the Position of the Cylinder, *Int. J. of Heat and Mass Transfer*, vol. 41, no. 20, Oct. 1998, pp. 3149–56. https://doi.org/10.1016/S0017-9310(98)00064-7.
13. Y.R. Li, Y.P. Hu, X.F. Yuan, Natural Convection of Water Near Its Density Maximum around a Cylinder Inside an Elliptical Enclosure along Slender Orientation, *Numer. Heat Transfer, Part A*, vol. 62, no. 10, Nov. 2012, pp. 780–97. https://doi.org/10.1080/10407782.2012.715978.
14. Y.P. Hu,Y.R. Li, X.F. Yuan, C.M. Wu, Natural Convection of Cold Water near Its Density Maximum in an Elliptical Enclosure

Containing a Coaxial Cylinder, *Int. J. of Heat and Mass Transfer*, vol. 60, May 2013, pp. 170–79. https://doi.org/10.1016/j.ijheatmasstransfer.2012.12.059.

15. C.V. Raghavarao, Y.V.S.S. Sanyasiraju, Natural Convection Heat Transfer of Cold Water in an Eccentric Horizontal Cylindrical Annulus — a Numerical Study, *Comput. Mech.*, vol. 18, no. 6, Dec. 1996, pp. 464–70. Springer Link, https://doi.org/10.1007/BF00350254.

16. Y.P. Hu, Y.R. Li, C.M. Wu, Comparison Investigation on Natural Convection of Cold Water near Its Density Maximum in Annular Enclosures with Complex Configurations, *Int. J. of Heat and Mass Transfer*, vol. 72, May 2014, pp. 572–84. https://doi.org/10.1016/j.ijheatmasstransfer.2014.01.047.

17. M.A. Medebber, R. Noureddine, Numerical Study of Natural Convection in a Vertical Cylindrical Partially Annular, *Mechanics and Mechanical Eng.*, vol. 22, no. 1, Jan. 2018, pp. 77–92. https://doi.org/10.2478/mme-2018-0008.

18. E.M. Sparrow, M. Charmchi. Natural Convection Experiments in an Enclosure between Eccentric or Concentric Vertical Cylinders of Different Height and Diameter, *Int. J. of Heat and Mass Transfer*, vol. 26, no. 1, Jan. 1983, pp. 133–43. https://doi.org/10.1016/S0017-9310(83)80015-5.

19. M. Charmchi, E. M. Sparrow, Analysis of Natural Convection in the Space Between Concentric Vertical Cylinders of Different Height and Diameter, *Numer. Heat Transfer*, vol. 5, no. 2, Apr. 1982, pp. 119–44. https://doi.org/10.1080/10407788208913439.

20. S.L. Braga, R. Viskanta. Effect of Density Extremum on the Solidification of Water on a Vertical Wall of a Rectangular Cavity, *Exp. Therm. and Fluid Sci.*, vol. 5, no. 6, Nov. 1992, pp. 703–13. https://doi.org/10.1016/0894-1777(92)90114-K.

21. C.J. Kim, S.T. Ro, J.S. Lee, M.G. Kim, Two-Dimensional Freezing of Water Filled between Vertical Concentric Tubes Involving Density Anomaly and Volume Expansion, *Int. J. of Heat and Mass Transfer*, vol. 36, no. 10, July 1993, pp. 2647–56. https://doi.org/10.1016/S0017-9310(05)80201-7.

22. S. Pandey, Y.G. Park, M.Y. Ha, An Exhaustive Review of Studies on Natural Convection in Enclosures with and without Internal Bodies of Various Shapes, *Int. J. of Heat and Mass Transfer*, vol. 138, Aug. 2019, pp. 762–95. https://doi.org/10.1016/j.ijheatmasstransfer.2019.04.097.

23. P.M. Teertstra, M.M. Yovanovich, J.R. Culham, Models and Experiments for Laminar Natural Convection From Heated Bodies in Enclosures, Volume 1, ASMEDC, 2004, pp. 443–53. https://doi.org/10.1115/HT-FED2004-56633.

24. S. Kumar and S.K. Mahapatra. An Experimental and Numerical Analysis of Natural Convection in a Partially Open Cuboid Enclosure with a Cylindrical Obstacle. *Therm. Sci. and Eng. Prog.*, vol. 45, Oct. 2023, p. 102118. https://doi.org/10.1016/j.tsep.2023.102118.

25. N.S. Gibanov, and M.A. Sheremet. Natural Convection in a Cubical Cavity with Different Heat Source Configurations. *Therm. Sci. and Eng. Prog.*, vol. 7, Sept. 2018, pp. 138–45. https://doi.org/10.1016/j.tsep.2018.06.004.

26. N. Zhan, L. Ding, Y. Chai, J. Wu and Y. Xu. Experimental Study on Natural Convective Heat Transfer in a Closed Cavity. *Therm. Sci. and Eng. Prog.*, vol. 9, Mar. 2019, pp. 132–41. https://doi.org/10.1016/j.tsep.2018.11.009.

27. S.S. Priam, M.Md. Ikram, S. Saha and S.C. Saha. Conjugate Natural Convection in a Vertically Divided Square Enclosure by a Corrugated Solid Partition into Air and Water Regions. *Therm. Sci. and Eng. Prog.*, vol. 25, Oct. 2021, p. 101036. https://doi.org/10.1016/j.tsep.2021.101036.

28. F. Kreith, R.M. Manglik, M.S. Bohn, *Principles of Heat Transfer 7th Edition*, Appendix 2: Data Tables, Table 13. Cengage Learning, 2011, p. A14.

29. J.P. Holman, *Transferencia de Calor*. 1st ed., Apéndice A, Tabla A9, McGraw-Hill, 1986, pp 600.

30. Y.A. Cengel, J.M. Cimbala, R.H. Turner, *Fundamentals of Thermal-Fluid Sciences 5th de., Appendix 1: Property Tables and Charts (SI units), Table A-15*, McGraw-Hill, New York, 2017, p. 994.

31. C. Greenshields, H. Weller. Notes on computational fluid dynamics: General principles, CFD Direct Ltd, Reading, UK, 2022.

32. R.I. Issa, Solution of the Implicitly Discretised Fluid Flow Equations by Operator-Splitting, *J. of Comput. Phys.*, vol.

62, no. 1, Jan. 1986, pp. 40–65. https://doi.org/10.1016/0021-9991(86)90099-9.

33. T. Michalek, T.A. Kowalewski, B. Sarler, Natural Convection for Anomalous Density Variation of Water: Numerical Benchmark, *Progress in Computational Fluid Dynamics, An International Journal*, vol. 5, no. 3/4/5, 2005, p. 158-169. https://doi.org/10.1504/PCFD.2005.006751.

34. M.P. Nguyen, N. Van Hap, Computational Overview of Fluid Structure Interaction, *Numerical Investigation of Natural Convection and Entropy Generation of Water near Density Inversion in a Cavity Having Circular and Elliptical Body*. IntechOpen, 2020. *www.intechopen.com*, https://doi.org/10.5772/intechopen.95301.

35. C.L. Yaws, *Chemical Properties Handbook: Physical, Thermodynamic, Environmental, Transport, Safety, and Health Related Properties for Organic and Inorganic Chemicals*. McGraw-Hill, 1999.

36. F. Kohlrausch, *Praktische Physik*, Band 3 – Tabellen und Diagramme, 23 Auflage, Table 65, B.G. Teubner Stuttgart, 1986, pp 88 – 90.

37. W.M. Haynes, Ed., *CRC Handbook of Chemistry and Physics 97th ed*., Section 6: Fluid Properties, CRC Press, Boca Raton, FL, 2017, pp 6-1 – 6-2.

38. D.W. Green, Ed., *Perry's Handbook of Chemical Engineer 8th Edition,* Section 2 Physical and Chemical Data, Table 2-32, McGraw-Hill, 2008; pp 2-103.

Appendix. Free convection inside a cavity

A square enclosed cavity model was developed to validate the appropriate water density model and mesh resolution. The cavity measured 38 mm by 38 mm, with the left wall maintained at a constant temperature of 10 ºC (283.15 K) and the right wall at 0 ºC (273.15 K). The upper and lower walls were thermally insulated and a no-slip boundary condition was applied to all walls. The cavity was discretized using a regular square mesh of 160 by 160 cells, totaling 25,600 cells. A coarser mesh of 16 by 16 cells was also simulated to assess the influence of mesh size on the results. For the simulations, the governing equations (Eqs. 1– 3, 5) and thermophysical property relations (Eqs. 5-8) were employed.

The results were compared with those reported by Michalek et al. (2005) [33] and Phu & Nguyen (2020) [34]. To facilitate this comparison, dimensionless numbers along both the vertical and horizontal centerlines of the cavity were analyzed. The dimensionless quantities used in the analysis were:

(Eq. A.1 – A.4)

where *x* and *y* are the horizontal and vertical coordinates, respectively; *L* is the length of the cavity, *Ux* and *Uy* are the horizontal and vertical components of the velocity vector, respectively; and *α* is the thermal diffusivity.

Figure A.1 presents the comparison through dimensionless velocity components along the central horizontal plane: Figure A.1a shows the horizontal component of the dimensionless velocity as a function of cavity length, while Figure A.1b displays the vertical component. As observed, the simulation results obtained using the refined mesh exhibit good agreement with those reported by Michalek et al., particularly near the center of the cavity. In contrast, the results from the coarser mesh display noticeable discrepancies, especially in the central region.

Figure A.2 displays the streamlines resulting from simulations performed with both coarse and refined meshes. The figure clearly illustrates that the coarse mesh fails to accurately capture the formation and structure of the vortices, in contrast to the refined mesh, which provides a more precise representation of the flow field. These findings support the conclusion that the average cell size used in the refined mesh is appropriate and can be reliably applied in the other simulations conducted in this study.

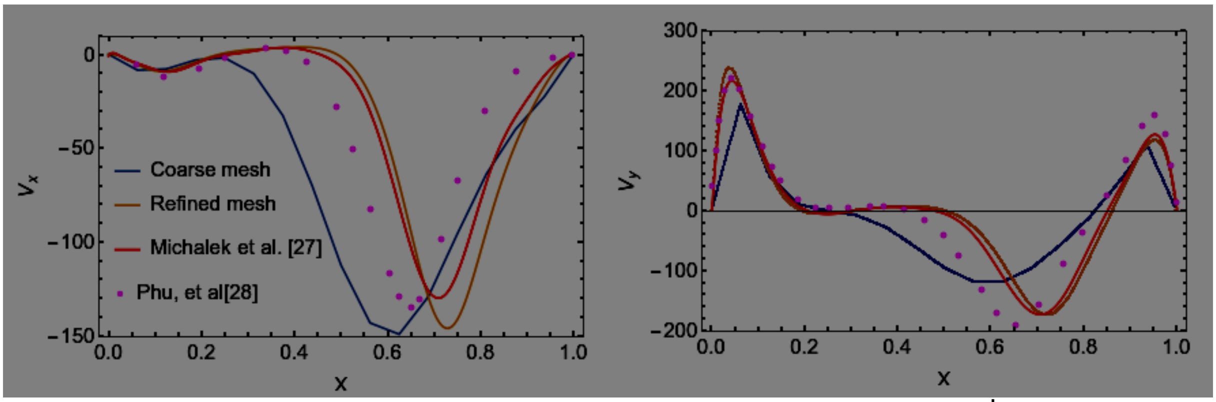

Fig. A.1. Dimensionless velocity along the central horizontal plane. x component (a), y component (b). Blue: coarse mesh simulation, orange: refined mesh, magenta dots: Nguyen data [34], red: Michalek data [33].

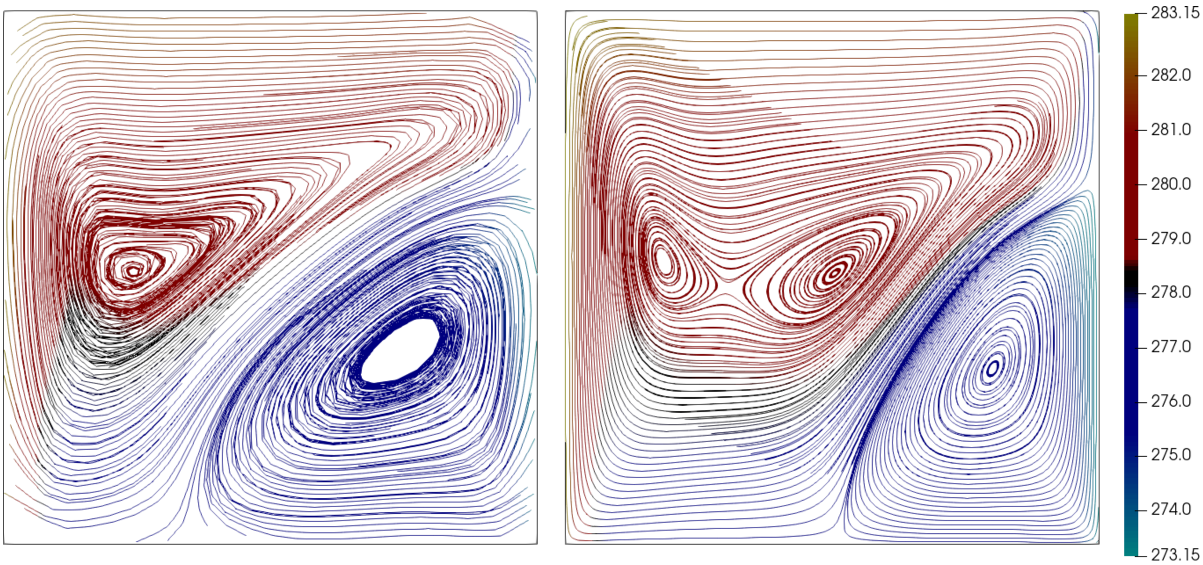

Fig. A.2. Streamlines colored by temperature. Left: coarse mesh simulation; right: refined mesh simulation.

RECyT
Year 27 / Nº 43 / 2025 /
DOI: https://doi.org/10.36995/j.recyt.2025.43.006

Chemical Stability, Viability, and *In Vitro* Gastrointestinal Resistance of the Probiotic *Bacillus* in Organic Mango Juice

Estabilidad Química, Viabilidad y Resistencia Gastrointestinal *In Vitro* del Probiótico *Bacillus* en Jugo de Mango Orgánico

Estabilidade Química, Viabilidade e Resistência Gastrointestinal *In Vitro* de *Bacillus* Probiótico em Suco de Manga Orgânico

Peron, Taciane[1, *]; dos Santos, Ramon Araújo[1, 4]; Lopes Martins, Maurílio[1]; de Castro Leite Júnior, Bruno R.[2]; Almeida do Nascimento Benevenuto, Wellingta C.[1]; de Souza Viana, Eliseth[3]; Furtado Martins, Eliane Maurício[1]

1- Federal Institute of Education, Science and Technology of Southeast Minas Gerais -IFSUDESTEMG, Rio Pomba, Minas Gerais, Brazil.
2- Federal University of Viçosa - UFV, Viçosa, Minas Gerais, Brazil.
3- Brazilian Agricultural Research Corporation - EMBRAPA, Cruz das Almas, Bahia, Brazil.
4- Federal Institute of Education, Science and Technology of Rio Grande do Norte - IFRN, Currais Novos, Rio Grande do Norte, Brazil.
* E-mail: taciane.peron@gmail.com

Received: 22/10/2024; Accepted: 17/03/2025

Abstract
Probiotic juices must ensure their survival after processing and in the gastrointestinal tract to achieve their benefits. This study was divided into two stages. Initially, the objective was to evaluate the pH and viability of *Bacillus clausii* and *Bacillus coagulans* BC30 in organic mango juices subjected to heat treatment and, subsequently, to simulated accelerated shelf-life conditions. In the second stage, the pH, acidity, total soluble solids, the viability of *B. clausii,* as well as its resistance to the *in vitro* gastrointestinal tract (GIT) digestion were evaluated. In the first stage, at all analyzed times, the juice with *B. clausii* presented a lower pH than the juice with *B. coagulans*. The *B. coagulans* count decreased during the accelerated shelf-life test, whereas the *B. clausii* count remained stable. In the second stage, the lowest count of *B. clausii* was observed in the juice subjected to simulated industrial heat treatment (96 °C/35 s). However, as regards the other treatments (non-heat-treated and 80°C/10 min), the probiotic count was > 10^6 CFU/mL. An excellent performance of *B. clausii* was found in the juice that was not heat-treated and stored at different temperatures (5°C and 25°C) after the GIT test, with counts of > 10^7 CFU/mL.

Keywords: tropical fruit juice, *Bacillus clausii,* shelf life, thermal treatments, resistance to i*n vitro* gastrointestinal digestion.

Resumen
Los jugos probióticos deben asegurar su supervivencia después del procesamiento y en el tracto gastrointestinal para lograr sus beneficios. Este estudio se dividió en dos etapas. Inicialmente, el objetivo fue evaluar el pH y la viabilidad de *Bacillus clausii* y *Bacillus coagulans* BC30 en jugos de mango orgánico sometidos a tratamiento térmico y, posteriormente a condiciones de vida útil acelerada. En la segunda etapa, se evaluó el pH, la acidez, los sólidos solubles totales, la viabilidad de *B. clausii* y, su resistencia a la digestión *in vitro* en el tracto gastrointestinal (TGI). En la primera etapa, en todos los tiempos analizados, el jugo con *B. clausii* presentó un pH menor que el jugo con *B. coagulans*. Durante la prueba de vida útil acelerada, el recuento de *B. coagulans* disminuyó, mientras que el recuento de *B. clausii* se mantuvo estable. En la segunda etapa, el recuento más bajo de *B. clausii* se observó en el jugo sometido a tratamiento térmico industrial simulado (96 °C/35 s). Sin embargo, en cuanto a los otros tratamientos (sin tratamiento térmico y 80 °C/10 min), el recuento fue > 10^6 UFC/mL. Se observó un excelente desempeño de *B. clausii* en el jugo que no fue tratado térmicamente y almacenado a diferentes temperaturas (5 °C y 25 °C) después de la prueba del tracto gastrointestinal *in vitro*, con recuentos > 10^7 UFC/mL.

Palabras clave: jugo de frutas tropicales, *Bacillus clausii*, duración, tratamientos térmicos, resistencia a la digestión gastrointestinal *in vitro.*

Resumo
Os sucos probióticos devem garantir sua sobrevivência após o processamento e no trato gastrointestinal para obter benefícios. Este estudo foi dividido em duas etapas. Inicialmente, objetivou-se avaliar o pH e a viabilidade de *Bacillus clausii* e *Bacillus coagulans* BC30, em sucos orgânicos de manga submetidos a tratamento térmico e

posteriormente expostos a condições de vida de prateleira acelerada. Na segunda etapa foram avaliados o pH, acidez, sólidos solúveis totais, viabilidade de *B. clausii* e sua resistência ao trato gastrointestinal *in vitro* (TGI). Na primeira etapa, em todos os tempos analisados, o suco com *B. clausii* apresentou pH menor que o suco com *B. coagulans*. A contagem de *B. coagulans* diminuiu ao longo do teste de vida de prateleira acelerada, enquanto a contagem de *B. clausii* permaneceu estável. Na segunda etapa, a menor contagem de *B. clausii* foi observada no suco submetido ao tratamento térmico industrial simulado (96 °C/35 s). Porém, para os outros tratamentos (não tratado termicamente e 80 °C/10 min), a contagem foi > 10^6 UFC/mL. Excelente resultado de *B. clausii* foi encontrado em suco não tratado termicamente e armazenado em diferentes temperaturas (5 e 25 °C), após ensaio *in vitro* do trato gastrointestinal, com contagens > 10^7 UFC/mL.

Palavras-chave: suco de frutas tropicais, *Bacillus clausii,* vida de prateleira, tratamentos térmicos, resistência à digestão gastrointestinal *in vitro*.

Introduction

Non-alcoholic ready-to-drink beverages have a considerable effect on the worldwide economy since they provide not only hydration to people, but also pleasure from consumption. In this context, to supply the demands from consumers, the industry began to develop formulae with the addition of functional ingredients and/or reduction or remotion of undesirable ingredients, with satisfying prices and flavors (1). Therefore, investing in the development of juices and beverages based on fruits enriched with healthy ingredients is important, since this factor has conditioned the consumer's purchase decision over the last few years.

The incorporation of probiotics in fruit juices to produce functional and nutraceutical food is notable for its potential to control lifestyle-related diseases, and increase the availability of food not only for lactose-intolerant populations, but also for vegetarians and those with certain dietary restriction (2,3).

Mango juice is rich in minerals and a natural source of vitamins, dietary fiber, phenolic, and photochemical compounds. It may also be an excellent alternative to the addition of probiotics. However, the development of these products involves shelf life-related studies, which are a challenge to science, but also, fundamentally, to the food industry. Thus, the accelerated shelf-life test is a quicker and more practical evaluation carried out at an industrial scale, aimed at simulating the product's storage under extreme temperature conditions. The incidence of both temperature and light is the main factor contributing to deterioration and is the most suitable option for this process (4).

Concerning this matter, the formulations must supply an adequate number of living probiotics (> 10^6 CFU/g or mL) and ensure their survival in the gastrointestinal environment to reach the desirable benefits (5). The spore-forming probiotic bacilli can be delivered in the human intestine through new products because the spores can bear high-temperature environments, acid conditions, and salinity. This makes them viable for the production of new functional food, thanks to the probiotic features of certain species and their great resistance to intrinsic and extrinsic stress conditions (6).

For that reason, the objective of this study was to assess the pH and evaluate the viability of *Bacillus clausii* and *Bacillus coagulans* BC30 probiotics in organic mango juice subjected to thermal treatment, which simulated the industrial process during the accelerated shelf-life test. Moreover, the evaluation of physical and chemical quality, the viability of *B. clausii,* and its resistance in the *in vitro* gastrointestinal tract when transported in organic mango juice was carried out. These evaluations were done using various thermal treatments during a 60-day storage period, under both ambient and refrigeration temperatures.

Materials and Methods

This research was carried out in two stages. In the first, there was simulation of thermal treatment used industrially to assess the accelerated shelf life of juices. In the second stage, a comparison between the simulated industrial thermal treatment and the proposed alternative for the product was made.

Addition of *Bacillus clausii* and *Bacillus coagulans* BC30 to Organic Mango Juices

Organic mango juices sold in glass bottles of 290 mL each were used, with the product consisting of organic mango pulp (52%), water, organic sugar, and citric acid.

In the first stage, after cleaning the packaging, the juices were homogenized and aseptically opened. Then, the juices were sampled in 100 mL to be transferred into sterile bottles, to which 5 mL of *B. clausii* (Enterogermina®, Italy) containing 4.0 x 10^9 spores was added to obtain 10^7 viable spores. The 100 mL juice sample from the bottles was homogenized, and the product was distributed in sterile threaded tubes, with 10 mL per tube.

To add *B. coagulans* BC30 (GanedenBC30®), 10 g of probiotic powder containing 1.0 x 10^9 spores for 100 mL of juice was used to obtain 10^7 viable spores, which were then homogenized and also distributed in sterile threaded tubes of 10 mL each. In the juices obtained from the first stage, there was an application of 96 ± 3°C/35 seconds of thermal treatment was applied to simulate the time and temperature used by the industry.

In the second stage, *B. clausii* (Enterogermina®, Italy) was selected for continuity of the experiments and, as mentioned above, 10^9 variable spores were added to the juices. After homogenizing the juice in the bottle, the product was distributed in sterile threaded tubes of 10 mL each, which were divided and identified as untreated and heat-treated juices for two time-temperature binominal (96 ± 3°C/35 seconds and 80 ± 1 °C/10 minutes). At the end of the heat treatments, half of the samples from both treatments were stored at 25°C, and the other half were stored under refrigeration (5°C) for 60 days.

Thermal Treatments Used

Industrial Thermal Treatment Simulation

To simulate industrial thermal treatment, with temperature variation, a water bath was used to reach the temperature of 96°C along with the COD digestive block (SL20 - SOLAB, Piracicaba, São Paulo, Brazil) for cooling at 85°C and 70°C. Then, after adding probiotics to the juices, the latter underwent pasteurization, with the time-temperature binomial similar to those described by Kunitake *et al*. (7). The pasteurization was carried out at 96 ± 3 °C/35s, with subsequent cooling at 85 °C/2.5 min and 70 °C/2.5 min. After reaching 70°C, juices were cooled to 25°C in cold water (± 8 °C), simulating the time and temperature used in the industrial process.

At the end of the first stage, juice samples were stored in an oven at 37ºC to perform pH analysis and the assessment of probiotics used over the course of six days at 37ºC to accelerate chemical degradation and/or physical changes in the product, characterizing the accelerated shelf-life test. Non-thermally treated juices were made from the product added with *B. coagulans* or *B. clausii* that were not subjected to thermal treatment.

On the other hand, at the end of the second stage, the juice samples were stored at 25ºC and under refrigeration at 5ºC for 60 days. During this time, physical chemical analysis was conducted along with the assessment of *B. clausii* spore viability in thermally treated and non-treated juices.

Alternative thermal treatment to the industrial one

This treatment was only used in the second stage. After adding probiotics to the juices, these underwent thermal treatment for 10 minutes with subsequent cooling to 25°C in cold water, similar to the one performed by Faraoni *et al.* (8). To reach the temperature of 80°C, a digesting block (SL20 – SOLAB, Piracicaba, São Paulo, Brazil) was used. The time count for the thermal treatment began when the bottles reached 80°C, using a bottle to control the temperature with a thermometer. The average time to reach the temperature of 80ºC was 10 minutes and 10 seconds (± 2 minutes).

After the thermal treatment, physical-chemical analyses were performed. Moreover, the determination of the viability of *B. clausii* spores in the juices was carried out, with subsequent storage of the samples at 25°C and under 5°C refrigeration, over the lapse of 60 days. Non-thermally treated juices added with *B. clausii* were also analyzed and stored under the same conditions.

Physical Chemical Evaluation of Juices

The determination of the pH was determined using a digital pH meter (Tecnopon NT PHM, Piracicaba, São Paulo, Brazil) (9). On the first stage, the pH was determined over the course of the six days of storage at 37 °C. The analyses were performed on days 0 and 6 for the juices not subjected to thermal treatment, and on days 0, 2, 4, and 6 days for the thermally treated juices.

In the second stage, the analysis of pH, acidity and total soluble solids (ºBrix) was performed on days 0, 20, and 60 for both non-treated juice samples and those thermally treated (industrial thermal treatment and alternative one), stored at 25°C and under refrigeration at 5°C.

The acidity was assessed by potentiometric volumetry and converted to citric acid percentage. A mixture of 10 g of the sample, dissolved in 100 mL of distilled water, was titrated with a standard solution of NaOH 0.1 mol/L (Impex, Diadema, São Paulo, Brazil) until reaching the pH value of 8.2–8.4, which is equivalent to the turning point of phenolphthalein (10).

The total soluble solids were analyzed by refractometry using a digital refractometer (Atago®, Ribeirão Preto, São Paulo, Brazil) according to manufacturer's instructions, and methodology described by Godshall (11).

Viability of *B. clausii* and *B. coagulans* BC30 in Organic Mango Juices

To analyze probiotic viability, a serial dilution was performed using 1 mL of homogenized mango juice in 9 mL of peptone saline solution, containing 0.85% of NaCl (Synth, Diadema, São Paulo, Brazil), and 0.1% of peptone (Acumedia, Michigan, USA), thus obtaining a 10^{-1} dilution. Serial dilutions (10^{-1} a 10^{-6}) were plated using the pour plate technique, with the addition of 1 mL of each dilution, and about 20 mL TSA in Petri plates. The plates were kept at 37°C for 72 hours, and after the incubation, colony-forming units (CFU) were calculated.

The viability assessment of *B. coagulans* BC30 and *B. clausii* in first-stage juices was performed on days 0 and 6 for non-thermally treated juices and on days 0, 2, 4, and 6 for thermally treated ones.

In the second stage, the counting of *B. clausii* was determined on days 0, 30, and 60 of storage at 25°C and 5°C for juice samples that were not thermally treated and for those thermally treated (industrial thermal treatment and the alternative one, respectively, under 96 ± 3 °C/35 s and 80 ± 1 °C for 10 minutes).

Evaluation of *B. clausii* Resistance to Simulated *In Vitro* Gastrointestinal Digestion

The *in vitro* simulation of gastrointestinal conditions was carried out in non-thermally treated mango juices from the second stage. It was performed according to the methodology described by Bedani, Rossi, and Saad (12) on days 0 (after addition of *B. clausii* to the juice), 30, and 60 of storage at 25°C and under refrigeration at 5°C. Initially, the gastric phase was simulated by preparing a 10^{-1} dilution of the sample in 0.85% saline solution, using 10 mL aliquots transferred to 100 mL dilution bottles. The pH was adjusted to 2.0 – 2.5 with 1 mol/L HCl (Impex, Diadema, São Paulo, Brazil), 3 g/L pepsin (isolated from porcine gastric mucosa, Sigma-Aldrich), and 0.9 mg/L of lipase (G Amano lipase, isolated from *Penicillium Camemberti*, Sigma-Aldrich), respectively. Then, all samples were incubated at 37°C for 2 at 150 rpm in a shaking incubator (Tecnal TE – 424, Piracicaba, São Paulo, Brazil).

After the incubation period, enteric stage I (corresponding to the small intestine) was simulated, in which the pH was adjusted to 4.5 – 5.5, using a pH 12.0 sodium phosphate solution. This solution was prepared from a mixture containing 150 mL NaOH 1 mol/L (Vetec, Duque de Caxias, Rio de Janeiro, Brazil), 14 g $NaH_2PO_4.2H_2O$ (Vetec, Duque de Caxias, Rio de Janeiro, Brazil) and distilled water until it reached 1000 mL, along with bile (bovine bile, Sigma-Aldrich) and pancreatin (porcine pancreas isolated pancreatin, Sigma-Aldrich), at concentrations of 10.0 g/L and 1.0 g/L, respectively. The bottles were incubated again for 2 hours, under the conditions previously described.

Afterward, enteric stage II (corresponding to the large intestine) was simulated, adjusting the pH to 6.8 – 7.2, using the same alkaline solution containing bile (10.0 g/L) and pancreatin (1.0 g/L). Subsequently, a third incubation period was conducted under the same conditions, resulting in an assay duration of six hours. At the end of each incubation cycle (2, 4, and 6 hours), which corresponded to the simulation of gastric and enteric stages I and II, a deep plating on TS was performed to assess probiotic viability. The Petri plates were incubated at 37 ± 1ºC for 72 hours, and the results of the assessment were measured in log CFU/mL.

Statistical analyses

The procedures were carried out in three independent repetitions, and the results obtained from them were expressed as the mean ± standard deviation. The unidirectional analysis of variance (ANOVA) was performed to compare the effects of the different treatments. The Tukey test was used to assess significant differences between the treatments at a 5% significance level ($p < 0.05$). The statistical analyses were carried out using the software Statistica (Statistical Analysis System - SAS Institute, Cary, NC, USA; version 9.2).

Results and Discussion

ph And Viability of *B. Clausii* and *B. Coagulans* in Organic Mango Juice after Thermal Treatment at 96 °C/35 s throughout 6 Days of Accelerated Shelf Life at 37°C

There was a difference in pH between juices containing *B. clausii* and *B. coagulans* ($p < 0.05$) for each analyzed time during the accelerated shelf-life test. However, no significant pH difference was observed ($p > 0.05$) in juices that underwent the same treatment during the storage time (Fig. 1). The juices containing probiotics and not thermally treated also did not present pH variation ($p > 0.05$) between day 0 (*B. clausii* 3.93 ± 0.12; *B. coagulans* 4.49 ± 0.03) and day 6 (*B. clausii* 3.92 ± 0.08; *B. coagulans* 4.50 ± 0.18).

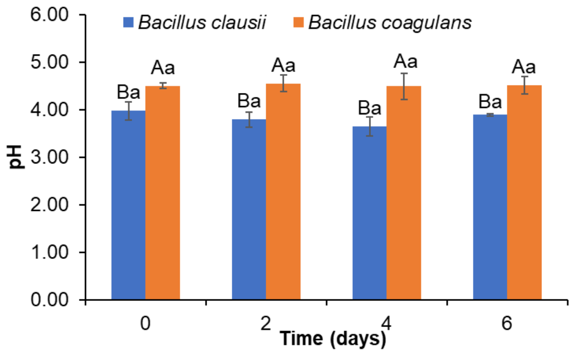

Fig 1. pH of organic mango juice after heat treatment at 96 °C/35 s during six days of accelerated shelf life at 37°C. Different uppercase letters indicate a significant difference between samples at the same time, while different lowercase letters indicate a difference between times for the same sample, using Tukey's test at a 5% probability level ($p < 0.05$).

These results demonstrate probiotic mango juices' pH stability throughout their accelerated shelf life, under extreme storage conditions, which indicates that the addition of probiotic bacilli is viable. Furthermore, this technique is believed to enable a simulation study under storage conditions similar to those that these products would undergo once available in the market.

Poshadri *et al.* (6) highlight that the spores can bear high-temperature environments, acid conditions and salinity, and that makes their usage promising for the production of new foods with stability throughout their shelf life, such as the juice analyzed in the present essay.

A difference in viability ($p < 0.05$) between juices containing *B. clausii* and *B. coagulans* was observed only after thermal treatment on day 0 (Fig. 2). There was a reduction ($p < 0.05$) of viability of *B. clausii* in juices after thermal treatment, but the counting kept stable ($p < 0.05$), reaching the end of accelerated shelf life at 4.29 log CFU/mL. However, as regards the juices containing *B. coagulans*, it was observed that there was a reduction in the count ($p < 0.05$) until day 4 of storage (Fig. 2), leading to a count of 3.60 log CFU/mL on day 6.

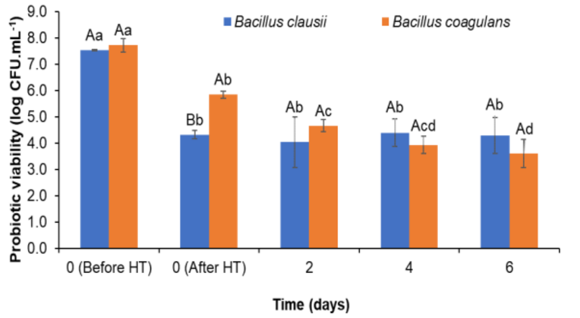

Fig 2. Viability of *Bacillus clausii* and *Bacillus coagulans* in organic mango juice after heat treatment at 96 °C/35 s during 6 days of accelerated shelf life at 37 °C. Different uppercase letters indicate a significant difference between samples at the same time, while different lowercase letters indicate a difference between times for the same sample, using Tukey's test at a probability level of 5% ($p < 0.05$).

The study conducted by the present research group on *B. coagulans* demonstrates sustenance or little alteration of this probiotic's viability after the storage period, as observed in the present study (13).

In non-thermally treated juices, a reduction in the viability ($p < 0.05$) of both probiotic microorganisms was observed over time. The magnitude of the difference for *B. clausii* was small: a reduction of 0.26 log CFU/mL (7.54 ± 0.03 to 7.28 ± 0.04). On the contrary, as for *B. coagulans*, the difference over time was of 1.15 log CFU/mL (7.72 ± 0.26 to 6.57 ± 0.35). Adebayo-Tayo, Olomitutu, and Adebami (2), when assessing probiotic mango juice with *Pediococcus pentosaceus* and *Pediococcus acidilactici* stored at 4ºC and 25 °C for 4 weeks, observed a reduction in the viability during the storage time, which indicates that the major benefits of probiotic juice can be obtained in the first week of storage.

However, Palencia-Argel *et al.* (14) highlight that the viability of probiotic microorganisms is generally affected by storage temperature, suggesting that refrigeration can extend these microorganisms' survival in beverages and fruit juices, while exposure to higher temperatures can cause adverse effects, such as those observed in this study.

In the international market, where probiotic juices are widely commercialized, it's possible to observe that some brands recommend storage under beverage refrigeration. For example, "Garden of Flavor, Surja Organic e Pressed Juicery" provides some juices added with *B. coagulans,* and "GoodBelly Probiotics", which commercializes juices with *Lactobacillus plantarum* 299V. In this way, it is believed that refrigerated storage can contribute to these microorganisms' continuation, and further studies on tropical mango juice are needed.

Physical Chemical Features of Mango Juice Containing *B. Clausii* after Simulated Industrial Thermal Treatment or the Alternative Method

There was no pH difference ($p > 0.05$) among mango juices containing *B. clausii* from different treatments during the 60 days of storage both for samples stored at ambient temperature and those kept under refrigeration (Fig. 3A). pH stability is a desirable result, since it can interfere on the total number of viable probiotic cells in fruit matrices. According to Cosme, Inês, and Vilela (15), the low pH of fruit juices is considered one of the main disadvantages for the counting and activity of probiotic bacteria.

As for the acidity figures, it was verified that the non-thermally treated juice kept at 5ºC and at 25ºC differed ($p < 0.05$) from those thermally treated at day 0 (Fig. 3B). The development of acidity is common when juices are subjected to thermal treatment due to the organic acid formation, and this may have occurred in the present study. On the other hand, the storage temperature did not influence ($p > 0.05$) juice acidity (Fig. 3B).

No alteration was observed ($p > 0.05$) in the total soluble solids of juices from different treatments stored at different temperatures (Fig. 3C), indicating that the probiotic bacteria did not cause physical and chemical alteration in the juices.

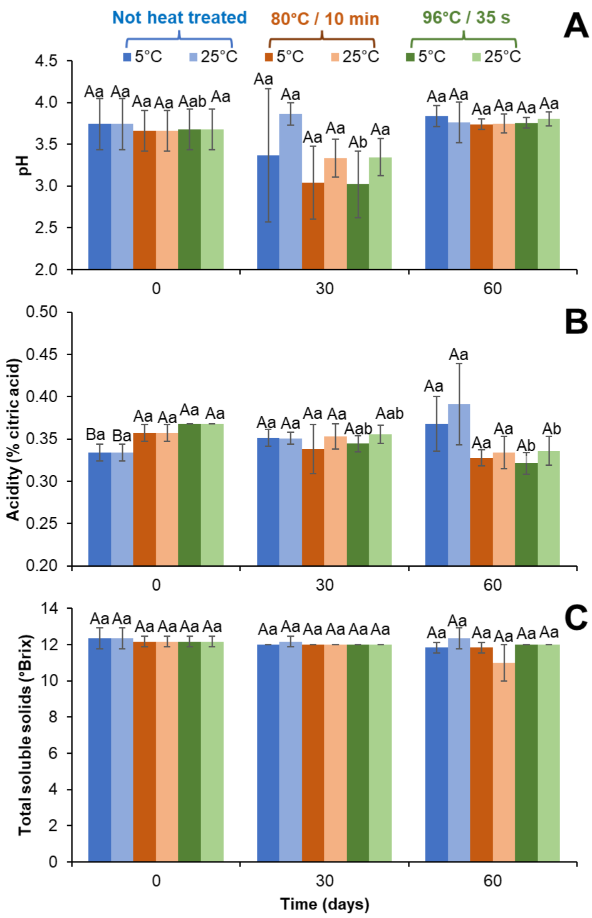

Fig 3. pH (A), acidity (B), and total soluble solids (C) of organic mango juice containing *B. clausii* subjected to different heat treatments (80 °C/10 min and 96 °C/35 seconds) during a 60-day storage period at 5 °C and 25 °C. Different uppercase letters indicate a significant difference between samples at the same time, while different lowercase letters indicate a difference between times for the same sample, using Tukey's test at a probability level of 5% ($p < 0.05$).

Viability and *In Vitro* Gastrointestinal Resistance *of B. Clausii* in Mango Juice after Simulated Industrial Thermal Treatment or the Alternative Method

The viability of *B. clausii* was not influenced ($p > 0.05$) by storage temperature (Fig. 4). However, the simulated industrial thermal treatment caused a reduction ($p < 0.05$) in *B. clausii* viability. These results reinforce the findings of Palencia-Argel *et al.* (14), who highlighted that the variables related to processing methods, especially thermal treatments, have an impact on probiotic counting.

The juices subjected to simulated industrial thermal treatment, with pasteurization at 96 ± 3°C/35 seconds, and then cooled at approximately 70°C for about 5 minutes, showed a considerable reduction in viability when compared to those non-thermally treated ($p < 0.05$), with figures higher than 2.0 log CFU/mL (Fig. 4).

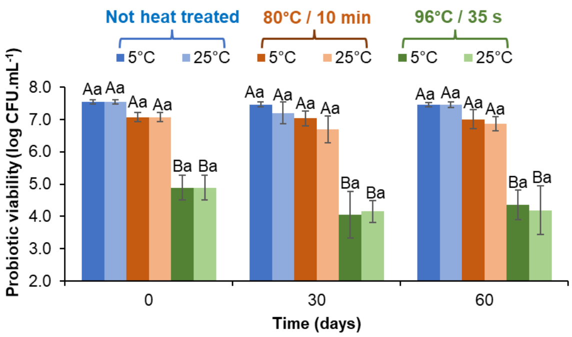

Fig 4. Viability of *B. clausii* in organic mango juice subjected to different heat treatments (80 °C/10 min and 96 °C/35 seconds) during a 60-day storage period at 5 °C and 25 °C. Different uppercase letters indicate a significant difference between samples at the same time, while different lowercase letters indicate a difference between times for the same sample, using Tukey's test at a probability level of 5% ($p < 0.05$).

Almada-Érix *et al.* (16), when assessing pasteurization at 95ºC for 30 seconds in orange juice with probiotic bacilli, also found a reduction at a range of 0.43–2.5 log CFU/mL. In the orange juice, pasteurization caused a larger viability reduction of *B. coagulans* BC30 in comparison to *B. subtilis* Bn1, showing the distinct resistance of microorganisms to thermal processing. Nonetheless, the authors highlight that the loss of viability observed in probiotic bacilli is still smaller compared to other non-spore-forming bacteria.

The usual portion of fruit juice consumption, according to Normative Instruction 75/2020, is 200 mL (17), which enables a proper supply of > 10^6 CFU/mL of probiotics from the present study, even after a viability reduction following thermal treatments.

As for the *in vitro* simulation of gastrointestinal conditions of mango juice containing *B. clausii*, non-thermally treated and stored at 5ºC and 25 °C showed excellent probiotic performance once viability was greater than 7.0 log CFU/mL throughout stages tested during 60 days (Fig. 5). The final count of *B. clausii* on enteric stage II, the final portion of the gastrointestinal tract was > 7.08 CFU/mL (Fig. 5). This was enough to increase defense in the host organism, suggesting that organic mango juice stored at ambient temperature is a promising matrix.

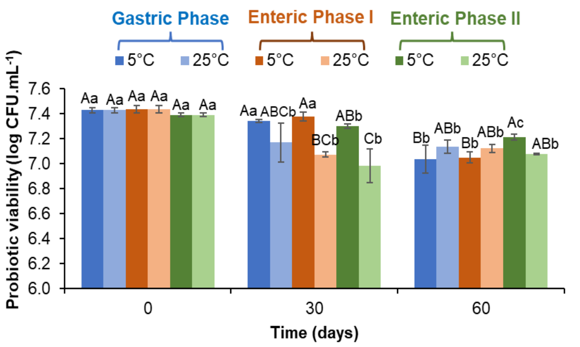

Fig 5. Viability of *B. clausii* after *in vitro* gastrointestinal digestion test in non-heat-treated mango juice during a 60-day storage period at 5 °C and 25 °C. Different uppercase letters indicate a significant difference between samples at the same time, while different lowercase letters indicate a difference between times for the same sample using Tukey's test at a probability level of 5% ($p < 0.05$).

Some studies indicate that mango is a promising matrix of non-lactic probiotic formulations, such as Moreira *et al.* (18), when developing Mango Ubá and Juçara juice, with addition of *Lactobacillus rhamnosus* GG; Oliveira *et al.* (19) with mixed mango juice and carrot as vehicle of probiotic lactobacilli; and Mousanejadi *et al.* (20) with the addition of *L. casei* UK 318 in mango juice.

In the literature, no studies were found about consumers' perception and behavior towards the administration form of probiotics. Nevertheless, considering the high acceptability and consumption of juices by the population, it is believed that having it as a matrix is also a positive way to make ingestion easier. In this case, it is worth highlighting that groups with major vulnerabilities, such as seniors and children, can also show greater difficulty and resistance to the ingestion of capsules and other forms of administration with an unpleasant taste. This is another relevant factor for choosing mango juice, which has a pleasant taste, as a vehicle for these microorganisms.

B. clausii is widely used for the treatment and prevention of diarrhea (21, 22, 23*)*, a clinical picture that requires attention to hydration. Thus, combining this probiotic with a product that can also help with this matter is a very promising alternative to the market.

Conclusion

The simulation of thermal industrial treatment in juices, after the addition of probiotic bacilli, promoted a viability reduction during the accelerated shelf life, this being more evident for *B. coagulans* BC30. The consumption of 100 mL of organic mango juice containing *B. clausii*, and that was thermally treated, provides more than 6.0 log CFU/mL of probiotic at the end of accelerated shelf life. The accelerated shelf-life test carried out in the first stage proved to be viable in simulating the storage conditions to which juices are subjected before consumption.

Mango juices added with *B. clausii*, submitted to different thermal treatments and stored for 60 days in ambient temperature and under refrigeration, presented good stability regarding pH and total soluble solids. The viability of *B. clausii* in juices was not altered when these were stored at ambient or refrigeration temperature. Although the industrial thermal treatment promoted a viability reduction of *B. clausii* compared to the non-thermally treated juice.

The *in vitro* simulation of the gastrointestinal conditions of organic mango juice containing non-thermally treated *B. clausii* and stored at 5 *in vitro* and 25°C has evidenced an excellent performance as regards the probiotic. Concerning the viability, it was greater than 7.0 log CFU/mL in the final portion of the simulated gastrointestinal tract for 60 days. The counting suggests that the organic mango juice stored at ambient temperature is a promising matrix for *B. clausii*.

Acknowledgements

The authors are grateful to the Federal Institute of Southeast Minas Gerais for their financial support, and to the GanedenBC30®/Kerry for the donation of *B. coagulans* BC30.

References

Acosta-Rodríguez-Bueno, C. P.; Abreu, A. T. A.; Guarner, F.; Guno, M. J. V.; Pehlivanoğlu, E.; Perez III, M. *Bacillus clausii for Gastrointestinal Disorders: A Narrative Literature Review*, Advances in Therapy, v. 39, p. 4854-4874, 2022. Available in: https://doi.org/10.1007/s12325-022-02285-0

Adebayo-Tayo, B. C.; Olomitutu, F. O.; Adebami, G. E. *Production and evaluation of probioticated mango juice using Pediococcus pentosaceus and Pediococcus acidilactici during storage at different temperature*. Journal of Agriculture and Food Research, v. 6, p. 100202, 2021. Available in: https://doi.org/10.1016/j.jafr.2021.100202

Almada-Érix, C. N.; Almada, C. N.; Pedrosa, G. T. S.; Lollo, P. C.; Magnani, M.; Sant'ana, A. S. *Development of a semi-dynamic in vitro model and its testing using probiotic Bacillus coagulans GBI-30, 6086 in orange juice and yogurt*. Journal of Microbiological Methods, v. 183, p. 106187, 2021. Available in: https://doi.org/10.1016/j.mimet.2021.106187

Bedani, R.; Rossi, E.A.; Saad, S. M. I. *Impact of inulin and okara on Lactobacillus acidophilus La-5 and Bifidobacterium animalis Bb-12 viability in a fermented soy product and probiotic survival under in vitro simulated gastrointestinal conditions*. Food Microbiology, v. 34, p. 382-389, 2013. Available in: https://doi.org/10.1016/j.fm.2013.01.012

Brasil. *Requisitos técnicos para a declaração da rotulagem nutricional dos alimentos embalados*. Instrução Normativa No 75 de 8 de outubro de 2020 da Agência Nacional de Vigilância Sanitária. Diário Oficial da União (DOU) de 09 de outubro de 2020.

Calligaris, S.; Manzocco, L.; Anese, M.; Nicoli, M. C.; *Accelerated shelf life testing*. In: GALANAKIS, C. M. (ed.). Food Quality and Shelf Life, New Delhi: Academic Press, 2019. Chapter 12, p. 359-392. Available in: https://doi.org/10.1016/B978-0-12-817190-5.00012-4

Castro, J. A.; Kesavelu, D.; Lahiri, K. R.; Chaijitraruch, N.; Chongsrisawat, V.; Jog, P. P. *Recommendations for the adjuvant use of the poly-antibiotic–resistant probiotic Bacillus clausii (O/C, SIN, N/R, T) in acute, chronic, and antibiotic-associated diarrhea in children: consensus from Asian experts.* Tropical Diseases, Travel Medicine and Vaccines, v. 6, p. 1-15, 2020. Available in: https://doi.org/10.1186/s40794-020-00120-4

Clark, D.H. *Fruits and Fruit Products*. In: JATIMER Jr. G.W. (ed.). Official Methods of Analysis of the Association of Official Analytical Chemists international, Rockville: AOAC International: 2016. p. 1-39.

Cosme, F.; Inês, A.; Vilela, A. *Consumer's acceptability and health consciousness of probiotic and prebiotic of non-dairy products*. Food Research International, v. 151, p. 110842, 2022. Available in: https://doi.org/10.1016/j.foodres.2021.110842

Ellis, C. *Vegetable Products, Processed*. In: JATIMER Jr. G.W. (ed.). Official Methods of Analysis of the Association of Official

Analytical Chemists international, Rockville: AOAC International: 2016. p. 1-14.
Faraoni, A.S.; Ramos, A.M.; Stringheta, P.C.; Laureano, J. *Efeito dos métodos de conservação, tipos de embalagem e tempo de estocagem na coloração de polpa de manga "Ubá" produzida em sistema orgânico*. Revista Ceres, v. 55, p. 504-511, 2008. Available in: https://www.redalyc.org/articulo.oa?id=305226820001
Ghelardi, E.; Mazzantini, D.; Celandroni, F.; Calvigioni, M.; Panattoni, A.; Lupetti, A.; Bois De Fer, B.; Perez, M. *Analysis of the microbial content of probiotic products commercialized worldwide and survivability in conditions mimicking the human gut environment*. Frontiers in Microbiology, v. 14, p. 1127321, 2023. Available in: https://doi.org/10.3389/fmicb.2023.1127321
Godshall, M.A. *Sugars and Sugar Products*. In: JATIMER Jr. G.W. (ed.). Official Methods of Analysis of the Association of Official Analytical Chemists International, Rockville: AOAC International: 2016. p. 1-53.
iiKunitake, M.; Ditchfield, C.; Silva, C.; Petrus, R. *Effect of pasteurization temperature on stability of an acidified sugarcane juice beverage*. Ciência e Agrotecnologia. v. 38, p. 554-561, 2014. Available in: https://doi.org/10.1590/S1413-70542014000600004
Moreira, R. M.; Martins, M. L.; Leite Júnior, B. R. C.; Martins, E. M. F.; Ramos, A. M.; Cristianini, M.; Campo, A. N. R.; Stringheta, P. C.; Silva, V. R. O.; Canuto, J. W.; Oliveira, D. C.; Pereira, D. C. S. *Development of a juçara and Uba mango juice mixture with added Lactobacillus rhamnosus GG processed by high pressure*. LWT - Food Science and Technology, v. 77, p. 259-268, 2017. Available in: https://doi.org/10.1016/j.lwt.2016.11.049
Mousanejadi, N.; Barzegar, H.; Behbahani, B. A.; Jooyandeh, H. *Production and evaluation of a functional fruit beverage consisting of mango juice and probiotic bacteria.* Journal of Food Measurement and Characterization, v. 17, p. 3240-3253, 2023. Available in: https://doi.org/10.1007/s11694-023-01862-3
Oliveira, P. M.; Leite Júnior, B. R. C.; Martins, E. M. F.; Martins, M. L.; Vieira, E. N. R.; Barros, F. A. R. *Mango and carrot mixed juice: a new matrix for the vehicle of probiotic lactobacilli.* Journal of Food Science and Technology, v. 58, p. 98-109, 2021. Available in: https://doi.org/10.1007/s13197-020-04518-y
Palencia-Argel, M.; Rodríguez-Villamil, H.; Bernal-Castro, C.; Díaz-Moreno, C.; Fuenmayor, C. A. *Probiotics in anthocyanin-rich fruit beverages: research and development for novel synbiotic products*. Critical Reviews in Food Science and Nutrition, v. 64, p. 110-126, 2022. Available in: https://doi.org/10.1080/10408398.2022.2104806
Pirozzi, C.; Opallo, N.; Coretti, L.; Lama, A.; Annunziata, C.; Comella, F. *Alkalihalobacillus clausii (formerly Bacillus clausii) spores lessen antibiotic-induced intestinal injury and reshape gut microbiota composition in mice*. Biomedicine & Pharmacotherapy, v. 163, p. 114860, 2023. Available in: https://doi.org/10.1016/j.biopha.2023.114860
Poshadri, A.; Deshpande, H. W.; Khodke, U. M.; Katke, S. D.; *Bacillus coagulans and its Spore as Potential Probiotics in the Production of Novel Shelf- Stable Foods*. Current Research in Nutrition & Food Science, v. 10, p. 858-870, 2022. Available in: https://dx.doi.org/10.12944/CRNFSJ.10.3.4
Soares, M. B.; Martinez, R. C. R.; Pereira, E. P. R.; Balthazar, C. F.; Cruz, A. G.; Ranadheera, C. S.; Sant'Ana, A. S. *The resistance of Bacillus, Bifidobacterium, and Lactobacillus strains with claimed probiotic properties in different food matrices exposed to simulated gastrointestinal tract conditions*. Food research international, v. 125, p. 108542, 2019. Available in: https://doi.org/10.1016/j.foodres.2019.108542
Tireki, S. *A review on packed non-alcoholic beverages: Ingredients, production, trends and future opportunities for functional product development*. Trends in Food Science & Technology, v. 112, p. 442-454, 2021. Available in: https://doi.org/10.1016/j.tifs.2021.03.058
Vivek, K.; Mishra, S.; Pradhan, R. C.; Nagarajan, M.; Kumar, P. K.; Singh, S. S.; Manvi, D.; Gowda, N. N. *A comprehensive review on microencapsulation of probiotics: technology, carriers and current trends*. Applied Food Research, v. 3, p. 100248, 2023. Available in: https://doi.org/10.1016/j.afres.2022.100248

RECyT
Year 27 / Nº 43 / 2025 /
DOI: https://doi.org/10.36995/j.recyt.2025.43.007

Phytochemical Profiling of *Clusia valerioi* (Standl.) Floral Resin and Its Correlation with the Chemical Composition of Propolis from Southern Costa Rica

Quimioprospección de la resina de la flor de *Clusia valerioi* (Standl.) y su relación con la composición química de propóleos de una región de la zona sur de Costa Rica

Segura-Víquez, Andrea[1]; Soto-Fallas, Roy M.[1, *]; Borbón-Alpízar, Henry[1]; Umaña-Rojas, Eduardo[2]; Zamora-Fallas, Gabriel[2]; Sánchez-Chaves, Luis[2]; Fallas-Matamoros, Natalia[2]; Montenegro-Hidalgo, Víctor[3]; Alfaro-Alarcón, Alejandro[3]; Guevara-González, Mariana[3]; Romero-Vega, Luis[3]; Loaiza-Montoya, Randall[4]; Picado-Canales, Natalin[4, 5]; Barrantes-Murillo Erika[4, 5]

1- Laboratorio de Productos Naturales y Ensayos Biológicos (LAPRONEB), Escuela de Química, Facultad de Ciencias Exactas y Naturales. Universidad Nacional de Costa Rica.
2- Centro de Investigaciones Apícolas Tropicales (CINAT). Facultad de Ciencias de la Tierra y el Mar. Universidad Nacional de Costa Rica.
3- Escuela de Medicina Veterinaria, Facultad de Salud. Universidad Nacional de Costa Rica.
4- Centro Nacional de Biotecnología (CENIBiot). Costa Rica.
5- Escuela de Biología, Facultad de Ciencias Exactas y Naturales. Universidad Nacional de Costa Rica.
* E-mail: roy.soto.fallas@una.cr

Received: 15/04/2024; Accepted: 16/04/2025

Abstract
Propolis are resinous byproducts produced by bees, known for their wide range of bioactive properties. The chemical composition of propolis is closely linked to the botanical environment surrounding the hive. *Clusia valerioi* (Standl.), a plant species endemic to Costa Rica, is commonly found in the country's southern region and produces floral resins that are collected by bees for propolis production. This ecological relationship suggests that chemical traceability between *C. valerioi* floral resins and propolis produced in nearby apiaries is feasible.
In this study, ethanolic extracts from propolis samples collected at eight apiaries, resin loads transported by forager bees, and floral resin samples from *C. valerioi* at four sites near two of these apiaries were analyzed using high-performance thin-layer chromatography (HPTLC). The analysis revealed three chemical markers—referred to as compounds A, B, and C—that support the traceability of chemical constituents from floral resin to propolis. Compound A was identified as a terpene derivative, while compound C was determined to be a flavonoid derivative (specifically a flavonol or flavanone). Compound B was isolated and identified as a polyprenylated polycyclic benzophenone, and was conclusively characterized as nemorosone based on proton (^{1}H-NMR) and carbon-13 (^{13}C-NMR) nuclear magnetic resonance spectra.

Keywords: Propolis; *Apis mellifera*; *Clusia valerioi* (Standl.); HPTLC; Nemorosone.

Resumen
Los propóleos son subproductos apícolas elaborados por abejas del género *Apis mellifera* y de otras especies, que presentan muchos tipos de bioactividad. Su origen y composición puede relacionarse con el entorno botánico del sitio de anidación de las abejas, tal es el caso de la planta *Clusia valerioi* (Standl.), especie endémica de Costa Rica, cuya flor produce una resina utilizada por las abejas que la visitan para la producción de propóleo. Lo anterior implica la posibilidad de establecer una trazabilidad de la composición química de la resina de la flor de *C. valerioi* y de los propóleos recolectados de apiarios ubicados en la Zona Sur de Costa Rica, en términos de relacionar la presencia de compuestos tipo flavonoides, ácidos fenólicos y del tipo benzofenonas policíclicas polipreniladas (nemorosoma) en ambos tipos de matrices, para la identificación de posibles biomarcadores activos para futuros estudios. Extractos etanólicos de muestras de propóleo de ocho apiarios visitados y extractos etanólicos de resina floral de *C. valerioi* de cuatro sitios cercanos a dos de estos apiarios, muestreados en la zona de Coto Brus (Costa Rica), fueron analizados y derivatizados con técnicas de HPTLC. Se estableció la presencia de 3 marcadores químicos importantes en el análisis (denominados como compuestos A, B y C), a partir de espectros de resonancia magnética nuclear de protones (^{1}H-NMR) y carbono-13 (^{13}C-RMN), espectros de absorción y cromatografías para 16 extractos de propóleos, resinas y flores *C. valerioi*. Se identificó el compuesto A como un compuesto derivado de los terpenos, el compuesto B como nemorosona y el compuesto C como un derivado de los flavonoides del tipo flavonol o flavonona.

Palabras clave: Propóleos; *Apis mellifera*; *Clusia valerioi* (Standl.); HPTLC; Nemorosona.

Introduction

Propolis are resinous substances produced by honeybees (*Apis mellifera*) from plant exudates collected in the vicinity of the apiaries (defined as two or more hives). Bees manipulate these exudates using their mandibles, enriching them with enzymes from their mandibular glands, and then deposit the material inside the hive, where it is mixed with small amounts of sugars and beeswax secreted by the bees themselves (Chaillou et al., 2004; Fernández, 2008; Salas, 2005). This resulting product, known as propolis, serves not only as a protective material for the hive's internal walls and entrance but also functions as a chemical defense mechanism, forming barriers that inhibit the growth of fungi and bacteria (Vargas et al., 2018; Rossana et al., 2010). Chemically, propolis is a complex mixture composed of approximately 55% aromatic balsams and resins, 30% waxes, 10% essential oils, 5% pollen grains, and other minor constituents.

Among the principal bioactive compounds found in propolis are flavonoids, including flavones such as apigenin, and flavonols such as quercetin and kaempferol. These are commonly present in European propolis derived from Populus nigra species collected by *Apis mellifera* bees (Umaña, 2013). Overall, approximately 38 types of flavones, 12 benzoic acid derivatives, 14 derivatives of cinnamyl alcohol and cinnamic acid (including 3,5-diprenyl-4-hydroxycinnamic acid, also known as artepillin C, found in Brazilian green propolis), 12 various alcohols, ketones, and phenols, 7 terpenes, 11 steroids, 7 sugars, and 2 amino acids have been identified. Within this extensive set of metabolites, flavonoids, phenolic acids, and their esters stand out for their well-documented pharmacological activity (Tolosa & Cañizares, 2002; Umaña, 2013).

Propolis has been shown to possess antimicrobial, antifungal, antitumor, anti-inflammatory, hepatoprotective, antidiabetic, cardioprotective, and immunomodulatory properties. From a therapeutic standpoint, these effects are primarily attributed to the presence of polyphenolic compounds, including flavonoids and phenolic acids, along with their esterified forms (Fernández-León et al., 2022). Such characteristics have generated significant scientific interest in studying both the composition of propolis and the botanical environments from which it originates. Given its broad therapeutic potential and natural origin, propolis is considered a promising candidate for the treatment of various diseases, including certain types of cancer and cardiovascular conditions (Fernández, 2008).

Ethnobotanical studies have demonstrated that certain members of the Clusiaceae family possess notable anti-inflammatory activity. Many of these species are characterized by the production of secondary metabolites such as terpenoids and polyphenols. Within this family, the genus Clusia is of particular interest, as its flowers produce a resin that is actively collected by various bee species for nest construction, where it functions as an adhesive and water-resistant protective agent within the hive (Herbert, 2021; Hochwallner & Weber, 2006; Meranti, 2015). This relationship between Clusia floral resin and its incorporation into hive architecture suggests that the resin's chemical profile may directly influence the chemical constituents of the resulting propolis. This hypothesis is supported by studies conducted in Mexico and by Cuban researchers who have observed an enhancement of the therapeutic properties of propolis derived from Clusia resins (Herrera, 2019; Monzote et al., 2011).

Clusia valerioi (Standl.) is a facultatively epiphytic tree with dark brown to black branches, native to humid, very humid, and pluvial forests along Costa Rica's Caribbean slope. It is found in the Tilarán, Central, and Talamanca mountain ranges, as well as in the plains of San Carlos, Tortuguero, the Coto Brus Valley, and the Golfo Dulce region. This species is readily distinguishable as the only member of its genus that features leaf blades (the flat, typically green portion of the leaf attached to the stem) that turn almost black upon drying. Its flowers are pink or red and exhibit anthers marked with a distinctive ring-like structure (Ley, 2013; Zwicky, 1937).

Species in the genus Clusia are notable for their production of resins rich in polyprenylated polycyclic benzophenones (notably nemorosone), which bees actively use in the synthesis of propolis (Herbert, 2021; Herrera, 2019). A total of 55 different benzophenones have been identified in this genus, occurring in flowers, fruits, stems, branches, and leaves. However, most of these compounds are concentrated in floral resins and fruits (Novais, 2016). Structurally, benzophenones can be classified into two categories: simple benzophenones, which consist of a 13-carbon skeleton featuring two aromatic rings joined by a carbonyl group, and polyprenylated benzophenones, which possess complex polycyclic frameworks with oxo bridges and isoprenyl groups (see Figure 1) (Novais, 2016; Hernández et al., 2014).

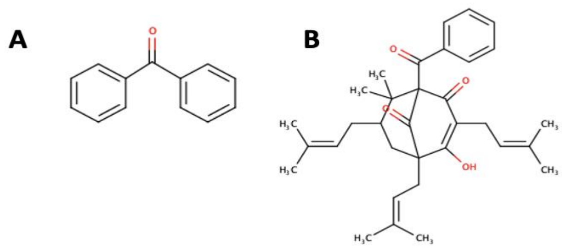

Figure 1. A) Chemical structure of a simple benzophenone. B) Chemical structure of nemorosone (a polyprenylated benzophenone). (Adapted from Novais, 2016).

In Costa Rica, three chemical types of propolis can be distinguished based on their overall composition—measured by Proton Nuclear Magnetic Resonance (^{1}H-NMR)—and their antioxidant capacity, assessed as the radical scavenging effect against 2,2-diphenyl-1-picrylhydrazyl (DPPH). Type I propolis primarily contains phenolic compounds such as n-coniferyl benzoate; Type II includes polyprenylated benzophenones like nemorosone; and Type III comprises terpenoid substances such as agatadiol. Propolis from Types I and II exhibit higher activity against the DPPH radical compared to Type III. Types I and III predominated in the North Pacific, Central Pacific, and Central Valley regions, whereas in the Southern Zone only Type II propolis was found. This Type II propolis was also present in the other studied regions but only incidentally. This geographical distribution pattern of the different propolis types was statistically significant. Based on these results, it is hypothesized that a species of Clusia sp. present in the southern region of the country plays a relevant role as a resin source for bees in propolis production (Umaña, 2013; Umaña et al., 2023).

The secondary metabolites present in the flowers of *Clusia valerioi* (Standl.) represent a source of natural products with pharmaceutical potential, both within the plant matrix and in derivative products. However, given the limited studies on this flower, the objective of the present research was to establish whether there is a correlation between polycyclic polyprenylated benzophenone compounds (such as nemorosone) and other compound classes found in the resin of *C. valerioi* flowers from the Southern Region of Costa Rica and those present in propolis from honeybee hives collected in the same area. To achieve this, the chemical nature of the main compound families in the flower resin and in the extracted propolis was determined using High-Performance Thin-Layer Chromatography (HPTLC). The results were further confirmed through melissopalynological analysis of pollen found in the most frequent resin loads transported by bees to the hives.

MATERIALS Y METHODS

Sampling Sites

Samples of flower receptacles and propolis from surrounding apiaries were collected in the Southern Region of Costa Rica, specifically during the flowering period of *Clusia valerioi* (Standl.) in this region (June–July 2022). A random sampling scheme was followed. This strategy involved the random selection of eight apiaries out of the total in the southern region, representing approximately 9% of the registered apiaries in the area (Ministry of Agriculture and Livestock, 2021). At each apiary, two propolis samples were randomly selected from different hives, yielding a total of 16 samples. Figure 2 details the coding used for the extracts prepared from the collected samples and the geographical locations of their origin.

Código de Muestra	Descripción	Provincia, Cantón, Distrito	Número de Ubicación en Mapa
CDRF 1	Propóleos de apiario	Puntarenas, Coto Brus, Pittier	5
CDRF 2	Extracto a partir de resina en corbículas de una abeja	Puntarenas, Coto Brus, Pittier	5
CDRF 3	Extracto de flores de *C. valerioi*	Puntarenas, Coto Brus, Pittier	5
CDRF 4	Extracto de flores de *C. valerioi*	Puntarenas, Coto Brus, Pittier	5
CD 02A	Extracto de flores de *C. valerioi*	Puntarenas, Coto Brus, Limoncito	10
CD 03B	Extracto de flores de *C. valerioi*	Puntarenas, Coto Brus, Limoncito	10
CD 05	Cúmulo de resinas en colmena (sin procesar)	Puntarenas, Coto Brus, Limoncito	10
CD 06A	Propóleos de apiario	Puntarenas, Coto Brus, Limoncito	10
CD 2A	Propóleos de apiario	Puntarenas, Buenos Aires, Buenos Aires	2
CD 3A	Propóleos de apiario	San José, Pérez Zeledón, Platanares	3
CD 4A	Propóleos de apiario	Puntarenas, Buenos Aires, Potrero Grande	4
CD 5A	Propóleos de apiario	Puntarenas, Coto Brus, Pittier	5
CD 7B	Propóleos de apiario	Puntarenas, Golfito, Puerto Jiménez	7
CD 8A	Propóleos de apiario	Puntarenas, Osa, Palmar	8
CD 9A	Propóleos de apiario	Puntarenas, Coto Brus, Gutiérrez Braun	9
CD 10B	Propóleos de apiario	Puntarenas, Coto Brus, Limoncito	10

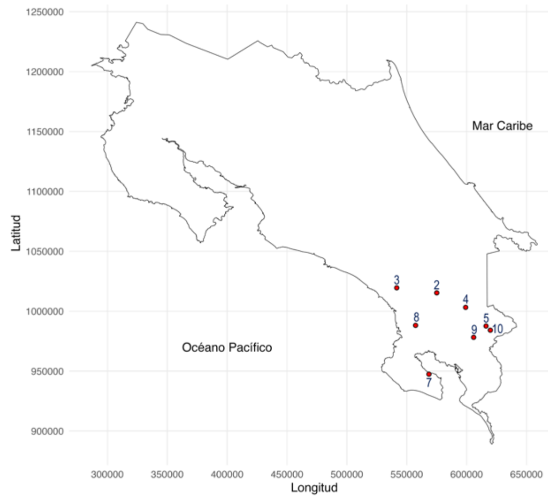

Figure 2. Coding of the analyzed extracts from flowers, resins, and propolis, along with their geographical locations based on GPS coordinates of the sampled apiaries (Global Positioning System).

Collection and Identification of Botanical Material

To determine and confirm the botanical origin of the samples, leaves, flowers, and flower buds of *Clusia valerioi* (Standl.) were collected from four sampling sites located in the localities of Santa Elena and Santa Fe de Pittier, as well as Limoncito de Coto Brus, in the province of Puntarenas. The plants sampled were located within the foraging areas of the visited apiaries. Additionally, samples of the same plant species were collected from another site outside the bees' foraging area, in the same region, but specifically in Santa Fe de Pittier.

Taxonomic verification of the material was performed by comparing the collected and pressed specimens with reference samples from the National Herbarium collection of the Department of Natural History at the National Museum of Costa Rica. This was supported by consultation of specialized literature (Hochwallner and Weber, 2006; Hochwallner et al., 2012; Alencar et al., 2020) and a final confirmation at the Juvenal Valerio Rodríguez Herbarium of the Faculty of Earth and Marine Sciences at the National University.

Collection of Resins from Bees and Apiaries

Two methods were employed to collect resin loads from bees. The first method involved collecting resin loads carried by foraging bees on their corbiculae. In this case, with the aid of forceps, the resin load was separated from ten individual bees from each of ten randomly selected hives at every apiary. The second method involved collecting recently deposited resin loads (unprocessed resin) from the upper frames of ten randomly selected hives in each apiary.

Determination of the Botanical Origin of the Resins

Resin samples or corbicular loads were sorted by color, and the frequency of each load type was established according to the dominance of a specific color relative to the total loads present. The most dominant loads were then analyzed microscopically to identify pollen grains via palynological analysis. For this, samples were stained with safranin and centrifuged in a 50% glycerol solution (v/v). The pollen grains, once precipitated and dried in an oven, were mounted on fixed slides for microscopic observation at 10X and 100X magnification. Microphotographs were then taken of the pollen grains present in the resins collected from corbiculae and hive frames. Subsequently, pollen from the anthers of identified flowers was prepared to compare and contrast the images with those of pollen from the resin samples (modified method of Erdtman, 1986).

Sample Processing and Extract Preparation

Once collected, all samples were transported at room temperature to the Tropical Apicultural Research Center (CINAT), where they were stored under refrigeration (4°C) prior to transfer and processing at the Natural Products and Biological Assays Laboratory (LAPRONEB) of the School of Chemistry at the National University (UNA).

Propolis samples were dehydrated for 24 hours in a lyophilizer. From this point, they were processed in duplicate following the methodology described by Umaña (2013). The samples were then pulverized using a mortar, and 400 mg of each were weighed on an analytical balance and placed into separate test tubes. Each sample was extracted with 10.0 mL of methanol (99.9%, Sigma-Aldrich) and subjected to ultrasonic bath treatment for 15 minutes at room temperature. Samples were subsequently centrifuged at 5000 rpm for 5 minutes at room temperature. The supernatants were concentrated, dispensed into capped vials, and stored refrigerated until use.

Samples from the flower receptacles of *C. valerioi* (Standl.) and resin samples were macerated in methanol (100%, Sigma Aldrich) in triplicate. These extracts were then concentrated under vacuum at 40°C using a rotary evaporator and subsequently refrigerated. Solutions were prepared at a concentration of 2 mg/mL from the concentrated extracts of the flowers, resin from a bee's corbicula, unprocessed resin obtained from hives, and the sampled propolis.

High-Performance Thin-Layer Chromatography (HPTLC)

High-Performance Thin-Layer Chromatography analyses were conducted using a CAMAG HPTLC system located at CINAT, National University (UNA). The system consisted of an ATS 4 Automatic TLC Sampler, ADC 2 Automatic Developing Chamber, Visualizer imaging system, Derivatizer, TLC Plate Heater, TLC Scanner 4 densitometer, and a computer running CAMAG VisionCATS 2.5 software for data management.

The stationary phase used was HPTLC silica gel 60 F254 plates, sized 20 cm × 10 cm on glass support (Merck). Aliquots of each sample, ranging from 1 to 20 µL, were applied to each plate using the ATS 4 sampler (15 samples per plate). Samples were applied 8 mm from the bottom edge of the plate, with an 8 mm application band length. Nitrogen gas was used by the ATS 4 for aerosolized sample application.

Chromatography was performed in the ADC 2 chamber. The mobile phase consisted of a dichloromethane:methanol solution (9:1). The chamber was saturated with 25 mL of mobile phase, and 10 mL were used for development. The procedure included 20 minutes of chamber saturation, 10 minutes of activation with $MgCl_2$ (to achieve 33% relative humidity), chromatographic development to 70 mm, and plate drying for 5 minutes.

Photographic records under visible light, UV light at 254 nm and 366 nm, derivatizations, and Rf calculations were performed with the Visualizer and VisionCATS 2.5 software.

Derivatizations

Derivatizing agents were applied using the Derivatizer. The following reagents were employed: natural products reagent (2-aminoethyl diphenylborinate), anisaldehyde, vanillin, and Dragendorff reagent. These reagents were prepared and applied according to the manufacturer's instructions for the Derivatizer. When necessary, chromatograms were heated using the TLC Plate Heater to complete derivatization.

Densitometry

Absorption spectra (ranging from 200 nm to 900 nm), densitometric assays at 206 nm and 307 nm, correlation tests, and spectral purity evaluations were conducted using the TLC Scanner 4 in combination with VisionCATS 2.5 software.

Creation of Chemical Fingerprints

From the chromatograms and densitometric data, image comparison views were generated using VisionCATS 2.5 software. These composite images, known as chemical fingerprints, were used in this study to identify the chemical families present in each sample. Interpretation of derivatizations was based on comparisons with specialized literature, particularly the works of Burnstein (1953), Conde et al. (1992), Foti et al. (2004), Matteini et al. (2011), Spangenberg (2008), Wagner and

Bladt (1996), and Waksmundzka-Hajnos et al. (2008).

Isolation and Purification of Compounds of Interest

Preparative Thin-Layer Chromatography (PTLC)

Compounds of interest were initially isolated using preparative thin-layer chromatography (PTLC) with Silica Gel 60 F254+366 plates (2 mm thickness, Merck) as the stationary phase and a dichloromethane:methanol (9:1) solution as the mobile phase, following the method described by Umaña (2013). After chromatographic development, the bands of interest were scraped off. The scraped silica gel was mixed with 100 mL of methanol and filtered through a funnel fitted with a Whatman #40 filter. The collected fraction was then concentrated by rotary evaporation at 40°C under reduced pressure, and the isolated fraction was dissolved in 4 mL of methanol. Finally, this solution was passed through a 0.45 µm syringe filter (Fisher Scientific) and dispensed into a vial, which was stored refrigerated (2–5°C) until use.

Isolation and Purification by Medium-Pressure Liquid Chromatography (MPLC)

The compounds of interest were isolated and purified by medium-pressure liquid chromatography. For this, a flash chromatograph (SepaCore®, Büchi) equipped with a reversed-phase column (Büchi RPC18ec) (12 mm × 150 mm), a detector with a monochromator, and an automatic fraction collector was employed. A 2 mL volume of a 20 mg/mL solution of the fractions to be purified was injected into the MPLC. A flow rate of 5 mL/min was applied using a mobile phase composed of methanol and water (75:25) for the purification of a compound referred to as B, and methanol and water (95:5) for the purification of a substance designated C. Chromatographies were performed under isocratic conditions. Based on the presumed structure, the absorbance of compound B was monitored at 307 nm and compound C at 206 nm. Fraction volumes of 5 mL were collected. Fractions were selected post-chromatography primarily based on purity criteria. The mobile phase was removed from the collected fractions by rotary evaporation under reduced pressure at 40°C followed by lyophilization. This procedure successfully isolated and purified two compounds of interest. The purity of the isolates was verified by HPTLC and their derivatization with a 1 mg/mL potassium permanganate solution. Purity was defined by the presence of only the band corresponding to the compound of interest on the chromatogram.

Structural Elucidation of the Isolated Substances

Of the two isolated substances, the first showed a spectral purity greater than 99.97% and was analyzed by infrared (IR) spectroscopy and nuclear magnetic resonance (NMR). The molecular structure of compound B was determined by comparing and correlating the NMR and IR data obtained with those reported in the literature (Cuesta-Rubio et al., 2001; Umaña, 2013; Umaña et al., 2023; Uwamori et al., 2012).

Infrared Spectrum

The infrared spectrum was recorded using an attenuated total reflectance (ATR) instrument, Thermo Scientific Nicolet iS50 FT-IR model.

Nuclear Magnetic Resonance (NMR)

Fifteen milligrams of compound B were dissolved in 750 µL of deuterated methanol (CD_3OD). The final solution (20 mg/mL) was transferred into NMR tubes. Spectra were recorded on a Bruker Avance III spectrometer equipped with a 50 mm probe, at 25°C, using a magnetic field of 400.13 MHz for proton NMR (^{1}H-NMR) and 100.62 MHz for carbon-13 NMR (^{13}C-NMR). In both cases, a 30° pulse was applied. Relaxation times were 1 s for ^{1}H-NMR and 2 s for ^{13}C-NMR. The free induction decay (FID) comprised 64K points in both cases.

RESULTS

Taxonomic Identification of the Species *Clusia valerioi* (Standl.)

The botanical material collected during the different field trips was used for the identification and classification of the sampled species.

Analysis of the resin samples carried by individual bees and those collected from the upper parts of the hive frames showed that the dominant loads (93%) were whitish in color and, after some time, turned pale orange or brown once deposited into vials. The other loads, considered incidental or accessory (7%), were pale yellow, red, and greenish, and retained their coloration over time.

Microscopic mounts of the dominant loads revealed that they corresponded almost entirely to the pollen of *C. valerioi* (see Figures 3 and 4). The pollen grains of *C. valerioi* are tricolporate, with circular to elliptical apertures, a tectate exine, and granular sexine. The grains are small, spheroidal in shape, measuring 22–24 µm (CINAT Pollen Image Database, 2024; Roubik and Moreno, 1991).

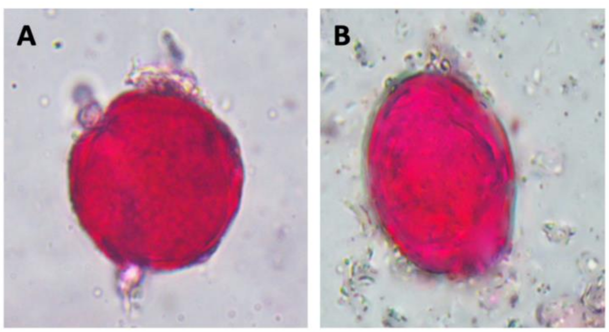

Figure 3. Microphotograph of *C. valerioi* pollen grains obtained from floral anthers (100X magnification). A) Polar view; B) Equatorial view.

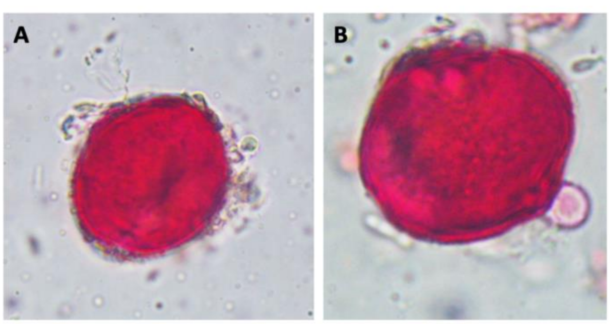

Figure 4. Microphotograph of polar views of *C. valerioi* pollen grains (100X magnification). A) Grain from resin collected by bees; B) Grain from resin collected on the upper parts of hive frames (unprocessed resin).

High-Performance Thin-Layer Chromatography (HPTLC) Assays

The results of the high-performance thin-layer chromatography assays and derivatizations are presented in Figures 5 and 1A of the Appendix. The chemical families of the compounds present in the extracts were identified based on the colors developed after exposure to the derivatizing reagent, and by comparison with information available in the literature (Burnstein, 1953; Conde et al., 1992; Foti et al., 2004; Matteini et al., 2011; Spangenberg, 2008; Wagner and Bladt, 1996; Waksmundzka-Hajnos et al., 2008).

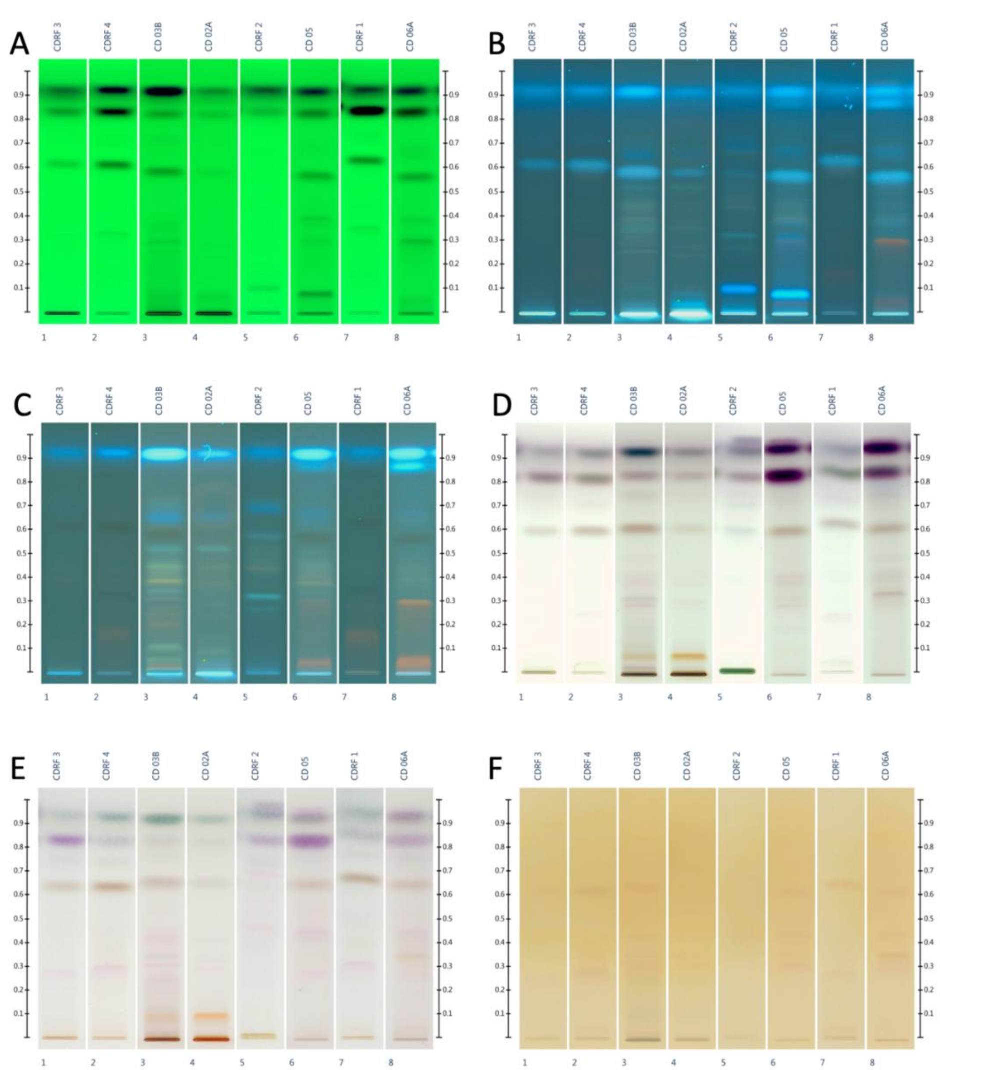

Figure 5. HPTLC chromatograms of extracts from *C. valerioi* (Standl.) flower samples, resins, and propolis from the southern region of Costa Rica, showing the results under various conditions: exposure to ultraviolet light at 254 nm (A), exposure to ultraviolet light at 366 nm (B), derivatization with the Natural Products Reagent under 366 nm light (C), derivatization with the anisaldehyde reagent under visible light (D), derivatization with the vanillin reagent under visible light (E), and derivatization with the Dragendorff reagent under visible light (F).

All of the extracts analyzed (100%) tested negative with the Dragendorff reagent, which is used to detect the presence of alkaloids. Therefore, the absence of alkaloids is reported in the analyzed samples.

Derivatization with the Natural Products Reagent revealed bands in yellow, orange, red, blue, and green hues within the Rf range of 0.01 to 0.60 in 77% of the samples. These colorations indicate the presence of phenolic compounds in the majority of the extracts, particularly flavanones and flavonols (see Figures 5 and 1A in the Annexes).

In 91% of the samples, three bands with Rf values between 0.61 and 1.00 were observed (Figure 6). The upper band (Rf = 0.93), assigned to a compound referred to as A, fluoresces under UV light at 366 nm and shows a blue hue when derivatized with the Natural Products Reagent. Upon reaction with the anisaldehyde reagent, it turns a very dark purple, and, based on its lack of response to the Dragendorff reagent, it is not an alkaloid. This chemical fingerprint suggests that compound A may be a terpene derivative. However, in some chromatograms, two closely adjacent intense blue bands were observed under UV light at 366 nm. Derivatization with vanillin yielded green tones in some bands and purple hues in others (see Figures 5 and 6). These results suggest the presence of two distinct compounds with very similar Rf values under the chromatographic conditions used. Therefore, a more in-depth analysis of compound A would first require an appropriate separation of its constituents.

The middle band (Rf = 0.83), assigned to a compound referred to as B, absorbs at 254 nm but is not visible under UV light at 366 nm and does not react with the Natural Products Reagent. However, upon derivatization with anisaldehyde and vanillin reagents, it develops purple hues. Like compound A, this behavior suggests that compound B may also be a terpene derivative.

The lower band (Rf = 0.63), attributed to a compound referred to as C, shows absorption under UV light at 254 nm, is not visible under UV light at 366 nm, and reacts with the Natural Products Reagent to produce an intense blue color. It also develops orange hues upon derivatization with anisaldehyde and vanillin reagents. Based on its chemical fingerprint, compound C is likely a phenolic compound, particularly a flavonol or flavanone. The chemical fingerprints of compounds A, B, and C are shown in Figure 6.

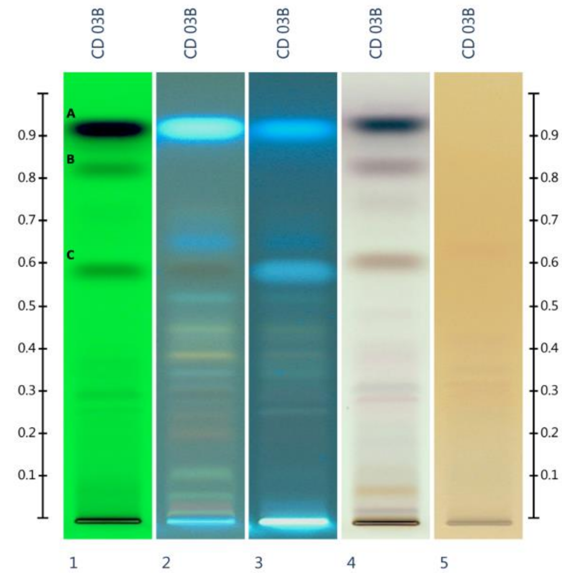

Figure 6. Chemical fingerprint of the flower resin extract from *C. valerioi* (sample CD 03B). The figure shows the results of various exposures to ultraviolet light and derivatizations for compounds A (Rf 0.93), B (Rf 0.83), and C (Rf 0.63). 1) exposure to UV light at 254 nm, 2) exposure to UV light at 366 nm, 3) derivatization with the Natural Products Reagent (viewed under 366 nm UV light), 4) derivatization with the anisaldehyde reagent (visible light exposure), 5) derivatization with the Dragendorff reagent (visible light exposure).

Subsequently, based on sample CD03B—derived from the resin extracts obtained from the flowers of *C. valerioi*—the absorption spectra of compounds B (Rf 0.83) and C (Rf 0.63) were determined through densitometric assays. Compound B exhibited a maximum absorption peak at 307 nm, while compound C showed a maximum absorption at 206 nm (see Figures 2A and 3A in Annexes).

Densitometric analyses were then performed at 206 nm and 307 nm. The results were subjected to peak integration analyses corresponding to the absorbance signals of compounds A, B, and C. This approach optimized the visualization of the constituents and enabled a more accurate assessment of the presence or absence of the target compounds. The results are presented in Figure 7 and Figure 4A of the Annexes.

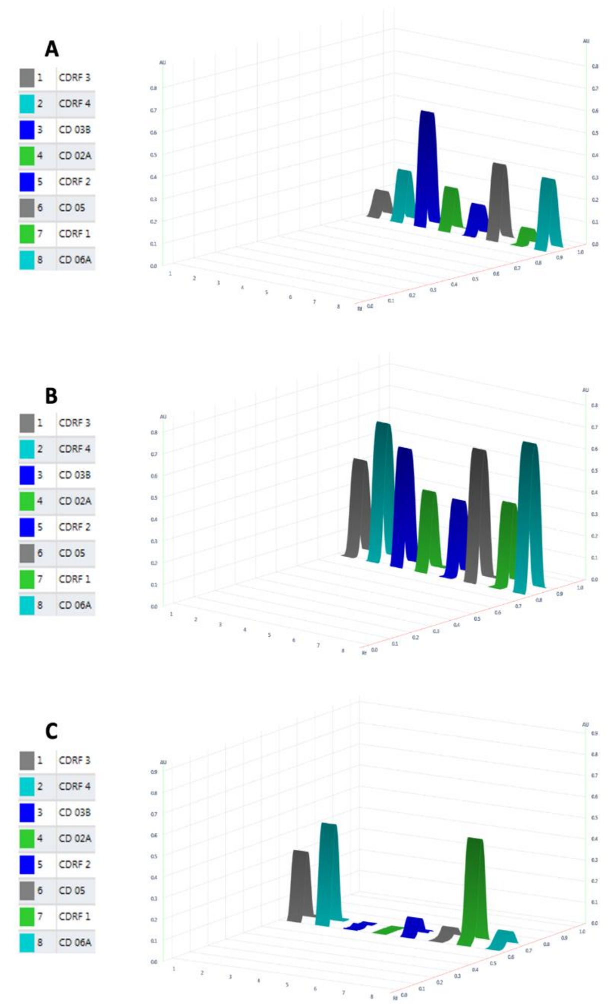

Figure 7. Densitometric analyses based on HPTLC chromatograms of extracts from *C. valerioi* flower samples, resins, and propolis collected from the southern region of Costa Rica. Absorption peaks corresponding to compounds A, B, and C were integrated to assess their presence in the samples. A) Densitometry at 307 nm for the evaluation of compound A. B) Densitometry at 307 nm for the evaluation of compound B. C) Densitometry at 206 nm for the evaluation of compound C.

All samples exhibited an absorption peak corresponding to compound A. Absorption peaks for compounds B and C were detected in all samples, with two exceptions: one propolis sample from Puerto Jiménez, Golfito (CD 7B) did not contain compound B, and one flower extract from Limoncito, Coto Brus (CD 02A) did not show evidence of compound C.
Absorption spectra (ranging from 200 nm to 900 nm) were recorded from chromatogram bands with Rf values corresponding to compounds B and C. Based on these results, correlation analyses of the absorption spectra were conducted. Pearson correlation coefficients of 0.995055 and 0.987449 were obtained for the bands assigned to compounds B and C, respectively. These values strongly suggest that both compounds are present in all samples, with the exception of those specifically mentioned above.
The constituents identified as compounds A, B, and C were found in *Clusia valerioi* (Standl.) flowers, in the resins carried by bees in their corbiculae, and within the hive, both in the unprocessed resin deposits and in the processed propolis.

Structural Identification of Compound B

The isolated substance with the highest purity, referred to as compound B, was identified as nemorosone. Its molecular structure was determined based on the consistency and comparison of data obtained from ^{1}H-RMN, ^{13}C-RMN, and IR spectroscopy with those previously reported in the literature by Cuesta-Rubio et al. (2001), Umaña (2013), Umaña et al. (2023), and Uwamori et al. (2012). The data supporting the structural elucidation of this compound are presented in Figures 5A to 8A and Tables 1A to 3A of the Annex. The optimization of the purification processes and subsequent structural elucidation of compounds A and C will be addressed in future studies.

DISCUSSION

The joint efforts in sampling and botanical identification of the plant collected during the various field trips, carried out by Lic. Luis Jorge Poveda and M.Sc. Luis Sánchez Chaves, confirm with full certainty that the specimen sampled near the apiaries corresponds to the species *Clusia valerioi* (Standl.). This finding aligns with the report by Hochwallner et al. (2012), who indicated that this species is common in the southern region of Costa Rica.
Furthermore, field observations by beekeepers in the southern region of Costa Rica (Bermúdez, 2019), corroborated by botanist Luis J. Poveda and confirmed by our own sampling visits, documented a high visitation rate by *Apis mellifera* bees to the flowers of *C. valerioi* (Standl.) for resin collection. These observations are supported by our analysis of the resins transported by bees and those

collected from the hive frames, where 93% of the dominant resin load corresponded to Clusiaceae (Figure 3). In addition, Hochwallner et al. (2012) reported frequent visits of *Apis mellifera* to both male and female flowers of *C. valerioi* (Standl.) for resin collection. This confirms that the pollen and resins of this plant are effectively transported to the apiaries, raising the possibility of their use in the production of bee-derived products—an aspect to be further evaluated.

The most direct way to determine whether the materials collected by the bees (pollen and resin) from *C. valerioi* (Standl.) flowers are incorporated into beehive products, specifically propolis, is by detecting the presence of shared chemical constituents—known as chemical markers—across these matrices. This is confirmed by the results shown in Figures 4 to 6.

The HPTLC chromatographic results of extracts from *C. valerioi* floral tissues, resins collected from the bees' corbiculae, unprocessed resin aggregates inside the hives, and the propolis samples from apiaries, generally show an absence of alkaloid-type compounds across all matrices. They also confirm the inconsistent presence of phenolic compounds, particularly flavanones and flavonols, with low to intermediate Rf values (below 0.60) in most samples (77%). However, at higher Rf values (above 0.60), a large majority of the samples (91%) exhibited three common bands that may serve as chemical tracers linking the chemical composition of *C. valerioi* floral resins, the resin collected by bees from these flowers, the resins transported to the hive, and the propolis ultimately produced within the apiary (Figures 4 to 6).

These three chemical tracers were designated as **Compound A**, **Compound B**, and **Compound C**. **Compound A** (Rf = 0.93), based on its derivatization behavior, appears to be a terpene derivative. Under different chromatographic conditions, it seems to consist of a mixture of two closely related substances—possibly isomers or tautomers—warranting further chromatographic separation and structural elucidation. **Compound B** (Rf = 0.83) was identified as the polyprenylated benzophenone nemorosone, based on its behavior during chemical derivatization and comparison with proton nuclear magnetic resonance (NMR) spectroscopy (Figures 5 and 6; Figures 5A and 6A; Table 1A of Annex), carbon-13 NMR (Figure 7A; Table 2A of Annex), and infrared (IR) spectroscopy (Figure 8A; Table 3A of Annex). Finally, **Compound C** (Rf = 0.63), based on its chemical reactivity with derivatizing agents, is likely a phenolic compound, specifically a flavonol or flavanone. It is worth noting that previous studies have shown other *Clusia* species to serve as resin sources for *Apis mellifera* in the production of propolis, such as *C. major* (syn. *C. rosea*), *C. minor*, and *C. scrobiculata* in Venezuela, and *C. major* (syn. *C. rosea*) in Cuba—these species are known for their richness in polyprenylated benzophenones like nemorosone and scrobiculactones A and B (Trusheva et al., 2004; Cuesta-Rubio et al., 2000).

In our case, the present study constitutes the first report of *C. valerioi* (Standl.) as a primary source of resins for *Apis mellifera* propolis in Costa Rica. Three chemical markers were identified in 94% (15 extracts) of the propolis samples analyzed, collected from apiaries both with and without confirmed presence of *C. valerioi* (Standl.) in their surroundings.

CONCLUSIONS

Based on the results obtained for the beekeeping sector or ecosystem studied—geographically located in the southern region of Costa Rica, specifically in Pittier, Coto Brus, and surrounding areas—it is concluded that the confirmed botanical identification of *Clusia valerioi* (Standl.) positions this species as a key floral source. The resin produced by its flowers is collected, transported, deposited, and processed by honey bees, and its chemical composition directly influences the chemical profile of the propolis produced.

This conclusion is supported by the HPTLC results, which demonstrate the presence of at least three relevant chemical markers, identified in this study as Compound A, Compound B, and Compound C. These findings were further validated by the presence of *C. valerioi* (Standl.) pollen in the resin loads predominantly transported by the bees to the hives.

Based on derivatization tests, Compound A was identified as a terpene derivative, potentially a mixture of isomers or tautomers, similar to Compound B, which also exhibited a terpenoid nature. Compound C, in turn, was identified as a phenolic derivative, likely a flavonol or flavanone.

Spectroscopic analysis of Compound B enabled the elucidation of its chemical structure, which was determined to be that of nemorosone. In the context of the broader research project, further spectroscopic studies are recommended for Compounds A and C—once the isomeric or tautomeric mixture of the former is resolved—to allow for more detailed structural identification of both chemical markers.

ACKNOWLEDGEMENTS

We thank the Research Vice-Rectory of the National University of Costa Rica for funding project FIDA0571-19, under which this research was conducted.

Special thanks to Guillermo Ramírez Arias, technician at the Tropical Apicultural Research Center (CINAT), for his valuable assistance during the sampling trips, and to Professor Emeritus Lic. Luis Jorge Poveda Álvarez of the National University for his essential support during the botanical identification phase at the Juvenal Valerio Herbarium of the School of Environmental Sciences, National University.

Annexes

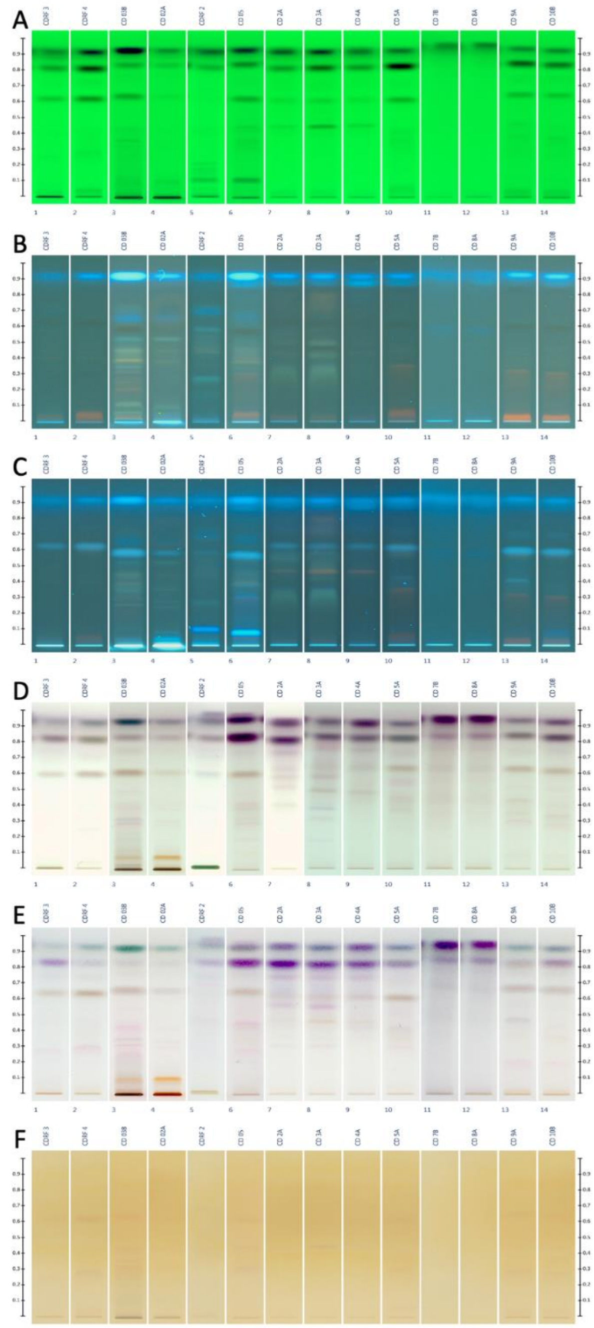

Figure 1A. HPTLC chromatograms of extracts from samples of *C. valerioi* (Standl.) flowers, resins, and propolis from the Southern Region of Costa Rica (part 2). A) Exposure to ultraviolet light at 254 nm, B) exposure to ultraviolet light at 366 nm, C) derivatization with the natural products reagent (exposure at 366 nm), D) derivatization with the anisaldehyde reagent (exposure under visible light), E) derivatization with the vanillin reagent (exposure under visible light), F) derivatization with the Dragendorff reagent (exposure under visible light).

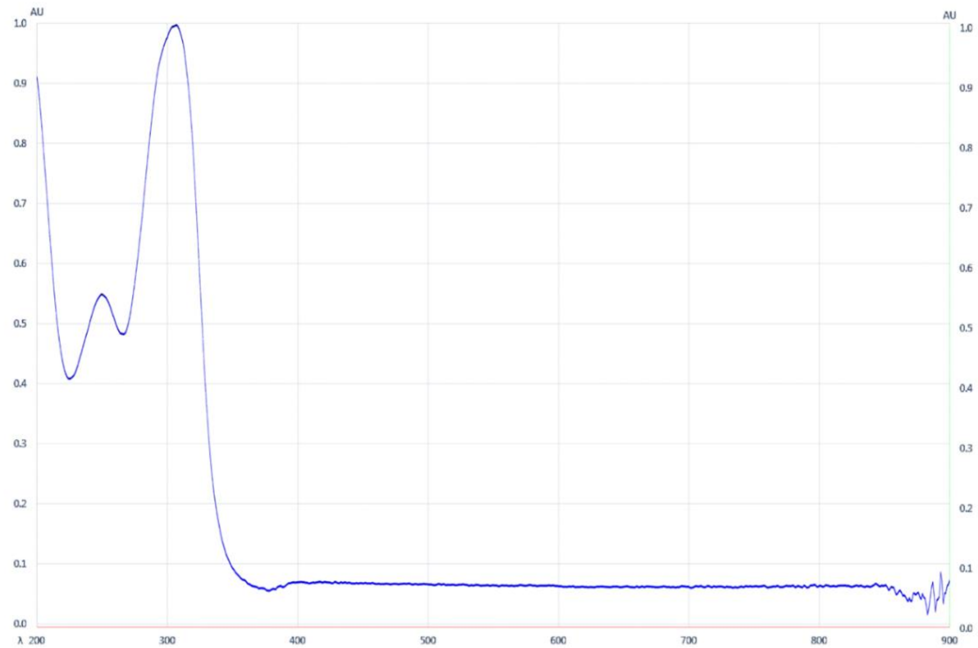

Figure 2A. Absorption spectrum from 200 nm to 900 nm for compound B.

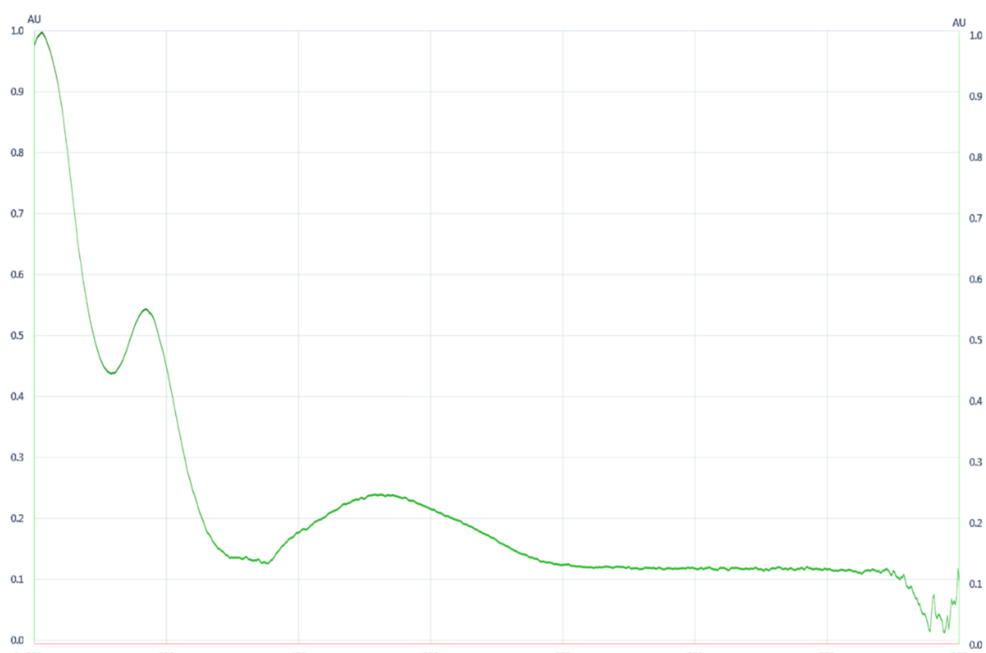

Figure 3A. Absorption spectrum from 200 nm to 900 nm for compound C.

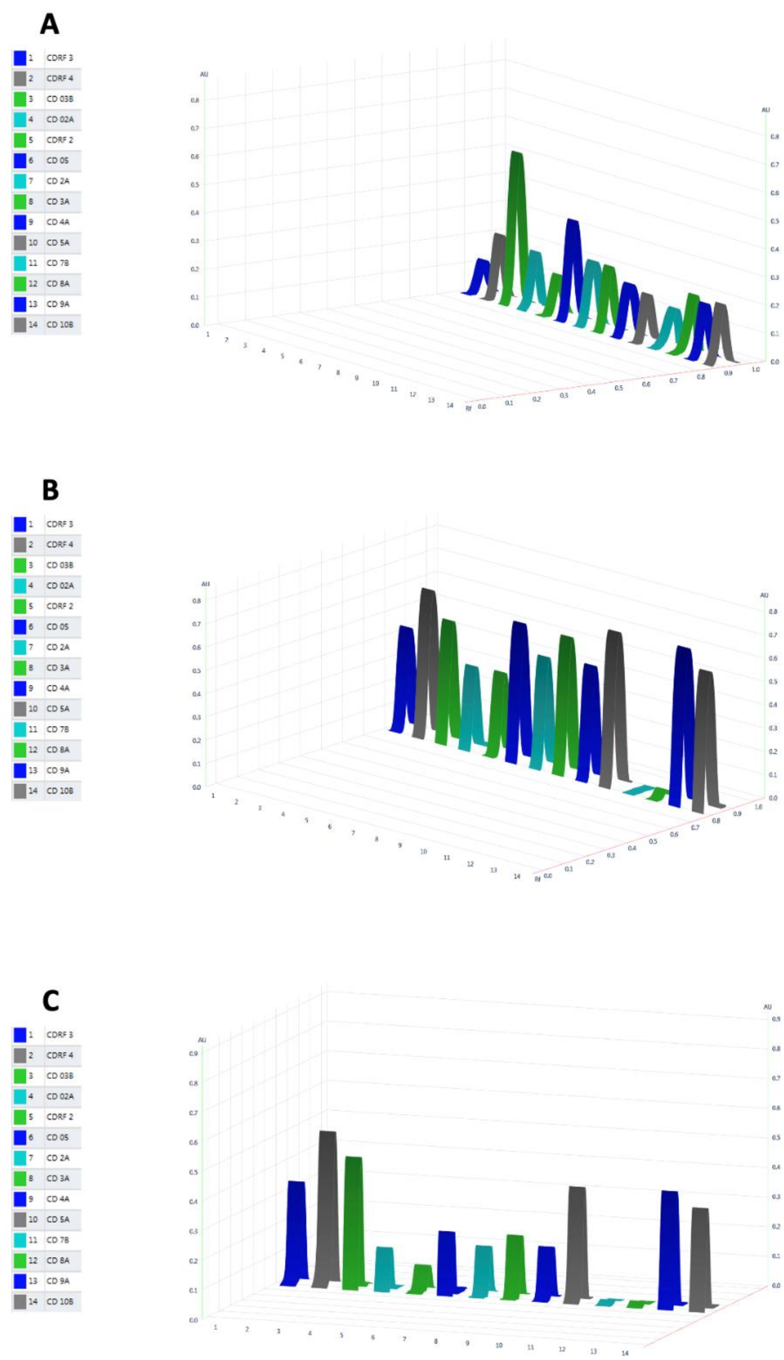

Figure 4A. Densitometric analyses from HPTLC chromatograms of extracts from samples of *C. valerioi* flowers, resins, and propolis from the southern region of Costa Rica (part 2). Absorption peaks corresponding to compounds A, B, and C were integrated to assess their presence in the samples. A) Densitometry at 307 nm for evaluating the presence of compound A. B) Densitometry at 307 nm for evaluating the presence of compound B. C) Densitometry at 206 nm for evaluating the presence of compound C.

Numeración de carbonos en Cuesta-Rubio et al (2001), Umaña et al (2023) y Uwamori et al (2012)	Numeración de carbonos en Umaña (2013)
1	P
2	D
3	O
4	C
5	Q
6	T
7	S
8	R
9	A
10	B
11	E
12, 16	J
13, 15	K
14	H
17	Z
18	L
19	I
20	B2
21	Y
22	U
23	N
24	F
25	D2
26	W
27	V
28	M
29	G
30	C2
31	X
32	A2
33	E2

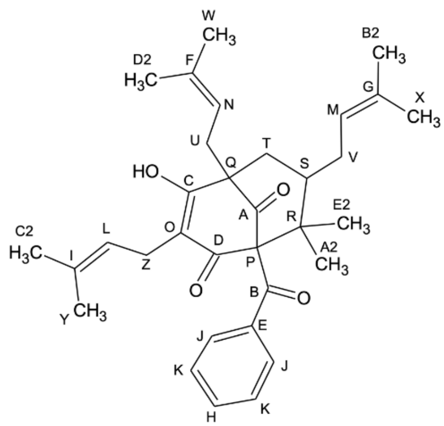

Figure 5A. Correspondence of alphanumeric assignments for carbon and hydrogen atoms used for nemorosone in the consulted literature.

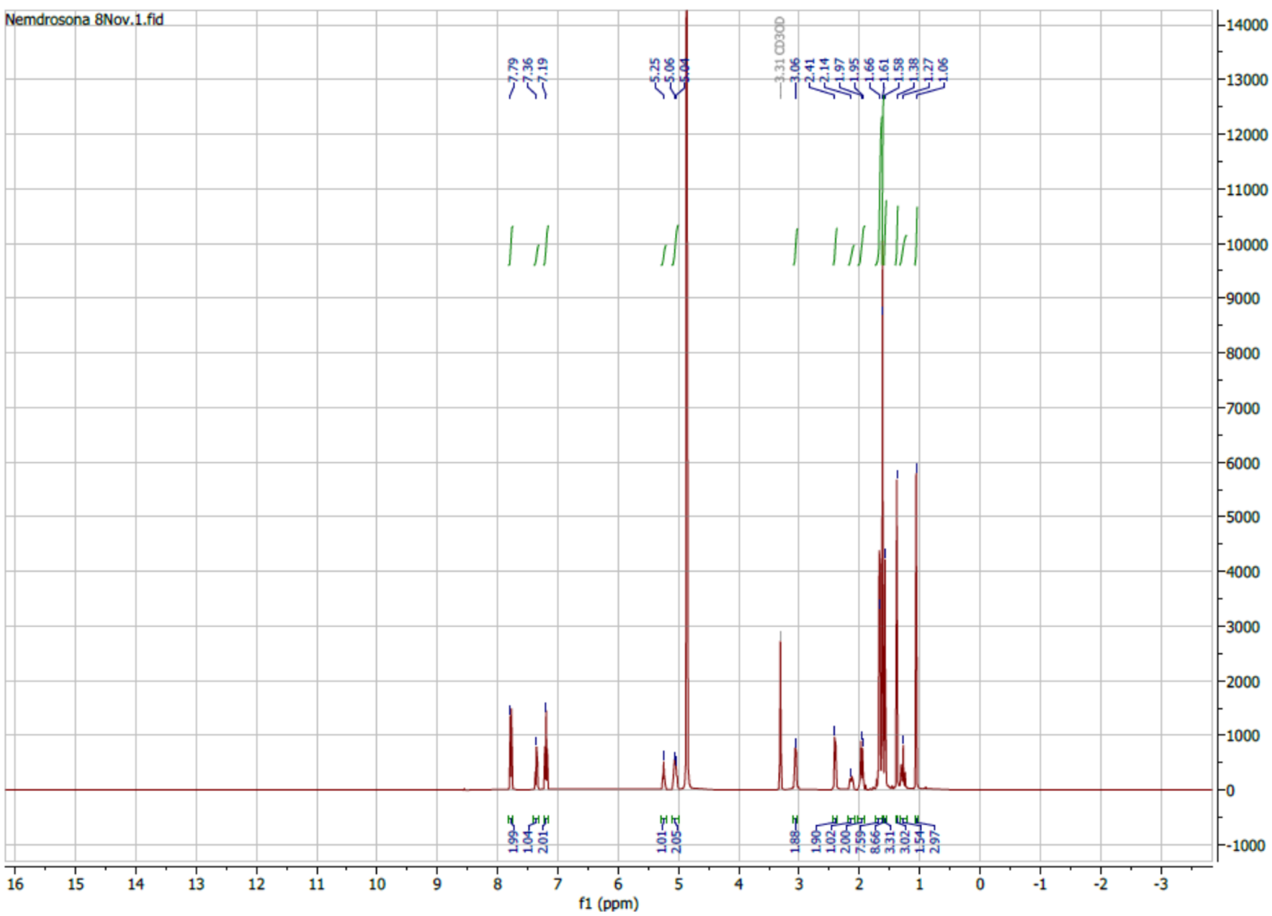

Figure 6A. Proton nuclear magnetic resonance ([1]H-RMN) spectrum of nemorosone in CD_3OD (reference 3.31 ppm) measured at 400.13 MHz.

Table 1A. Comparison of the ^{1}H-RMN data of nemorosone isolated from the propolis extract CD 5A with data reported in the literature.

Hydrogen atom assignment	Nemorosone isolated from extract CD 5A / CD_3OD / ppm (integration), (multiplicity, coupling constant)	Umaña (2013), Umaña et al. (2023) / CD_3OD / ppm (integration), (multiplicity, coupling constant)	Cuesta-Rubio (2001) CDCl3 / -55°C / Tautomer a / Tautomer b / ppm (integration), (multiplicity, coupling constant)	Synthetic nemorosone (Uwamori et al., 2012) / CD_3OD / ppm (integration), (multiplicity, coupling constant)
6 a (T1)	1.97 (1), (m)	1.96 (1), (m)	2.09 /1.97 (1), (dd, J = 13.5, 4 Hz)	2.02 (1), (dd, J =13.0, 3.5 Hz)
6 b (T2)	1.27 (1), (m)	1.27 (1), (m)	1.47/1.42 (1), (t, J = 13.3)	1.43 (1), (t, J = 13.0 Hz)
7 (S)	1.95 (1), (m)	1.96 (1), (m)	1.68/1.70 (1), traslapado	1.79-1.71, (m)
12,16 (J)	7.78 (2), (dd, J = 8.6, 1.2 Hz)	7.78 (2), (dbr, J=8.6 Hz)	7.53/7.67 (2), (dd, J = 7.5, 1 Hz)	7.56 (2), (d, J = 7.5 Hz)
13,15 (K)	7.20 (2), (tbr, J = 8.0 Hz)	7.20 (2), (dd, J = 8.4, 7.8 Hz)	7.31/7.35 (2), (t, J = 7.5 Hz)	7.26 (2), (t, J = 7.5 Hz)
14 (H)	7.36 (1), (tt, J = 7.4, 1.2 Hz)	7.36 (1), (tbr, J = 7.8 Hz)	7.47/7.51 (1), (t, J = 7.5 Hz)	7.43 (1), (t, J = 7.5 Hz)
17 (Z)	3.06 (2), (m)	3.06 (2), (dbr, J = 6.5 Hz)	3.14/3.20 (1), (dd, J = 16, 7) / (dd, J = 16.5, 7); 3.20/3.28 (1), (dd, J = 16, 7) / (dd, J = 16.5, 7)	3.13 (1), (dd, J = 15.0, 7.5 Hz); 3.08 (1), (dd, J = 15.0, 7.5 Hz)
18 (L)	5.25 (1), (tq, J = 7.2, 1.3 Hz)	5.24 (1), (tq, J = 7.0, 1.4 Hz)	4.89/5.23 (1), (m)	5.09 (1), (t, J = 7.5 Hz)
20 (B2)	1.62 (3), (s)	1.62 (3), (s)	1.56-1.76/1.56-1.76 (3), (s)	1.65 (3), (s)
21 (Y)	1.66 (3), (s)	1.66 (3), (s)	1.66-1.8/1.66-1.8 (3), (s)	1.66 (3), (s)
22 (U)	2.41 (2), (m)	2.40 (2), (dd, J = 6.6, 1.7 Hz)	2.47/2.47(1), (dd, J = 15, 7.5) / (dd, J =14, 7); 2.65/2.56 (1), (dd, J = 15, 7.5) / (dd, J = 14,7)	2.53 (1), (dd, J = 14.5, 6.5 Hz); 2.48 (1) (dd, J = 14.5, 6.5 Hz)
23 (N)	5.07 (1), (m)	5.06 (1), (m)	5.11/5.13 (1), (m)	5.01 (1), (sbr)
25 (D2)	1.58 (3), (s)	1.57 (3), (s)	1.56-1.76/1.56-1.76 (3), (s)	1.59 (3), (s)
26 (W)	1.62 (3), (s)	1.62 (3), (s)	1.66-1.8/1.66-1.8 (3), (s)	1.65 (3), (s)
27 a (V1)	2.14 (1), (m)	2.14 (1), (m)	2.16/2.11 (1), (dd, J = 13, 4) / (dd, J = 13.5, 4)	2.19-2.10, (m)
27 b (V2)	1.66-1.67 (1), (m)	1.66-1.67 (1), (m)	1.80/1.71 (1) (traslapados)	1.79-1.71, (m)
28 (M)	5.04 (1), (m)	5.04 (1), (m)	4.94/4.98 (1)	5.01 (1), (sbr)
30 (C2)	1.62 (3), (s)	1.62 (3), (s)	1.56-1.76/1.56-1.76 (3), (s)	1.65 (3), (s)
31 (X)	1.67 (3), (s)	1.67 (3), (s)	1.66-1.8/1.66-1.8 (3), (s)	1.69 (3), (s)
32 (A2)	1.38 (3), (s)	1.38 (3), (s)	1.35/1.40 (3), (s)	1.34 (3), (s)
33 (E2)	1.06 (3), (s)	1.06 (3), (s)	1.13/1.17 (3), (s)	1.11 (3), (s)

Notation: s = singlet, d = doublet, t = triplet, q = quartet, dd = doublet of doublets, tt = triplet of triplets, m = multiplet, br = broad

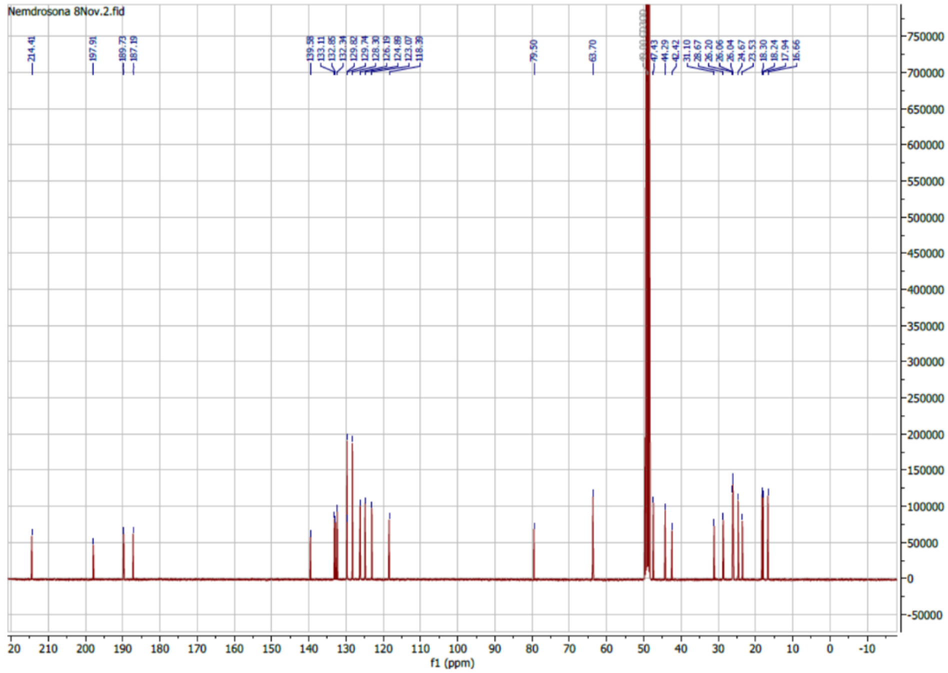

Figure 7A. The carbon-13 nuclear magnetic resonance (^{13}C-RMN) spectrum of nemorosone in CD_3OD (reference at 49.00 ppm) was measured at 100.62 MHz.

Table 2A. Comparison of the ^{13}C-RMN data of nemorosone isolated from the propolis extract CD 5A with data reported in the literature.

Assigned Carbon Atom	Nemorosone Isolated from CD 5A (CD_3OD, ppm)	Umaña (2013), Umaña et al. (2023) (CD_3OD, ppm)	Cuesta-Rubio et al. (2001) (CDCl3, -55°C, Tautomer a/Tautomer b, ppm)	Nemorosone Synthetic (Uwamori et al., 2012) (CD_3OD, ppm)
1 (P)	79.5	79.5	78.0/71.4	78.3
2 (D)	187.2	187.2	192.2/168.2	Not reported due to tautomerism.
3 (O)	118.4	118.4	117.6/117.2	121.07
4 (C)	189.7	189.7	170.9/195.0	Not reported due to tautomerism.
5 (Q)	63.7	63.7	57.1/64.8	62.1
6 (T)	42.4	42.4	39.4/42.1	42.4
7 (S)	44.3	44.3	42.9/42.1	44.7
8 (R)	47.4	47.4	48.2/47.3	49.1
9 (A)	214.4	214.4	207.3/207.6	209.7
10 (B)	197.9	197.9	193.2/193.1	195.2
11 (E)	139.6	139.5	136.6/135.9	138.4
12,16 (J)	129.7	129.7	128.1/128.0	129.7
13,15 (K)	128.3	128.3	127.9/127.9	128.9
14 (H)	132.3	132.4	132.4/132.6	133.5
17 (Z)	24.7	23.5	21.6/21.7	24.5
18 (L)	126.2	126.2	119.6/119.1	124.2
19 (I)	129.8	129.8	138.2/139.5	133.2
20 (B2)	18.3	18.3	17.9/17.9	18.4
21 (Y)	26.0	26.0	25.9/25.9	26.15
22 (U)	31.1	31.1	28.9/29.2	30.6
23 (N)	123.1	123.0	118.4/119.3	121.1

24 (F)	133.1 o 132.8	133.1 o 132.9	135.2/134.7	135.2
25 (D2)	18.2	18.2	18.0/18.0	18.3
26 (W)	26.2	26.2	26.0/26.0	26.4
27 (V)	28.7	28.7	26.4/27.3	28.3
28 (M)	124.9	124.9	122.1/122.1	122.5
29 (G)	133.1 o 132.8	133.1 o 132.9	133.6/133.6	134.3
30 (C2)	17.9	18.3	18.2/18.2	18.1
31 (X)	26.1	26.2	26.3/26.3	26.17
32 (A2)	23.5	23.5	23.2/24.1	23.9
33 (E2)	16.7	16.7	15.6/15.6	16.4

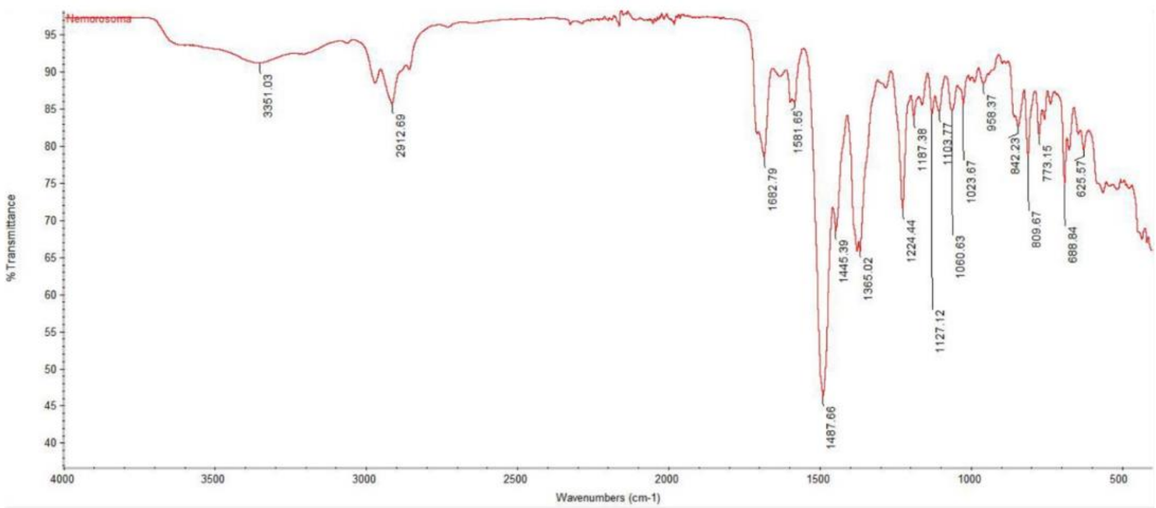

Figure 8A. Infrared spectrum (ATR) of nemorosone.

Table 3A. Comparison of the infrared spectra of nemorosone isolated from extract CD5A with literature data.

Signal (assignment)	Nemorosone isolated from extract CD 5A / cm^{-1}	Cuesta-Rubio et al. 2001 / cm^{-1}	Uwamori et al. (2001) / cm^{-1}
1 (O-H)	3351	3431	3297
2 (C-H)	2913	2969	2923
3 (C=O	1713	1708	1723
4 (C=O)	1683	NR	1699
5 (C=C)	1582	1590	1581
6 (C=C)	1445	NR	1446
7 (C-O-H)	1365	NR	1372
8 (C-O-H)	1224	NR	1220
9 (C-O-H)	1187	NR	1186

Notation: NR=Not reported

REFERENCES

Alencar, A., Dantas, E., Lischka, J. 2020. New perspectives on secretory structures in *Clusia* (Clusiaceae–Clusiod clade): production of latex or resins. Botany, 98, 3:137-183.

Bermúdez, Benjamín. Comunicación personal. 2019.

Burstein S. 1953. Reduction of Phosphomolybdic Acid by Compounds Possessing Conjugated Double bonds. Analytical Chemistry. Vol. 25. No.3. pp 422-424. Chaillou, L. L., Herrera, H. A., Maidana, J. F. (2004). Estudio del propóleos de Santiago del Estero, Argentina. Ciência e Tecnologia de Alimentos, 24(1), 11–15.

Conde, E., Cadahía, E., García-Vallejo, M. (1992). Optimization of TLC for research on the flavonoids in wood and bark of species of the genus Eucalyptus L'Héritier. Chromatographia, 33(9), pp.418-426.

Cuesta-Rubio, O., Frontana-Uribe, B., Ramírez, Apan-t., Cárdenas, J. (2000). Polyisoprenylated benzophenones in Cuban propolis; biological activity of nemorosone. Z. Naturforsch. 57c, 372-378.

Cuesta-Rubio, O., Velez-Castro, H., Frontana-Uribe, B. A., Cardenas, J. (2001). Nemorosone, the major constituent of floral resins of *Clusia rosea*. Phytochemistry 57, 279–283.

Erdtman, G. (1986). Pollen Morphology and Plant Taxonomy Angiosperms: An introduction to the study of pollen grains and spores. Brill Academic Pub.

Fernández, M. (2008). Estudio químico de propóleos rojos cubanos. 5–21.

Fernández-León, K. J., Rodríguez-Díaz, J. A., Reyes-Espinosa, L., Duquesne-Alderete, A., Solenzal-Valdivia, Y. O., Rives-Quintero, A., Hernández-García, J. E. (2022). Comparison of in vitro anti- *Staphylococcus aureus* activity of eight antibiotics and four dilutions of propolis. Journal of the Selva Andina Research Society, 13(1), 35–48.

Foti, M., Daquino, C., Geraci, C. (2004). Electron-transfer reaction of cinnamic acids and their methyl esters with the DPPH•Radical in alcoholic solutions. The Journal of Organic Chemistry, 69(7), pp.2309-2314.

Herbert, L. A. (2021). Metabolitos bioactivos de *Clusia* spp. Tesis doctoral. Centro de Investigación Científica de Yucatán, México.

Hernández, J. E., Reyna, L. F., Ortiz, E., Salomón, M. C., Treviño, R. (2014). Espectroscopia infrarroja: Acetofenona, Ácido Benzoico, Benzofenona, Ácido Acetilsalicílico y Anhidrido Ftálico. Academia Journals, 2, 1–12.

Herrera, M. (2019). Caracterización química y actividad biológica de propóleos producidos en el estado de Yucatán. 25–135.

Hochwallner, H., Weber, A. (2006). Flower development and anatomy of *Clusia valerioi*, a Central American species of Clusiaceae offering floral resin. Flora: Morphology, Distribution, Functional Ecology of Plants, 201(5), 407–418.

Hochwallner, H., Vogel, S., Huber, W., Hammel, B. E., Weber, A. Aspects of reproductive ecology of *Clusia valerioi* Standl. and *Clusia peninsulae* Hammel (sp. nov.), two Central American species of Clusiaceae with resin flowers. 2012. Plant Biol. (Stuttg).14(1):198-207.

Ley López, J. M. (2013). Los árboles de la Península de Osa sector Piro Una guía para su identificación. Osa Conservation, 19–26.

Matteini, P., Agati, G., Pinelli, P., Goti, A. (2011). Modes of complexation of rutin with the flavonoid reagent diphenylborinic acid 2-aminoethyl ester. Monatshefte für Chemie - Chemical Monthly, 142(9), pp.885-893

Meranti, D. I. K. (2015). Evaluación de la capacidad reguladora de extractos de *Clusia ellipticifolia* en la producción de citoquinas y quimioquinas pro-inflamatorias en astrocitos activados con lipopolisacáridos (LPS). II, 1–15.

Ministerio de Agricultura y Ganadería de Costa Rica. Comunicación personal. 2021

Monzote, L., Cuesta-Rubio, O., Matheeussen, A., Van Assche, T., Maes, L., Cos, P. (2011). Antimicrobial evaluation of the polyisoprenylated benzophenones nemorosone and guttiferone A. Phytotherapy Research, 25(3), 458–462.

Novais, C. S. (2016). Estudo fitoquímico de espécies de Clusia presentes no cerrado com potencial atividade biológica. Tese (Doutorado). Universidade Federal de Goiás, Goiânia, Brasil. 179 p.

Rossana, Lady, García, P., Paúl, J., Galán, M., Mario, C., Pajón, G. (2010). Caracterización Fisicoquímica y Actividad antimicrobiana de propóleos en el Municipio de la Unión. 63(1), 5373–5383.

Roubik, D., Moreno, J. (1991). Pollen and spores of Barro Colorado Island. Monographs in Sistematic Botany. Vol. 36. Missouri Botanical Garden.

Salas, R. (2005). Manual Técnico de Apicultura. Dicta. Sac., 1–32.

Spangenberg, B. (2008). Derivatization, detection, quantification and identification of compounds online. En: M. Waksmundzka-Hajnos, J. Sherma and T. Kowalska, ed., Thin

Layer Chromatography in Phytochemistry. Boca Raton, Florida: CRC Press, pp.175-192.

Tolosa, L., Cañizares, E. P. (2002). Obtención, caracterización y evaluación de la actividad antimicrobiana de extractos de propóleos de Campeche, México. Ars Pharmaceutica, 43, 1–2.

Trusheva, B., Popova, M., Naydenski, H., Tsveykova, I., Rodríguez, J.G., Bankova, V. (2004). New polyisoprenylated benzophenones from Venezuelan propolis. Fitoterapia 75, 683-689.

Umaña, E. (2013). Análisis multivariado de huellas digitales de metabolitos secundarios mayoritarios de propóleos de Costa Rica empleando Resonancia Magnética Nuclear protónica (^{1}H-RMN). Tesis de Maestría. Universidad de Costa Rica, Costa Rica.

Umaña, E., Solano, G., Zamora, G., Tamayo-Castillo, G. (2023). Costa Rican propolis chemical compositions: nemorosone found to be present in an exclusive geographical zone. Molecules 28, 7081.

Uwamori, M., Saito, A., Nakada, M. (2012). Stereoselective total synthesis of nemorosone. The Journal of Organic Chemistry 77, 5098-5107.

Vargas D, Torres G, y Sánchez A. (2018). El Propóleo: Conservador potencial para la industria alimentaria. Interciencia, 38(10), 705–713.

Wagner, H., Bladt, S. (1996). Plant drug analysis. 2nd ed. Berlin: Springer.

Waksmundzka-Hajnos, M., Sherma, J., Kowalska, T. (2008). Thin layer chromatography in phytochemistry. Boca Ratón, Florida: CRC Press, pp.451-605.

Zwicky, F. (1937). *Clusia valerioi* Standl., Fl. of Costa Rica. Zhurnal Eksperimental’noi i Teoreticheskoi Fiziki, 5(1), 21–34.

RECyT
Year 27 / Nº 43 / 2025 /
DOI: https://doi.org/10.36995/j.recyt.2025.43.008

Methodology proposal for isolating fungi from *Manihot esculenta* Crantz storage roots with rot symptoms

Propuesta metodológica para el aislamiento de hongos a partir de raíces almacenadoras de *Manihot esculenta* Crantz con síntomas de pudrición

Lucas M., Madrassi[1, 2, *]; Pedro D., Zapat [1, 2]; Cecilia I., Mónaco[3]; Adriana E., Alvarenga[1, 2]

1- Laboratorio de Biotecnología Molecular. Instituto de Biotecnología Misiones "Dra. María Ebe Reca". Facultad de Ciencias Exactas, Químicas y Naturales. Universidad Nacional de Misiones. Posadas, Misiones, Argentina.
2- Consejo Nacional de Investigaciones Científicas y Técnicas. Ciudad autónoma de Buenos Aires, Buenos Aires, Argentina.
3- Centro de Investigaciones en Fitopatología. Facultad de Ciencias Agrarias y Forestales. Universidad Nacional de La Plata. La Plata, Buenos Aires, Argentina.

* E-mail: lmmadrassi@hotmail.com

Received: 20/03/2025; Accepted: 03/05/2025

Abstract
Cassava (*Manihot esculenta Crantz*) is a vital staple food for millions of people worldwide, primarily valued for its edible storage roots. However, these roots are vulnerable to Cassava Root Rot Disease (CRRD), often caused by fungal pathogens such as *Fusarium*, *Lasiodiplodia*, and *Phytophthora*. This disease poses a significant threat to food security in tropical and subtropical regions. Accurate microbial identification is essential for understanding CRRD pathology. However, conventional methods for isolating microorganisms from diseased roots—particularly fungi—have limitations. For instance, incomplete surface sterilization can lead to the isolation of non-axenic fungal colonies. To address this issue, we propose a modified methodology that includes a surface particle-removal step and sterility controls to validate its effectiveness. Our method significantly improved the isolation of axenic fungal colonies from CRRD-affected roots compared to traditional techniques across three different culture media. Out of 60 samples per method, the proposed method yielded a statistically higher proportion of axenic fungal colonies (88.3%) than the traditional approach (30%). Although the proposed method facilitates microbial isolation, further validation is needed to assess its reliability across various pathogens and environmental conditions.

Keywords: Cassava; Isolation; Microorganisms; Root rot disease; Root sample.

Resumen
La mandioca (*Manihot esculenta* Crantz) es un alimento básico para millones de personas en todo el mundo, principalmente debido a sus raíces almacenadoras comestibles. Sin embargo, dichas raíces son susceptibles a la Pudrición Radical de la Mandioca (PRM), enfermedad causada frecuentemente por hongos (*Fusarium*, *Lasiodiplodia* o *Phytophthora*), que es una amenaza para la seguridad alimentaria en regiones tropicales y subtropicales. Una identificación precisa de los microorganismos involucrados es fundamental para mejor comprensión de la PRM. En este sentido, los métodos convencionales de aislamiento de microorganismos a partir de raíces enfermas, en particular hongos, presentan ciertas limitaciones. Por ejemplo, una incompleta esterilización superficial de las muestras puede conducir al aislamiento de colonias fúngicas no axénicas. En este trabajo, se propone una metodología modificada, que incorpora un paso de remoción de partículas superficiales y controles de esterilidad que permiten validar la eficacia de esta etapa. Nuestro método mejoró significativamente el aislamiento de colonias fúngicas axénicas a partir de raíces con síntomas de PRM en comparación con las técnicas tradicionales en tres medios de cultivo distintos. De 60 muestras procesadas por cada método, la metodología propuesta logró un porcentaje estadísticamente superior de colonias fúngicas axénicas (88.3%) en comparación con el enfoque tradicional (30%). A pesar de que el método propuesto facilitó el aislamiento microbiológico, se requiere una validación adicional para evaluar su robustez frente a distintos patógenos y condiciones ambientales.

Palabras clave: Mandioca; Aislamiento; Microorganismos; Pudrición radical; Muestra de raíz.

Introduction

Cassava (*Manihot esculenta* Crantz), a member of the Euphorbiaceae family, is a perennial shrub (1) cultivated in tropical and subtropical regions (2,3). Its storage roots (SRs) serve as a staple food in South and North America, Central Africa, and Southeast Asia (4). In 2021, global cassava production reached 315 million tonnes, with a total trade value of 3.65 billion USD (5).

The anatomical structure of the SR comprises three distinct layers: the peel, pulp, and central fibers (6). The peel includes both the periderm, located on the external surface, and the cortex layer (6,7). The pulp, which constitutes the edible portion, is mainly composed of starch-rich secondary xylem tissue (7). At the core, the central fibers contain rows of parenchyma and xylem sclerenchyma vessels (8).

The productivity and quality of storage roots (SR) can be severely affected by various diseases, including Cassava Root Rot Disease (CRRD). CRRD leads to root necrosis, which alters the consistency and appearance of the edible pulp and results in yield losses ranging from 30% to 100% (9). It is frequently caused by microbial pathogens, particularly fungi such as *Fusarium*, *Neoscytalidium*, *Lasiodiplodia*, and *Phytophthora* (10–12).

Understanding the diversity and characteristics of microorganisms associated with CRRD is crucial for developing effective disease management strategies (9,10,13). As noted by Hochmuth et al. (2012), the examination of plant tissue supports both nutrient monitoring and diagnostic efforts. Another important objective is to determine the microbial composition within and surrounding the plant tissue (15). Diagnosing microbial pathogens involves identifying both the causative agent of the disease and its associated characteristics and symptoms (15). The search for an optimal technique to investigate root–microorganism interactions, particularly those involving fungi, remains a significant challenge (16,17).

Microbial pathogen diagnosis involves identifying the causative agent of a disease, along with its characteristics and symptoms (15). In particular, diagnosing microbial pathogens in roots presents additional complexity compared to detection in other plant tissues. Roots are embedded in the soil matrix, where they host a diverse community of microorganisms (18,19), and they engage in early interactions with both the soil and its microbial inhabitants (18,19). Traditional methods for isolating fungi from plant tissues, including storage roots (SR), typically begin with the removal of visible soil debris by rinsing with tap water (21), followed by dissection. The resulting root pieces are then surface-sterilized and cultured to isolate microorganisms (15).

During microbial isolation from decayed root samples, a major limitation is the practical impossibility of removing all soil particles using only water rinsing (22–24), particularly those lodged within or between root tissues (19,25,26). As a result, cleaning—specifically the separation of debris—becomes a complex and labor-intensive task (21). Residual soil particles contribute a substantial microbial load (27), increasing the likelihood of mixed microbial cultures and thereby complicating both isolation and analysis (23). Although sequential sterilization steps are intended to reduce microbial contamination, they do not always ensure complete asepsis. Addressing the challenges of microbial diagnosis in CRRD requires the development of novel procedures that retain consensus protocols while remaining efficient and practical (28). To overcome some of these limitations and enhance the qualitative isolation of microorganisms from storage roots (SR) showing CRRD symptoms, we proposed a modified isolation method. This method built upon the traditional workflow by incorporating an additional surface-particle removal step, thereby increasing the probability of obtaining axenic fungal colonies.

Two Sterility Controls (SCs) were included to evaluate the effectiveness of the surface-particle removal step: surface imprinting onto culture media (SC1) (29–31) and cultivation of an aliquot of the final wash water after mechanical agitation (SC2) (32–34). SC1 involved transferring potential surface microorganisms onto the agar by pressing the root sample directly onto the medium surface. Imprinting is suitable for various surface types, including smooth, rough, and irregular textures (35). SC1 was critical in confirming that the isolated fungi were not present on the surface of the sample. Similarly, SC2 confirmed the absence of microbial load detaching from the sample surface, thereby verifying the effectiveness of the washing process. Together, SC1 and SC2 served as baseline controls to differentiate microorganisms introduced during handling.

Materials and methods

<u>Collection of the CRRD samples</u>

Field collection was carried out in accordance with local regulations governing access to natural and genetic resources in the province of Misiones. Prior informed consent was obtained from the Misiones Institute of Biodiversity (Resolution No. 44/24). A total of 20 storage roots (SR) exhibiting CRRD symptoms (36) were collected from a cassava field near the town of Wanda, Misiones, Argentina (25º 95′ S; 54º 52′ W), where the soil is classified as Ultisol (37). The SR were stored at 18 ± 2 ºC in plastic bags for less than 24 hours (21) before arrival at the laboratory.

Description of the isolation methods tested

In this study, two isolation methods were evaluated: the traditional method (A) and the proposed method (B) (Fig. **1**). Method A was adapted from Nyaka et al. (2015) (38), Oliveira et al. (2016) (39), and Sangpueak et al. (2023) (13), and included the following steps: (I) Cleaning: removal of soil debris using tap water. (II) Dissection: cutting the roots into small pieces (approximately 5–25 mm). (III) Sterilization: sequential treatment of the root pieces with 70% ethanol, followed by 1% sodium hypochlorite, and finally 90% ethanol, for 1 minute each. (IV) Inoculation: placing the root sample in a sterile 90 mm Petri dish containing 20 mL of culture medium. (V) Cultivation.

Method B consisted of the following steps: (I) Cleaning: removal of visible soil debris using tap water. (II) Dissection: cutting the roots into small pieces (approximately 5-25mm) differentiating pulp-only samples. (III) Sterilization: sequential treatment with 70% ethanol, 1% sodium hypochlorite, and 90% ethanol, for 5 minutes each. (IV) Surface-particle removal: agitating the root pieces in an analog vortex at medium speed for 3 minutes (34,40) in tubes containing sterile distilled water (SDW). The samples are then transferred to new tubes with fresh SDW, and the step is repeated until no sediments are released after agitation. The number of washes should be first guided by visual clarity of the wash water and then confirmed using the sterility controls (SCs). (V) Inoculation: for each sample, inoculate 20 µL of the water from the final rinse (SC2), perform the imprinting technique (SC1), and place the root piece in a sterile 90 mm Petri dish containing 20 mL of culture medium. (VI) Cultivation. For the investigation of potential CRRD causal agents, only samples yielding axenic microbial colonies should be considered. In Method B, this condition is confirmed by the absence of microbial growth in both sterility controls (see Case 1 in Fig. **2**).

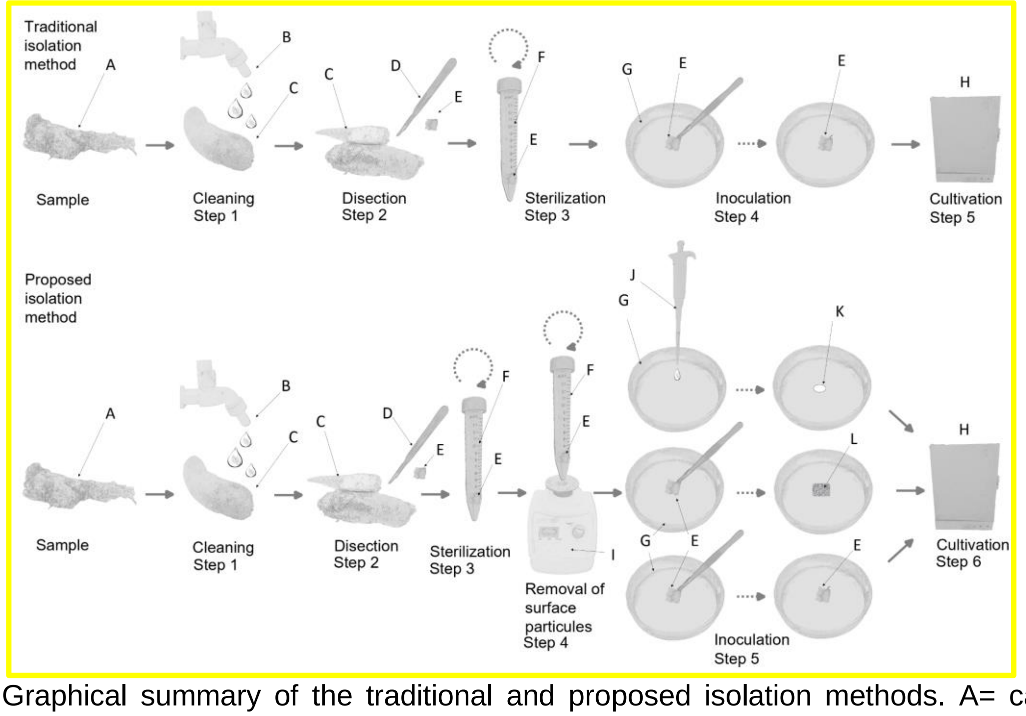

Fig. 1 Graphical summary of the traditional and proposed isolation methods. A= cassava storage root embedded with soil. B= tap water. C= cassava storage root. D= bistoury. E= cassava storage root sample. F= centrifuge tube. G= Petri dish. H= incubator. I= analog vortex. J= micropipette. K= water from the last wash. L= imprinting.

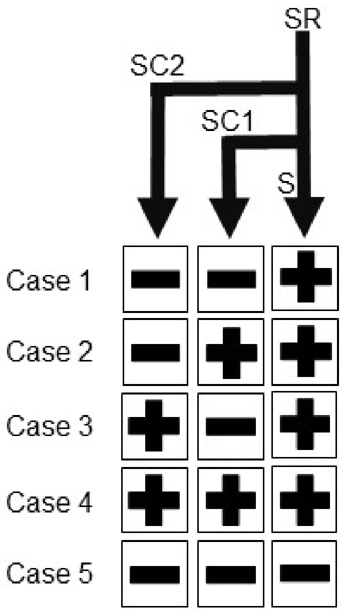

Fig. 2 Schematic representation of possible outcomes in the proposed method. SR= storage root. S= dissected root sample. SC1= sterility control 1 (imprinting). SC2= sterility control 2 (water from the last wash). The symbols **+** and **-** indicate microbial growth and absence of microbial growth, respectively. Case 1: microbial growth is observed only in **S**. Case 2: microbial growth is observed in **S** and **SC1**. Case 3: microbial growth is observed in **S** and **SC2**. Case 4: microbial growth is observed in **S**, **SC1**, and **SC2**. Case 5: no microbial growth is observed.

Calibration of the number of washes (step IV)

To determine the optimal number of washes during the surface particle removal step, four washing frequencies were tested: 0 washes (Level 1), 1 wash (Level 2), 3 washes (Level 3), and 5 washes (Level 4). For this experiment, a total of 80 SR samples were cultivated, with 20 samples allocated to each level. The samples were placed in sterile 90 mm Petri dishes containing 20 mL of PDA and incubated in darkness at 28 ± 2 °C for 7–10 days. Following the cultivation period, the colonies were classified into two categories: axenic samples, containing only one type of fungal colony, and non-axenic samples, containing two or more types of fungal colonies (Fig. **3** and Fig. **4**).

For the statistical analysis, the number of washes was considered the independent variable, and the classification of fungal colonies was the dependent variable. Level 1 (no surface-particle removal, as in the traditional method) was used as the reference category. The levels were coded as 0, 1, 3, and 5, corresponding to the number of washes in each treatment. The assumptions of homogeneity across levels and a linear trend were assessed using the chi-square (χ^2) test at a significance level of 0.05, using Epidat v3.1 (41).

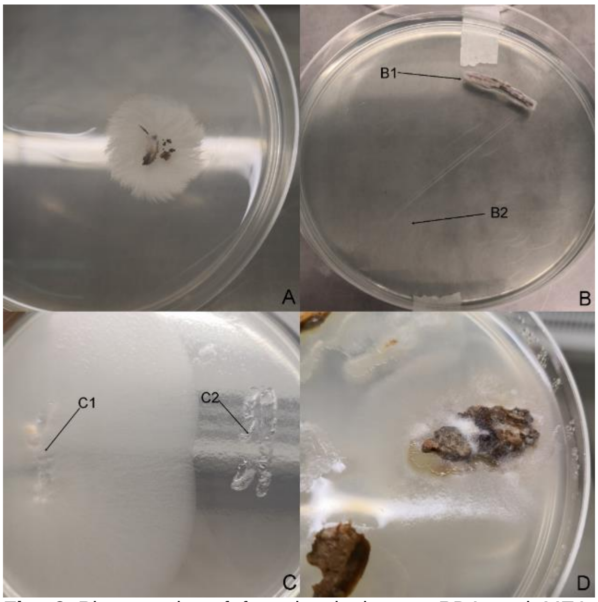

Fig. 3 Photographs of fungal colonies on PDA and MEA obtained during the isolation of microorganisms from cassava root rot samples. A= axenic colony. B= axenic colony (B1) with no microbial growth in the imprinting (B2). C= Imprints with (C1) and without (C2) microbial growth. D= sample showing more than one type of microbial colony (non-axenic).

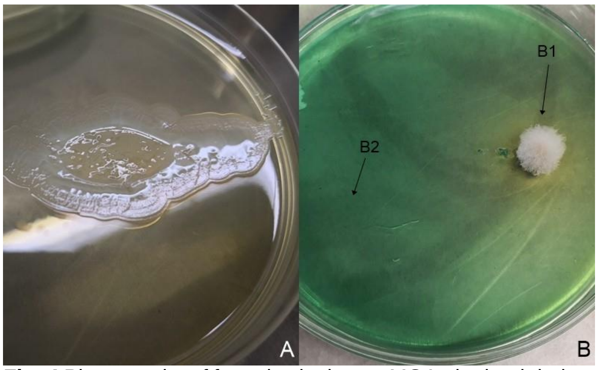

Fig. 4 Photographs of fungal colonies on MGA obtained during the isolation of microorganisms from cassava root rot samples. A= Imprint with microbial growth on MGA. B= axenic colony (B1) with no microbial growth in the imprinting (B2) on MGA.

Comparison in the proportion of axenic fungal colonies between the isolation methods

The traditional method (A) and the proposed method (B, with the optimal number of washes) were tested using a stratified design. Three types of culture media were used: Potato Dextrose Agar (PDA), Malt Extract Agar (MEA), and Malachite Green Agar (MGA), the latter being a selective medium for *Fusarium* species (42). A total of 120 SR samples were cultivated, with 60 samples processed using method A and 60 using method B. For each method, the 60 samples were evenly distributed across the three media types, with 20 samples per medium. The samples were placed in sterile 90 mm Petri dishes containing 20 mL of the corresponding culture medium (PDA, MEA, or MGA) and incubated in darkness at 28 ± 2 ºC for 7–10 days. Following the incubation period, the fungal colonies from each sample were classified as previously described—either axenic or non-axenic (Fig. **3** and Fig. **4**). For the statistical analysis, two independent variables (methods A and B) within three strata (PDA, MEA, and MGA) and one dependent variable (classification of fungal colonies) were considered. Homogeneity across strata was assessed using the X^2 (chi-square) test with a significance level of 0.05. To evaluate potential statistically significant differences between the two isolation methods in the proportion of axenic fungal colonies isolated from SR with CRRD symptoms (i.e., association across strata), the Mantel-Haenszel test was applied, also with a significance level of 0.05, using Epidat v3.1 (41).

Results

Preliminary calibration of the proposed method

It was observed that relatively small samples (approximately 25 mm or less) were optimal for isolation. Preliminary data showed that all samples exhibited microbial growth following a 5-minute duration for each sterilization step. However, some samples did not produce microbial growth with extended sterilization times (see case 5 in Fig. **2**). Therefore, a sterilization time of 5 minutes was deemed sufficient for this step. Additionally, different numbers of samples per Petri dish were tested preliminarily. Up to 2–3 samples per dish were manageable, considering a cultivation period of 7–10 days. Optionally, samples in a single Petri dish could include those from tissue incubation, imprinting, and the water from the last rinse. Fungal growth was apparent from the 2nd day of cultivation, becoming more vigorous by day 10. After this period, most microbial colonies began to overlap.

Calibration of the number of washes (step IV)

Results indicated a statistically significant difference ($P < 0.01$) in the proportion of axenic colonies across the levels studied (0 to 5 washes), with a clear linear trend ($P < 0.001$). The highest proportion of axenic fungal colonies (85%) was observed with five washing repetitions, while the lowest (25%) was recorded with no washing (Fig. **5**). Based on these findings, five washing repetitions (level 4) were selected for use in the proposed method in subsequent analyses.

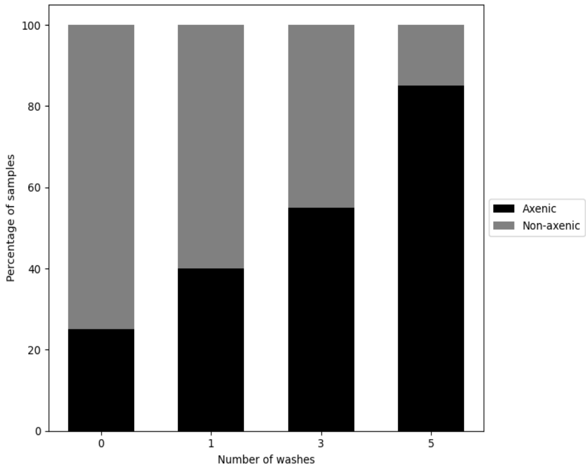

Fig. 5 Proportion of axenic (black bars) and non-axenic (grey bars) fungal cultures obtained from SR samples subjected to varying numbers of washes during the surface-particle removal step.

Comparison in the proportion of axenic fungal colonies between the isolation methods

Results indicated a statistically significant difference ($P < 0.001$) in the proportion of axenic colonies between the two isolation methods (Fig. **6**). Overall, Method A yielded 18 axenic colonies out of 60 samples (30%), whereas Method B yielded 53 axenic colonies (88.3%). No statistically significant differences were observed across culture media strata ($P > 0.5$); however, a significant association between the isolation method and the proportion of axenic colonies was detected after adjusting for culture medium using the Mantel-Haenszel test ($P < 0.001$). Therefore, results can be analyzed as a whole (independently of strata), indicating that the type of culture media did not significantly influence the proportion of axenic fungal colonies. In other words, the observed differences were attributable to the isolation method used. Notably, non-axenic colonies obtained with Method B also exhibited microbial growth in both sterility controls.

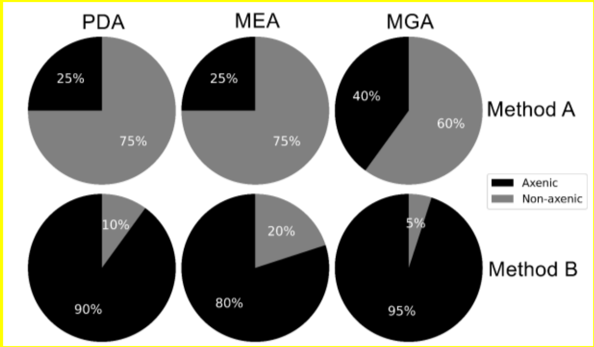

Fig. 6 Proportion of axenic (black) and non-axenic (grey) fungal cultures obtained from SR samples processed using two isolation methods (A and B) across three different culture media: potato dextrose agar (PDA), malt-extract agar (MEA) and malachite green agar (MGA).

Discussion

In the proposed method for isolating fungi from SR with CRRD symptoms (method B), specific improvements were introduced compared to the traditional approach (method A). Both methods begin with the same initial steps (steps I-III: cleaning, dissection and sterilization). The order of steps II and III was carefully considered. Although reversing the sequence is possible, it is recommended to perform dissection before sterilization. This sequence allows for more precise and localized sterilization, potentially reducing both the required waiting time and the amounts of sterilizing agents used.

During dissection (step II), the size and selection of the samples should be considered. In this experiment, samples were cut specifically to target the pulp tissues, as it is the main component of the root where symptoms are observed. However, further differentiation between tissue types may become crucial for understanding fungal distribution within the root. Although the optimal size for fungal recovery requires further evaluation, preliminary experiments showed that even small samples contained a high microbial load.

Although both methods used ethanol and sodium hypochlorite solutions for sterilization (step III), it is important to assess whether these agents are the most effective at eliminating all potential surface contaminants. Further studies could explore alternative disinfectants or variations in the concentration and duration of the disinfection process to optimize sterilization (43), while introducing none or only minimal artifacts to the samples.

Our results indicated that the removal of surface soil particles (step IV) played a crucial role in improving sample cleanliness, thereby reducing the risk of microbial contamination during subsequent processes. Additionally, two sterility controls were included for this step. Ideally, these sterility controls should show no microbial growth, indicating the absence of contaminants on the sample surface. Consequently, if microbial growth is observed only in the root sample, it can be inferred that the microbes originated exclusively from inside the sample and not from its surface (see case 1 in Fig. **2**).

In case of severe necrosis where tissue differentiation is impossible, it would be unclear which root tissue the fungi originated from. However, even in such cases, the proposed method may reduce the likelihood of obtaining isolates from external sources (e.g., soil particles attached to the roots), due to validation through SCs.

More than five agitation cycles may be necessary in step IV when samples are highly decayed or damaged (44). This is supported by the observation that non-axenic colonies obtained with method B also showed fungal growth in SC1 and SC2. However, it is important to note that axenic colonies exhibiting growth in the sterility controls, but with morphology consistent with the colony from the pulp sample, may still be relevant in the context of CRRD (see cases 2, 3 and 4 in Fig. **2**), although their exact tissue origin cannot be determined (16).

The removal of surface soil particles could be further improved by substituting SDW with alternative solutions (23). Evidence indicates that chelating agents, detergents, or saline solutions enhance particle detachment (24). Incorporating such solutions into the agitation process can improve the removal of surface contaminants, leading to cleaner and more reliable samples for microbial isolation. Additionally, exploring alternative mechanical agitation techniques (24) can further optimize surface soil particle removal in method B. For instance, Cuske *et al.* 2014 (45) demonstrated the effectiveness of ultrasonic agitation for cleaning plant samples. However, it should be noted that these techniques might damage fragile cells (22), warranting further investigation.

Exploring different incubation conditions could offer valuable insights into enhancing the growth and differentiation of fungal colonies during the isolation process. In this study, incubation was carried out under standard conditions: in darkness at a temperature of 28 ± 2 ºC for 7-10 days. However, varying incubation temperatures (20,40,46) or durations could be investigated to optimize the isolation procedure.

Regarding the culture media, this study utilized PDA and MEA —both non-selective, nutrient rich media commonly employed for fungal isolation of cassava SR samples with CRRD symptoms (47)—as well as the selective medium MGA. However, it would be valuable to investigate whether isolation efficiency could be improved by incorporating inhibitors such as antibiotics (39) or specific nutrients into the growth media (40,43). Testing different media types (16), including additional selective or general-purpose media that support the growth of a wide range of fungi, could provide further insights into the diversity and composition of the fungal community associated with CRRD.

Ensuring quality control during the isolation process is essential for obtaining accurate and reliable results. Visual inspection, as suggested by Zhu *et al.* (2008) (48), can complement the proposed method by serving as an additional checkpoint for contamination. Moreover, incorporating a mechanical purification step on agar plates —such as the hyphal tip technique (15) or the method proposed by Shi *et al.* (2019) (49)—can further validate sample cleanliness.

Regarding the practical applicability and reproducibility of the proposed method, it was developed by introducing minor modifications to the widely used protocol for isolating fungi from SR (11,12), making it easily implementable across various laboratory settings. The central idea behind the proposed method was to maintain practicality and accessibility for researchers familiar with conventional techniques, as recommended by Fischer and Zigmond (2010) (28). Although the proposed method slightly increases the complexity of the process —requiring relatively more resources and time during the isolation of microorganisms from CRRD samples—this investment is offset by a reduced risk of handling non-axenic fungal colonies in subsequent steps and the achievement of more consistent results (50).

The wide-ranging assortment of cultivable cassava varieties and their cultivation across diverse soil profiles (24) highlights the need for a versatile approach to investigating CRRD, emphasizing the importance of accounting for the heterogeneous nature of the disease (10). Different forms of CRRD can be caused by various pathogens, each requiring a tailored investigative strategy. In this context, the necessity of cross-validating the proposed method—considering different types of pathogens and field conditions—is evident. Moreover, it is important to recognize that CRRD may involve microbial succession throughout the progression of the disease (51), meaning that the diagnostic perspective could shift depending on the specific timing of sample collection.

Sharing practical tips and addressing potential challenges encountered during microbial isolation from plant tissue could support the successful adoption of more advanced methods by researchers (28,52). Additionally, discussing practical limitations—such as the time, resources, and expertise required to implement the method in larger-scale studies— would be beneficial (53).

Conclusions

The proposed method resulted in a statistically significant increase in the proportion of axenic colonies isolated from cassava SR samples with CRRD symptoms, offering a more systematic approach to mitigating the effects of incomplete surface sterilization. This method has the potential to contribute to a more precise understanding of the microbial dynamics involved in CRRD.

List of abbreviations

CRRD= Cassava Root Rot Disease
MEA= Malt-Extract Agar
MGA= Malachite Green Agar
PDA= Potato Dextrose Agar
PRM= Pudrición Radical en Mandioca
SC= Sterility Control
SDW= Distilled Sterilized Water
SR= Cassava Storage Roots

Acknowledgements

This work was funded by the Secretaría General de Ciencia y Técnica UNaM (16/Q1647–PDTS) and the Agencia Nacional de Promoción de la Investigación, el Desarrollo Tecnológico y la Innovación (UNaM PICTO 02022–00029).

The authors would like to thank Sofía Alexandra Madrassi for her advice on image editing and Andrea Liliana Onetto for assistance with writing and grammar.

Data availability statement

All data generated during this study are included in this published article.

Conflict of interest

On behalf of all authors, the corresponding author states that there is no conflict of interest.

References

1. Mohidin SRNSP, Moshawih S, Hermansyah A, Asmuni MI, Shafqat N, Ming LC (2023) Cassava (*Manihot esculenta* Crantz): A systematic review for the pharmacological activities, traditional uses, nutritional values, and phytochemistry. JEBIM 28, 2515690X231206227

2. Falade KO, Akingbala JO (2010) Utilization of cassava for food. Food Rev. Int. 27(1):51-83

3. OECD/FAO. OECD-FAO Agricultural Outlook 2023-2032. c2023. Available at: https://www.oecd-ilibrary.org/agriculture-and-food/oecd-fao-agricultural-outlook-2023-2032_08801ab7-en. Accessed on August 14, 2023

4. Jiang D, Wang Q, Ding F, Fu J, Hao M (2019) Potential marginal land resources of cassava worldwide: A data-driven analysis. Renew. Sustain. Energy Rev. 104:167-73

5. Otekunrin, O. A. (2024). Cassava (*Manihot esculenta* Crantz): a global scientific footprint—production, trade, and bibliometric insights. Discov. Agric. 2(1): 94

6. Carluccio AV, David LC, Claußen J, Sulley M, Adeoti SR, Abdulsalam T, *et al*. (2022) Set up from the beginning: The origin and early development of cassava storage roots. Plant, Cell & Environ. 45(6):1779-95

7. Adetan DA, Adekoya LO, Aluko OB (2003) Characterisation of some properties of cassava root tubers. J. Food Eng. 59(4):349-53

8. Wilhelm J, Wojciechowski T, Postma JA, Jollet D, Heinz K, Böckem V, *et al*. (2022) Assessing the storage root development of cassava with a new analysis tool. Plant Phenomics 2022/9767820

9. Hohenfeld CS, Passos AR, De Carvalho HWL, De Oliveira SAS, De Oliveira EJ (2022) Genome-wide association study and selection for field resistance to cassava root rot disease and productive traits. PLoS one 17(6):e0270020

10. Teixeira JHDS, Guimarães MAS, Cardoso SC, Brito ADS, Peixouto YS, Ribeiro SO, *et al*. (2021) Distribution of resistance of cassava genotypes to dry, soft and black root diseases and correlation to yield parameters. J Phytopathol. 169(6):350-9

11. Pham CV, Tran HT (2021) *Cunninghamella elegans* causing cassava root rot in Vietnam. Australasian Plant Dis Notes 16(1):14

12. Silva IO, Amorim EPDR, Nascimento Junior NA, Carnauba JP, Araújo Neto VFD, Peixinho GS (2022) The first report about *Fusarium falciforme* that causes root rot in cassava cv Rosinha, in Alagoas state, Brazil. RSD 11(12):e221111234369

13. Sangpueak R, Duchanee S, Saengchan C, Papathoti NK, Hoang NH, Thanh TL, *et al.* (2023) Identification of cassava black stem and root rot agents in Thailand. Chil. J. Agric. Res. 83(1):70-82

14. Hochmuth GJ, Maynard D, Vavrina C, Hanlon E, Simonne E. Plant Tissue Analysis and Interpretation for Vegetable Crops in Florida. Gainesville: EDIS. Available at: https://doi.org/10.32473/edis-ep081-2004. Accessed on July 14, 2024

15. Thilagam R, Kalaivani G, Hemalatha N (2018) Isolation and identification of phytopathogenic fungi from infected plant parts. Int. J. Curr. Pharm. Sci. 10(1):26

16. Harley JL, Waid JS (1955) A method of studying active mycelia on living roots and other surfaces in the soil. TBMS 38(2):104-18

17. Unestam T, Stenström E (1989) A method for observing and manipulating roots and root associated fungi on plants growing in nonsterile substrates. Scand. J. For. Res. 4(1-4):51-8

18. Parkinson D, Taylor GS, Pearson R (1963) Studies on fungi in the root region: I. The development of fungi on young roots. Plant Soil 19(3):332-49

19. Fahey TJ, Yanai RD, Gonzales KE, Lombardi JA (2017) Sampling and processing roots from rocky forest soils. Ecosphere 8(6)

20. L Lübeck M, Lübeck PS (2018) Isolation and screening of cellulolytic filamentous fungi. In: Lübeck M. (Ed.) Cellulases: Methods and Protocols. New York: Springer. p. 37-45

21. Böhm W (1979) Techniques of Root Washing. In: Böhm W (Ed.) Methods of

Studying Root Systems. Berlin: Springer Berlin Heidelberg. p. 115-24
22. Macdonald RM (1986) Sampling soil microfloras: Dispersion of soil by ion exchange and extraction of specific microorganisms from suspension by elutriation. Soil Biol. Biochem. 18(4):399-406
23. Azcue JM (1996) Comparison of different cleaning procedures of root material for analysis of trace elements. J. Environ. Anal. Chem. 62(2):137-45
24. Riis V, Lorbeer H, Babel W (1998) Extraction of microorganisms from soil: evaluation of the efficiency by counting methods and activity measurements. Soil Biol. Biochem. 30(12):1573-81
25. Hunt HW, Reuss DE, Elliott ET (1999) Correcting estimates of root chemical composition for soil contamination. Ecology 80(2):702-7
26. Janzen JH (2002) Correcting mathematically for soil adhering to root samples. Soil Biol. Biochem. 34(12):1965-8
27. Verran J, Boyd RD (2001) The relationship between substratum surface roughness and microbiological and organic soiling: A review. Biofouling 17(1):59-71
28. Fischer BA, Zigmond MJ (2010) The essential nature of sharing in science. Sci. Eng. Ethics. 16(4):783-99
29. Parsa S, García-Lemos AM, Castillo K, Ortiz V, López-Lavalle LAB, Braun J, *et al*. (2016) Fungal endophytes in germinated seeds of the common bean, *Phaseolus vulgaris*. Fungal Biol. 120(5):783-90
30. Sanhueza T, Herrera H, Arriagada C (2022) Microbial antagonism against phytopathogenic *Botrytis cinerea* in highbush blueberry (*Vaccinium corymbosum* L.) cultivars. Contribution of leaf-associated microorganisms from native *Andean Ericaceae*. Preprint at https://doi.org/10.21203/rs.3.rs-2039166/v1
31 Hofbauerová M, Rusková M, Puškárová A, Bučková M, Annušová A, Majková E, *et al*. (2023) Protection and disinfection activities of oregano and thyme essential oils encapsulated in poly(ε-caprolactone) nanocapsules. Molecules 28(3):1018
32. Ikediugwu FEO, Ejale AU (1980) Root-surface mycoflora of cassava (*Manihot esculenta*) and post harvest rot of the tubers. Mycopathologia 71(2):67-71
33. Dennis PG, Miller AJ, Clark IM, Taylor RG, Valsami-Jones E, Hirsch PR (2008) A novel method for sampling bacteria on plant root and soil surfaces at the microhabitat scale. J. Microbiol. Methods 75(1):12-8
34. Sumiati T, Suryadi H, Suryadi H, Suryadi H (2022) Isolation of white rot fungi from rotten wood from bogor botanical garden in Indonesia and its ligninolytic enzymes activity. Pharmacognosy J. 14(1):68-75
35. Hirsch P, Eckhardt FEW, Palmer RJ (1995) Methods for the study of rock-inhabiting microorganisms—A mini review. J. Microbiol. Methods 23(2):143-67
36. Bandyopadhyay R, Mwangi M, Aigbe SO, Leslie JF (2006) *Fusarium* species from the cassava root rot complex in west Africa. Phytopathology 96(6):673-6
37. Gunther DF, Correa de Temchuk F, Lysiak E (2008) Zonas agroeconómicas homogéneas en Misiones. INTA 113 p. Available at: https://redbus.usal.edu.ar/cgi-bin/koha/opac-detail.pl?biblionumber=117415&shelfbrowse_itemnumber=183564
38. Nyaka NAIC, Kammegne DP, Ntsomboh NG, *et al*. (2015) Isolation and identification of some pathogenic fungi associated with cassava (*Manihot esculenta* Crantz) root rot disease in Cameroon. Afr. J. Agric. Res. 10:4538–4542
39. Oliveira SAS de, Boas SAV, Bragança CAD, *et al*. (2016) First report of *Phytophthora melonis* causing cassava wilt and root rot in Bahia State, Brazil. Summa Phytopathologica 42:107–107
40. Macher JM (2001) Evaluation of a procedure to isolate culturable microorganisms from carpet dust: isolation of culturable microorganisms from dust. Indoor Air 11(2):134-40
41. Santiago Pérez MI, Hervada Vidal X, Naveira Barbeito G, Silva LC, Fariñas H, Vázquez E *et al*. (2010) El programa epidat: usos y perspectivas. RPSP 27(1):80-3. Available at: https://pesquisa.bvsalud.org/portal/resource/pt/lil-577027
42. Castellá G, Bragulat MR, Rubiales MV, Cabañes FJ (1997) Malachite green agar, a new selective medium for *Fusarium* spp. Mycopathol. 137(3):173-8
43. Verma VC, Gond SK, Kumar A, Kharwar RN, Boulanger LA, Strobel GA (2011) Endophytic fungal flora from roots and fruits of an indian neem plant *Azadirachta indica* A. Juss., and impact of culture media

on their isolation. Indian J. Microbiol. 51(4):469-76
44. Waid JS (1956) Root dissection: a method of studying the distribution of active mycelia within root tissue. Nature 178(4548):1477-8
45. Cuske M, Karczewska A, Gałka B. Ultrasonic cleaning of plant roots in their preparation for analysis on heavy metals. Zielona Góra: Oficyna Wydawnicza Uniwersytetu Zielonogórskiego. Available at: https://zbc.uz.zgora.pl/repozytorium/dlibra/publication/51610?language=pl. Accessed on April 19, 2024
46. Nakae T (1966) Method of temperature-gradient incubation and its application to microbiological examinations. J Bacteriol. 91(5):1730-5
47. Guo H, Li CP, Shi T, Fan CJ, Huang GX (2012) First report of *Phytophthora palmivora* causing root rot of cassava in China. Plant Dis. 96(7):1072-1072
48. Zhu C, Gore M, Buckler ES, Yu J (2008) Status and prospects of association mapping in plants. Plant Genome 1(1)
49. Shi XX, Qiu HP, Wang J yu, Zhang Z, Wang YL, Sun GC (2019) A handy method to remove bacterial contamination from fungal cultures. PLoS one 14(11)
50. Lakhani KR, Jeppesen LB, Lohse PA, Panetta JA. The value of openness in scientific problem solving. Cambridge: HBS Working Paper. Available at: http://hbswk.hbs.edu/item/5612.html. Accessed on January 29, 2024
51. Gray L, Kernaghan G (2020) Fungal succession during the decomposition of ectomycorrhizal fine roots. Microb. Ecol. 79(2):271-84
52. Bousari RG, Hassanzadeh M (2012) Factors that affect scientists' behavior to share scientific knowledge. CJSIM 6(2):215-27
53. Tenopir C, Allard S, Douglass K, Aydinoglu AU, Wu L, Read E, *et al*. (2011) Data sharing by scientists: practices and perceptions. PLoS one 6(6):e21101

RECyT
Year 27 / Nº 43 / 2025 /
DOI: https://doi.org/10.36995/j.recyt.2025.43.009

Virtual therapeutic exercise system for the treatment of metabolic syndrome

Sistema de ejercicios terapéuticos para el tratamiento del síndrome metabólico desde la virtualidad

Cristina, Carrera Valdés[1, *]; Lisset Haydeé, Romero Sánchez[1]; Arnaldo, Herrera- Ponce[1]; Leidys, Escalante Candeaux[1]

1- University of Physical Culture and Sport Sciences “Manuel Fajardo” (UCCFD). Santa Catalina 12453, Primelles and Boyeros, Cerro, Havana, Cuba.

* E-mail: crisvalded9@gmail.com

Received: 07/06/2024; Accepted: 31/03/2025

Abstract
Introduction: Metabolic syndrome is characterised by the appearance of obesity, diabetes mellitus and arterial hypertension. In Cuba, people are limited in their practice of therapeutic exercises to control this disease due to the lack of access to gyms. Therefore, this research provided a didactic means and an alternative for performing therapeutic exercises virtually. Research objective: To evaluate the effectiveness of the implementation of a virtual therapeutic exercise system for the control of abdominal obesity in the metabolic syndrome. Methods: A pre-experimental, analytical, minimal control study was conducted, incorporating a pre-test and post-test for a single control group, which was established within a Facebook group. Results: The system of therapeutic exercises carried out on the Facebook platform successfully reduced the levels of abdominal obesity, with the vast majority of participants reducing their weight, despite remaining in the same grade II obesity range and conducting the therapeutic exercises in a virtual environment. Conclusion: The analysis of the theoretical-methodological foundations supports the effectiveness of the virtual therapeutic exercise system in controlling abdominal obesity in metabolic syndrome, and justifies the particularities of the process through virtuality on how to programme, dose, control, and evaluate systematic practitioners with metabolic syndrome.

Keywords: Obesity, Virtuality, dose and practitioners.

Resumen
Introducción: el síndrome metabólico se caracteriza por la aparición de la obesidad, diabetes mellitus e hipertensión arterial. En Cuba las personas se limitan en la práctica de los ejercicios terapéuticos para el control de esta enfermedad dejando de asistir a los gimnasios, por lo que esta investigación aportó un medio didáctico y una alternativa para realizar ejercicios terapéuticos a través de la virtualidad. Objetivo de investigación: Evaluar la efectividad de la implementación de un sistema de ejercicios terapéuticos virtuales para el control de la obesidad abdominal en el síndrome metabólico. Métodos: se realizó un estudio analítico pre-experimental de control mínimo con pre-test y post-test para un solo grupo de control, incorporados a un grupo de Facebook. Resultados: el sistema de ejercicios terapéuticos realizado en la plataforma de Facebook consiguió reducir los niveles de obesidad abdominal, disminuyendo la gran mayoría de ellas el peso, a pesar de permanecer en el mismo rango de obesidad grado II y realizar los ejercicios terapéuticos desde un entorno virtual. Conclusión: el análisis de los fundamentos teóricos-metodológicos sustentan la efectividad del sistema de ejercicios terapéuticos virtuales para el control de la obesidad abdominal en el síndrome metabólico y justifican las particularidades del proceso a través de la virtualidad del como programar, dosificar, controlar y evaluar a los practicantes sistemáticos con síndrome metabólico.

Palabras claves: Obesidad, virtualidad, dosificar y practicantes.

Introduction

The metabolic syndrome is composed of a set of metabolic diseases that appear simultaneously, constituting risk factors in the same individual. It is characterised by the appearance of obesity, diabetes mellitus and arterial hypertension, which is why patients with this pathology must continue their treatment (Carrera *et al.*, 2020).

In this sense, the Master's thesis of Carrera (2023), entitled “Physical exercise programme for the treatment of metabolic syndrome from a virtual environment” was used as a reference. This study was conducted during the COVID-19 pandemic, during which participants successfully utilised virtuality as an alternative. For women with metabolic syndrome, with a predominance of obesity accompanied by hypertension and diabetes mellitus, this research provided a didactic means to perform therapeutic exercises using virtual learning environments to continue their therapeutic exercise treatment. (González *et al.*, 2022)

The first description of a patient with metabolic syndrome and hypertriglyceridaemia was made by Nicolaes Tulp (1593-1674), a Dutch surgeon and anatomist who went down in history for having posed for Rembrandt in his masterly canvas “Anatomy Lesson of Dr. Tulp”, displayed in the Mauritshuis Museum in The Hague. However, in 1641, Tulp described the milky (lipemic) blood of a patient and established the relationship between this phenomenon and the consumption of fats, obesity, and the tendency to ‘sanguinisation’ (perhaps high blood pressure) (Marqués and Ordoñez, 2023).

Approximately 250 years ago, Giovanni Battista Morgagni (1682-1771), in the twilight of his life, wrote ‘De sedibus et causis morborum per anatomenindagatis’, a work that laid the foundations of modern pathological anatomy as a basis for pathology and clinical practice. In it, he described for the first time the increase in omental and mediastinal fat associated with abdominal obesity. He warned of the association between visceral obesity, hypertension, gout and arteriosclerosis. Morgagni's discoveries did not transcend the physicians of his time, and the importance of intra-abdominal fat accumulation was not considered again until later years (Belloni, 1974).

Vague (1911-2003), from the University of Marseille, described two distinct patterns of obesity, characterised by the distribution of body fat: android and gynoid. However, the definitive demonstration of the importance of abdominal obesity came with the Swedish epidemiological studies that introduced the waist-to-hip ratio as a more straightforward method of measuring abdominal obesity than the system devised by Vague. These studies confirmed that the waist-to-hip ratio was an independent predictor of cardiovascular mortality (Márquez and Ordoñez, 2023), and all these criteria for the diagnosis of metabolic syndrome remain valid today.

After explaining these problems, it is possible to emphasise the importance of identifying metabolic syndrome indicators promptly and understanding their relationship with therapeutic exercises (Romero, 2023).

It is essential to recognise that a lack of physical activity is a significant contributor to the development of diseases in humans. According to the International Federation of Sports Medicine (FIMS), a sedentary lifestyle is a significant risk factor for the development of chronic non-communicable diseases (diabetes mellitus type II, hypertension, fat metabolism disorders, degenerative joint diseases and osteoporosis), which are the leading causes of disease and mortality worldwide. It should be noted that therapeutic exercise is the systematic execution with a planning of postures, movements and physical activities with a defined purpose which is usually that the patient can have the means to enhance and improve physical functioning, psychological, mood, body aesthetics, reduce or prevent risk factors for health and optimise the general state of health in which it is located (Ripoll, 2020).

The research addressed practitioners who are obese and have limited time to perform therapeutic exercises in gyms or rehabilitation centres. Hence, the proposal is to use the platform to perform exercises at home. This research was conducted in a post-pandemic environment, from September 2023 to February 2024.

The virtual environment has had and continues to have an impact on modern lifestyle changes, contributing significantly to making women with obesity feel more comfortable. It enables them to engage in physical exercise in a relaxed and safe context that is more suitable for their needs. It is difficult to structure and organise groups of obese people in the community, and sometimes they feel ashamed or embarrassed about their physical appearance, which is why this virtual environment makes it easier for them to carry out their physical activities comfortably and without prejudice (Carrera, 2023).

Another aspect is that people often lack the time to perform exercises in a gym or rehabilitation centre, so they do them at home. This has led to the development of new methods for conducting therapeutic exercises through virtual platforms. From the exploration carried out, it was detected that the majority of the systematic practitioners had participated in the aforementioned research, which they enjoyed because they did not have the time to attend the rehabilitation centre, hence the need to maintain their body weight through the virtual practice of therapeutic exercises and avoiding the increase in risk factors for this group of women with metabolic syndrome in our country. Thus, it is necessary to utilise virtual environments to maintain continuity in the therapeutic exercises, in this case, on the Facebook platform. In line with the above, the scientific question is stated as follows: Is the implementation of this virtual therapeutic exercise system effective in treating metabolic syndrome in women? To address this problem, the research objective is to evaluate the effectiveness of implementing a virtual therapeutic exercise system for controlling abdominal obesity in individuals with metabolic syndrome.

Methods

The research was conducted from September 2023 to February 2024. The sample selection consisted of women with metabolic syndrome who gave their consent to participate in the research and were also users of the Facebook platform. This was an analytical pre-experimental study with minimal control, incorporating a pre-test and post-test for a single control group, which was established within a Facebook group created to facilitate and monitor the therapeutic exercises proposed for the research.

The study population consisted of 100 women with metabolic syndrome who, before the pandemic, attended the Antonio Guiteras sports centre, located in the Habana del Este municipality, Province of Havana, Cuba.

Correspondingly, a Facebook group was created with the selected sample, which consisted of 80 women in total. The entire sample was made up of women with metabolic syndrome, aged between 45 and 55 years, who had abdominal obesity, diabetes mellitus and arterial hypertension, android phones, digital weights, measuring tapes and were Facebook users. The exclusion criteria consisted of women being over 55 years old. This platform was used to send the study instruments, including surveys, data for the instruments (body weight and height), videos explaining what MS is and the importance of practising therapeutic exercises, educational talks, and infographics on metabolic syndrome.

The advantages and disadvantages of using a virtual environment were analysed to make the therapeutic exercise system viable for people with metabolic syndrome who, due to their work duties, find it difficult to attend a specialised centre for this purpose or a gym in their community.

The methods and means that could be adapted from the virtual environment for use in a therapeutic exercise system were analysed.

Furthermore, the system, with adaptations made from the virtual environment, was presented to a group of experts so that they could evaluate the proposal. The recommendations were evaluated in order to reorganise and complete the system of therapeutic exercises.

The anthropometric indices used were body mass index and waist-hip ratio. At the same time, height and body weight in kilograms were measured using digital scales in their homes and evaluated once a week to assess the differences between each of the research weeks.

Similarly, body weight in kg and height in cm were measured to determine BMI before and at the end of the therapeutic exercises.

Arterial hypertension was monitored using a digital sphygmomanometer, and measurements were taken before the start and at the end of the therapeutic exercises.

In the same way, heart rate measurements were taken before, during and at the end of the therapeutic exercises throughout the entire period of the study. The training pulse of each participant served as a starting point to maintain control over the dosage at each stage of the research.

Subsequently, the practice of therapeutic exercises began through the virtual Facebook platform, guided by a virtual instructor. In the same way, measurements of body weight in kg and height in cm squared were taken to determine the BMI before the exercises and at the end. Simultaneously, the heart rate was monitored through the platform group throughout the entire study period, using the training pulse of each participant as a starting point to maintain control of the dosage at each stage of the research. The exercises were performed from Monday to Friday, with a duration of 1 hour, at a medium intensity, and a maximum frequency of 50-80%.

Among the therapeutic exercises chosen to be performed on the platform are low-impact aerobic exercises, which are the most recommended, as they produce an increase or maintenance of cardiorespiratory function or functional capacity, expressed by maximum oxygen consumption, an element considered a predictor of survival; they are generally of a continuous type and use large muscle groups (Jorquera and Cancino, 2012). Among the benefits that this type of activity has on cardiovascular system pathologies is the reduction of risk factors associated with metabolic syndrome. Hence, general strength exercises were performed, which allowed for the strengthening of the organism. Regarding physical capacity, flexibility was utilised to increase the ranges of joint amplitude and muscle and ligament elongation (Chávez and Zamarreño, 2016).

At the end of the research period, the final measurements of body weight and waist circumference were taken after the therapeutic exercise system had been implemented for 6 months.

The questions and surveys were administered to the study sample through a group created on the Facebook platform. To obtain the data for this research, an online survey technique (see Appendix 1: Survey) was used, which consisted of questions developed by a group of experts for the variable of metabolic syndrome and therapeutic exercises from the virtual environment, using a pilot test, where the therapeutic exercises with the adaptations made from the virtual environment were presented to a group of experts in the area of physical culture so that they could evaluate the proposal. The recommendations were evaluated to reorganise and complete the therapeutic exercises as part of the first round, and the suggestions made by the experts to the therapeutic exercises were taken on board.

Subsequently, in the second round, the experts reevaluated the proposal, which yielded positive results in each of the assessed aspects. This allowed for the practical testing of the proposed therapeutic exercises in a small sample, in the form of piloting, to verify whether the assessment made by the experts was achievable in practice. Additionally, the documentary compilation technique was employed, allowing for the collection of relevant information with a high degree of veracity.

Therefore, for the validation of the therapeutic exercise system applied to the participant sample with metabolic syndrome, SPSS software for Windows, version 20, was used. In addition, the descriptive statistical techniques applied were the mean, standard deviation, coefficient of variation, standard error of the mean and the T-test for related samples.

Table 1. Therapeutic Exercise System.

Modality	Exercises Dosage Time %20-30 minutes Average Intensity
Body *vive* (aerobic)	March
	Touching Steps
	Crossing Steps
	Knee Lift Steps
	Forward Touch Steps
	Lateral Touch Steps
	Toe Forward Touch Steps
	Touch steps with toe support to the front left
	Touch steps with toe support backwards
	Leg lift steps backwards.
Modality	Exercises
Yoga (Flexibility)	*UrdhvaMukhaSvanasana* or Upward Facing Dog Pose
	Eka Pada Supta Pavanmuktasana or Knee to Chest Lying Down Posture
	Supta Padangustasana or Lying Down Big Toe Posture
	Urdhva Prasarita Padasana or Legs Raised Upward Posture
Modality	Exercises
Body Pump (Strength)	Triceps Push-up
	Crunch
	Alternating single-leg Extensions

Source: Authors.

Results

Immediately after the therapeutic exercise system was implemented in the virtual Facebook environment, users decreased their levels of abdominal obesity, with the vast majority reducing their weight, despite remaining in the same grade II obesity range, according to the body mass index (Tarriba *et al.*, 2023). The above can be confirmed through the descriptive statistical technique used in this research, indicating that the therapeutic exercise system was revealing, as it determined changes in the results of the practitioners, specifically in terms of waist-hip index (WHI), body mass index, and body weight in kilograms.

After structuring and implementing the therapeutic exercise system for the virtual Facebook environment, the practitioners showed interest and practiced them systematically, managing to reduce their levels of abdominal obesity, reducing the vast majority of them their weight, despite remaining in the same range of obesity grade II, according to the body mass index (Tarriba *et al*., 2023). The above can be confirmed through the descriptive statistical technique used in this research, which indicates that the therapeutic exercise system was revealing, as it determined changes in the results of the practitioners, specifically in terms of waist-hip index (WHI), body mass index, and body weight in kilograms.

The height and weight in kilograms were used to estimate the degree of obesity in the women of the sample under study. The initial and final BMI evaluations showed that the average behaviour was in a lower range, despite remaining within the degree of obesity II, after having carried out the therapeutic exercise system, which demonstrated homogeneity, indicating a decrease in the values of the systematic practitioners.

In terms of the Waist-Hip Index (WHI), the initial and final mean values were very significant <0.001 in the results obtained, which indicates that the therapeutic exercise system for the treatment of metabolic syndrome was effective, demonstrating that although the therapeutic exercises were carried out virtually, it is a judicious alternative that helped the practitioners to get out of their comfort zone, reduce cardiovascular risk factors and improve their quality of life.

Subsequently, a summary table is presented, displaying the statistical data for weight, BMI, standard error of the mean, and WHI, which includes the data for each variable. These results indicate that the smaller the standard error, the more representative the study sample is of the general population.

Table 2. Summary of the statistical data of weight, BMI and WHI.

Statistical	Weight		BMI		WHI	
	Initial	End	Initial	End	Initial	End
Mean	100,16	95,53	37,09	35,37	97,44	88,61
Standard deviation	2,48	1,63	1,51	1,22	15,58	2,30
Coe. V.	2,47	1,70	4,07	3,44	15,98	2,59
Standard error of the mean	0,27	0,18	0,16	0,13	1,74	0,25
Sig	<0,001		<0,001		<0,001	

Source: Authors.

References

WHI: waist-hip index
BMI: Body Mass Index
Sig: p value
Coe. V.: coefficient of variation

Discussion

In the research reviewed, most authors recommend the practice of therapeutic exercises as a treatment. According to Alonso (2008), there is no specific pharmacological treatment for this diagnosis. Its treatment consists of treating the underlying diseases and performing physical exercises (García, 2022). Above all, the prevention of cardiometabolic disease with dietary interventions and lifestyle changes may be more effective in preventing the development of metabolic syndrome than pharmacological treatment. (Alonso, 2008, cited in Julitbert, 2022).

In this sense, we agree with García (2022), as it attaches great importance to the practice of therapeutic exercise and recommends it as part of the treatment that a person with MS should receive, in addition to basic treatment. In Cuba, people with an active lifestyle see their possibilities of continuing with their therapeutic treatments reduced, due to the little time they have to practice therapeutic exercises to control the risk factors of MS (Carrera, 2023).

The study allowed for the assessment of the level of obesity in the population through BMI. Initially, it was found that the entire study sample presented with obesity, a finding consistent with those of Gonzales *et al.* (2021) and other researchers, who have observed that obesity affects the health of the population.

Therefore, it is necessary to highlight that an elevated Body Mass Index is a fundamental component in the diagnosis of MS as a risk factor, as stated by PAHO (2019) in its study. Hence, the importance of maintaining an adequate weight in middle age through physical activity is emphasised.

According to the WHO (2018, cited in PAHO, 2019), therapeutic exercise is an indispensable medicine for the most vulnerable patients with metabolic syndrome; this research demonstrates this with the results obtained in the study. It was necessary to transfer the therapeutic exercises to other environments, such as virtual ones. That is why the contribution of this research was the adaptation of the

therapeutic exercise system to enable its implementation in virtual environments (PAHO, 2019).
In this sense, the author used Facebook's virtual environment for the research, as it is interactive and has a great capacity to connect several users at the same time, as well as being linked to the Messenger application, which in 2016 introduced group video calls of up to 50 participants where only six people can use the camera at the same time and the rest communicate through voice messages. This application is the most suitable alternative for exercising a group of people with SM. The creation of this Facebook group made it possible to send information, such as surveys, videos, educational talks, infographics about SM and therapeutic exercises.
We agree with Juanes and Rodríguez (2021), who recognise that virtual physical education has become an effective tool that can contribute to the quality of life of people in isolation and for people who do not have time to attend rehabilitation centres or gyms. The pedagogy of therapeutic exercises has been oriented towards discovering new methods and strategies to reach more people in the most effective way. The study suggests that a virtual environment can serve as an alternative to traditional therapeutic exercise practice.
Díaz-Canel (2023) stated that hybrid education as a teaching-learning modality became particularly relevant during the confinement caused by the COVID-19 pandemic. At present, it remains as a viable option for teaching innovation by combining the face-to-face and virtual modality, in addition to broadening the spectrum of didactic and methodological alternatives in a context of digital transformation characterised by an extensive use of Information and Communication Technologies (ICT) in all areas of society, especially in the area of therapeutic exercise (Inguanzo and Otero, 2024).

Conclusions

The analysis of the theoretical-methodological foundations that support the therapeutic exercises in the treatment of metabolic syndrome provided elements that justify that, through virtuality, it was possible to control a group of women with this metabolic syndrome, which allowed them to reduce the risk of suffering from cardiovascular diseases.
Through the use of the virtual environment and the therapeutic exercises, it was possible to reduce body weight and thus control the body mass index, as well as the abdominal waist, which made it possible to control the waist-hip index, thus reducing the risk factors involved in metabolic syndrome, after having carried out the therapeutic exercises from the Facebook platform.
The evaluation of the results obtained from the virtual application of therapeutic exercises was positive, demonstrating their relevance through the criteria of specialists, as well as the effectiveness of the exercises and their subsequent practical verification, which was developed through virtual means.

Funding

This work has not received any specific grants from funding bodies in the public, commercial or non-profit sectors.

Bibliographical reference

Belloni, L., Morgagni, G., y Gillispie, C. (1974). Dictionary of scientific biography. New York, Schribner's sons, *volume. (9)*, pp. 510-512. https://www.historiadelamedicina.org/morgagni.html
Carrera, C., Martínez, C., y Calderín, G. (2020). Physical activity for the management of metabolic syndrome in COVID-19, *Action Magazine*, *Volume (16)*, pages 1-4. Public Studies [Online], 2020. [cited 03/06/2020]. Available at: http://accion.uccfd.cu.
Carrera, C. (2023). Physical exercise programme for the treatment of metabolic syndrome in a virtual environment. Master's thesis for the Master's degree in Therapeutic Physical Culture.
Chávez, V., y Zamarreño, H. (2016). Physical exercise and physical activity in the therapeutic approach to obesity and sedentary lifestyles. *Cuban Journal of Physical Medicine and Rehabilitation, Volume (16)* Number 2.https://www.medigraphic.com/cgi-bin/new/resumenI.cgi?IDARTICULO=70537
García, J. (2022). People suffering from diseases characterised by insulin resistance, such as diabetes and hyperinsulinaemia, are more likely to have metabolic syndrome.

*University of Navarra clinic.*https://www.cun.es/enfermedades-tratamientos/enfermedades/sindrome-metabolico
Gonzáles, G., Gavidia, J., Gutiérrez, M., Ibáñez, E., Aro, R., y Díaz, R. (2021) *Evaluación nutricional y actividad física de docentes y administrativos de la Facultad de Farmacia y Bioquímica, Universidad Nacional de Trujillo-Perú. Magazine Pharm.; 2:79-87*. Available at: https://revistas.unitru.edu.pe/index.php/farmabioq/article/view/77721
González, S., Domínguez, C., y Campos, S. (2022). *Actividades y Recursos de Moodle para enseñar Física en la formación de ingenieros civiles. Cuban Light Magazine from Holguin*, *Volume (21),* Number 1. http://scielo.sld.cu/scielo.php?script=sci_arttext&pid=S1814-151X2022000100093.
Inguanzo, M., y Otero, J. (2024) *Auto ejercitación del ejercicio físico en los estudiantes de Educación Física de la Educación Superior.* Pinar del Río, *Magazine Podium, vol. (19)* no. 1. http://scielo.sld.cu/scielo.php?script=sci_arttext&pid=S1996-24522024000100018
Jorquera, A., y Cancino, L. (2012). Exercise, Obesity and Metabolic Syndrome. *Las Condes Clinic Magazine*. https://www.elsevier.es/es-revista-revista-medica-clinica-las-condes-202-articulo-ejercicio-obesidad-sindrome-metabolico-S071686401270305X.
Juanes, B. y Rodríguez, C. (2021) *Educación física en tiempos de COVID-19. Valoraciones a partir de la utilización de las TIC*. *Conrado 17 (79). Cienfuegos Magazine Epub* 02. http://scielo.sld.cu/scielo.php?script=sci_arttext&pid=S1990-86442021000200032
Julitbert, A. (2020). *Ingesta lipídica y síndrome metabólico en adultos con alto riesgo cardiovascular.* https://www.google.com/search.
Márquez, E., y Ordoñez, L. (2023). *Síndrome metabólico, alarma temprana de enfermedades prevenibles.* https://jorcienciapdcl.sld.cu/index.php/jorcienciapdcl23/2023/paper/viewFile/394/547.
Ripoll, M. (2020). *Eficacia del ejercicio terapéutico en fisioterapia para el manejo del dolor lumbar crónico no específico en adultos. NPUNTO Magazine*, *Volume (III),* Number 31. (PDF) p.102. https://www.npunto.es/revista/31/eficacia-del-ejercicio-terapeutico-en-fisioterapia-para-el-manejo-del-dolor-lumbar-cronico-no-especifico-en-adultos
Rodríguez, A., Martínez, J., y Cortina, M. (2023). *Evaluación del índice de masa corporal de los estudiantes de La Institución Educativa Santa Rosa De Lima. Scientific Magazine, Volume (3),* Number *4.* https://www.google.com/search.https://dialnet.unirioja.es/servlet/articulo?codigo=9094330
Romero, M. (2023). *Síndrome metabólico y su relación con la actividad física en los docentes de la Institución Educativa Privada Bethel Christian School, Juliaca.* https://repositorio.continental.edu.pe/bitstream/20.500.12394/13997/1/IV_FCS_507_TE_Romero_Quispe_2023.pdf.
OPS, (2019). *Comunicando sobre COVID-19 informar a las poblaciones sobre los riesgos sanitarios que plantea el COVID-19.* https://www.paho.org/es/temas/coronavirus/brote-enfermedad-por-coronavirus-covid-19/comunicando-sobre-covid-19

Appendix # 1

Survey of Physical Culture experts
Name and surname:
Occupation:
Years of experience:
School level:

You have been selected to evaluate a therapeutic exercise system for the treatment of metabolic syndrome from a virtual environment. Mark with an x the answer you consider in each question. If you mark “No”, please justify your choice. Your answers are important for this research. Thank you for your collaboration.

1. Do you know any system for metabolic syndrome from a virtual environment?
a) Yes____ b) No____ c) I don't know____
2. Do you think that the proposed therapeutic exercises are suitable for the treatment of metabolic syndrome?
a) Yes____ b) No____ c) I don't know____
3. Out of the aerobic exercises presented, do you consider that they correspond to the system of therapeutic exercises?
a) Yes____ b) No____ c) I don't know____
4. Do you consider that the proposed yoga exercises can be worked on virtually?
a) Yes___ b) No____ c) I don't know____
5. Out of the proposed strength exercises, such as Body Pump, do you think that they

are in accordance with the system of therapeutic exercises presented?

a) Yes____ b) No____ c) I don't know____

6. Do you think that therapeutic exercises for patients with metabolic syndrome can be evaluated virtually?

a) Yes____ b) No____ c) I don't know____

7. Do you consider that the system of therapeutic exercises with the content of Body Pump and Body *Vive* is suitable for people with metabolic syndrome?

a) Yes___ b) No____ c) I don't know____

8. Do you think that this therapeutic exercise system can be applied to a group of people with metabolic syndrome in a virtual environment?

a) Yes___ b) No____ c) I don't know____

RECyT
Year 27 / Nº 43 / 2025 /
DOI: https://doi.org/10.36995/j.recyt.2025.43.010

Designing a Packed Column for Ammonia Recovery: Evaluating Two Packing Types

Diseño de una columna empacada en la recuperación de amoníaco: evaluación de dos tipos de empaque

Amaury, Pérez Sánchez[1, *]; Helen M., Alfonso Fernández[1]; Greisy I., Valero Almanza[2]; Nadia, Corpas Rodríguez[1]; Alicia M., Gómez Julián[1]

1- Facultad de Ciencias Aplicadas. Universidad de Camagüey “Ignacio Agramonte Loynaz”. Carretera Circunvalación Norte, Km. 5½, e/ Camino Viejo de Nuevitas y Ave. Ignacio Agramonte, Camagüey, Cuba.
2- Departamento de Gestión Ambiental. Centro de Ingeniería Ambiental de Camagüey. Avenida Finlay km. 2½, Puerto Príncipe, Camagüey, Cuba.
*Correo electrónico: amauryps@nauta.cu

Received: 01/02/2023; Accepted: 06/05/2025

Abstract
Gas absorption is a mass transfer operation that involves separating components from a gaseous mixture by contacting them with a suitable liquid, typically performed in packed columns. In this study, a packed column was designed for the absorption of gaseous ammonia using water as a solvent, and two types of packing were evaluated: ceramic Raschig rings and metallic Hiflow rings. The use of Hiflow rings resulted in a 30.35% reduction in column diameter compared to Raschig rings. Furthermore, the total pressure drop of the gas-liquid system at 70% flooding was 17.81% lower for Hiflow rings (522.16 Pa/m) than for Raschig rings (615.16 Pa/m). The calculated convective mass transfer coefficients for both liquid and gas phases were also higher when using Hiflow rings compared to Raschig rings. Based on these findings, Hiflow rings are recommended for this mass transfer application due to the smaller column internal diameter and lower pressure drop obtained, as well as the higher mass transfer coefficients achieved with this packing type compared to Raschig rings.

Keywords: Packed column; Internal diameter; Pressure drop; Mass-transfer coefficients; Design.

Resumen
La absorción gaseosa es una operación de transferencia de masa que consiste en la separación de componentes de una mezcla gaseosa mediante el contacto con un líquido adecuado, típicamente llevada a cabo en columnas empacadas. En el presente trabajo se diseñó una columna empacada para efectuar la absorción de amoníaco gaseoso usando agua como solvente y evaluando dos tipos de empaque, anillos Raschig cerámicos y anillos Hiflow metálicos. Los anillos Hiflow redujeron el diámetro de la columna en un 30.35% comparado con los anillos Raschig, mientras que la caída de presión total del sistema gas-líquido a 70% de inundación fue un 17.81% menor para los anillos Hiflow (522.16 Pa/m) que para los anillos Raschig (615.16 Pa/m). Los valores calculados de los coeficientes de transferencia de masa convectivos para las fases líquida y gaseosa fueron superiores para los anillos Hiflow en comparación con los anillos Raschig. Basado en estos resultados, se recomienda los anillos Hiflow para esta aplicación de transferencia de masa, debido a los bajos valores obtenidos para el diámetro interno de la columna y caída de presión, así como también los valores superiores de los coeficientes de transferencia de masa alcanzados para este tipo de empaque comparados con los anillos Raschig.

Palabras claves: Columna empacada; Diámetro interno; Caída de presión, Coeficientes de transferencia de masa; Diseño.

Introduction

Unit operation techniques in the chemical process industries (CPI) facilitate the separation of a mixture or mixtures into their individual components. These operations are commonly referred to as diffusional or mass transfer operations. The techniques employed in the CPI to achieve these separations include: distillation, absorption, liquid extraction, drying, leaching, crystallization, and gas adsorption [1].

In counter-current separation processes, such as distillation, extraction, and gas absorption, the separation relies on the transfer of one or more components between the contacting fluid phases [2]. Following distillation, gas/liquid absorption is arguably the second most crucial separation operation utilized in the chemical and related industries [3].

Gas-liquid absorption is a heterogeneous process that involves the transfer of a soluble component from a gas phase into a relatively non-volatile liquid absorbent [4]. There are instances where a solute diffuses through a vapor phase and is subsequently absorbed into an immiscible fluid phase, as exemplified by the absorption of ammonia from air using water [5].

To enhance the efficiency of this process by increasing mass transfer between the phases, the contact between these phases is intensified through the application of phase contactor devices, namely trays (plates) or packings. The contact between the phases is stagewise when using trays, and continuous when using packings [2].

One of the most prevalent and rapidly developing methods used to perform the absorption process on an industrial scale is the packed column (Figure 1).

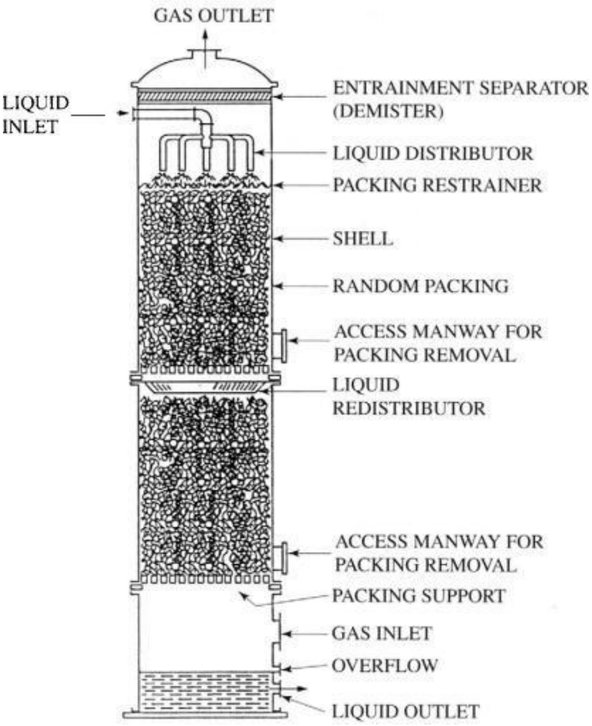

Figure 1. Packed tower with random packing and its sections.

A packed column is essentially a vertical pipe filled with an inert material, commonly known as packing materials [6]. Typically, a packed tower operates in a countercurrent manner, where the liquid enters from the top and wets the surfaces of the packing, while the gas stream containing the effluent enters from the bottom. As the two streams come into intimate contact, the effluent components are absorbed into the liquid. The liquid surface area available for mass transfer and the time available for the diffusion of gaseous molecules into the liquid are considered crucial factors affecting the process's performance. Mass transfer to the liquid continues until the liquid approaches saturation, at which point equilibrium is established between the two phases [7].

To meet the requirements of column size optimization (in terms of height and diameter) and pressure drop limitation, efficient and high-capacity packings, along with appropriate designs for the gas and liquid distributors, are essential [8]. The distribution of the liquid and gas phases within the packing is ensured by gas-liquid tray distributors located at the top of each packed bed and a bottom gas distributor at the column's base [8]. In a packed column, the packing section is responsible for providing the surface area where the liquid and gas phases contact, making it a critical component of the column [4].

The packing section plays a vital role in the absorption process by providing surface area for gas and liquid phases to interact. Broadly, two main types of packing materials are available for gas absorption: random packing (e.g., Pall rings, IMTP, Hiflow, Raschig rings) and structured packing (e.g., Flexipac, Mellapak, Gempak, BX) [9]. These are manufactured from a variety of construction materials, including polymers, plastics, ceramics, and metals [5].

Random packings, which are porous solids of various shapes such as spheres, coils, mesh, and cylinders, have been in use since the early 20th century. They consist of discrete structural elements randomly dumped into a column to form the absorption section. Typical sizes for random packings range from 1 to 10 cm. In contrast, structured packings are composed of corrugated metal sheets or wire mesh arranged vertically in the column as blocks of assembled layers. The corrugation sizes typically fall between 0.5

and 2 cm, with block sizes on the order of 25 cm [2].

The primary objective of any packing is to maximize efficiency for a given capacity at a reasonable cost. To achieve this, packing materials are designed with the following characteristics in mind [10]:

- Maximize the specific surface area: This maximizes the vapor-liquid contact area, thereby enhancing efficiency.
- Ensure uniform surface area distribution: This improves vapor-liquid contact and, consequently, efficiency.
- Maximize the void space per unit column volume: This minimizes resistance to gas up-flow, thereby increasing packing capacity.
- Minimize friction: This is facilitated by an open shape with favorable aerodynamic characteristics.
- Minimize cost.

According to [9], the two most critical factors for selecting packing material are surface area and void fraction. Additionally, the material should be chemically inert to the fluids being processed and possess sufficient structural strength for easy handling and installation [11].

The Raschig ring, first patented by Dr. Fritz Raschig in Germany in 1907, was the inaugural standardized packing. Until the 1960s, packed columns were predominantly filled with Raschig rings or Berl saddles, collectively known as first-generation packings. Raschig rings are hollow cylinders with diameters ranging from 6 to 100 mm or more (Figure 2a). They can be manufactured from metal, ceramic, or plastic [11]. Due to their high porosity, Hiflow rings (Figure 2b) are considered third-generation packings, making them suitable for high gas flow rates and thus well-suited for treating industrial gaseous effluents [12].

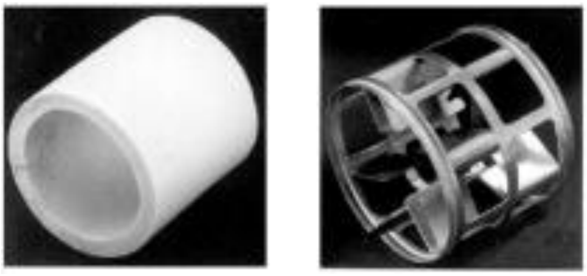

a) b)

Figure 2. Two common packing types used in packed columns.
a) Ceramic Raschig ring.
b) Metal Hiflow ring.

The selection of column internals necessitates a thorough understanding of the specific purpose of the gas/liquid absorption application, along with precise knowledge of the characteristics of the gas and liquid solvent flows throughout the packed bed. This includes their hydrodynamic behavior (e.g., pressure drop, flooding) and mass transfer properties (e.g., gas-side and liquid-side mass transfer coefficients) [8].

Despite their considerable industrial success, packed columns encounter various operational challenges, including flooding, channeling, entrainment, and foaming [13]. Nevertheless, their advantages include lower liquid holdup, reduced pressure drops [5], higher capacity, and increased interfacial area [2].

A comprehensive understanding of a gas absorption process hinges on several parameters. These include fluid stream analysis, the study of the packed column's hydrodynamic features, determination of fluid mass balance, calculation of mass transfer coefficients, and the calculation of drag and flooding flows. It also involves examining the physicochemical properties and composition of the fluids, component recovery from the fluid streams, industrial design, process simulation, evaluation of influencing factors (e.g., column diameter, packing height, mass transfer coefficient, molar flow rates), process design, countercurrent two-phase flow studies, optimization of the stream ratio (inert liquid to gas), effective packing surface area, the influence of packing type, and the assessment of column efficiency for fractionators, absorbers, and strippers [5].

Gas/liquid absorption is widely employed in recovering vapors from gas streams, treating gases in refineries, and for industrial waste treatment [5]. It also finds numerous industrial applications, such as acid gas removal, solvent-based post-combustion carbon dioxide (CO2) capture [8], sour gas scrubbing, and petroleum refining operations [7].

Packed columns are increasingly utilized across diverse applications within the chemical process industries. This trend is driven by an increase in the availability of design information, the development of higher-capacity and more efficient mass-transfer packings, and advancements in distributors and support plates. Today, packings can be considered for most services requiring a high number of theoretical stages for mass transfer [1].

Numerous studies have evaluated or investigated packed columns for various applications and services. These include:

- The absorption of sulfur dioxide from air into a sodium hydroxide solution using HelieR packing [14].
- CO2 absorption into aqueous solutions of single and blended alkanolamines in a bench-scale absorber packed with high-efficiency packings [15].
- The absorption of CO2 in monoethanolamine and 2-amino-2-methyl-1-propanol using a counter-current absorber containing DX structured packing [13].
- The determination of hydrodynamic characteristics and mass transfer in a pilot plant packed bed absorption column filled with Raschig rings for CO2 absorption from air using water [3].
- The absorption of CO2 into aqueous ammonia solution in a packed column containing 8-mm ceramic Raschig [16].
- Physical modeling, computational fluid dynamics analysis, and experimental analysis of a packed column containing 25-mm polypropylene Pall rings, used for flue gas desulfurization to reduce sulfur dioxide emissions [17].
- The absorption of CO2 into aqueous ammonia solution using a packed column containing 8-mm ceramic Raschig rings as packing material. This study experimentally evaluated the packed column's performance under various conditions to reveal the effects of several process parameters, including CO2 partial pressure in the gas phase, gas flow rate, liquid flow rate, ammonia concentration, and temperature [18].
- The evaluation of CO2 absorption into aqueous ammonia solution using a packed column with 8-mm ceramic Raschig rings to assess overall CO2 absorption rates. This revealed the effects of several process parameters, including ammonia concentration, liquid flow rate, CO2 inlet concentration, gas flow rate, and the temperatures of the ammonia solution and the gas [19].
- The development and validation of a model for CO2 absorption using 3 wt% dilute aqueous ammonia solution in both rotating packed beds and standard packed beds, utilizing experimental data. The resulting model was then employed to design absorbers for various throughput rates, ranging from 0.01 to 1,000 tons of CO2 capture per day [20].

The removal efficiencies for gas absorbers vary depending on the pollutant-solvent system and the type of absorber used. Most absorbers achieve removal efficiencies exceeding 90%, with packed tower absorbers potentially reaching efficiencies as high as 99.9% for some pollutant-solvent systems [7].

Currently, most modern industrial plants implement gas treatment systems to mitigate emissions of harmful air pollutants generated during their processes. Specifically, ammonia gas is a significant contributor to air pollution, leading to the deterioration of the atmospheric environment. Given that packed tower operation is considered cost-effective, ammonia-water absorption columns are increasingly popular today for addressing environmental issues linked to ammonia emissions [7].

Several authors have evaluated packed columns for gaseous ammonia absorption. For instance, [21] investigated the ammonia absorption rate from air by water in a 1-foot-diameter tower packed with carbon Raschig rings. They also examined the effect of gas rate, liquor rate, temperature, ring size, degree of inlet gas humidification, and the reproducibility of a given tower filling. Individual film coefficients were calculated using Sherwood and Holloway's liquid film correlation. Similarly, [22] explored the absorption of ammonia from an air stream in a multiple-stage crosscurrent packed column, suitable for gas-liquid mass transfer. Water served as the solvent in this study, Pall rings were selected as the packing material for all experimental runs, and the ammonia-air-water system was chosen due to its high commercial importance, relative safety, ease of handling with proper precautions, and readily available thermodynamic and physical data. The absorption column in this study consisted of a rectangular box constructed from Plexiglas and metal, with deflection baffles strategically placed at regular intervals on opposite sides of a central packed section to divert the gas phase into the packing, thereby creating a crisscross gas-liquid flow pattern.

Other authors also studied the absorption of ammonia from an air stream into water in a packed tower, publishing their findings in two papers. In the first [23], they measured pressure loss, holdup, and liquid distribution for a standard 10 mm glass Raschig ring packing contained in a Quickfit packed tower with a 10.2 cm inside diameter. In the second [24], they outlined a simple modification of gas absorption theory for this setup, enabling the determination of mass transfer coefficients in laboratory apparatus that have been successfully used in industrial equipment design. These authors concluded that the theory can be developed to an increasing degree of mathematical sophistication to address the most complex experimental situations. The general method derived in this study has clear applications to other mass transfer processes, particularly those employing packed towers.

Likewise, [7] described two new empirical models based on the composite desirability function methodology for predicting packed column diameter and packing height in physical ammonia absorption problems. A computational analysis encompassing a total of 131 absorption scenarios was conducted for six fundamental operating parameters: inlet gas flow rate (500-5000 m^3/h), solute concentration in the inlet gas (5-10%), desired removal efficiency (87-98%), operating temperature (10-60 °C), percentage of the minimal liquid-to-gas flow rates ratio (24-52%), and percent of flooding velocity (30-80%). Ceramic Raschig rings were chosen as one of the most common packing types for this study. The paper's aim was to provide a tool for researchers, students, engineers, and others, enabling rapid calculation of packing height and packed column diameter for physical ammonia absorption with Raschig rings, without requiring the full theoretical procedures detailed in the literature. It also aimed to offer a practical, novel reference for absorber designers, researchers, manufacturers, absorber-equipment engineers, and end-user industries for real-life packed tower design under varying ammonia absorption data using common operating parameters.

Furthermore, [4] reported an experimental evaluation of perlite from Lamba, Albay, Bicol, as a packing material for gaseous ammonia absorption using liquid water as a solvent, with the goal of subsequently designing a packed column based on the obtained results. Finally, [25] developed a model to predict the performance of a packed bed absorber for an ammonia-water absorption refrigeration system, evaluating two packing types: Raschig rings and Berl Saddles. The resulting model was used in a parametric study to investigate the effect of several design and operating parameters on the absorber's performance.

In the present work, a packed column is designed for the absorption of gaseous ammonia using water as a solvent. This study evaluates two different packing types: ceramic Raschig rings and metal Hiflow rings. Key parameters such as column inside diameter, total pressure drop of the gas-liquid system at 70% flooding, and the convective mass transfer coefficients for both phases are determined. The objective is to identify which packing type is most appropriate for this mass transfer service, considering the results obtained for the key parameters for both packings. To achieve this objective, the methodology proposed in [11] is applied.

Materials and methods

Problem definition

The objective is to recover ammonia from a dry air stream, where the ammonia concentration is 8% mol. The total inlet flow rate of the ammonia/air gas stream is 40 kmol/h, with an inlet temperature of 303 K and a pressure of 1 atm. The desired ammonia recovery is 90%, utilizing pure liquid water as a solvent. The available water flow rate is 1,700 kg/h, and its feed temperature and pressure are 298 K and 101.3 kPa, respectively. Two packing materials will be evaluated for this mass transfer service::

- 25-mm ceramic Raschig rings.
- 25-mm metal Hiflow rings.

For both packing materials, the following must be determined:

a) Column inside diameter.
b) Pressure drop for operation at 70% of flooding.
c) Mass transfer coefficients for both phases.

The total pressure drop of the gas-liquid system at 70% of flooding must not exceed 600 Pa/m for either packing.

Collection of initial data:

- Mole fraction of air in the gas phase (y_{air}) = 0.92.
- Mole fraction of ammonia in the gas phase (y_{NH3}) = 0.08.
- Molar flow rate of the gas phase (V) = 40 kmol/h.
- Inlet temperature of the gas phase (T_G) = 303 K.
- Inlet pressure of the gas phase (P_G) = 101.3 kPa = 1.013 bar = 1 atm.
- Inlet temperature of water (T_L) = 298 K.
- Inlet pressure of water (P_L) = 1 atm.
- Mass flow rate of the inlet liquid (L) = 1,700 kg/h.
- Ideal gas constant (R) = 8.314 J/mol.K = 0.08205 atm.m^3/kmol.K [10].
- Percentage of ammonia to be scrubbed ($\%S_{NH3}$) = 0.9.
- Molecular weight of ammonia (M_{NH3}) = 17.03 g/mol.
- Molecular weight of air (M_{air}) = 28.96 g/mol.
- Density of water at T_L and P_L (ρ_L): 997 kg/m^3 [10].
- Viscosity of water at T_L and P_L (μ_L): 0.000890 Pa.s [10].
- Packing factor for 25-mm ceramic Raschig rings (F_P) = 179 [11].
- Packing factor for 25-mm metal Hiflow rings (F_P) = 42 [11].
- Viscosity of dry air at 303 K and 1 atm (μ_{air}) = 0.00001869 Pa.s [10].
- Viscosity of ammonia at 303 K and 1 atm (μ_{NH3}) = 0.00001030 Pa.s [10].

Column inside diameter

Most packed columns consist of cylindrical vertical vessels. According to [7], if the gas velocity through the column is gradually increased by utilizing columns with progressively smaller diameters, a point is reached where the liquid flowing downwards over the packing begins to be retained within the void spaces of the packing. A further increase in gas velocity beyond this loading point causes the liquid to completely fill the packing's void spaces. Ultimately, the liquid forms a layer over the top of the packing, preventing any further downward flow through the tower. This condition is termed flooding, and the gas velocity at which it occurs is known as the flooding velocity. For this reason, standard practice dictates sizing a packed column diameter to operate below the flooding velocity, specifically at a certain percentage of it.

The column diameter is determined to safely avoid flooding and ensure operation in the preloading region, with a pressure drop not exceeding 1.2 kPa/m of packed height (equivalent to 1.5 in. of water head per foot of packed height) [11]. Flooding establishes the minimum possible diameter for the absorber column, and the typical design operates at 50 to 75 percent of the flooding velocity [7]. It is assumed that by operating within this range, the gas velocity will also remain below the loading point.

Step 1. Molecular weight of the inlet gas (ammonia-air mixture) (M_G):

$$M_G = M_{air} \cdot y_{air} + M_{NH3} \cdot y_{NH3} \quad (1)$$

Step 2. Mass flow rate of the gas phase (V'):

$$V' = \frac{V \cdot M_G}{3{,}600} \quad (2)$$

Step 3. Density of the gas phase (ρ_G):

$$\rho_G = \frac{P_G \cdot M_G}{R \cdot T_G} \quad (3)$$

Where P_G = 101.3 kPa.

Step 4. Volumetric flow rate of the gas phase (Q_G):

$$Q_G = \frac{V'}{\rho_G} \quad (4)$$

Step 5. Ammonia absorbed (A_{NH3}):

$$A_{NH3} = V \cdot y_{NH3} \cdot \%S_{NH3} \cdot M_{NH3} \quad (5)$$

Step 6. Mass flow rate of the exiting liquid (L'):

$$L' = \frac{L + A_{NH3}}{3{,}600} \quad (6)$$

Step 7. Flow parameter (X):

$$X = \frac{L'}{V'} \cdot \left(\frac{\rho_G}{\rho_L}\right)^{0.5} \quad (7)$$

Step 8. Pressure drop parameter under flooding (Y_{flood}):

$$lnY_{flood} = -[3.5021 + 1.028 \cdot lnX + 0.11093 \cdot (lnX)^2] \quad (8)$$

Step 9. Parameter Cs under flooding (Cs_{flood}):

$$Cs_{flood} = \left[\frac{Y_{flood}}{F_p \cdot \mu_L^{0.1}}\right]^{0.5} \quad (9)$$

Step 10. Superficial gas velocity at flooding (v_{GF}):

$$v_{GF} = \frac{Cs_{flood}}{\left[\frac{\rho_G}{\rho_L - \rho_G}\right]^{0.5}} \quad (10)$$

Step 11. Pressure drop at flooding (ΔP_{flood}):

$$\Delta P_{flood} = 93.9 \cdot F_p^{0.7} \quad (11)$$

Step 12. Superficial gas velocity at 70% of flooding (v_G):

$$v_G = 0.7 \cdot v_{GF} \quad (12)$$

Step 13. Column inside diameter (D)

$$D = \left[\frac{4 \cdot Q_G}{\pi \cdot v_G}\right]^{0.5} \quad (13)$$

Total pressure drop for operation at 70% flooding

The pressure drop (ΔP) through a packed bed accounts for frictional losses, kinetic energy losses through the packing, and the force exerted by the operating liquid holdup. At a constant ΔP, the packed bed exhibits less volumetric liquid holdup in systems with high liquid density. Conversely, with low-density liquids, the volumetric liquid holdup can be significantly greater than that for water at the same ΔP [1].

Step 14. Hydraulic parameters for both random packings:

According to [11], the two random packings evaluated in this study exhibit the hydraulic parameters presented in Table 1.

Table 1. Hydraulic parameters of the two random packings evaluated.

Parameter	Symbol	Units	Raschig	Hiflow
Mass-transfer surface area per unit volume	a	m^2/m^3	190	202.9
Porosity or void fraction	ε	-	0.680	0.962
Packing constant C_h	C_h	-	0.577	0.799
Packing constant C_p	C_p	-	1.329	0.689

Step 15. Effective particle diameter (d_p):

$$d_p = 6 \cdot \left(\frac{1-\varepsilon}{a}\right) \quad (14)$$

Step 16. Wall factor (K_W):

$$K_W = \frac{1}{1 + \frac{2}{3} \cdot \left(\frac{1}{1-\varepsilon}\right) \cdot \frac{d_p}{D}} \quad (15)$$

Step 17. Viscosity of the gas phase (μ_G):

$$\mu_G = \frac{M_G}{\frac{y_{air} \cdot M_{air}}{\mu_{air}} + \frac{y_{NH3} \cdot M_{NH3}}{\mu_{NH3}}} \quad (16)$$

Step 18. Reynolds number of the gas phase (Re_G):

$$Re_G = \frac{v_G \cdot d_p \cdot \rho_G \cdot K_W}{(1-\varepsilon) \cdot \mu_G} \quad (17)$$

Step 19. Dry-packing resistance coefficient (Ψ_0):

$$\Psi_0 = C_p \cdot \left(\frac{64}{Re_G} + \frac{1.8}{Re_G^{0.08}}\right) \quad (18)$$

Step 20. Dry-gas-pressure drop ($\frac{\Delta P_0}{Z}$):

$$\frac{\Delta P_0}{Z} = \Psi_0 \cdot \frac{a}{\varepsilon^3} \cdot \frac{\rho_G \cdot v_G^2}{2} \cdot \frac{1}{K_W} \qquad (19)$$

Step 21. Liquid mass velocity (G_L):

$$G_L = \frac{4 \cdot L'}{\pi \cdot D^2} \qquad (20)$$

Step 22. Reynolds number of the liquid phase (Re_L):

$$Re_L = \frac{G_L}{a \cdot \mu_L} \qquad (21)$$

Step 23. Liquid Froude number (Fr_L):

$$Fr_L = \frac{G_L^2 \cdot a}{\rho_L^2 \cdot g} \qquad (22)$$

Step 24. Ratio of specific areas ($\frac{a_h}{a}$):

- For $Re_L < 5$:

$$\frac{a_h}{a} = C_h \cdot Re_L^{0.5} \cdot Fr_L^{0.1} \qquad (23)$$

- For Re_L ε 5

$$\frac{a_h}{a} = 0.85 \cdot C_h \cdot Re_L^{0.25} \cdot Fr_L^{0.1} \qquad (24)$$

Step 25. Specific liquid holdup (h_L):

$$h_L = \left[12 \cdot \frac{Fr_L}{Re_L}\right]^{1/3} \cdot \left[\frac{a_h}{a}\right]^{2/3} \qquad (25)$$

Step 26. Total pressure drop of the gas-liquid system at 70% flooding ($\frac{\Delta P}{Z}$):

$$\frac{\Delta P}{Z} = \frac{\Delta P_0}{Z} \cdot \left(\frac{\varepsilon}{\varepsilon - h_L}\right)^{1.5} \cdot exp\left(\frac{Re_L}{200}\right) \qquad (26)$$

Mass transfer coefficients

Step 27. Lennard-Jones parameters for air and ammonia:
According to [26] the Lennard-Jones parameters for both the air and ammonia are as follows:
Air:

- σ_{air} = 3.620 Å
- ε_{air}/k = 97.0 K

Ammonia:

- σ_{NH3} = 2.900 Å
- ε_{NH3}/k = 558.3 K

Step 28. Mass-transfer parameters for both packings:
As stated by [11], the mass-transfer parameters for the two random packings evaluated are:

25-mm ceramic Raschig rings:

- C_L = 1.361
- C_V = 0.412

25-mm metal Hiflow rings:

- C_L = 1.641
- C_V = 0.402

Step 29. Molar volume for ammonia at normal boiling point [$V_{b(NH3)}$]:
As reported by [11], the molar volume of ammonia at its normal boiling point is $V_{b(NH3)}$ = 25.8 cm^3/mol.

Step 30. Parameter δ:

$$\delta = \frac{9.58}{V_{b(NH3)}} - 1.12 \qquad (27)$$

Step 31. Liquid diffusion coefficient of ammonia in the aqueous solution (D_L):

$$D_L = 1.25 \times 10^{-8} \cdot \left(V_{b(NH3)}^{-0.19} - 0.292\right) \cdot T_L^{1.52} \cdot (\mu_L \cdot 1{,}000)^{\delta} \cdot 0.0001 \qquad (28)$$

Step 32. Molecular weight of the gaseous mixture (M_{AB}):

$$M_{AB} = 2 \cdot \left[\frac{1}{M_A} + \frac{1}{M_B}\right]^{-1} \qquad (29)$$

Step 33. Average collision diameter (σ_{AB}):

$$\sigma_{AB} = \frac{\sigma_{air} + \sigma_{NH3}}{2} \qquad (30)$$

Step 34. Average Lennard-Jones parameter ($\frac{\varepsilon_{AB}}{k}$):

$$\frac{\varepsilon_{AB}}{k} = \sqrt{\frac{\varepsilon_{air}}{k} \cdot \frac{\varepsilon_{NH3}}{k}} \qquad (31)$$

Step 35. Parameter T^*:

$$T^* = \frac{T_G}{\frac{\varepsilon_{AB}}{k}} \qquad (32)$$

Step 36. Diffusion collision integral (Ω_D):

$$\Omega_D = \frac{1.06036}{(T^*)^{0.15610}} + \frac{0.193}{exp(0.47635 \cdot T^*)} + \frac{1.03587}{exp(1.52996 \cdot T^*)} + \frac{1.76474}{exp(3.89411 \cdot T^*)} \qquad (33)$$

Step 37. Gaseous diffusion coefficient of ammonia in air (D_G):

$$D_G = \frac{\left[3.03 - \frac{0.98}{M_{AB}^{0.5}}\right] \cdot (10^{-3}) \cdot T_G^{1.5}}{P_G \cdot M_{AB}^{0.5} \cdot \sigma_{AB}^2 \cdot \Omega_D \cdot 0.0001} \quad (34)$$

Where P_G = 1,013 bar.

Step 38. Liquid velocity (v_L):

$$v_L = \frac{4 \cdot L'}{\pi \cdot \rho_L \cdot D^2} \quad (35)$$

Step 39. Convective mass-transfer coefficient in dilute liquid phase (k_L):

$$k_L = 0.757 \cdot C_L \cdot \left[\frac{D_L \cdot a \cdot v_L}{\varepsilon \cdot h_L}\right]^{0.5} \quad (36)$$

Step 40. Schmidt number for gaseous phase (Sc_G):

$$Sc_G = \frac{\mu_G}{\rho_G \cdot D_G} \quad (37)$$

Step 41. Convective mass-transfer coefficient in gaseous phase (k_G):

$$k_G = 0.1304 \cdot C_V \cdot \frac{D_G \cdot P_G}{R \cdot T_G} \cdot \frac{a}{[\varepsilon \cdot (\varepsilon - h_L)]^{0.5}} \cdot \left[\frac{Re_G}{K_W}\right]^{0.75} Sc_G^{0.667} \quad (38)$$

Where R = 0.08205 atm.m^3/kmol.K [10] and P_G = 1 atm.

Results and discussion

The numerical results obtained for the main parameters determined using the packed column design methodology for both evaluated packings are presented below. These parameters include the column inside diameter, the pressure drop of the gas-liquid system at 70% flooding, and the mass transfer coefficients for both the liquid and gaseous phases.

Column inside diameter

Table 2 displays the results of the parameters determined in Steps 1-13, which were ultimately used to calculate the packed tower diameter for both packings.

Table 2. Results of the parameters determined in steps 1-13 for both packings.

Step	Parameter	Symbol	Raschig	Hiflow	Units
1	Molecular weight of the inlet gas	M_G	28.01	28.01	g/mol
2	Mass flow rate of the gas phase	V'	0.311	0.311	kg/s
3	Density of the gas phase	ρ_G	1.126	1.126	kg/m^3
4	Volumetric flow rate of the gas phase	Q_G	0.276	0.276	m^3/s
5	Ammonia absorbed	A_{NH3}	49.05	49.05	kg/h
6	Mass flow rate of the exiting liquid	L'	0.486	0.486	kg/s
7	Flow parameter	X	0.052	0.052	-
8	Pressure drop parameter under flooding	Y_{flood}	0.238	0.238	-
9	Parameter Cs under flooding	Cs_{flood}	0.052	0.107	m/s
10	Superficial gas velocity at flooding	v_{GF}	1.547	3.184	m/s
11	Pressure drop at flooding	ΔP_{flood}	3,545.38	1,285.11	Pa/m
12	Superficial gas velocity at 70% of flooding	v_G	1.083	2.229	m/s
13	Column inside diameter	D	0.570	0.397	m

According to the values presented in Table 2, the calculated column inside diameter (D) for the Hiflow rings (0.397 m) is 30.35% lower than the value calculated for the Raschig rings (0.570 m). This difference is primarily attributed to the lower packing factor (F_P) of Hiflow rings compared to that of Raschig rings. Specifically, a lower F_P for Hiflow rings leads to an increased Cs_{flood} parameter, which in turn raises the superficial gas velocity under flooding (v_{GF}) as well as the superficial gas velocity at 70% flooding (v_G), ultimately resulting in a smaller column inside diameter.

Table 2 also indicates that 49.05 kg/h of ammonia are absorbed for each packing. Furthermore, the superficial velocity of the gas under flooding is 51.41% higher for Hiflow rings (3.184 m/s) compared to Raschig rings

(1.547 m/s). This difference causes the pressure drop at flooding to be 63.75% higher for Raschig rings (3,545.38 Pa/m) than for Hiflow rings (1,285.11 Pa/m).

Yetilmezsoy [7] investigated the physical absorption of ammonia from an air stream using water as a solvent in a packed column equipped with ceramic Raschig rings. He presented two new empirical models based on the composite desirability function methodology for predicting packed column diameter and packing height. According to Yetilmezsoy's findings, the packed column diameter was 0.799 m for an average inlet gas flow rate of 2,750 m³/h, an average ammonia concentration in the inlet gas of 7.5%, an average desired removal efficiency of 92.5%, an operating temperature of 35 °C, and a flooding velocity percentage of 55%. As reported by this author, increasing the flooding velocity percentage will decrease the column diameter for the same inlet gas flow rate.

Total pressure drop for operation at 70% flooding

Table 3 presents the results of the parameters calculated in Steps 15-26, which were used to determine the total pressure drop of the gas-liquid system at 70% flooding for both packings.

Table 3. Results of the parameters determined in Steps 15-26 for both packings.

Step	Parameter	Symbol	Raschig	Hiflow	Units
15	Effective particle diameter	d_p	0.010	0.001	m
16	Wall factor	K_W	0.965	0.958	-
17	Viscosity of the gas phase	μ_G	0.000018	0.000018	Pa.s
18	Reynolds number of the gas phase	Re_G	2043.02	3515.26	-
19	Dry-packing resistance coefficient	Ψ_0	1.341	0.658	-
20	Dry-gas pressure drop	$\frac{\Delta P_0}{Z}$	554.83	438.04	Pa/m
21	Liquid mass velocity	G_L	1.906	3.928	kg/m^2.s
22	Reynolds number of the liquid phase	Re_L	11.27	21.75	-
23	Liquid Froude number	Fr_L	0.000071	0.000321	-
24	Ratio of specific areas [using equation (24) since Re_L ε 5]	$\frac{a_h}{a}$	0.346	0.655	-
25	Specific liquid holdup	h_L	0.021	0.042	-
26	Total pressure drop of the gas-liquid system at 70% flooding	$\frac{\Delta P}{Z}$	615.16	522.16	Pa/m

According to the results presented in Table 3, the total pressure drop of the gas-liquid system at 70% flooding is 17.81% higher for Raschig rings (615.16 Pa/m) compared to Hiflow rings (522.16 Pa/m). This difference is attributed to several factors: the Reynolds number of the liquid phase (Re_L) is 48.18% higher for Hiflow rings (21.75) than for Raschig rings (11.27), and the porosity and void fraction (ε) of Hiflow rings are 29.31% higher than those for Raschig rings. This outcome is further influenced by the fact that the dry gas pressure drop is 21.05% lower for Hiflow rings (438.04 Pa/m) compared to Raschig rings (554.83 Pa/m). As can be observed, the calculated total pressure drop for the gas-liquid system at 70% flooding for the Raschig rings exceeded the maximum limit established for the process, which is 600 Pa/m. Consequently, it is concluded that Raschig rings cannot be employed for the desired mass transfer service due to the excessive pressure drop obtained.

Mass transfer coefficients

Table 4 displays the results of the parameters calculated in Steps 30-41, which were used to determine the mass transfer coefficients for both the liquid and gaseous phases for the two considered packings.

Table 4. Results of the parameters determined in Steps 30-41 for both packings.

Step	Parameter	Symbol	Raschig	Hiflow	Units
30	Parameter ™	δ	-0.749	-0.749	-
31	Liquid diffusion coefficient	D_L	1.94x10^{-9}	1.94x10^{-9}	m^2/s
32	Molecular weight of the gaseous mixture	M_{AB}	21.46	21.46	g/mol
33	Collision diameter	σ_{AB}	3.26	3.26	Å
34	Average Lennard-Jones parameter	$\frac{\varepsilon_{AB}}{k}$	232.71	232.71	K
35	Parameter $T*$	T^*	1.302	1.302	-
36	Diffusion collision integral	Ω_D	1.274	1.274	-
37	Gaseous diffusion coefficient of ammonia in air	D_G	2.34x10^{-5}	2.34x10^{-5}	m^2/s
38	Liquid velocity	v_L	0.002	0.004	m/s
39	Convective mass-transfer coefficient in dilute liquid phase	k_L	2.34 x10^{-4}	2.45x10^{-4}	m/s
40	Schmidt number for gaseous phase	Sc_G	0.683	0.683	-
41	Convective mass-transfer coefficient in gaseous phase	k_G	0.00347	0.00389	kmol/m^2.s

Considering the results presented in Table 4, the convective mass-transfer coefficient in the diluted liquid phase (k_L) is 4.49% higher for Hiflow rings (2.45x10^{-4} m/s) than for Raschig rings (2.34x10^{-4} m/s). This occurred because the values for the mass-transfer surface area per unit volume (a), liquid velocity (v_L), and the mass transfer parameter C_L are all higher for Hiflow rings compared to Raschig rings. On the other hand, the convective mass transfer coefficient in the gaseous phase (k_G) is 10.79% higher for Hiflow rings (0.00389 kmol/m²·s) than for Raschig rings (0.00347 kmol/m²·s). This is due to higher values for the parameters mass-transfer surface area per unit volume (a), mass transfer parameter C_V, and Reynolds number of the gas phase (Re_G) for Hiflow rings, while the wall factor (K_W) is lower.

From the numerical results obtained during the packed column design, we conclude that Hiflow rings should be used instead of Raschig rings. This is because Hiflow rings yield a smaller internal diameter, a lower total pressure drop, and higher mass-transfer coefficients. These conclusions align with findings reported in [11], which also indicated a lower column inside diameter and pressure drop for Hiflow rings compared to Raschig rings for a similar ammonia absorption mass-transfer service.

Conclusions

A packed column was designed for the absorption of gaseous ammonia using water as a solvent, with two packing types evaluated. The metallic Hiflow rings proved to be optimal for this mass transfer service, resulting in a column diameter 30.35% lower (0.397 m) and a pressure drop 17.81% lower (522.16 Pa/m) than the ceramic Raschig rings. Furthermore, Hiflow rings yielded higher mass-transfer coefficients for both the gaseous (0.00389 kmol/m²·s) and liquid (2.45x10^{-4} m/s) phases.

Nomenclature

$\frac{a_h}{a}$	Ratio of specific areas	-
A_{NH3}	Ammonia absorbed	kg/h
C_h	Packing constant	-
C_L	Mass-transfer parameter	-
C_p	Packing constant	-
Cs_{flood}	Parameter under flooding	m/s
C_V	Mass-transfer parameter	-
d_p	Effective particle diameter	m
D	Column inside diameter	m
D_G	Gaseous diffusion coefficient	m^2/s
D_L	Liquid diffusion coefficient	m^2/s
F_P	Packing factor	-
Fr	Froude number	-
G	Mass velocity	kg/m^2.s

h_L	Specific liquid holdup	-
k_G	Convective mass-transfer coefficient in gaseous phase	$kmol/m^2.s$
k_L	Convective mass-transfer coefficient in dilute liquid phase	m/s
K_W	Wall factor	-
L	Mass flow rate of the inlet liquid	kg/h
L'	Mass flow rate of the exiting liquid	kg/s
M	Molecular weight	g/mol
M_{AB}	Molecular weight of the gaseous mixture	g/mol
P	Inlet pressure	kPa/atm/bar
ΔP_{flood}	Pressure drop at flooding	Pa/m
$\frac{\Delta P}{Z}$	Total pressure drop of the gas-liquid system at 70% of flooding	Pa/m
$\frac{\Delta P_0}{Z}$	Dry-gas-pressure drop	Pa/m
Q	Volumetric flow rate	m^3/s
R	Ideal gas constant	J/mol.K or $atm.m^3/kmol.K$
Re	Reynolds number	-
Sc	Schmidt number	-
$\%S_{NH3}$	Percentage of ammonia to be scrubbed	-
T	Inlet temperature	K
T^*	Parameter	-
v_G	Superficial gas velocity at 70% of flooding	m/s
v_{GF}	Superficial gas velocity at flooding	m/s
v_L	Liquid velocity	m/s
V	Molar flow rate of the gas phase	kmol/h
V'	Mass flow rate of the gas phase	kg/s
X	Flow parameter	-
y	Mole fraction	
Y_{flood}	Pressure drop parameter under flooding	-

Greek symbols

δ	Parameter	-
ε	Porosity or void fraction	-
ρ	Density	kg/m^3
μ	Viscosity	Pa.s
σ	Collision diameter	Å
ε/k	Average Lennard-Jones parameter	K
Ψ_0	Dry-packing resistance coefficient	-
Ω_D	Diffusion collision integral	-

Subscripts

air	Air
G	Gas phase
L	Liquid phase
NH3	Ammonia

References

1. Coker, A. K. (1995). Chapter 7. Mass Transfer. In *FORTRAN Programs for Chemical Process Design, Analysis and Simulation*. Texas, USA: Gulf Publishing Company.
2. Hegely, L., Roesler, J., Alix, P., Rouzineau, D., & Meyer, M. (2017). Absorption Methods for the Determination of Mass Transfer Parameters of Packing Internals: A Literature Review. *AIChE Journal, 63*(8), 3246-3275. doi: 10.1002/aic.15737.
3. Sovilj, M. N., Nikolovski, B. G., Spasojević, M. Đ., & Mauhar, S. M. (2019). Packed bed absorption column: hydrodynamics and mass transfer. *Acta Periodica Technologica, 50*(1-352), 260-267. doi: 10.2298/APT1950260S.
4. Mateo, B. S., Valorozo, J., Yturralde, M. N. J., & Pestaño, L. D. (2019). Development and characterization of perlite from Lamba, Albay, Bicol as packing material and the design of a packed column for the absorption of ammonia gas. *MATEC Web of Conferences, 268*(04001), 1-7. doi: 10.1051/matecconf/201926804001.
5. Beltrán, J. C., & Kolomazník, K. (2019). Parameters Determination for Column Design in Gas Absorption Systems. *WSEAS Transactions on Fluid Mechanics, 14*, 124-130.
6. Cussler, E. L. (1997). *Absorption. Diffusion: Mass Transfer in Fluid Systems* (2nd ed.). USA: Cambridge University Press.
7. Yetilmezsoy, K. (2011). Composite desirability function-based empirical modeling for packed tower design in physical ammonia absorption. *Asia-Pacific Journal of Chemical Engineering, 7(6),* (6), 795–813. doi:1002/apj.635.
8. Haroun, Y., & Raynal, L. (2016). Use of Computational Fluid Dynamics for Absorption Packed Column Design. *Oil & Gas Science and Technology, 71*(43), 1-18. doi:10.2516/ogst/2015027.

9. Arachchige, U. S. P. R., & Melaaen, M. C. (2012). Selection of Packing Material for Gas Absorption. *European Journal of Scientific Research, 87*(1), 117-126.
10. Green, D. W., & Southard, M. Z. (2019). *Perry's Chemical Engineers' Handbook* (9th ed.). USA: McGraw-Hill Education.
11. Benitez, J. (2009). *Principles and modem applications of mass transfer operations* (2nd ed.). USA: John Wiley & Sons.
12. Heymes, F., Demoustier, P. M., Charbit, F., Fanlo, J.-L., & Moulin, P. (2006). Hydrodynamics and mass transfer in a packed column: Case of toluene absorption with a viscous absorbent. *Chemical Engineering Science, 61*(15), 5094 - 5106. doi: 10.1016/j.ces.2006.03.037.
13. deMontigny, D., Tontiwachwuthikul, P., & Chakma, A. (2005). Comparing the Absorption Performance of Packed Columns and Membrane Contactors. *Industrial & Engineering Chemistry Research, 44*(15), 5726–5732. doi:10.1021/ie040264k.
14. Brunazzi, E., Nardini, G., & Paglianti, A. (2002). An Economical Criterion for Packed Absorption Column Design. *Chem. Biochem. Eng. Q., 14*(4), 199-206.
15. Aroonwilas, A., & Veawab, A. (2004). Characterization and Comparison of the CO2 Absorption Performance into Single and Blended Alkanolamines in a Packed Column. *Industrial & Engineering Chemistry Research, 43*(9), 2228-2237. doi:10.1021/ie0306067.
16. Nair, P. S., & Selvi, P. P. (2014). Absorption of Carbon Dioxide in Packed Column. *International Journal of Scientific and Research Publications, 4*(4), 1-11.
17. Maheswari, C., Krishnamurthy, K., & Parameshwaran, R. (2014). Modeling and experimental analysis of packed column for SO2 emission control process. *Atmospheric Pollution Research, 5*, 464-470. doi:10.5094/APR.2014.054.
18. Zeng, Q., Guo, Y., Niu, Z., & Lin, W. (2011). Mass Transfer Coefficients for CO2 Absorption into Aqueous Ammonia Solution Using a Packed Column. *Industrial & Engineering Chemistry Research, 50*(17), 10168-10175. doi:10.1021/ie101821b.
19. Zeng, Q., Guo, Y., Niu, Z., & Lin, W. (2013). The absorption rate of CO2 by aqueous ammonia in a packed column. *Fuel Processing Technology, 108*, 76-81. doi:10.1016/j.fuproc.2012.05.005.
20. Kang, J.-L., Wong, D. S.-H., Jang, S.-S., & Tan, C.-S. (2016). A comparison between packed beds and rotating packed beds for CO2 capture using monoethanolamine and dilute aqueous ammonia solutions. *International Journal of Greenhouse Gas Control, 46*, 228-239. doi: 10.1016/j.ijggc.2016.01.017.
21. Dwyer, O. E., & Dodge, B. F. (1941). Rate of Absorption of Ammonia by Water in a Packed Tower. *Industrial en Engineering Chemistry, 33*(4), 485-492. doi:10.1021/ie50303a004.
22. Zuehlsdorff, D. A. (1979). *Absorption of Ammonia in Water Using a Multiple Stage Crosscurrent Packed Column.* (Master of Science), Oregon State University, Oregon, USA.
23. Spedding, P. L., Munro, P. A., & Jones, M. T. (1986). Ammonia Absorption into Water in a Packed Tower I: Characterization of Packing and Liquid Distribution. *The Chemical Engineering Journal, 32*(2), 65-76. doi:10.1016/0300-9467(86)80053-3.
24. Spedding, P. L., Jones, M. T., & Lightsey, G. R. (1986). Ammonia Absorption into Water in a Packed Tower II: Measurement of Mass Transfer Coefficients. *The Chemical Engineering Journal, 32*(3), 151-163. doi:10.1016/0300-9467(86)80003-x.
25. Selim, A. M., & Elsayed, M. M. (1999). Performance of a packed bed absorber for aqua ammonia absorption refrigeration system. *International Journal of Refrigeration, 22*(4), 283–292. doi:10.1016/s0140-7007(98)00066-8.
26. Reid, R. C., Praunitz, J. M., & Poling, B. E. (1987). *The Properties of Gases and Liquids* (4th ed.). USA: McGraw-Hill.